Unconventional metrology: Merging nanophotonics with computational imaging

Ph.D. thesis University of Amsterdam, December 2020
Unconventional metrology: Merging nanophotonics with computational imaging
Ruslan Röhrich

ISBN 978-94-92323-44-6

A digital version of this thesis can be downloaded from https://ir.amolf.nl/.

Unconventional metrology: Merging nanophotonics with computational imaging

ACADEMISCH PROEFSCHRIFT

ter verkrijging van de graad van doctor
aan de Universiteit van Amsterdam
op gezag van de Rector Magnificus
prof. dr. ir. K. I. J. Maex
ten overstaan van een door het College voor Promoties ingestelde
commissie, in het openbaar te verdedigen in de Agnietenkapel
op vrijdag 11 december 2020, te 13:00 uur

door

Ruslan Röhrich

geboren te Altajskoje

Promotor:	prof. dr. A. F. Koenderink	Universiteit van Amsterdam
Copromotor:	dr. S. M. Witte	Vrije Universiteit Amsterdam
Overige leden:	prof. dr. P. Banzer	FAU Erlangen-Nürnberg
	prof. dr. A. den Boef	Vrije Universiteit Amsterdam
	prof. dr. P. C. M. Planken	Universiteit van Amsterdam
	prof. dr. A. Polman	Universiteit van Amsterdam
	dr. R. J. C. Spreeuw	Universiteit van Amsterdam

Faculteit der Natuurwetenschappen, Wiskunde en Informatica

This work was carried out at the
Center for Nanophotonics, AMOLF,
Science Park 104, 1098 XG Amsterdam, The Netherlands
and at the *Advanced Research Center for Nanolithography (ARCNL),*
Science Park 106, 1098 XG Amsterdam, The Netherlands,
where a limited number of copies of this dissertation is available.

This work is part of the Dutch Research Council (NWO)
and was performed at the research institute AMOLF.
This work has been carried out at ARCNL,
a public-private partnership of UvA, VU, NWO and ASML.

Contents

1

Introduction

"At present the most instructed persons are, I suppose, very far from perceiving the full and close coincidence between all the facts of light and the physical account of them which the theory supplies. If perfect, the theory would be able to give a reason for every physical affection of light; whilst it does not do so, the affections are in turn fitted to develop the theory, to extend and enlarge it if true, or if in error to correct it or replace it by a better."

— Michael Faraday, *The Bakerian Lecture - Experimental relations of gold (and other metals) to light*, 1857

1

1.1. Measuring with light

The goal of this thesis is to study applications of nanophotonics and computational imaging in optical metrology. Optical metrology is the science of *measuring* with *light*. This thesis particularly aims at *dimensional metrology* challenges, i.e., physical size or distance measurements, that are typically encountered in the semiconductor industry and other demanding nanotechnology areas. Over the years, a wide variety of optical concepts has been discovered and exploited for optical metrology. In essence, these techniques can be categorized into *imaging* techniques on one hand, such as microscopy, and *non-imaging* approaches on the other hand, such as using spectroscopic or diffractive fingerprints of displacement. A crucial difference is that microscopy aims to image arbitrary geometrical features with the best possible resolution over a large field of view, whereas non-imaging approaches focus on retrieving a given parameter in an already quite accurately known sample with the highest precision. There are two main reasons why light is so broadly applied in metrology. First, using the wavelength of light as a 'ruler' ultimately traces its precision to the optical frequency and coherence properties of the light source, which can be very precisely known. Secondly, light is a non-invasive probe that is easily converted into an electrical signal. Various instruments, i.e. CMOS/CCD cameras or photodetectors, make the process of digital light recording uncomplicated, fast, and with a performance at the shot-noise limit afforded by the photon budget. The recent advancements in computer technology allow researchers to make optimal use of these digital signals. At the forefront of current developments is the pursuit of a higher resolution in microscopy aided by computer algorithms, and the extraction of precise information about an object of interest from the light it interacted with.

This work particularly focuses on optical metrology at small length scales, i.e., micrometer to nanometer distances, which is the realm of length scales that require microscopes to visualize them. The optical microscope is one of the most powerful and widespread instruments in today's laboratories since it allows scientists to effortlessly observe small features of an object under study. The basic idea that curved glass can be used to magnify images has existed for many centuries. Even though since the 17th century microscopes have undergone significant developments, and though microscopes consist of many individual parts, to this day its most critical components remain the lenses [1]. With the best microscope objectives, one can for instance observe biological samples at a cellular level. At the same time, objects constituting the cells that are below $< 200\,\mathrm{nm}$ in size remain blurred. This is caused by a fundamental resolution limit in optical microscopy, discovered by Ernst Abbe in the 19th century [2]. The Abbe diffraction limit states that for two point-like objects to be resolvable, their distance should exceed

$$d = \frac{\lambda}{2\mathrm{NA}}, \tag{1.1}$$

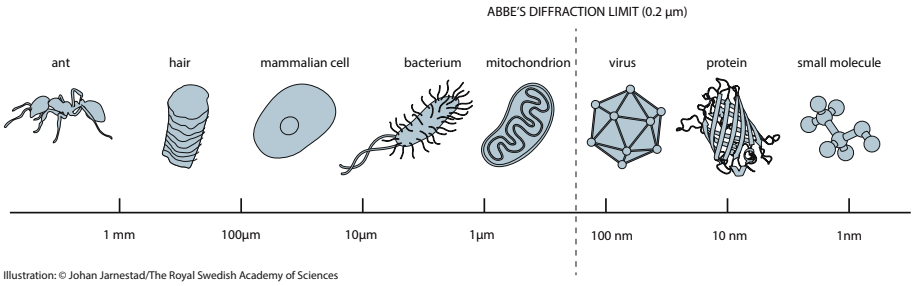

Figure 1.1: Size overview of macro- to nanoscopic biological objects below and above Abbe's diffraction limit. (reproduced with permission, Johan Jarnestad/The Royal Swedish Academy of Sciences).

where λ is the illumination wavelength and $\mathrm{NA} = n \sin\theta$ is the numerical aperture of the optical system. From Eq. (1.1) one concludes that the resolution of an optical system can be improved by collecting a larger cone of angles θ and using a higher refractive index (n) immersion medium. High-NA objectives that are available today typically collect a cone of angles up to 72° and use immersion oil with $n \approx 1.45$. This results in a maximally attainable resolution of around 200 nm for visible light ($\lambda = 400\,\mathrm{nm} - 700\,\mathrm{nm}$). Figure 1.1 gives an overview of typical biological objects one can and cannot resolve due to the diffraction limit. In practice, additional factors such as signal-to-noise ratio and aberrations can hinder a diffraction-limited optical resolution. Indeed, modern microscope objectives feature optimized arrangements of high-quality optical elements in compound microscope objectives lenses to combat aberrations and thereby reach, but not exceed, the best possible imaging resolution predicted by Ernst Abbe.

With all the evidence pointing towards a fundamental resolution limit at roughly half the wavelength, for many years any far-field technique claiming to *break* the diffraction barrier was met with skepticism. In the past two decades, however, it has been demonstrated that far-field techniques can break the diffraction barrier, both in imaging and in optical metrology contexts. Generally, the key to these advancements is an advanced understanding of the imaging process, as well as the use of prior knowledge about the sample, as input or constraint for algorithmic reconstruction approaches. In this introductory chapter, different relevant concepts that will be used in this work are introduced. In Section 1.2, we will introduce the concept of non-imaging optical nanometrology techniques commonly used in the semiconductor industry. Furthermore, this section will also introduce inverse problems, which are a recurring motif in this thesis. Section 1.3.1 introduces the Fourier-space microscopy technique. Sections 1.3.2 and 1.3.3 mathematically describe the diffraction limit in coherent and incoherent microscopy, while Section 1.3.4 deals with super-resolution techniques

in fluorescence microscopy. Section 1.4 will describe digital holography, which is a common approach to retrieve phase information from intensity measurements. Further, Section 1.4.3 deals with computational phase retrieval methods. These treat imaging as a purely mathematical problem, that can be solved using the appropriate algorithm. Some computational methods even go as far as removing all the imaging optics from the setup, which is why they are referred to as 'lensless'. Finally, since the emphasis of this thesis is on leveraging concepts from nanophotonics for optical metrology, we will briefly highlight a few fundamental concepts and existing applications of nanophotonics in Sec. 1.6, before giving an outline of this thesis in Sec. 1.7.

1.2. Optical nanometrology

Optical nanometrology is a key enabler of many scientific and information technology applications. Nowadays, nanotechnology is all around us in the form of CMOS circuitry in everyday appliances and in the smartphones sitting in our pockets. This increasing pervasiveness of information technology in our daily lives is enabled by, and at the same time spurs, rapid developments in the semiconductor industry. Over the years, the minimum feature size of semiconductor devices has been aggressively reduced, roughly doubling their component count every two years [3]. While this semiconductor miniaturization has led to exponentially faster computation performance, the requirements on process metrology are becoming more and more stringent [4]. IC circuits are defined by a sequence of spatial patterning steps, with a required relative alignment tolerance that shrinks with the minimum feature size of the technology node.

As mentioned in the last section, the optical resolution limit hinders imaging at the required scale of $\lesssim 10$ nm, which is a common size of the smallest elements inside of today's computer chips. To circumvent this imaging resolution challenge, optical nanometrology focuses on retrieving only a few essential dimensional parameters of nano-objects, as opposed to striving for collecting a full image. Optical nanometrology techniques solve the inverse problem of light scattering by accurately modeling the measurement process. In the following, the concept of inverse problems is briefly introduced, before proceeding to review currently used approaches in optical nanometrology.

1.2.1. Inverse problems

Optical nanometrology is a typical example of an *inverse problem*, in which one attempts to quantitatively reconstruct the *cause* of an observed *effect* [5]. This should be contrasted to *direct problems*, which have the goal of finding the effect due to a known cause. Unfortunately, in many applications the parameters one wishes to identify can only be measured indirectly, requiring the solution of an inverse problem. The main difficulty when trying to

solve inverse problems is that in some cases the accessible data is ambiguous and the reconstruction process unstable. In 1923 Hadamard classified inverse problems in two groups, namely *ill-* and *well-posed* problems [6]. He defined a problem to be well-posed only if the following three conditions are satisfied:

1. the inverse problem has a solution;
2. the solution is determined uniquely;
3. the solution depends continuously on the data.

If any of these conditions are violated the problem becomes ill-posed. Even though these three conditions seem straightforward, they are often not met in problems encountered in physics and engineering. For instance, light scattering measurements typically contain statistical or systematic noise and usually do not uniquely determine the underlying parameters of the scatterer. Other prominent examples of ill-posed problems are deconvolution (deblurring) of images [7, 8] or the phase problem [9], which will be further discussed in Sec. 1.4.3. In general, ill-posedness indicates a lack of information that prevents one from obtaining an unambiguous solution of the inverse problem. Over the years, many techniques have been introduced in order to deal with ill-posed problems in imaging [7, 10]. A core aspect of most approaches is the reformulation of the inverse problem as a minimization of an error functional, which describes the mismatch between the actually measured and modeled data. An established approach to solving such ill-posed minimization problems is through *regularization*. In regularization, the effect of ill-posedness is relaxed by slightly altering the initial problem to create another better behaved one [11]. Commonly, this can be done through the addition of prior knowledge into the reconstruction process, which reduces the number of possible solutions.

1.2.2. Model-based optical metrology

In *model-based optical metrology* the inverse problem of light scattering is solved by accurately modeling the measurement process, while heavily relying on prior knowledge [12]. The goal of these techniques is to retrieve select parameters of a nanostructure under test with much higher precision than is possible with a standard microscopic imaging approach. Examples of such parameters are the relative position of two known objects (e.g., the 'overlay' of two patterned layers on a wafer) or a size parameter describing a nanoscale feature (e.g., 'critical dimension'). Important applications of model-based optical metrology are in the semiconductor and nanomanufacturing industry [4]. During the semiconductor manufacturing process, critical dimension (CD) and overlay (OV) errors are monitored and corrected to achieve a high *yield*, i.e., a high percentage of correctly working devices per wafer. Upcoming process nodes require a sub-nanometer range CD and OV error precision,

which poses an increasing challenge for metrology [13, 14]. In addition to a high yield, chip production needs a high throughput rate to be economically viable. This leads to stringent requirements on the available time to perform all the necessary metrology operations. Besides, the metrology tool should be non-destructive, and highly accurate [13, 14]. *Scatterometry* is a model-based metrology technique that fulfills these industry needs. This non-contact and non-destructive method offers a high speed and sub-nanometer precision, even when based in visible wavelength instrumentation [15–18]. Alternative methods such as scanning electron microscopy (SEM), atomic force microscopy (AFM), transmission electron microscopy (TEM) and small-angle X-ray scattering (SAXS), have the drawback of a lower operation speed and a higher price. A further disadvantage of SEM and TEM is that they often cause damage to the imaged region (for TEM the sample even needs to be cross-sectioned) [13, 14]. Despite its disadvantages, SEM is still heavily used for CD measurements as it does have the advantage of a high resolution and easily interpretable results.

Figure 1.2 illustrates a common procedure used in scatterometry and other model-based optical metrology techniques, which allows one to solve the inverse diffraction problem. It consists of two essential aspects: the acquisition of the *scattered signature* of a nanostructure under test and the replication of the measurement *in-silico* using a simulation technique, also known as the *forward model*. In order to acquire the scattering signature, one can use several scatterometry configurations, such as angular or spectroscopic implementations that record reflectometry or ellipsometry signals [16–18]. In the simulation step, the experiment is recreated in a parametrized way and a series of scattering signatures are calculated. Since the scattering object (metrology target) is usually approximately known, the investigated parameter space can be limited in size. The resulting scattering signatures are stored in a so-called library, which is effectively a lookup table for the precise relationship between different nanostructure parameters and the corresponding diffraction signals. Essential for such a forward model approach is the speed and accuracy of the simulation technique used to calculate the optical response of the sample by solving Maxwell's equations. Currently, the most widely adapted forward modeling method is rigorous coupled-wave analysis (RCWA) [19]. Other available techniques include the boundary element method (BEM) [20], the finite element method (FEM) [21] and the finite-difference time-domain (FDTD) [22] technique. Before comparing the measurement and simulation signature, usually some sort of compression or feature extraction is performed. Popular feature extraction strategies include singular value decomposition, principal component analysis, independent component analysis or Fourier transform analysis [23]. The inverse diffraction problem is solved by finding the closest match between measured and simulated features. This is done by either searching library data or by directly optimizing the simulation to match the measured signature [16–18].

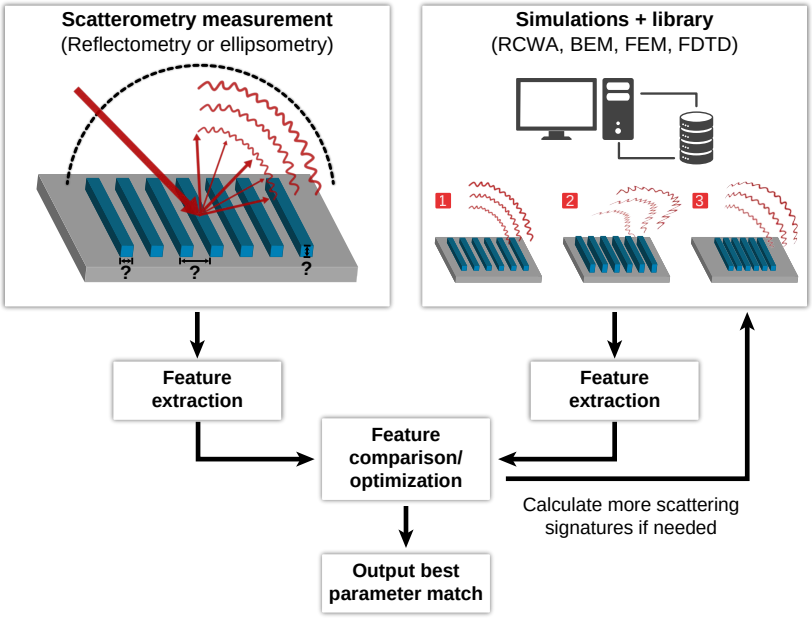

Figure 1.2: Model-based optical metrology workflow, which relies on a library search strategy to solve the inverse diffraction problem. Features from the measured scattering signature are extracted and compared to features obtained from simulations. The closest match yields the desired parameters of the scattering sample.

Fourier scatterometry is an extension of scatterometry that uses the full back-focal plane image of a high-NA detection system to gather information about diffraction gratings [24–26]. The advantage of this method is that it allows measurements of multiple diffraction orders of two-dimensional (2D) gratings at the same time. The diffracted light pattern can be further used to gain characteristic information about the grating itself, such as pitch and orientation of the grating [26]. As will be discussed in Chapter 4, Fourier scatterometry or back-focal plane imaging can be augmented by polarimetry and digital holography, in order to additionally collect polarization and phase information and therefore gain even more insight about the scattering object.

Scatterometry is widely applied for OV error determination in semiconductor wafer manufacturing, an application domain in which the technique is referred to as diffraction-based overlay (DBO) metrology. In DBO light back-scattered from an overlay target is measured and analyzed. This target typically consists of a stack of two line gratings, one of them buried in already processed layers, while the top grating is often the photoresist layer on top of the half-finished wafer [17]. The two gratings both provide ±1st diffraction orders. Depending on the lateral displacement (overlay) between gratings, interference causes a measurable unbalance between the intensity in the 1st

and −1st diffraction order. An outstanding challenge in DBO is to separate this signature of overlay from systematic errors, such as fabrication fluctuations [13]. Chapter 3 contributes to resolving this challenge, as we study novel two-dimensional overlay target designs in terms of their robustness to fabrication errors.

1.3. Important microscopy concepts

1.3.1. Fourier-space microscopy

In conventional microscopy, a lens-based system is used to create a wide-field image of the sample plane. In Figure 1.3(a), an optical ray-trace of a regular microscopy configuration is shown that creates a magnified image of a sample on a detector. In this 'infinity-corrected' microscope, the sample is placed in the front-focal plane of the objective and a magnified image is formed on an image sensor by the so-called tube lens. In the setup configuration, shown in Figure 1.3(b), an additional lens is placed downstream of the objective such that the back-focal plane (BFP) of the microscope objective is projected onto the detector. In the BFP light rays traveling at the same angle (same color in Fig. 1.3(b)) from sample plane to objective converge at the same position, with the position in the BFP a direct measure for the angle.

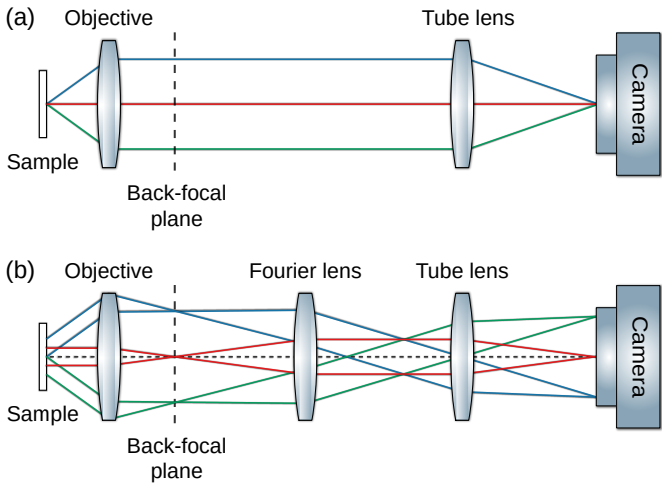

Figure 1.3: A sketch showing the operating principle of regular (real-space) and Fourier-space microscopy. (a) In regular microscopy, the objective (infinity-corrected) collects a cone of angles from every sample position. Further downstream the different angles are focused by a tube lens onto a single point on the camera. (b) In Fourier-space microscopy an additional lens (Fourier lens) is introduced to project the back-focal plane onto the camera. This causes light rays scattered at the same angle (same colored lines) converge to the same position on the camera.

This microscopy technique, which is also known as 'Fourier-space' microscopy or 'conoscopy', can be used to measure the directionality of light scattering or emission [27–29]. The term 'Fourier-space' imaging derives from the fact that a lens performs a Fourier transform operation, rendering the Fourier transform of the front-focal plane in its back-focal plane. All light scattered at angles higher than the maximal acceptance angle of the lens is blocked. As will be explained in the next section this is equivalent to low-pass Fourier filtering and causes a blurred image to appear behind the lens.

1.3.2. Coherent imaging

Coherent imaging involves measurement of light scattering by an object that is illuminated with a source such as a single-mode laser, that provides a large temporal coherence (i.e., monochromatic illumination) and transverse spatial coherence (e.g, plane waves, or a single-mode exiting from a glass fiber). A detailed definition of coherence will be given in Sec. 1.5. Mathematically, the coherent imaging process can be expressed as a convolution of the *complex amplitude* of the sample $A(x,y)$ with the coherent point spread function cPSF [30]

$$M(x,y) = A(x,y) \otimes \mathrm{cPSF}(x,y), \tag{1.2}$$

where $M(x,y)$ denotes the 'blurred' complex image and $\otimes$ a 2D convolution. The cPSF describes the optical field one would attain when imaging a point source with the optical system. This blurring process, can be described in a more computationally efficient manner by transforming Eq. 1.2 into the Fourier domain:

$$\mathcal{F}\{M(x,y)\} = \mathcal{F}\{A(x,y)\} \cdot \mathrm{CTF}, \tag{1.3}$$

where $\mathcal{F}$ denotes the 2D Fourier transform operation and CTF, which represents a Fourier transformed cPSF, is the so-called coherent transfer function. The imaging process described by Eq. 1.3 is demonstrated in Fig. 1.4. It amounts to a simple Fourier space filtering operation, whereby the CTF represents the Fourier space filter. As shown in Fig. 1.4(c), the CTF can be modeled as a circle in Fourier-space with a radius, that is referred to as the cutoff frequency k_{cutoff}. The cutoff frequency for coherent imaging can be expressed as

$$k_{\mathrm{cutoff}} = \mathrm{NA} \cdot k_0 = \mathrm{NA} \cdot \frac{2\pi}{\lambda_0}, \tag{1.4}$$

where λ_0 is the illumination wavelength. The region spanned by the CTF is referred to as the passband of the optical system and it carries the information about the complex object that is transported through the optical system. The signal outside of the passband is lost during the imaging process, whereby information about finer object features are remove. This low-pass Fourier filtering causes the image to look blurred, and is the root cause of Abbe's diffraction limit.

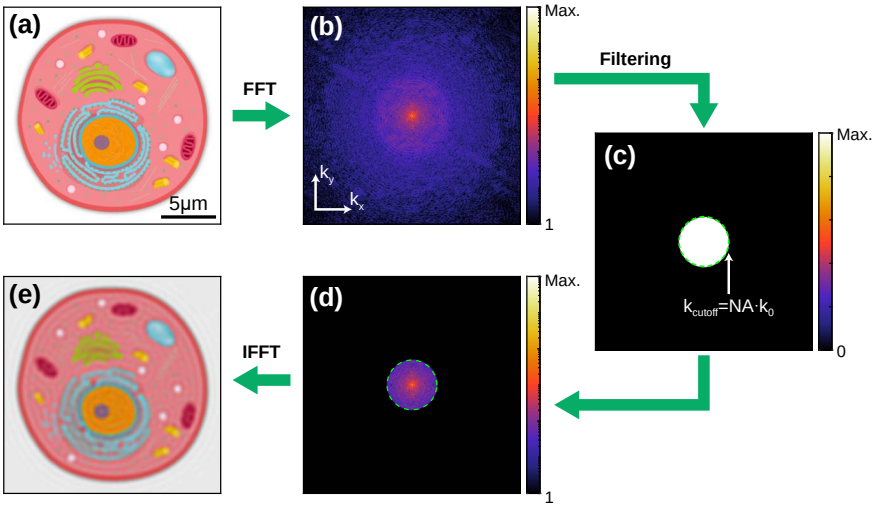

Figure 1.4: Simulation of the coherent imaging process via Fourier processing. (a) The real part of the high-resolution sample amplitude $A(x,y)$. (b) The magnitude of the Fourier transform of $A(x,y)$. (c) Coherent transfer function assuming an NA $= 0.85$ and $\lambda_0 = 561.3\,\text{nm}$. (d) The magnitude of the Fourier transform of $A(x,y)$ multiplied with the CTF. (e) The real part of the blurred sample image $M(x,y)$, which was calculated by taking inverse Fourier transform of (d). Panels (b) and (d) use a logarithmic color scale.

1.3.3. Incoherent imaging

Fluorescence microscopy is a prime example of an incoherent imaging process. Fluorescent samples contain materials that are able to absorb photons and re-emit them at randomized points in time, with a random phase, and often with emission energy in a wide spectrum. This re-emission has lower energy and therefore a longer wavelength $\lambda_{\text{em}} > \lambda_0$. To separate this emission light from the excitation light, fluorescence microscopes use a dichroic mirror in combination with a high-pass filter. For incoherent imaging, it is characteristic that emission from different points on the sample adds up incoherently, i.e., without interference effects playing a role. This should be contrasted to coherent imaging, where field radiated by distinct points on the sample interferes on the detector.

Similarly to the coherent case, the incoherent imaging process can be mathematically expressed as a convolution of the sample *intensity* $S(x,y)$ with the incoherent point spread function PSF

$$M(x,y) = S(x,y) \otimes \text{PSF}(x,y), \tag{1.5}$$

where $M(x,y)$ denotes the 'blurred' intensity image. The PSF can be understood as the intensity one would measure when imaging a point source using the optical system. Once again, by going to the Fourier domain the expensive

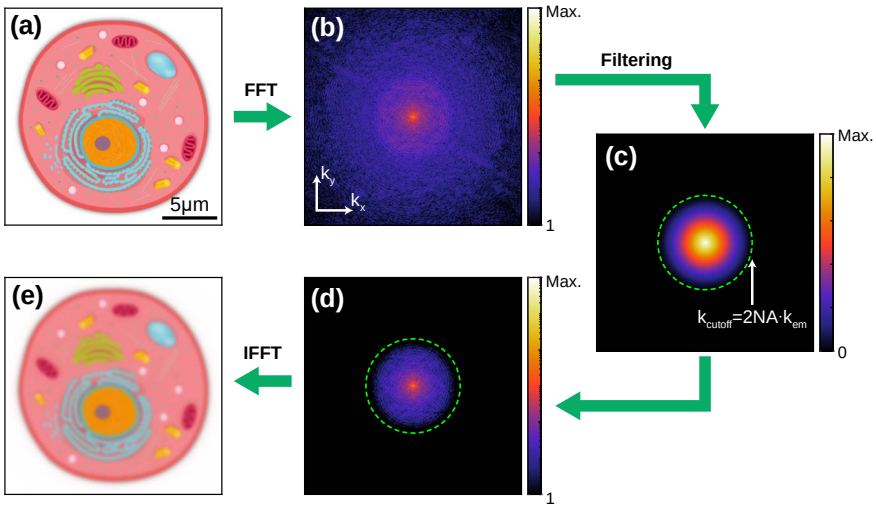

Figure 1.5: Simulation of the incoherent imaging process via Fourier processing. (a) High resolution sample intensity image $S(x,y)$. (b) Magnitude of the Fourier transform of $S(x,y)$. (c) Optical transfer function assuming NA $= 0.85$ and $\lambda_{\text{em}} = 577\,\text{nm}$. (d) Magnitude of the Fourier transform of $S(x,y)$ multiplied with the OTF. (e) Blurred sample image $M(x,y)$ calculated by taking inverse Fourier transform of (d). Panels (b) and (d) use a logarithmic color scale.

convolution operation can be avoided and Eq. 1.5 can be written as:

$$\mathcal{F}\{M(x,y)\} = \mathcal{F}\{S(x,y)\} \cdot \text{OTF}, \tag{1.6}$$

where OTF is the so-called optical transfer function, that can be calculated by Fourier transforming the PSF. The imaging process as described by Eq. 1.6, i.e. Fourier-space filtering with an OTF, is demonstrated in Fig. 1.5. It assumes NA $= 0.85$ and $\lambda_{\text{em}} = 577\,\text{nm}$. The OTF, shown in Fig. 1.5(c), looks distinctly different from the CTF, shown in Fig. 1.4(c). Instead of a sharp cut-off, it features a linearly declining amplitude from $k = 0$ to $k = k_{\text{cutoff}}$. The cutoff frequency, i.e. the frequency at which the OTF reaches a value of zero, has also changed to

$$k_{\text{cutoff}} = 2\text{NA} \cdot k_{\text{em}} = 2\text{NA} \cdot \frac{2\pi}{\lambda_{\text{em}}}. \tag{1.7}$$

Here, the OTF is modeled by first generating the coherent transfer function CTF as a circle of radius $k_{\text{cutoff}} = \text{NA} \cdot k_{\text{em}}$. Then, the PSF is computed as the absolute value squared of the coherent point spread function $\text{cPSF} = \mathcal{F}^{-1}\{\text{CTF}\}$. Finally, the OTF is calculated as $\text{OTF} = |\mathcal{F}\{\text{PSF}\}|$. A Matlab implementation of the procedure described above can be found in Ref. [31].

1.3.4. Super-resolution fluorescence microscopy

Against the conventional wisdom of a fundamental resolution limit, many scientists have pursued the idea that the resolution in fluorescence microscopy can be improved well beyond the Abbe limit, essentially by bypassing its underlying assumptions. These assumptions are that the imaging process is linear and that thereby Fourier analysis gives a metric for the highest resolvable spatial frequency. Before the advent of SR microscopy, minor resolution improvements were possible through the method known as deconvolution, which is a purely computational approach of deblurring an image by using the PSF of the optical system [8]. True SR techniques use either nonlinearity, or they use prior knowledge about the object to circumvent the Fourier-transform limit on resolution. Nowadays, super-resolution (SR) microscopy techniques that result from these efforts are broadly used, particularly after their pioneers Eric Betzig, Stefan Hell, and William E. Moerner were awarded the Nobel prize in 2014.

Nonlinear SR techniques include two-photon excitation microscopy (2PEM) [32], and the celebrated stimulated emission depletion microscopy (STED) [33]. In STED, one performs raster-scanning fluorescence microscopy, while making use of an intrinsic nonlinearity that derives from the quantum mechanical level structure of fluorophores (i.e., the depletion of stimulated emission depletion by a donut-shaped beam around the fluorescence excitation beam) to narrow the point spread function. Instead, stochastic optical reconstruction microscopy (STORM) [34] and photo activated localization microscopy (PALM) [35] make heavy use of prior knowledge to reconstruct images. In particular, if one is *certain* that a point-like object is isolated, it can be located with accuracy much better than the 200-nm wide point spread function by fitting. In PALM and STORM one performs fluorescence imaging by locating isolated fluorophores in individual camera frames, building up a full image of dense samples by combining many frames, ensuring that fluorophores are usually off, but sometimes randomly switched on as triggered by a stochastic process. Both STED and PALM/STORM based approaches can reach 5 nm resolution, i.e., below $\lambda/100$. However, they are limited to fluorescence microscopy, require very specific fluorescence species, and in the case of PALM/STORM also a very detailed knowledge of the microscope point spread function. Recent reviews on SR fluorescence microscopy are given in Refs. 36 and 37.

In this thesis, a particular emphasis is put on structured illumination microscopy, or SIM [38], which is a generally applicable fluorescence imaging method that can increase the OTF passband by a factor of two using the moiré effect. Figure 1.6(a) demonstrates the effect. The superposition of two patterns results in the appearance of a third pattern with a lower spatial frequency (higher period). In SIM this effect is being applied to shift high spatial frequency information from outside of the passband down into the passband of the microscope [38]. This is done by illuminating the sample with a light

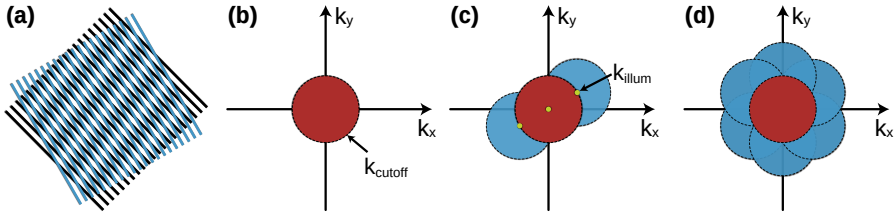

Figure 1.6: Concept of structured illumination microscopy (SIM). (a) Demonstration of the moiré effect. (b) Fourier-space representation of the passband of a conventional fluorescence microscope. Spatial frequencies up to a maximal cutoff frequency k_{cutoff} are transported through the optical system. (c) Additionally recovered spatial frequency regions of the sample (shown in blue), using the moiré effect and sinusoidal illumination patterns, which were shifted three times over the sample. The yellow circles represent the spatial frequencies of the sinusoidal intensity patterns. The maximal spatial frequency k_{illum} of this illumination patterns is chosen to be close to the cutoff frequency k_{cutoff}. (d) Repeating this process for three different orientations allows to effectively double the radius of the fluorescence microscopy passband.

grid possessing a sinusoidal intensity and a spatial frequency k_{illum} close to the cutoff frequency k_{cutoff} of the OTF, see Fig. 1.6(c). In the example from Fig. 1.6(a), this illumination is the first pattern, while the second pattern that is required for the moiré effect is provided by the sample. After recording several sample images, which are illuminated by a series of shifted and rotated light grid patterns, the reconstructed OTF passband can be doubled in size, as shown in Fig. 1.6(d).

Compared to STED, SIM allows for lower required illumination intensity, thereby preventing photobleaching. Compared to STORM and PALM, SIM is compatible with standard fluorophores and does not require the fluorescent labels to be localized in space [39]. Furthermore, compared to the other techniques, SIM requires fewer raw image acquisitions, making it fast enough for live-cell imaging [40]. Despite the numerous advantages SIM offers, one of its main drawbacks is that the resolution enhancement is only moderate. For this purpose, many concepts have been introduced to enhance the SIM technique, with recent reviews given in Refs. 41–43. One concept that will be further expanded upon in Chapter 2 is SIM using illumination with spatial frequencies that are above the passband of the objective, which allows moving even higher spatial frequencies into the passband [44, 45]. For instance, such an illumination would be possible by using the near-field of periodic plasmonic nanoparticle arrays of hexagonal symmetry, which are excited by single tilted beams [46]. In this thesis, we expand on this concept by using plasmonic nanoantenna arrays illuminated by two beams, which leads to a mixing of physical grating and light grating spatial frequencies.

1

1.4. Wavefront imaging

1.4.1. Origins of holography

Regular photodetectors record only the intensity of a light wave, thereby removing all phase information. This consists of a problem in object reconstruction, as without the phase the inverse problem has to deal with incomplete and ambiguous input. Over the years, several techniques have been introduced to address this *phase problem*. The significance of phase imaging becomes evident when considering how widespread *phase objects* are, i.e., specimens that possess only phase contrast. Prominent examples of such phase objects include cellular structures and semiconductor wafers, which both possess uniform brightness and only sub-wavelength thickness or refractive index variations and are therefore invisible under a regular microscope. In order to convert phase variations intro brightness variations, thereby making phase objects visible, regular microscopes typically offer two phase-contrast techniques as optional add-ons, namely differential interference and Zernike phase contrast [9, 47]. However, due to the non-linear dependence of the generated brightness variations on the actual phase profile, both of these techniques are considered *non-quantitative*. A *quantitative* phase imaging (QPI) technique, on the other hand, would allow direct access to specimen properties, such nanometer-scale thickness and refractive index changes[1].

A major step towards the development of QPI is Dennis Gabor's invention of *holography*, which he initially conceived as a means to improve the resolution of electron microscopy [48]. In a proof-of-principle demonstration using optical fields, he showed that it is possible to record the wave's amplitude and phase on an optical film, which can be read out later on. The introduction of off-axis holography by Emmett Leith and Juris Upatnieks in 1962 represents a big step towards practical applications of holography since it solved the twin-image problem that affected Gabor's originally proposed in-line configuration, which spurred further developments in this field [49, 50].

1.4.2. Digital holography

Over the years, the optical film used for hologram recordings was replaced by electronic image sensors, which marked the beginning of *digital holography* [51–56]. In digital holography an object wave $E_O(x,y) = A_O(x,y)\exp[-i\varphi_O(x,y)]$ with real-valued amplitude $A_O(x,y)$ and phase distribution $\varphi_O(x,y)$ is brought to interference with a reference wave $E_R = A_R\exp[+i\varphi_R]$. For simplicity, both the real-valued amplitude A_R and the phase φ_R of the reference wave are assumed to be spatially uniform,

[1] Note that, due to the integration time of the photodetector being much larger than the optical period (in the order of femtoseconds for visible light), in all QPI techniques one can only attain averaged phase quantities and not the actual instantaneous phase of a light wave (as is possible at radio frequencies).

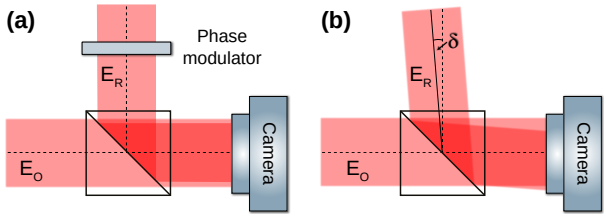

Figure 1.7: (a,b) On-axis and off-axis digital hologram recording configurations.

i.e., a plane wave. The resulting interference pattern or hologram is digitally recorded and can be expressed as

$$\begin{aligned} H &= |E_O + E_R|^2 \\ &= |E_O|^2 + |E_R|^2 + E_O^* E_R + E_O E_R^* \\ &= {A_O}^2 + {A_R}^2 + 2A_O A_R \cos\left[\varphi_O(x,y) + \varphi_R\right], \end{aligned} \tag{1.8}$$

where * denotes a complex conjugate operation. The hologram in Eq. (1.8) consists of the DC (zero-order) term $|E_O|^2 + |E_R|^2$, which does not depend on the phase of E_O or E_R and the interference terms $E_O^* E_R$ and $E_O E_R^*$, which contain the phase $\varphi_O(x,y)$ one wishes to retrieve. To separate the DC term from the interference terms two different approaches are generally used, namely the on-axis/phase-shifting [54, 56] or the off-axis [55] technique.

In the on-axis implementation, shown in Fig. 1.7(a), the object and reference wave impinge parallel onto the detector and a variable phase shift between the two waves is introduced [56]. By recording a series of N phase shifted holograms

$$H_m = {A_O}^2 + {A_R}^2 + 2A_O A_R \cos\left[\varphi_O(x,y) + \varphi_R + m2\pi/N\right], \tag{1.9}$$

where $m = 1, 2, ..., N$ and $N \geq 3$, a set of equations can be established from which one can solve for $\varphi_O(x,y)$ [54].

The off-axis approach uses spatial instead of temporal modulation for phase retrieval. As shown in Fig. 1.7(b), it works by introducing a slight tilt between the object and reference wave [55]. The reference beam can be expressed as $E_R = A_R \exp\left[i\vec{k}\cdot\vec{x}\sin\delta\right]$, where $\vec{k}$ is its wave vector and δ the tilt angle relative to E_O. The interference pattern can be written as

$$\begin{aligned} H = {A_O}^2 + {A_R}^2 + A_O A_R^* \exp\left[-i\left(\varphi_O(x,y) + \vec{k}\cdot\vec{x}\sin\delta\right)\right] \\ + A_O^* A_R \exp\left[+i\left(\varphi_O(x,y) + \vec{k}\cdot\vec{x}\sin\delta\right)\right]. \end{aligned} \tag{1.10}$$

The spatial frequency $\left|\vec{k}\right|\sin\delta$ introduced by the tilt angle is referred to as the

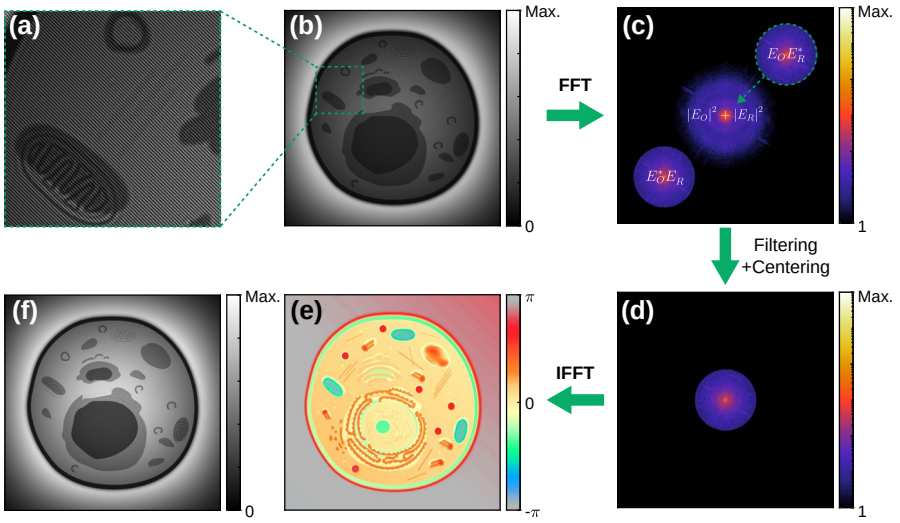

Figure 1.8: Off-axis hologram reconstruction. Zoomed-in (a) and full image (b) of a simulated off-axis hologram. (c) Magniture of the Fourier transform of the hologram showing the zero-order and interference terms. (d) Shifted and masked Fourier transformed hologram from (c). (e,f) Reconstructed amplitude and phase of the wavefront. Panels (c) and (d) use a logarithmic color scale. The hologram was apodized with a 2D Hann window to avoid FFT artifacts.

spatial carrier frequency[2]. Because of the spatial carrier frequency the two interference terms, i.e., $E_O^* E_R$ and $E_O E_R^*$, can be separated from the DC term via a Fourier transform [53]. After filtering, centering and inverse Fourier transforming the interference term, the phase distribution can be obtained. Figure 1.8 demonstrates this reconstruction procedure using simulated data. Note, that the width of the Fourier filter, which is usually chosen to be circular, should be larger than the bandwidth of the interference term to prevent loss of information. The main advantage of the off-axis approach is its single-shot operation, which reduces the measurement time and the influence of vibrations.

Although, acquiring holograms with a digital camera is much more convenient than with an optical film, special care needs to be taken to avoid undersampling of the signal. Due to the finite pixel size Δx of the detector the largest recorded spatial frequency of the hologram is given by the *Nyquist criterion*

$$\nu_{\max} = \frac{1}{2\Delta x}. \tag{1.11}$$

In case of under-sampled fringes aliasing artifacts can occur. For the off-axis

[2]The expression 'carrier frequency' originates from telecommunications, where it describes a wave that was modulated to *carry* a signal.

configuration this relation defines the maximal allowed angle $\theta_{\max}$ between the reference and object planes

$$\theta \leq \theta_{\max} = \frac{\lambda}{2\Delta x}. \tag{1.12}$$

Further details on the necessary recording sensor requirements (detector space–bandwidth product) when recording a hologram in the Fourier plane of a sample in on-axis and off-axis configurations are discussed in Ref. 57.

Several years after the discovery of digital holography it was already applied to microscopy, which enabled phase (and amplitude) imaging with high lateral resolution and was referred to as digital holographic microscopy (DHM) [58–61]. An important application of DHM is label-free imaging of living cells, where the additional phase information can be crucial for scientists studying the physiology and pathology of cells [59, 61]. Metrology is another well-established application area of QPI, where the technique provides non-destructive testing and quality control of microstructures with sub-wavelength axial resolution [58–61]. Novel applications include detection of femtometer-scale sample vibrations [62], full optical characterization of individual nanoparticles [63] and wafer metrology [64]. Recent reviews focused on QPI using DHM are given in Refs. 65 and 66.

1.4.3. Computational wavefront imaging

With the advent of faster computing, alternative phase retrieval approaches have been developed, that solve the phase problem in a computational manner. Compared to the aforementioned interferometric methods, these *computational wavefront sensing* techniques usually process a series of observed intensity images, to retrieve the underlying wavefields. These images are for instance taken from the same object using different illuminations, or instead different detection geometries. Similarly to other inverse problems (see Sec. 1.2.1), algorithmic phase retrieval works by minimizing the discrepancy between measured and expected scattering patterns. To prevent stagnation and non-unique solutions, the reconstruction algorithms are typically aided by some sort of a-priori known constraints (regularization).

An important development in computational imaging, that originates from the field of X-ray crystallography, is known as coherent diffraction imaging (CDI) [67]. In this technique, one records the angle-resolved intensity in diffraction patterns of an object, which in the 1st Born approximation for scattering is equivalent to recording the modulus of the Fourier transform of the scattering potential. The CDI method can recover the phase of a wavefront from the modulus of its Fourier transform while making use of a real-space and a Fourier constraint. Similar phase retrieval reconstruction algorithms have been pioneered by Gerchberg and Saxton and Fienup [68, 69]. Since CDI is a lensless imaging technique, its resolution is not limited by the quality of X-ray optics and a diffraction-limited resolution can be achieved [70, 71].

More recently, a scanning type CDI scheme called *ptychography* has gained considerable attention [72–75]. Originally proposed by Hoppe as early as 1969 [76], ptychography uses a spatially confined probe to scan over an object on a 2D grid to collect a series of diffraction patterns. The fact that the probe beam region is partially overlapping in between scan points, creates redundancy in the ptychographic data set. This redundancy is used in the iterative reconstruction algorithm to achieve a successful convergence. In contrast, to other non-scanning computational techniques and holography, which only recover a complex wavefront, ptychography can separate between the probe beam profile and the object function. Instead of using real-space and Fourier support constraints as in CDI, ptychography relies on a large set of diffraction patterns with known scan positions as its constraint. In addition to CDI and ptychography, a wide range of algorithmic phase retrieval approaches have been developed that do not rely on support constraints but rather on intensity diversity, which can be introduced by recording at multiple propagation distances [77, 78], angles of incidence [79] or using different wavelengths [80]. Recent reviews of this field are given in Refs. 81 and 82.

While the reconstruction process of algorithmic phase retrieval techniques can be computationally intensive, such approaches can offer significant advantages. Indeed, since one requires no reference wave, a less sophisticated setup with significantly relaxed mechanical tolerances can be used. In addition, the lack of a reference can also lead to improved phase accuracy compared to holography, where imperfections in the reference cause artifacts in the retrieved phase. A further advantage of reference-free techniques over holography is a reduced requirement on light source coherence and setup stability [83]. The ability to use lower coherent light sources, such as light-emitting diodes (LEDs), allows to significantly reduce the effect of speckle noise, which one commonly encounters in interferometric methods [84]. A further advantage, which we make use of in Chapter 5, is that computational imaging techniques can jointly recover additional information such as the coherence properties of the beam [85].

1.5. Coherence

When shining two light sources, such as two flashlights, at a black screen one would generally expect the intensity in the region where the two beams overlap, to simply add up. However, as discussed in Sec. 1.4 in some cases the two beams interfere with each other, resulting in spatially alternating minima and maxima of intensity. The ability of two light waves to form such interference patterns is governed by their degree of coherence, which is the topic of this section. For simplicity scientists often assume either completely incoherent or fully coherent waves. However, in reality one commonly encounters a middle ground between those two extremes, which is referred to as *partial*

coherence. The field of optical coherence theory was pioneered by van Cittert and Zernike in the 1930s. Additionally, in the 1950s Emil Wolf laid much of the theoretical groundwork on statistical properties of light [86]. A catalyst for more research on the subject was the invention of the laser in 1960. A broad range of applications can benefit from coherence theory including diffraction tomography, photovoltaics, light-emitting diodes, beam shaping, and speckle suppression in imaging [86–88].

We can separate between two forms of coherence properties: *temporal* and *spatial coherence*. In order to fully describe the coherence properties of a wave E, the *mutual coherence function* can be calculated as [89]

$$\Gamma(\mathbf{r}_1, \mathbf{r}_2, \tau) = \langle E(\mathbf{r}_1, t) E^*(\mathbf{r}_2, t+\tau) \rangle, \tag{1.13}$$

where $\mathbf{r}_1$ and $\mathbf{r}_2$ denote two positions, τ is a time delay and $\langle \cdot \rangle$ stands for the time-average integral, which is defined as

$$\langle f(t) \rangle = \lim_{T \to \infty} \frac{1}{T} \int_{-T/2}^{T/2} f(t)\, \mathrm{d}t. \tag{1.14}$$

To make Eq. 1.13 more accessible, in the following the effects of temporal and spatial coherence are examined separately.

1.5.1. Temporal coherence

Temporal coherence is the correlation of a wave with itself at two different instances of time. To quantify the effect of a temporal coherence the so-called *complex degree of self-coherence* can be calculated as [89]

$$\gamma(\mathbf{r}_1, \tau) = \frac{\Gamma(\mathbf{r}_1, \tau)}{\Gamma(\mathbf{r}_1, 0)}. \tag{1.15}$$

Specifically, $\gamma(\mathbf{r}_1, \tau)$ describes how well a wave can interfere with itself after a certain time delay τ. This effect can be easily observed in a Michelson interferometer, where two waves coming from the same source travel along two separate paths and are later recombined on a screen forming an interference pattern. Changing the length of one of the interferometer arms introduces a time delay τ between the two interfering waves and influences the *visibility* of the observed interference fringes, which is defined as

$$\mathcal{V} \equiv \frac{I_{\max} - I_{\min}}{I_{\max} + I_{\min}}, \tag{1.16}$$

where $I_{\max}$ and $I_{\min}$ denote adjacent maximum and minimum values of the interferogram, respectively. This fringe visibility is directly proportional to the modulus of $\gamma(\mathbf{r}_1, \tau)$ [89]

$$\mathcal{V} = \frac{2A_0 B_0}{A_0^2 + B_0^2} \big|\gamma(\tau)\big|, \tag{1.17}$$

where A_0 and B_0 are the amplitudes of the two interfering waves. As the optical path difference in the interferometer and therefore τ increase, $\left|\gamma(\tau)\right|$ decreases in value. The time delay, at which $\left|\gamma(\tau)\right|$ falls to approximately zero, is defined as the *coherence time* τ_C. At this point the path length difference in the interferometer has surpassed the *coherence length* L_C, which is the distance travelled by light during the time interval τ_C

$$L_C = \tau_C \cdot c = \frac{c}{\Delta f}, \tag{1.18}$$

where c is the speed of light, Δf is the spectral width that corresponds to the finite pulse length τ_C. From Eq. (1.18) it becomes apparent that temporal coherence indicates how monochromatic a source is. Since a laser generally features a very narrow bandwidth (e.g. a stabilized He-Ne laser has $L_C \approx 10\,\text{cm}$ and $\Delta f \approx 3\,\text{GHz}$), its temporal coherence is considered high. Knowledge of the coherence length becomes important when constructing a holography experiment since there the optical path difference between the object and reference beams should be smaller than the coherence length to observe interference.

1.5.2. Spatial coherence

Spatial coherence is given by the correlation of a wavefield at different points in space. Using the so-called mutual intensity (MI), the correlation between any two points of a wavefield can be mathematically expressed as

$$J(\mathbf{r}_1,\mathbf{r}_2) = \Gamma(\mathbf{r}_1,\mathbf{r}_2,0) = \langle E(\mathbf{r}_1)E^*(\mathbf{r}_2)\rangle. \tag{1.19}$$

The normalized form of the MI can be expressed as

$$\gamma(\mathbf{r}_1,\mathbf{r}_2) = \frac{J(\mathbf{r}_1,\mathbf{r}_2)}{\sqrt{I(\mathbf{r}_1)I(\mathbf{r}_2)}}, \tag{1.20}$$

where $I(\mathbf{r}_1)$ and $I(\mathbf{r}_2)$ are the observed intensities at the two locations defined as

$$I(\mathbf{r_0}) \equiv \langle E^*(\mathbf{r}_0)E(\mathbf{r}_0)\rangle. \tag{1.21}$$

The case of $\gamma(\mathbf{r}_1,\mathbf{r}_2) = 1$ denotes perfect spatial coherence between the points $\mathbf{r}_1$ and $\mathbf{r}_2$; $\gamma(\mathbf{r}_1,\mathbf{r}_2) = 0$ indicates complete spatial incoherence; the remaining cases $0 < \gamma(\mathbf{r}_1,\mathbf{r}_2) < 1$ indicate partial spatial coherence. To make these equations more intuitive, we can consider Young's double pinhole experiment with a monochromatic but extended light source, where the two pinhole positions are at $\mathbf{r}_1$ and $\mathbf{r}_2$. If there are no correlations between the waves emitted from pinhole 1 and 2 ($\gamma(\mathbf{r}_1,\mathbf{r}_2) = 0$), no interference fringes will be observed on a plate further away from the pinholes. In case of $\gamma(\mathbf{r}_1,\mathbf{r}_2) > 0$ interference

effects become visible. Similarly to Eq. 1.17, the fringe visibility in the double pinhole experiment can be expressed as

$$\mathcal{V} = \frac{2A_0B_0}{A_0^2 + B_0^2}\left|\gamma(\mathbf{r}_1, \mathbf{r}_2)\right|, \tag{1.22}$$

where A_0 and B_0 are the wave amplitudes of the two pinholes.

An alternative description of spatially partially coherent light was introduced by Emil Wolf and is referred to as the modal expansion [90]. In this approach, the MI is decomposed into an orthonormal basis $\{\phi_m\}$ with $m = 1, ..., M$,

$$J(\mathbf{r}_1, \mathbf{r}_2) = \sum_m \lambda_m \phi_m^*(\mathbf{r}_1)\phi_m(\mathbf{r}_2), \tag{1.23}$$

where the 'coherent modes' ϕ_m are eigenfunctions with non-negative and real eigenvalues λ_m that fulfill the Fredholm integral equation

$$\int_{-\infty}^{\infty} J(\mathbf{r}_1, \mathbf{r}_2)\phi(\mathbf{r}_1)\,\mathrm{d}^2 r_1 = \lambda_m \phi_m(\mathbf{r}_2). \tag{1.24}$$

The strength of this coherent mode decomposition is the ability to bypass the computationally expensive operations on the multi-dimensional mutual intensity function, by instead directly manipulating the coherent modes, which constitute the MI. For instance, to evaluate the MI at different propagation distances, one can individually propagate the coherent modes to the desired distance and reevaluate Eq. 1.23. Chapter 5 will further elaborate on this approach and present a lensless computational imaging method, which is able to retrieve these modes.

Contrary to temporal coherence, spatial coherence is greatly influenced by objects the wave propagates through (i.e beam defining apertures) and the distance from the source. For example, the light from a source that consists of a collection of independent emitters, such as the sun, can be regarded as completely spatially incoherent when the MI is measured close to this source. However, once one views the source from a sufficient distance (i.e., the sun-earth distance, which is of order 151 million km), it becomes partially coherent. A mathematical description of this effect is provided by the *van Cittert–Zernike theorem* [91]. It states that the mutual intensity in the far-field zone of an incoherent source is proportional to a two-dimensional Fourier transform of the source intensity distribution. Further, this suggests that the spatial coherence of a wave field can be controlled by the spatial filtering of an incoherent source. We will use exactly this concept in Chapter 5 to synthesize different MI functions.

1.6. Nanophotonics

This thesis aims to combine nanophotonics and computational imaging concepts to improve optical metrology, and conversely suggests how insights

from computational imaging and metrology may further the understanding of nanophotonics. *Nanophotonics* is the study of light and light-matter interactions at the nanoscale and has over the years attracted a high level of interest in fundamental research and nanotechnology [92, 93]. Potential applications of nanophotonic platforms include super-lensing [44, 94, 95], single molecule sensing [96, 97], optical nonlinearity enhancement [98, 99], flat optics [100] and more recently all-optical machine learning [101]. Another widely studied application of nanophotonics lies in super-resolution imaging [102, 103]. In the following, we will briefly introduce three nanophotonic concepts that are used in the different chapters of this thesis.

Plasmonics is a well-established field in nanophotonics that investigates phenomena observed in nanostructured metals. A characteristic of metals at optical frequencies is that they do not simply behave as near-perfect conductors ($\epsilon = -\infty$), as a consequence of the fact that the intrinsic response time of the free electron sea in metals becomes comparable to the duration of an optical cycle. This finite response time of the electron plasma causes a strong coupling of charge density waves and light. At metal surfaces, this expresses itself as *Surface plasmon polaritons* (SPPs). These quasiparticles are composed of coupled charge density and electromagnetic field oscillations that can *propagate* along metal-dielectric interfaces while decaying exponentially normal to the interface. The wave vector in the propagation direction of these transverse-magnetic bound surface waves can be expressed in the dispersion relation

$$k_{\mathrm{SPP}} = k_0 \sqrt{\frac{\varepsilon_{\mathrm{m}} \cdot \varepsilon_{\mathrm{d}}}{\varepsilon_{\mathrm{m}} + \varepsilon_{\mathrm{d}}}}, \tag{1.25}$$

where $k_0 = \omega/c$ denotes the free space spatial frequency and ε_{m} and ε_{d} denote the frequency-dependent permittivities of the metal and the dielectric, respectively [104]. As embodied by the Drude model the real part of the dielectric function ϵ_{m} for metals is strongly negative at RF and IR frequencies (near-perfect conductors), but approaches $\epsilon_{\mathrm{m}} = 0$ for frequencies nearing the plasma frequency, which for most metals lies in the visible/UV range. The real part of ϵ_m is hence expected to cross $-\epsilon_d$, causing guided waves with a large in-plane wave vector, and strong out-of-plane confinement. The propagation distance of the SPP is mainly limited by absorption in the metal and can be characterized by the propagation length $L = 1/(2\mathrm{Im}[k_{\mathrm{SPP}}])$. Since SPPs have a larger momentum than free space $|k_{\mathrm{SPP}}| > k_0$, the surface plasmons are confined to the interface, unless momentum matching between light and SPPs can be achieved. Approaches for momentum matching make use of surface roughness, nano-sized particles, apertures, or periodic gratings [105, 106]. In this work, surface plasmons on periodic gratings are leveraged for their ability to alter phase the polarization of light scattered into the far-field in Chapter 4. Furthermore, in Chapter 5, plasmonic nanostructures are used to alter the spatial coherence properties of the incident light.

Another striking phenomenon in plasmonics are so-called *localized surface plasmon resonance*s (LSPRs). Similar to SPPs they are based on coupled charge density and light wave oscillations, with the difference of being non-propagating. Such LSPR modes can arise inside sub-wavelength metal nanoparticles and become observable as resonances in optical extinction spectra [107]. To understand this effect one can consider a spherical particle with radius a, which is located inside a uniform field $\mathbf{E}_0$. In case the radius a is small compared to the incident wavelength λ, the electro-static approximation can be used to calculate the changes induced by the sphere on its surrounding electric field. In this approximation the particle is treated as as an *ideal dipole* with induced dipole moment $\mathbf{p} = \alpha \cdot \mathbf{E}_0$, where the polarizability α is given by

$$\alpha = 4\pi a^3 \varepsilon_0 \sqrt{\frac{\varepsilon_\mathrm{m} - \varepsilon_\mathrm{d}}{\varepsilon_\mathrm{m} + 2\varepsilon_\mathrm{d}}}. \tag{1.26}$$

Considering a particle in vacuum ($\varepsilon_\mathrm{d} = 1$), one expects a resonance when $\mathrm{Re}[\varepsilon_\mathrm{m}(\lambda_\mathrm{res})] = -2$ is fulfilled, which for Ag and Au occurs in the visible part of the spectrum. This polarizability resonance at λ_res leads to a resonantly induced dipole moment, which in turn causes strongly enhanced local fields and absorption as well as strong scattering. The strong local field enhancements in the so-called *nearfield* zone make plasmonic nanoparticles highly interesting for enhanced molecular sensing [96, 97] and nonlinear optical effects [98, 99]. In this work, in Chapter 2, we use the unique ability of LSPRs to concentrate light in nanometer-sized regions of space in combination with structured illumination to enhance the resolution of fluorescence microscopy.

In the case of larger nanoparticles, the quasi-static approximation breaks down due to considerable phase delay of the incident field over the particle volume. Instead, to simulate the scattering of a spherical particle with a size comparable to the incident wavelength, whether made of metal or dielectric media, one can use *Lorentz-Mie theory* (LMT), which is an exact solution to Maxwell's equation for the case of a uniform sphere [108]. In this theory, the scattered and internal fields are expanded into a series of normal modes described by vector spherical harmonics. While LMT is only valid for single particles, an extended version of LMT using the T-matrix formalism was developed for assemblies of nanoscatters and is referred to as *generalized multi-particle Mie theory* (GMMT) [109]. Over the years, Mie theory-based techniques have been applied to a large diversity of problems ranging from atmospheric optics to plasmonics, optical trapping [110] and inverse problems involving particle size [111] or morphology [112] determination. In Chapter 3, GMMT will be applied to diffraction-based overlay metrology, where we study the performance of different metrology target designs consisting of periodic and non-periodic dielectric nanoparticle arrangements.

1

1.7. Outline of this thesis

The goal of this thesis is to study applications of nanophotonics and computational imaging in optical metrology. To this end, each of the four remaining chapters introduces a separate imaging or sensing modality, see Fig. 1.9 for a setup overview. At first, they appear dissimilar, however each presented technique algorithmically solves an inverse light scattering problem with potential applications in optical metrology. A reoccurring concept is Fourier-space engineering: Chapters 2, 3 and 4 use nanostructures to scatter light in a designed manner, while Chapters 2 and 5 use spatial light modulators to program the wavefront of the incident light. The first two methods focus on breaking the optical resolution barrier. While the former technique creates a super-resolved image as an output, the latter retrieves a single parameter about an otherwise known object, which as discussed in Sec. 1.2 allows it to have a much higher resolution. The last two methods are both able to retrieve amplitude and phase but in two distinct ways. The setup in Fig. 1.9(c) uses off-axis digital holography (see Sec. 1.4.2), whereas the setup in Fig. 1.9(d) uses a lensless ptychographic approach (see Sec. 1.4.3).

This thesis is organized as follows: In **Chapter 2**, we report on a new SR imaging technique, which combines structured illumination with LSPRs to increase the lateral resolution in fluorescence imaging. A sketch of the SIM setup is shown Fig. 1.9(a). Although techniques that break the diffraction limit in fluorescence imaging (see Sec. 1.3.4), cannot be directly applied to wafer metrology, nanophotonics assisted optical focusing is a highly promising approach that could have an impact on future metrology applications.

In **Chapter 3**, we investigate how OV metrology based on Fourier scatterometry can benefit from alternative metrology target designs. We develop a statistical method, to determine the OV measurement uncertainty of different 2D target designs based on their far-field scattering signature as simulated using GMMT. The proposed setup, depicted in Fig. 1.9(b), records the far-field intensity by imaging the back-focal plane of a microscope objective.

In **Chapter 4**, we report on an experimental technique for quantitative analysis of amplitude, phase, directivity, and polarization of wavefronts scattered by single nano-objects. The Fourier polarimetry setup combined with off-axis holography is outlined in Fig. 1.9(c). As a demonstration, the spin and orbital angular momentum imposed by plasmonic spiral nano-antennas are analyzed.

In **Chapter 5**, we report how mixed-state ptychography can be used to quantitatively assess the spatial coherence of quasi-monochromatic wavefields, see Fig. 1.9(d) for the imaging part of the lensless setup. The accuracy of the method is confirmed through numerical simulations, back-propagation to the source plane, and a quantitative phase comparison. Furthermore, we demonstrate the ability of the method to experimentally study SPP-mediated spatial coherence modulations.

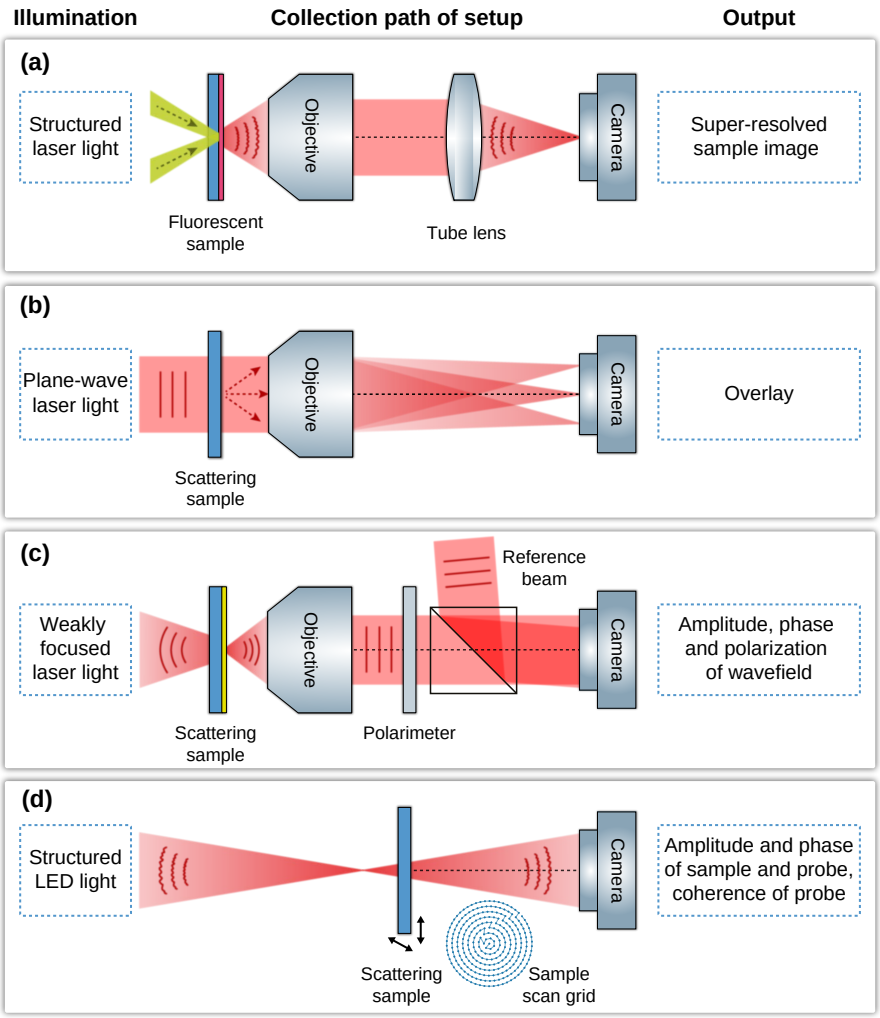

Figure 1.9: Overview of the different setups studied in this thesis. The figure highlights the light source, the setup collection path, and the output generated after additional data analysis. (a) In Chapter 2, a microscope is used to image a fluorescent sample, which is illuminated with structured laser light. (b) In Chapter 3, a Fourier scatterometry setup is simulated to determine overlay from the back-focal plane intensity profile. (c) In Chapter 4, a Fourier polarimetry setup is combined with off-axis holography to measure the scattered wavefront of single plasmonic antennas. (d) In Chapter 5, a lensless ptychographic setup in combination with structured partially coherent LED light is used to recover the complex sample and probe function, as well as the spatial coherence of the probe.

References

1. S. Bradbury, *The evolution of the microscope* (Elsevier Science, 2014).
2. E. Abbe, *Beiträge zur Theorie des Mikroskops und der mikroskopischen Wahrnehmung*, Arch. Mikrosk. Anat. **9**, 413 (1873).
3. G. E. Moore, *Progress in digital integrated electronics*, in *Electron devices meeting*, Vol. 21 (1975) pp. 11–13.
4. A. C. Diebold, *Handbook of silicon semiconductor metrology* (CRC Press, Boca Raton, 2001).
5. J. B. Keller, *Inverse problems*, Am. Math. Mon. **83**, 107 (1976).
6. J. Hadamard, *Lectures on Cauchy's problem in linear partial differential equations* (Yale University Press, 1923).
7. P. Boccacci and M. Bertero, *Introduction to inverse problems in imaging* (Taylor & Francis Group, 1998).
8. W. Wallace, L. H. Schaefer, and J. R. Swedlow, *A workingperson's guide to deconvolution in light microscopy*, Biotechniques **31**, 1076 (2001).
9. F. Zernike, *Phase contrast, a new method for the microscopic observation of transparent objects*, Physica **9**, 686 (1942).
10. G. De Villiers and E. Pike, *The limits of resolution*, Optics and Optoelectronics (CRC Press, Taylor & Francis Group, CRC, Boca Raton, 2016).
11. A. N. Tikhonov, A. V. Goncharsky, V. V. Stepanov, and A. G. Yagola, *Numerical methods for the solution of ill-posed problems*, Mathematics and its applications (Springer Netherlands, 1995).
12. X. Colonna de Lega, *Model-based optical metrology*, in *Optical imaging and metrology* (John Wiley & Sons, Ltd, 2012) Chap. 13, pp. 283–304.
13. B. Bunday, E. Solecky, A. Vaid, A. Bello, and X. Dai, *Metrology capabilities and needs for 7nm and 5nm logic nodes, Metrology, Inspection, and Process Control for Microlithography XXXI*, Proc. SPIE **10145**, 102 (2017).
14. N. G. Orji, M. Badaroglu, B. M. Barnes, C. Beitia, B. D. Bunday, U. Celano, R. J. Kline, M. Neisser, Y. Obeng, and A. Vladar, *Metrology for the next generation of semiconductor devices*, Nat. Electron. **1**, 532 (2018).
15. K. P. Bishop, S. M. Gaspar, L.-M. Milner, S. S. H. Naqvi, and J. R. McNeil, *Grating line shape characterization using scatterometry*, Proc. SPIE **1545**, 64 (1991).
16. C. Raymond, *Overview of scatterometry applications in high volume silicon manufacturing*, in *AIP Conference Proceedings*, Vol. 788 (American Institute of Physics, 2005) pp. 394–402.
17. A. J. den Boef, *Optical wafer metrology sensors for process-robust CD and overlay control in semiconductor device manufacturing*, Surf. Topogr. Metrol. Prop. **4**, 023001 (2016).
18. M. H. Madsen and P.-E. Hansen, *Scatterometry—fast and robust measurements of nano-textured surfaces*, Surf. Topogr. Metrol. Prop. **4**, 023003 (2016).
19. M. G. Moharam and T. K. Gaylord, *Rigorous coupled-wave analysis of planar-grating diffraction*, J. Opt. Soc. Am. **71**, 811 (1981).
20. Y. Nakata and M. Koshiba, *Boundary-element analysis of plane-wave diffraction from groove-type dielectric and metallic gratings*, J. Opt. Soc. Am. A **7**, 1494 (1990).
21. G. Bao, Z. Chen, and H. Wu, *Adaptive finite-element method for diffraction gratings*, J. Opt. Soc. Am. A **22**, 1106 (2005).
22. B. Xu, L. Ma, X. Zou, L. Dong, and Y. Wei, *A diffraction-based overlay model based*

on FDTD method, Proc. SPIE **10959**, 109592X (2019).
23. S. Pandev, F. Fang, Y. K. Kim, J. Tsai, A. Vaid, L. Subramany, D. Sanko, V. Ramanathan, R. Zhou, K. Venkataraman, *et al.*, *Signal response metrology (SRM): a new approach for lithography metrology, Metrology, Inspection, and Process Control for Microlithography XXIX*, Proc. SPIE **9424**, 94241P (2015).
24. Z. R. Hatab, J. R. McNeil, and S. Sohail H. Naqvi, *Sixteen-megabit dynamic random access memory trench depth characterization using two-dimensional diffraction analysis*, J. Vac. Sci. Technol., B **13**, 174 (1995).
25. J. Petit, P. Boher, T. Leroux, P. Barritault, J. Hazart, and P. Chaton, *Improved CD and overlay metrology using an optical Fourier transform instrument*, Proc. SPIE **5752**, 420 (2005).
26. M. H. Madsen, P. Boher, P.-E. Hansen, and J. F. Jørgensen, *Alignment-free characterization of 2D gratings*, Appl. Opt. **55**, 317 (2016).
27. A. G. Curto, G. Volpe, T. H. Taminiau, M. P. Kreuzer, R. Quidant, and N. F. van Hulst, *Unidirectional emission of a quantum dot coupled to a nanoantenna*, Science **329**, 930 (2010).
28. I. Sersic, C. Tuambilangana, and A. F. Koenderink, *Fourier microscopy of single plasmonic scatterers*, New J. Phys. **13**, 083019 (2011).
29. L. Helmbrecht, M. Tan, R. Röhrich, M. H. Bistervels, B. O. Kessels, A. F. Koenderink, B. Kahr, and W. L. Noorduin, *Directed emission from self-assembled microhelices*, Adv. Funct. Mater. **30**, 1908218 (2020).
30. J. W. Goodman, *Frequency analysis of optical imaging systems*, in *Introduction to Fourier optics* (Roberts and Company Publishers, 2005) p. 127 to 172.
31. G. Zheng, *Basic concepts in Fourier optics*, in *Fourier ptychographic imaging*, 2053-2571 (Morgan & Claypool Publishers, 2016) pp. 1–1 to 1–9.
32. W. Denk, J. H. Strickler, and W. W. Webb, *Two-photon laser scanning fluorescence microscopy*, Science **248**, 73 (1990).
33. S. W. Hell and J. Wichmann, *Breaking the diffraction resolution limit by stimulated emission: stimulated-emission-depletion fluorescence microscopy*, Opt. Lett. **19**, 780 (1994).
34. M. J. Rust, M. Bates, and X. Zhuang, *Sub-diffraction-limit imaging by stochastic optical reconstruction microscopy (STORM)*, Nat. Methods **3**, 793 (2006).
35. E. Betzig, G. H. Patterson, R. Sougrat, O. W. Lindwasser, S. Olenych, J. S. Bonifacino, M. W. Davidson, J. Lippincott-Schwartz, and H. F. Hess, *Imaging intracellular fluorescent proteins at nanometer resolution*, Science **313**, 1642 (2006).
36. L. Schermelleh, R. Heintzmann, and H. Leonhardt, *A guide to super-resolution fluorescence microscopy*, J. Cell Biol. **190**, 165 (2010).
37. J. Vangindertael, R. Camacho, W. Sempels, H. Mizuno, P. Dedecker, and K. P. F. Janssen, *An introduction to optical super-resolution microscopy for the adventurous biologist*, Method. Appl. Fluoresc. **6**, 022003 (2018).
38. M. G. L. Gustafsson, *Surpassing the lateral resolution limit by a factor of two using structured illumination microscopy*, J. Microsc. **198**, 82 (2000).
39. R. Heintzmann and M. G. Gustafsson, *Subdiffraction resolution in continuous samples*, Nat. Photonics **3**, 362 (2009).
40. P. Kner, B. B. Chhun, E. R. Griffis, L. Winoto, and M. G. Gustafsson, *Super-resolution video microscopy of live cells by structured illumination*, Nat. Methods **6**, 339 (2009).
41. F. Ströhl and C. F. Kaminski, *Frontiers in structured illumination microscopy*, Optica

3, 667 (2016).
42. R. Heintzmann and T. Huser, *Super-resolution structured illumination microscopy*, Chem. Rev. **117**, 13890 (2017).
43. Y. Wu and H. Shroff, *Faster, sharper, and deeper: structured illumination microscopy for biological imaging*, Nat. Methods **15**, 1011 (2018).
44. Z. Liu, S. Durant, H. Lee, Y. Pikus, N. Fang, Y. Xiong, C. Sun, and X. Zhang, *Far-field optical superlens*, Nano Lett. **7**, 403 (2007).
45. A. Sentenac, K. Belkebir, H. Giovannini, and P. C. Chaumet, *Subdiffraction resolution in total internal reflection fluorescence microscopy with a grating substrate*, Opt. Lett. **33**, 255 (2008).
46. J. L. Ponsetto, F. Wei, and Z. Liu, *Localized plasmon assisted structured illumination microscopy for wide-field high-speed dispersion-independent super resolution imaging*, Nanoscale **6**, 5807 (2014).
47. R. D. Allen and G. B. David, *The Zeiss-Nomarski differential interference equipment for transmitted-light microscopy*, Z. Wiss. Mikrosk. Mikrosk. Tech. **69**, 193 (1969).
48. D. Gabor, *A new microscopic principle*, Nature (1948).
49. E. N. Leith and J. Upatnieks, *Reconstructed wavefronts and communication theory*, J. Opt. Soc. Am. **52**, 1123 (1962).
50. P. Hariharan, *Optical holography: Principles, techniques and applications*, 2nd ed., Cambridge Studies in Modern Optics (Cambridge University Press, 1996).
51. J. W. Goodman and R. W. Lawrence, *Digital image formation from electronically detected holograms*, Appl. Phys. Lett. **11**, 77 (1967).
52. J. H. Bruning, D. R. Herriott, J. E. Gallagher, D. P. Rosenfeld, A. D. White, and D. J. Brangaccio, *Digital wavefront measuring interferometer for testing optical surfaces and lenses*, Appl. Opt. **13**, 2693 (1974).
53. M. Takeda, H. Ina, and S. Kobayashi, *Fourier-transform method of fringe-pattern analysis for computer-based topography and interferometry*, J. Opt. Soc. Am. **72**, 156 (1982).
54. J. E. Greivenkamp, *Generalized Data Reduction For Heterodyne Interferometry*, Opt. Eng. **23**, 350 (1984).
55. U. Schnars and W. Jüptner, *Direct recording of holograms by a CCD target and numerical reconstruction*, Appl. Opt. **33**, 179 (1994).
56. I. Yamaguchi and T. Zhang, *Phase-shifting digital holography*, Opt. Lett. **22**, 1268 (1997).
57. D. Claus, D. Iliescu, and P. Bryanston-Cross, *Quantitative space-bandwidth product analysis in digital holography*, Appl. Opt. **50**, H116 (2011).
58. E. Cuche, P. Marquet, and C. Depeursinge, *Simultaneous amplitude-contrast and quantitative phase-contrast microscopy by numerical reconstruction of Fresnel off-axis holograms*, Appl. Opt. **38**, 6994 (1999).
59. C. J. Mann, L. Yu, C.-M. Lo, and M. K. Kim, *High-resolution quantitative phase-contrast microscopy by digital holography*, Opt. Express **13**, 8693 (2005).
60. F. Charrière, J. Kühn, T. Colomb, F. Montfort, E. Cuche, Y. Emery, K. Weible, P. Marquet, and C. Depeursinge, *Characterization of microlenses by digital holographic microscopy*, Appl. Opt. **45**, 829 (2006).
61. B. Kemper and G. von Bally, *Digital holographic microscopy for live cell applications and technical inspection*, Appl. Opt. **47**, A52 (2008).
62. E. Leirset, H. E. Engan, and A. Aksnes, *Heterodyne interferometer for absolute amplitude vibration measurements with femtometer sensitivity*, Opt. Express **21**, 19900

(2013).
63. S. Khadir, D. Andrén, P. C. Chaumet, S. Monneret, N. Bonod, M. Käll, A. Sentenac, and G. Baffou, *Full optical characterization of single nanoparticles using quantitative phase imaging*, Optica **7**, 243 (2020).
64. C. Messinis, V. T. Tenner, J. F. De Boer, S. Witte, and A. Den Boef, *Impact of coherence length on the field of view in dark-field holographic microscopy for semiconductor metrology: theoretical and experimental comparisons*, Appl. Opt. **59**, 3498 (2020).
65. Y. Park, C. Depeursinge, and G. Popescu, *Quantitative phase imaging in biomedicine*, Nat. Photonics **12**, 578 (2018).
66. T. Cacace, V. Bianco, and P. Ferraro, *Quantitative phase imaging trends in biomedical applications*, Opt. Lasers Eng. , 106188 (2020).
67. J. Miao, P. Charalambous, J. Kirz, and D. Sayre, *Extending the methodology of X-ray crystallography to allow imaging of micrometre-sized non-crystalline specimens*, Nature **400**, 342 (1999).
68. R. W. Gerchberg and W. O. Saxton, *A practical algorithm for the determination of phase from image and diffraction plane pictures*, Optik **35**, 237 (1972).
69. J. R. Fienup, *Reconstruction of an object from the modulus of its Fourier transform*, Opt. Lett. **3**, 27 (1978).
70. J. Miao, T. Ishikawa, I. K. Robinson, and M. M. Murnane, *Beyond crystallography: Diffractive imaging using coherent x-ray light sources*, Science **348**, 530 (2015).
71. D. F. Gardner, M. Tanksalvala, E. R. Shanblatt, X. Zhang, B. R. Galloway, C. L. Porter, R. Karl Jr, C. Bevis, D. E. Adams, H. C. Kapteyn, *et al.*, *Subwavelength coherent imaging of periodic samples using a 13.5 nm tabletop high-harmonic light source*, Nat. Photonics **11**, 259 (2017).
72. J. M. Rodenburg and H. M. L. Faulkner, *A phase retrieval algorithm for shifting illumination*, Appl. Phys. Lett. **85**, 4795 (2004).
73. P. Thibault, M. Dierolf, A. Menzel, O. Bunk, C. David, and F. Pfeiffer, *High-resolution scanning X-ray diffraction microscopy*, Science **321**, 379 (2008).
74. A. M. Maiden, J. M. Rodenburg, and M. J. Humphry, *Optical ptychography: a practical implementation with useful resolution*, Opt. Lett. **35**, 2585 (2010).
75. J. Marrison, L. Räty, P. Marriott, and P. O'toole, *Ptychography–a label free, high-contrast imaging technique for live cells using quantitative phase information*, Sci. Rep. **3**, 2369 (2013).
76. W. Hoppe and G. Strube, *Beugung in inhomogenen Primärstrahlenwellenfeld. II. Lichtoptische Analogieversuche zur Phasenmessung von Gitterinterferenzen*, Acta Crystallogr. Sect. A **25**, 502 (1969).
77. N. Streibl, *Phase imaging by the transport equation of intensity*, Opt. Commun. **49**, 6 (1984).
78. L. Allen and M. Oxley, *Phase retrieval from series of images obtained by defocus variation*, Opt. Commun. **199**, 65 (2001).
79. W. Choi, C. Fang-Yen, K. Badizadegan, S. Oh, N. Lue, R. R. Dasari, and M. S. Feld, *Tomographic phase microscopy*, Nat. Methods **4**, 717 (2007).
80. D. W. E. Noom, K. S. E. Eikema, and S. Witte, *Lensless phase contrast microscopy based on multiwavelength Fresnel diffraction*, Opt. Lett. **39**, 193 (2014).
81. A. Greenbaum, W. Luo, T.-W. Su, Z. Göröcs, L. Xue, S. O. Isikman, A. F. Coskun, O. Mudanyali, and A. Ozcan, *Imaging without lenses: achievements and remaining challenges of wide-field on-chip microscopy*, Nat. Methods **9**, 889 (2012).

82. J. R. Fienup, *Phase retrieval algorithms: a personal tour [Invited]*, Appl. Opt. **52**, 45 (2013).
83. D. Paganin and K. A. Nugent, *Noninterferometric phase imaging with partially coherent light*, Phys. Rev. Lett. **80**, 2586 (1998).
84. V. Bianco, P. Memmolo, M. Leo, S. Montresor, C. Distante, M. Paturzo, P. Picart, B. Javidi, and P. Ferraro, *Strategies for reducing speckle noise in digital holography*, Light Sci. Appl. **7**, 1 (2018).
85. P. Thibault and A. Menzel, *Reconstructing state mixtures from diffraction measurements*, Nature **494**, 68 (2013).
86. O. Korotkova and G. Gbur, *Applications of optical coherence theory*, in *Progress in optics*, Vol. 65, edited by T. D. Visser (Elsevier, 2020) pp. 43–104.
87. G. Xie, M. Chen, M. Mazilu, S. Zhang, A. Bansal, K. Dholakia, and I. D. W. Samuel, *Measuring and structuring the spatial coherence length of organic light-emitting diodes*, Laser Photonics Rev. **10**, 82 (2016).
88. W. Li and S. Fan, *Nanophotonic control of thermal radiation for energy applications [invited]*, Opt. Express **26**, 15995 (2018).
89. J. W. Goodman, *Statistical optics*, New York, Wiley-Interscience Wiley Series in Pure and Applied Optics (2015).
90. E. Wolf, *New spectral representation of random sources and of the partially coherent fields that they generate*, Opt. Commun. **38**, 3 (1981).
91. E. Wolf, *Introduction to the theory of coherence and polarization of light* (Cambridge University Press, Cambridge, 2007).
92. L. Novotny and B. Hecht, *Principles of Nano-Optics*, 2nd ed. (Cambridge University Press, 2012).
93. A. F. Koenderink, A. Alù, and A. Polman, *Nanophotonics: Shrinking light-based technology*, Science **348**, 516 (2015).
94. V. G. Veselago, *Electrodynamics of substances with simultaneously negative values of ϵ and μ*, Phys.-Usp. **10**, 509 (1968).
95. J. B. Pendry, *Negative refraction makes a perfect lens*, Phys. Rev. Lett. **85**, 3966 (2000).
96. K. Kneipp, Y. Wang, H. Kneipp, L. T. Perelman, I. Itzkan, R. R. Dasari, and M. S. Feld, *Single molecule detection using surface-enhanced Raman scattering (SERS)*, Phys. Rev. Lett. **78**, 1667 (1997).
97. C. E. Talley, J. B. Jackson, C. Oubre, N. K. Grady, C. W. Hollars, S. M. Lane, T. R. Huser, P. Nordlander, and N. J. Halas, *Surface-enhanced Raman scattering from individual Au nanoparticles and nanoparticle dimer substrates*, Nano Lett. **5**, 1569 (2005).
98. V. Valev, *Characterization of nanostructured plasmonic surfaces with second harmonic generation*, Langmuir **28**, 15454 (2012).
99. R. Kolkowski, L. Petti, M. Rippa, C. Lafargue, and J. Zyss, *Octupolar plasmonic meta-molecules for nonlinear chiral watermarking at subwavelength scale*, ACS Photonics **2**, 899 (2015).
100. N. Yu and F. Capasso, *Flat optics with designer metasurfaces*, Nat. Mater. **13**, 139 (2014).
101. Q. Zhang, H. Yu, M. Barbiero, B. Wang, and M. Gu, *Artificial neural networks enabled by nanophotonics*, Light Sci. Appl. **8**, 1 (2019).
102. K. A. Willets, A. J. Wilson, V. Sundaresan, and P. B. Joshi, *Super-resolution imaging and plasmonics*, Chem. Rev. **117**, 7538 (2017).
103. Z. Liu, ed., *Plasmonics and super-resolution imaging* (CRC Press, 2017).

104. J. R. Sambles, G. W. Bradbery, and F. Yang, *Optical excitation of surface plasmons: An introduction*, Contemp. Phys. **32**, 173 (1991).
105. H. Raether, *Surface plasmons on gratings*, in *Surface plasmons on smooth and rough surfaces and on gratings* (Springer Berlin Heidelberg, Berlin, Heidelberg, 1988) pp. 91–116.
106. H. Ditlbacher, J. R. Krenn, N. Félidj, B. Lamprecht, G. Schider, M. Salerno, A. Leitner, and F. R. Aussenegg, *Fluorescence imaging of surface plasmon fields*, Appl. Phys. Lett. **80**, 404 (2002).
107. C. F. Bohren and D. R. Huffman, *Particles small compared with the wavelength*, in *Absorption and scattering of light by small particles* (John Wiley & Sons, Ltd, 1983) Chap. 5, pp. 130–157.
108. C. F. Bohren and D. R. Huffman, *Absorption and scattering by a sphere*, in *Absorption and scattering of light by small particles* (John Wiley & Sons, Ltd, 1983) Chap. 4, pp. 82–129.
109. D. W. Mackowski and M. I. Mishchenko, *Calculation of the T matrix and the scattering matrix for ensembles of spheres*, J. Opt. Soc. Am. A **13**, 2266 (1996).
110. A. Ashkin, J. M. Dziedzic, J. E. Bjorkholm, and S. Chu, *Observation of a single-beam gradient force optical trap for dielectric particles*, Opt. Lett. **11**, 288 (1986).
111. S. Arridge, P. Van Der Zee, D. Delpy, and M. Cope, *Particle sizing in the Mie scattering region: singular-value analysis*, Inverse Prob. **5**, 671 (1989).
112. K. Sokolov, R. Drezek, K. Gossage, and R. Richards-Kortum, *Reflectance spectroscopy with polarized light: is it sensitive to cellular and nuclear morphology*, Opt. Express **5**, 302 (1999).

2

DOUBLE MOIRÉ LOCALIZED PLASMON STRUCTURED ILLUMINATION MICROSCOPY

Structured illumination microscopy (SIM) is a well-established fluorescence imaging technique, that is able to increase spatial resolution by up to a factor of two. This chapter reports on a new way to extend the capabilities of structured illumination microscopy, by combining ideas from the fields of illumination engineering and nanophotonics. We conduct an in-depth study of this technique using simulations and preliminary experiments to show how the proposed technique can break the factor of two resolution enhancement barrier of regular SIM.

2.1. Introduction

SPATIAL resolution in optical microscopy possesses a fundamental limit. This so-called Abbe-Rayleigh diffraction limit causes object features that are sized at around half the wavelength to appear blurred. To circumvent this effect several super-resolution (SR) microscopy techniques have been introduced. This work presents an extension of SIM, which is a widely popular fluorescence SR microscopy technique in which the sample is illuminated by a series of non-uniform light patterns, typically obtained by simple two-beam interference (Figure 2.1(a)), resulting in a lateral resolution improvement of up to a factor of two [1, 2].

While other fluorescence SR methods, such as stochastic optical reconstruction microscopy [3], photo activated localization microscopy [4] or stimulated emission depletion microscopy [5] can offer significantly higher resolution improvements, a major advantage of SIM is its simple implementation in a fluorescence microscope without any specific modifications of the photophysics of the fluorescent species that is imaged. SIM thus stands out for versatility, speed, and its simple working principle. The general principle behind SIM is the moiré effect, which states that the overlap of two patterns introduces a third lower frequency pattern. More specifically, in SIM sample frequency information is down-modulated through a mixing of the spatial frequencies of the object with spatial frequencies of the illumination k_{illum}. This allows otherwise inaccessible information about fine sample features to be shifted inside of the spatial frequency passband of the microscope, also known as the optical transfer function (OTF). The highest spatial frequency still transferred through the OTF passband is called the cutoff frequency k_{cutoff}. Together with k_{illum} it determines the highest recoverable spatial frequency $k_{\mathrm{reconst,max}}$ in moiré-based techniques:

$$k_{\mathrm{reconst,max}} = k_{\mathrm{cutoff}} + k_{\mathrm{illum}}. \tag{2.1}$$

As the illumination patterns are typically offered through the same objective as is used for collection, SIM usually leads to a factor two resolution gain.

Since its establishment, SIM has undergone continuous advancements including resolution improvements above the initial two-fold resolution gain limit [6–8]. The key to these improvements is that the moiré technique for downsampling high spatial frequencies into the passband of collection optics also works if one is somehow able to offer illumination wave vectors k_{illum} higher than those that fit the far-field optics passband. An early approach for such a resolution improvement is called non-linear SIM or saturated patterned excitation microscopy, which relies on a non-linear fluorophore response to effectively imbue the response to simple sinusoidal illumination patterns with higher order spatial frequencies [9]. A drawback is that this approach requires a non-linear fluorophore response either through the use of high illumination intensities or special photoswitchable fluorescent labels, which limits its appli-

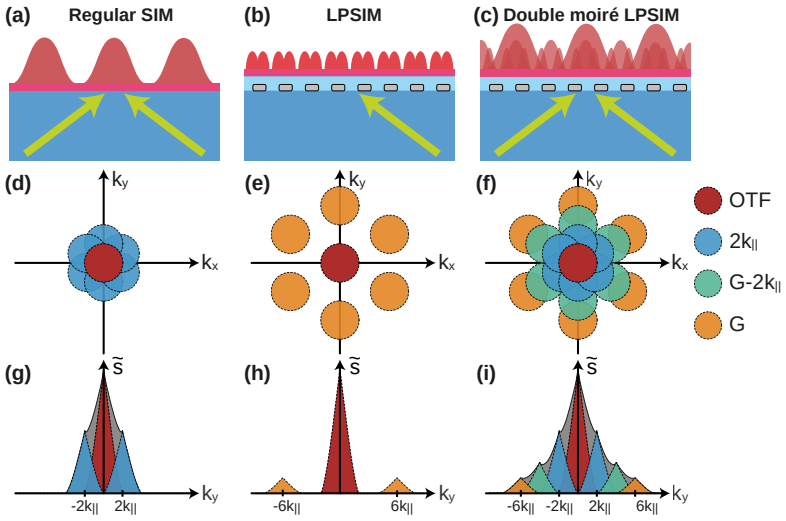

Figure 2.1: Concept of double moiré localized plasmon SIM (DM-LPSIM). (a-c) Schematics of the illumination configurations in regular SIM, localized plasmon SIM (LPSIM) and DM-LPSIM. (d-i) Illustration of the resulting Fourier transformed object reconstructions $\tilde{s}$ in the three different techniques in the k_x-k_y (d-f) and the k_y-$\tilde{s}$ planes (g-i). The colors indicate different illumination frequency contributions.

cability in biological imaging [10, 11]. Another compelling idea is to illuminate the sample not with simple pairs of plane waves but to combine several plane waves at once, to obtain an intensity pattern pumping the fluorophores that contains a multitude of difference wave vectors [12]. This approach has been realized for illumination by four wave vectors simultaneously, and was coined *Double Moiré SIM* or DMSIM [13]. The resulting interference pattern of four distinct spatial frequencies allows to recover a wider region of Fourier space as compared to regular SIM, which however is still limited by the OTF extend of the illumination optics.

A route to truly break the resolution limits in SIM is by offering illumination spatial frequency beyond the OTF. As suggested in Refs. 14 and 15, this would be possible by using the near-field of nanophotonic systems as the illumination source. In particular, the use of near-field patterns of periodic plasmonic nanoparticle arrays of hexagonal symmetry was suggested as a source of illumination, dubbed localized plasmon SIM (LPSIM) [16–18]. As depicted in Fig. 2.1(b), in this technique the plasmonic array is illuminated by just a single plane wave. Although by itself the plane wave does not represent a space varying intensity at the sample plane, the plane wave can excite evanescent grating orders with strong plasmonic local field enhancements. By scanning the polar and azimuthal angle of this illuminating plane wave a sequence of measurements is collected and used to reconstruct the super-

resolved object. Since in LPSIM the plasmonic nanoparticles act as far- to near-field transducers, maximal illumination frequencies far larger then the cutoff frequency $k_{\text{illum}} > k_{\text{cutoff}}$ are possible (only limited by the performance of nanofabrication techniques) and therefore $k_{\text{reconst,max}} > 2 \cdot k_{\text{cutoff}}$. While LPSIM can generate high spatial frequencies, a high spatial frequency illumination alone is not sufficient to achieve high-resolution, artifact-free imaging. Essential is not just to maximize the largest reconstructed wave vector $k_{\text{reconst,max}}$, but also to sample as best as possible all wave vectors up to that maximum. This ideal should be contrasted to the LPSIM scheme, in which one only collects information around $k = 0$, and around the grating reciprocal lattice vector $\mathbf{G}$, but not in between. Figure 2.1(e) illustrates this shortcoming for $G = 3 \cdot k_{\text{cutoff}}$, which shows that image reconstruction should suffer from lack of information about intermediate Fourier components. Figure 2.1(h) highlights this fact by showing a 1D cross-cut of the Fourier transformed SR object reconstruction $\tilde{s}$ along y-axis. This leads to image artifacts such as significant side lobes [18].

Here, we investigate a method to which we in the following refer to as Double Moiré Localized Plasmon SIM (DM-LPSIM). It maintains the benefits of high spatial frequencies generated in LPSIM while leveraging the idea of double moiré SIM by sampling a large area of Fourier space. The idea is that a plasmonic grating is illuminated by two beams simultaneously, see Fig. 2.1(c). This leads to an illumination pattern which consists of not only the light grating spanned by the two incident plane waves, and not only of the plasmonic grating frequency but also of their sum and difference frequencies. The resulting set of spatial frequencies covers a wide region of k-space, see Fig. 2.1(f,i). A similar concept has been previously theoretically proposed by Sentenac et. al in Ref. 19 and an initial implementation using two gratings with 1D resolution enhancements was reported by S. Liu et. al in Ref. 20.

In this chapter, a detailed analysis of the DM-LPSIM technique is presented. First, Section 2.2 reports on numerical simulations using a full-wave approach, demonstrating how under ideal conditions super-resolved image reconstruction is possible using the pattern-illuminated Fourier ptychography algorithm for reconstruction [21]. Further, in Section 2.3, initial experimental results are presented. Finally, a conclusion is given and the illumination and reconstruction algorithm requirements to achieve an optimal resolution enhancement are discussed.

2.2. Simulation results

This section deals with the numerical implementation of the DM-LPSIM experiment. First, electrodynamic full-wave simulations are performed, to calculate pump intensity patterns in the near-field of the plasmonic gratings. Next, these pump intensity patterns are used in fluorescence imaging simulations. The resulting synthesized data sets serve as inputs of the SR im-

age reconstruction algorithm. The resolution enhancing ability of different pump fields is assessed quantitatively using the modulation transfer function method.

2.2.1. Pump field simulation framework

To thoroughly test the DM-LPSIM technique and identify compatible reconstruction strategies, simulations of the electromagnetic field distribution at the plasmonic gratings based on the finite element method (FEM) were performed. On the basis of earlier LPSIM reports [16–18] this work focuses on Ag nanodisk arrays of hexagonal symmetry. Given the experimental realization, which is also reported in this chapter, the nanodisks are assumed to be fabricated on glass, to be covered by a thin glass planarizing spacer, on top of which the specimen is coated. The specimen in this work is a thin polymethyl methacrylate (PMMA) layer doped with fluorophores.

Two crucial parameters when designing DM-LPSIM experiments are (1) the pitch p of the hexagonal array, since it controls the magnitude of the smallest grating wave vector $G = 2\pi/p \cdot 2/\sqrt{3}$ and (2) the incident in-plane wave vector $k_{\parallel} = k_0 \sin\left(\theta_{\text{glass}}\right) n_{\text{glass}}$, where $k_0 = 2\pi/\lambda_0$ is the free space wave vector, θ_{glass} the polar angle in glass and n_{glass} the refractive index of glass, see Fig. 2.2(a,b). As depicted in Fig. 2.1(f), in order to maximize the spatial frequency domain coverage of the reconstructed/virtual aperture, the light and plasmonic grating wave vectors ideally have the same orientation, and the magnitude of the plasmonic grating wave vector G needs to be three times larger than the pump-intensity grating wave vector in absence of the plasmonic particles. This imposes $G = 3 \cdot 2k_{\parallel}$. To avoid gaps in the reconstructed aperture, k_{cutoff} needs to be at least as large as the separation between adjacent frequency components of the illumination, which in this case equals $2k_{\parallel}$, as depicted in Fig. 2.1(i). In a fluorescence imaging system the cutoff frequency is set by the numerical aperture (NA) as $k_{\text{cutoff}} = 2\text{NA} \cdot k_{\text{em}}$, where $k_{\text{em}} = 2\pi/\lambda_{\text{em}}$ is the wave number for the (vacuum) emission wavelength λ_{em}. This means that for a given NA there is an optimal configuration of illumination wave vector $k_{\parallel}$ and plasmonic grating vector G.

Here, simulations with two parameter sets are presented, which target two different NA values, to which we from now on refer to as A_1 and A_2. The first parameter set A_1 is designed for an NA of 1.4, and therefore assumes an array with pitch $p = 115.1\,\text{nm}$ and a polar angle $\theta_{\text{glass}} = 40°$. The parameters of A_2 are optimized for NA $= 0.55$, requiring $p = 286\,\text{nm}$ and $\theta_{\text{glass}} = 15°$. Note, that the relatively large pitch and low NA of A_2 were chosen deliberately in view of the experiment, in which DM-LPSIM is tested at an NA of 0.55, so that we have access also to high-resolution reference images taken at an NA of 1.4, as will be shown in Sec. 2.3.3. The simulations are performed with single s-polarized plane waves incident at the six azimuthal angles $\phi = [30°, 90°, 150°, 210°, 270°, 330°]$, which are aligned to six smallest

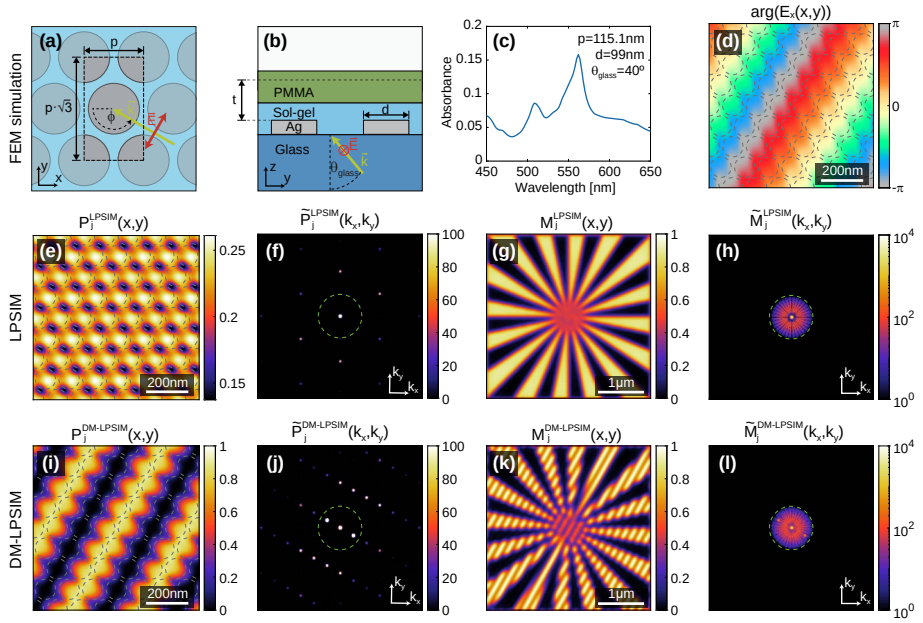

Figure 2.2: Simulation procedure. (a) Top view of the hexagonal array with the pitch p and the nanodisk diameter d. The dashed rectangle indicates the unit cell. (b) Side view of the system indicating the material composition of the sample stack and the incident s-polarized plane wave. (c) The absorbance spectrum of the hexagonal Ag array A_1. (d) Phase profile $\arg(E_x(x,y))$ of 7×4 combined unit cells. (e,f) Example LPSIM illumination pattern and its Fourier transform. (g,h) A simulated LPSIM measurement and its Fourier transform. (i,j) Example DM-LPSIM illumination pattern and its Fourier transform. (k,l) A simulated DM-LPSIM measurement and its Fourier transform. The dashed circles in the panels (d),(e), and (i) indicate the size and positions of the nanodisks. The green dashed circles in the Fourier plots indicate the cutoff frequency of WF imaging. Panels (d-l) show results at an extraction height $t = 40\,\text{nm}$ and an azimuthal angle $\phi = 150°$. The color scale in the panels (h) and (l) is logarithmic and otherwise linear.

plasmonic wave vector components. For both arrays, the diameter of the nanodisk was tuned to have maximal absorbance at the excitation wavelength of $\lambda_0 = 561.3\,\text{nm}$. A_1 has the nanodisk diameter $d = 99\,\text{nm}$ and the absorbance spectrum shown in Fig. 2.2(c). The absorbance spectrum for A_2 is shown in the Appendix in Fig. 2.A.1(c).

As a first step, we extract electric field profiles in 2D planes at multiple heights above the nanodisk array ($t = [40, 50, 60, 70, 80]\,\text{nm}$ for A_1), so that the reconstruction performance at different proximities to the plasmonic hot spots can be assessed. The hexagonal array unit cell, which was simulated in COMSOL using Floquet boundary conditions, is indicated in Fig. 2.2(a). In order to generate large area patterns, the simulation for a single unit cell is exported from COMSOL and in the subsequent MATLAB based analysis is

replicated in the x and y direction 60×35 times in case of A_1, which results in a field of view of around 7 µm. At the same time, the phase offset that the obliquely incident plane wave accumulates between unit cells is taken into account, as verified by the $\arg(E_x(x,y))$ plot in Fig. 2.2(d). For better visibility Fig. 2.2(d) shows a zoomed-in area corresponding to 7×4 unit cells, while the dashed circles indicate the nanodisk position and size. In addition to that, Fig. 2.2(e) shows an example of a LPSIM intensity pattern at the distance $t = 40$ nm, i.e., the field intensity $|\mathbf{E}(x,y)|^2$ generated by just a single plane wave incident at $\theta_{\text{glass}} = 40°$ and $\phi = 150°$. This pattern features hot spots with the same periodicity as the nano-sized array itself. This becomes evident in the frequency domain as peaks at the grating wave vectors $\mathbf{G}$, see Fig. 2.2(f).

Next, a set of DM-LPSIM illumination patterns is calculated through coherent superposition of the simulated field profiles $\mathbf{E}_{\text{FEM}}(\mathbf{k}_{\parallel,j})$ and $\mathbf{E}_{\text{FEM}}(-\mathbf{k}_{\parallel,j})$ generated by two opposing parallel wave vectors:

$$P_j^{\text{DM–LPSIM}}(x,y) = |\mathbf{E}_{\text{FEM}}(\mathbf{k}_{\parallel,j}) + \mathbf{E}_{\text{FEM}}(-\mathbf{k}_{\parallel,j}) \cdot e^{i\varphi_j}|^2, \tag{2.2}$$

where φ_j is the j^{th} phase offset to one of the excitation plane waves and $j = 1, 2, ..., L$. This phase shift φ_j is varied in 9 equal steps in the interval from 0 to 2π, to obtain a controllable shift of the incident pump light standing wave on the sample plane. The process is continued for each of the three azimuthal wave vector orientations, which leads to a set of $L = 27$ simulated near-field DM-LPSIM illumination patterns. In Figure 2.2(i), a zoom-in of such a pattern is shown and in Fig. 2.2(j) its Fourier transform $\tilde{P}_j^{\text{DM–LPSIM}}$. The appearance of the spatial frequency components $2\mathbf{k}_{\parallel}$ and $\mathbf{G} \pm 2\mathbf{k}_{\parallel}$ can be clearly observed[1]. More simulation details and analogous results for configuration A_2 are provided in Appendix 2.A.

As a benchmark comparison, regular SIM illumination patterns are created using the squared coherent sum of two plane waves:

$$P_j^{\text{SIM}}(x,y) = \left|\exp\left(i\mathbf{k}_{\parallel,j} \cdot \mathbf{r}\right) + \exp\left(-i\mathbf{k}_{\parallel,j} \cdot \mathbf{r} + i \cdot \varphi_j\right)\right|^2, \tag{2.3}$$

where the incident wave vectors $\mathbf{k}_{\parallel,j}$ and phase shifts φ_j were chosen identical to the DM-LPSIM illumination. Strictly for regular SIM $L = 9$ images would suffice. Despite this, the same number of input images ($L = 27$) as for DM-LPSIM were used, in order to create a more fair comparison of the reconstructions results.

[1] To generate the Fourier transform plots in Fig. 2.2(f,j,h,l) we used the full area (60×35 unit cells) of the down-scaled (effective pixel size of 27.4 nm) illumination patterns and windowed the images with a 4-term Blackman-Harris function, to avoid FFT artifacts.

2.2.2. Forward model of the SIM imaging process

The incoherent imaging process is simulated using the regular SIM forward imaging model, which can be expressed as

$$M_j(x,y) = \left|\mathcal{F}^{-1}\left[\mathcal{F}\left\{s(x,y)\cdot P_j(x,y)\right\}\cdot \mathrm{OTF}\right]\right|, \tag{2.4}$$

where $\mathcal{F}$ denotes the 2D Fourier transform, $s(x,y)$ the perfectly resolved specimen and $P_j(x,y)$ the j^{th} illumination pattern. Figure 2.2(g,k) shows examples of simulated measurements with the LPSIM and DM-LPSIM illumination for the parameter set A_1. The corresponding Fourier transformed measurements are shown and in Fig. 2.2(j,l). Since the plasmonic grating illumination is not optically resolved, the LPSIM intensity pattern M_j^{LPSIM}, shown in Fig. 2.2(g), lacks any spatial intensity variations. The DM-LPSIM measurement pattern $M_j^{\text{DM–LPSIM}}$ on the other hand, still contains spatial intensity variations caused by the interference of the two plane waves. The specimen $s(x,y)$ is a Siemens star target, which consists of a circular pattern of spokes. This resolution test target is employed, since it allows the examination of the imaging resolution at a broad range of azimuthal angles. The OTF is modeled by first generating the coherent transfer function CTF as a circle of radius $k_{\text{cutoff}}^{\text{coherent}} = \mathrm{NA}\cdot k_{\text{em}}$ and then computing $\mathrm{PSF} = \left|\mathcal{F}^{-1}\left(\mathrm{CTF}\right)\right|^2$. Finally, the OTF is calculated as $\mathrm{OTF} = \left|\mathcal{F}\left(\mathrm{PSF}\right)\right|$. The emission wavelength is $\lambda_{\text{em}} = 577\,\text{nm}$ and the two simulated configurations use NA values of 1.4 and 0.55.

2.2.3. Reconstructions using simulation data

By performing the above described imaging simulation for each of the generated DM-LPSIM and regular SIM illumination patterns, we obtained data sets containing the diffraction-limited simulated measurements $\left\{M_j\right\}_{j=1..L}$, the illumination patterns $\left\{P_j\right\}_{j=1..L}$ and the OTF, which we subject to image reconstruction.

The aim of the reconstructions is to ascertain if such a data set would allow to retrieve the specimen image $s(x,y)$ with a high resolution. The amount of necessary inputs or a priori knowledge varies depending on the reconstruction algorithm one uses. In the 'non-blind' reconstruction approach of the following section, the set of illumination patterns $\left\{P_j\right\}$ is assumed to be known. Therefore, the algorithm makes use of the full data set including OTF, $\left\{M_j\right\}$ and $\left\{P_j\right\}$. Later, in the experimental implementation discussed in Sec. 2.3.3 we will make use of 'blind' reconstruction approaches, where $\left\{P_j\right\}$ is not considered as known input, but jointly retrieved during the reconstruction.

Since the plasmonic near-fields in DM-LPSIM are far from harmonic or sinusoidal patterns, a standard SIM reconstruction method is not applicable.

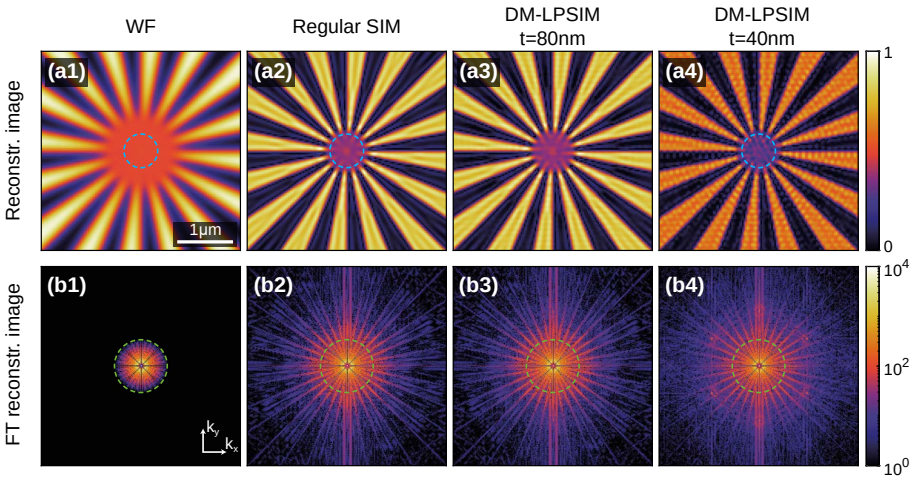

Figure 2.3: Reconstruction results for simulation configuration A_1. (a1) WF image at NA = 1.4. (a2-a4) Reconstructed images using regular SIM and DM-LPSIM illuminations at $t = 80\,\text{nm}$ and $t = 40\,\text{nm}$ respectively. (b1-b4) Fourier transforms of (a1-a4). The blue dashed circles in panels (a1), (a2) and (a4) indicate the radius of the cross-cuts shown in Fig. 2.4(c). The green dashed circles in panels (b1-b4) indicate the cutoff frequency of WF imaging.

To tackle this problem, we made a comparative study of several iterative reconstruction algorithms, which do not pose restrictions on the type of the illumination pattern. Of the investigated algorithms the pattern-illuminated Fourier ptychography (piFP) reconstruction algorithm was found to offer the best results [21, 22]. This iterative algorithm is an extension of the regular Fourier ptychographic microscopy approach and was recently successfully demonstrated in combination with saturated SIM and total internal reflection SIM [23–25]. In the following, to establish the best-case scenario for DM-LPSIM we report reconstruction results using this piFP reconstruction approach with known illumination patterns ('non-blind'). The piFP implementation here slightly differs from the originally proposed version, in order to handle different illumination patterns instead of one shifted pattern as explained in Appendix 2.B. The same $N = 2000$ piFP iterations are performed for both regular SIM and DM-LPSIM to ensure that the reconstruction results only differ in terms of the illumination conditions.

For a visual comparison Figure 2.3(a1) depicts the result one would get in case of widefield (WF) microscopy with NA = 1.4, while Fig. 2.3(a2) shows the result using regular SIM illumination and piFP reconstruction. Figure 2.3(a3,a4) shows the piFP reconstruction results for DM-LPSIM illumination at heights $t = 80\,\text{nm}$ and $t = 40\,\text{nm}$ above the particles respectively. It is evident that all forms of structured illumination yield a resolution improvement over WF imaging. The corresponding Fourier

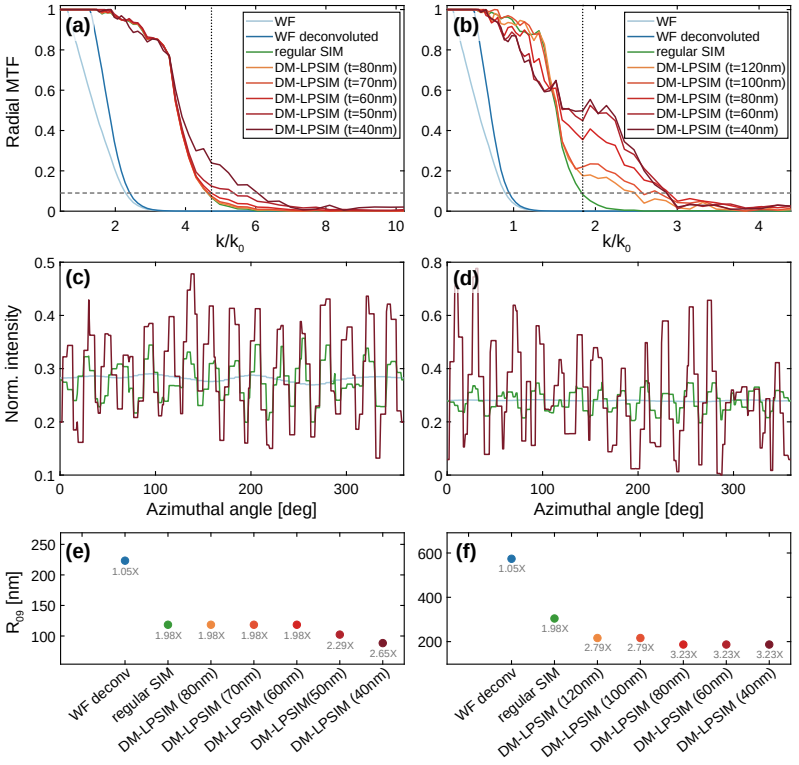

Figure 2.4: Quantitative assessment of the resolution enhancement in simulation configuration A_1 (left panels) and A_2 (right panels). (a,b) Modulation transfer function (MTF) of the reconstructed images for WF imaging, regular SIM, and DM-LPSIM at different distances t from the plasmonic array. The dashed horizontal lines indicate the Rayleigh criterion of 9% contrast. (c,d) The normalized intensities at image cross-cuts along circles, which are indicated in Figs. 2.3 and 2.A.2, for WF imaging (blue), regular SIM (green) and DM-LPSIM at $t = 40$ nm (dark red). (e,f) The minimally resolved distances according to the Rayleigh criterion. The resolution improvement compared to WF imaging is indicated under each data point. The dotted vertical lines in panels (a) and (b) indicate the normalized wave vectors at which the cross-cuts in panels (c) and (d) were taken, respectively.

transformed images are shown in Fig. 2.3(b1-b4), suggesting that DM-LPSIM provides additional information at higher wave vectors and small distances t. At the same time, at small distances t periodic artifacts appear in the image reconstructions, which are visible as peaks at the grating orders **G** in the Fourier transformed images. This is because the high spatial frequency components at the wave vector **G** (and multiples thereof) are not phase shifted during the measurement sequence. Physically this means that plasmonic gratings present nanoscale hotspots that are pinned to the plasmonic particles and that do not shift. We will further elaborate on this in Sec. 2.4.

In order to quantitatively assess the resolution of the reconstructed images, the modulation transfer function (MTF) method is used as described in Ref. 26. It uses the fact that the Siemens star target features gradually increasing spatial frequencies towards its center. Therefore, this approach allows to quantify the ability of an imaging system to transfer contrast at a particular frequency from the object to the image plane. The MTF results are summarized in Fig. 2.4(a) for A_1 and in Fig. 2.4(b) for A_2. For both cases, DM-LPSIM shows an increased MTF towards the tail end of the MTF curve of regular SIM, which increases with a decreasing distance t to the particles. The Rayleigh criterion for incoherent imaging assumes a minimal detectable MTF value of 9 % (indicated as dashed horizontal line in Fig. 2.4(a,b)) [27]. Figure 2.4(c,d) reports normalized intensities at image cross-cuts along circles concentric with the Siemens star origin for WF imaging, regular SIM and DM-LPSIM at $t = 40\,\text{nm}$. The radii, at which these cross-cut were taken, correspond to the normalized wave vectors, at which the regular SIM contrast falls below 9 %, i.e., offers imaging performance below the one required by the Rayleigh criterion. The exact cross-cut radii are indicated as blue dashed circles in Fig. 2.3 for A_1 and in Fig. 2.A.2 for A_2. The corresponding normalized wave vectors are shown as vertical dotted lines in Fig. 2.4(a,b). It is evident that at this radius, the DM-LPSIM reconstruction shows a higher contrast compared to regular SIM. In Figure 2.4(e,f), the wave vector at the Rayleigh criterion for each technique is converted into a distance, which corresponds to the minimal distance between two resolved points. For each imaging method in addition to this Rayleigh resolution, the resolution improvement compared to WF imaging is shown. In the case of A_1, we find a resolution improvement of up to 2.65 at a distance of $t = 40\,\text{nm}$ from the plasmonic array. When the distance increases to $t > 50\,\text{nm}$ the MTF contrast becomes almost identical to that of regular SIM. This is due to the non-propagating nature of the wave vectors of array A_1. In the case of array A_2, we find a resolution improvement of up to 3.23 at a distance $t = 40\,\text{nm}$ (reconstructed images are shown in Fig. 2.A.2 of the Appendix). This value significantly exceeds the resolution improvement with mere SIM in absence of plasmonic effects. For larger distances, the MTF contrast decreases, as the contribution of the high wave vectors is associated with evanescent diffracted modes that decay with distance away from the particles. Note, that the 4-fold resolution enhancement reported for DMSIM in Ref. 13 was only possible because the initial numerical aperture (NA = 0.4) was chosen to be relatively low. Since contrary to DMSIM the illumination spatial frequency of DM-LPSIM is not limited by the OTF of the illumination optics, the proposed technique has the potential to improve upon a higher initial NA.

2.3. Experiment results

2.3.1. Optical setup

In addition to numerical simulations, we conducted a series of experiments aimed at characterizing the wave vector content of plasmonic array illumination and testing the DM-LPSIM technique. To this end, the custom-built setup, shown in Fig. 2.5(a), was used, which consists of an inverted bright-field optical microscope complemented by an illumination unit. This illumination unit uses a reflective, phase-only spatial light modulator (Meadowlark 1920×1152 XY Phase Series SLM) to achieve an effective amplitude and phase modulation in the first grating order as described in Refs. 28 and 29.

A CW DPSS laser (Lasos DPSS, 561.3 nm wavelength, 50 mW power) beam is expanded by the lenses L_1 ($f_1 = -20\,\text{mm}$) and L_2 ($f_2 = 300\,\text{mm}$). After passing through the half-wave plate HWP_1, which rotates the incident linear polarization towards the director axis of the liquid crystals in the SLM, the beam is reflected off the SLM. The effective amplitude modulation is accomplished by displaying blazed phase gratings in small regions of the SLM screen (see inset in Fig. 2.5(a) for an example SLM image). Light from these regions of the beam profile is deflected into the 1^{st} grating order, while the rest is reflected into the 0^{th} order. By placing an iris in the focal point of lens L_3 ($f_3 = 250\,\text{mm}$), the 1^{st} order light is transmitted and the 0^{th} order light blocked. After that, lens L_4 ($f_4 = 300\,\text{mm}$) projects the transmitted light on the back-focal plane of an oil objective (Nikon 100×, Plan Apo VC, NA 1.4). The telescope consisting of lenses L_3 and L_4 magnifies the SLM pixels slightly from their initial size of 9.2 µm to 11.0 µm in the objective back-focal plane. The second half-wave plate HWP_2, which is controlled by a motorized rotation mount, rotates the polarization of the two incident beams to be s-polarized. Since the SLM screen and the sample plane lie in Fourier planes of each other, selecting just two points/small disks on the SLM is equivalent to illuminating the sample with two oblique plane waves. At the same time, the angular divergence of the beam at the SLM controls the illuminated area or the field of view on the sample. Choosing the distance between L_1 and L_2 to be smaller than the sum of their focal distances, causes a slight convergence of the beam, which in turn increases the field of view in the sample plane to around 15 µm. In the imaging path emitted fluorescence light is separated from laser light by a 561 nm dichroic mirror (Semrock Di03-R561-t1-25x36) and a 561 nm long-pass emission filter (Semrock BLP02-561R-25). The lenses L_5 to L_7 ($f_5 = f_6 = f_7 = 200\,\text{mm}$) are used to relay the fluorescence sample image onto the CCD (Andor Clara). Alternatively, the fluorescence can be redirected to a spectrometer (Shamrock 303i spectrometer with iVAC CCD). Further details on the alignment and measurement procedure are described in Appendix 2.C.

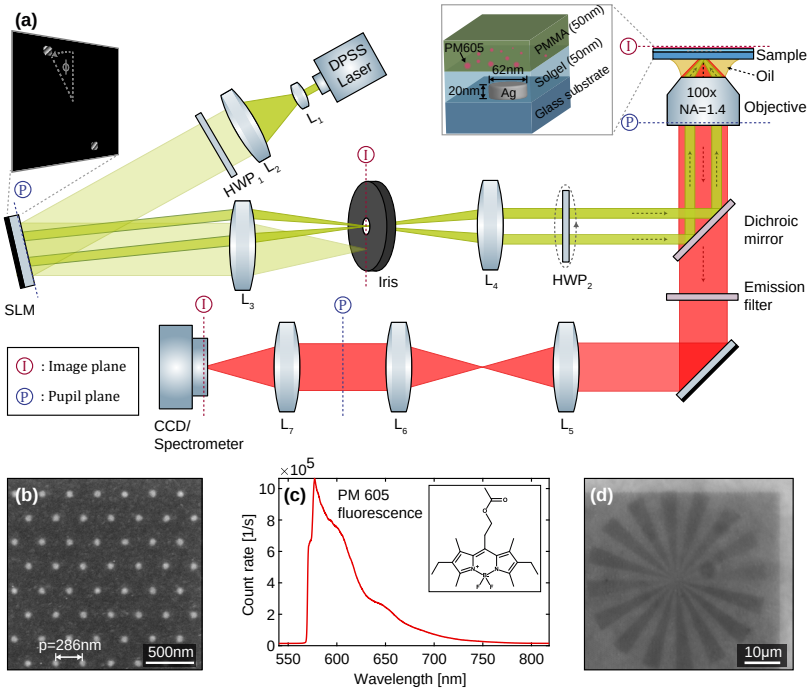

Figure 2.5: Experimental setup and sample fabrication. (a) A schematic drawing of the structured illumination setup. The red and blue dashed lines indicate positions of conjugate image and back-focal planes respectively. L, lens; HWP, half-wave plate; SLM, spatial light modulator. The inset on the left shows example SLM images, which are used creates two circular beams in the back-focal plane of the objective. The right inset shows the material stack and parameters of the fabricated DM-LPSIM sample. (b) SEM image of the hexagonal Ag nanodisk array. (c) PM605 fluorescence emission spectrum excited at a 561.3 nm wavelength. The inset shows a sketch of the PM605 molecule. (d) WF fluorescence image (excited at $\lambda = 532\,\text{nm}$) of the Siemens star target patterned into a PM605 embedded in a PMMA matrix using EBL on top of the plasmonic array.

2.3.2. DM-LPSIM sample fabrication

The samples for experimental measurements resemble parameter set A_2 assumed for the simulations. They consist of hexagonal arrays of Ag nanodisks created by electron beam lithography (EBL), covered by a thin protective layer of partially planarizing sol-gel and a patterned fluorescent layer on top, as shown in the inset of Fig. 2.5(a).

The fabrication starts by cleaning a 170 µm thick glass cover slip using a base piranha solution and an O_2 plasma etch. Next, the samples are prepared for the first EBL step by spin-coating 100 nm of PMMA (MicroChem 495K A8), evaporating 20 nm of Ge and spin-coating 50 nm of CSAR (Allresist AR-P 6200:09). The CSAR layer, which serves as the e-beam resist, is thin to improve resolution. The Ge layer is used as a hard etch mask and as a charge dissipa-

tion layer. The PMMA layer is used for lift-off. The EBL exposure is done in a Raith Voyager system (50 keV, dose 130 $\mu C/cm^2$), which defines the hexagonal array patterns ($50 \times 50\,\mu m^2$ sized, MBMS path) and four alignment markers ($100 \times 100\,\mu m^2$ sized crosses positioned around the field of arrays) into the resist. After exposure, the CSAR resist is developed in a pentylacetate bath for 60 s. An O_2:SF_6 (1 : 5) plasma is used for 60 s, to etch away the exposed part of the Ge layer. Subsequently, a 60 s long O_2 plasma etch is used to remove the exposed PMMA and create an undercut. Next, a 3 nm thick Cr adhesion layer and a 20 nm thick Ag layer (at 0.9 Å/s) are thermally evaporated. The Ag film is lifted off by dissolving the PMMA spacer layer in acetone while leaving the Ag nanodisk arrays and markers on the substrate. The sample is rinsed in isopropanol and blow-dried with N_2. Following this, a 50 nm layer of sol-gel (V7, SCIL Nanoimprint Solutions) is spin-coated on top to planarize the surface. This glass-like material cures in air at room temperature and serves as a protective layer for the Ag nanodisks. Figure 2.5(b) shows a scanning electron microscope (SEM, FEI Helios Nanolab 600) image of the hexagonal array before it was embedded in sol-gel. For the purpose of SEM imaging, a 60 nm thick conductive electra layer was spin-coated. It is removed afterwards using demi-water and isopropanol.

As a fluorescent material, we spin-coat a 50 nm layer of PMMA (MicroChem 950K A8 dissolved in anisole), in which a concentration of 20 mMol of the commercially available dye pyrromethene 605 (Exciton PM605, MW = 376.25 g/mol) was embedded. The molecular structure of PM605 is shown in the inset of Fig. 2.5(c) (drawn using PubChem Sketcher V2.4). The choice of PMMA as the host medium for pyrromethene was motivated based on reports of its positive effects on thermo- and photostability of the dye [30]. The baking step, which is needed to evaporate the anisole solvent from the PMMA solution, was performed at a relatively low temperature of 100°C for 10 mins to prevent thermal bleaching of the PM605. A measured emission spectrum of the fluorescent PM605 dye embedded in PMMA and excited using a laser wavelength of 561.3 nm is demonstrated Fig. 2.5(c), displaying a pronounced emission peak just above the excitation wavelength.

For patterning of this fluorescent layer, a second EBL step was conducted. To avoid charging effects, an additional 60 nm, thick layer of electra (Allresist AR-PC 5090) is spin-coated. We found that electron beam exposure without subsequent chemical development of the polymer matrix, caused fluorescence contrast to appear. The result is a fluorescent image without physical height corrugation that would cause scattering. Using this EBL-based technique four Siemens resolution test targets (sized $25 \times 25\,\mu m^2$) were exposed (50 keV, dose 170 $\mu C/cm^2$) on top of each $100 \times 100\,\mu m^2$-sized Ag array were patterned. The position and orientation of the two EBL steps were aligned by locating three

of the Ag alignment markers, that were written in the first EBL step[2]. For reference measurements, additional Siemens stars were exposed in regions without nanodisks. Finally, the conducting electra layer is removed by rinsing the sample in demi-water and isopropanol. Figure 2.5(d) shows a widefield fluorescence image of the Siemens star target on top of the plasmonic array. The plasmonic array appears dark in the fluorescent image. The spatial resolution of this patterning method is assumed to be far better than the upcoming optical measurements, which is why we selected it for the generation of our resolution test targets. Note, that since the fluorescence contrast decays over time scales of weeks, the experiment is performed quickly after exposure. However, the fact that the nanodisk arrays are embedded in sol-gel, allows to remove and replace the fluorescent top layer multiple times before the sample is degraded.

2.3.3. Optical measurements

The generation of high wave vector components in the illumination and their transfer to the fluorescent object is a key ingredient for DM-LPSIM. To test for the presence of these high wave vector components we perform a characterization at a higher resolution (HR), prior to attempting DM-LPSIM with a lower resolution (LR). To this end, we record fluorescence images at NA $=$ 1.4, and consider their Fourier transforms. Figure 2.6(a) shows an example measurement M_j^{HR} at $\theta_{\mathrm{glass}} = 15°$ and Fig. 2.6(b) its 2D Fourier transform $\tilde{M}_j^{\mathrm{HR}}$. The red dashed circle indicates the actual cutoff frequency of the NA $=$ 1.4 microscope objective. In addition, the green dashed circle indicates the LR cutoff frequency corresponding to NA $= 0.55$, which was used to create the input images for the DM-LPSIM construction. When the correct polar and azimuthal angles are set, the Fourier peaks are distributed equidistantly in the Fourier plane, as shown in Fig. 2.6(b). Figure 2.6(c) shows a 1D profile along $\phi = 30°$ in Fig. 2.6(b). The wave vectors from just the two-beam illumination $(2k_{\|})$, the grating, and their mixing can be clearly discerned.

Figure 2.6(d) shows a measurement of the two incident beams in the back focal plane (BFP) of the objective, which was used to calibrate the angle of incidence of the two beams[3]. Such a measurement is performed by moving the objective over a reflective region on the sample (Ag film), removing the long-pass filter, and flipping out lens L_6 from the setup, shown in Fig. 2.5(a), which relays the BFP image onto the CCD camera. BFP measurements were also used to align the center of the SLM to the BFP, as described in Appendix 2.C.

[2] An initial estimate of marker position was found using the edge of the substrate and the EBL design of the first layer. Then, an SEM image is acquired to select the exact center of the markers. Due to the low thickness of the Ag markers and the additional layers (sol-gel, PMMA, and electra) on top of it, the markers only become visible at relatively long acquisition times.

[3] The NA of the microscope objective is calibrated using the sharp discontinuity in fluorescence emission at the total internal reflection angle of the air and glass interface at NA $= 1$ that is visible in BFP imaging of homogeneous dye films at an air-glass interface [31].

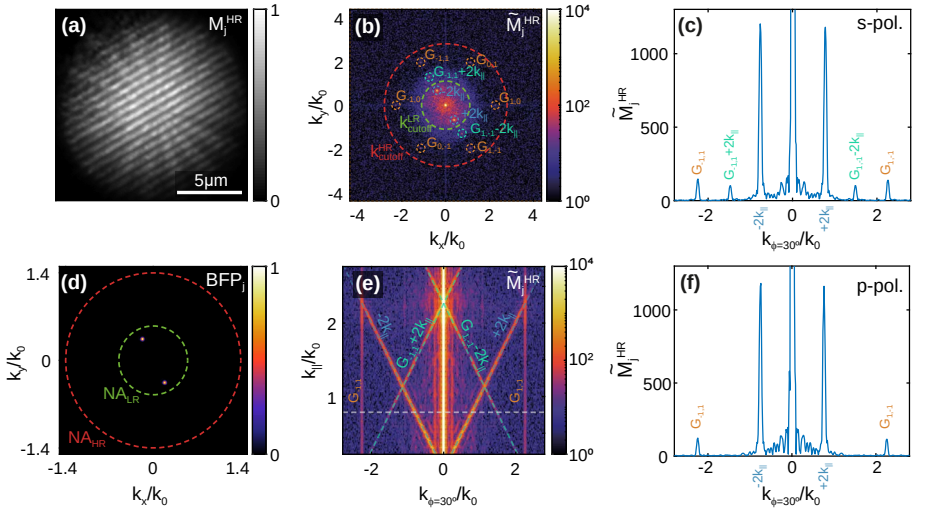

Figure 2.6: Experimental DM-LPSIM illumination characterization. (a) DM-LPSIM measurement with s-polarization, $\theta_{\text{glass}} = 15°$ and $\phi = 30°$. (b) 2D Fourier transform of (a). The green dashed circle indicates $k_{\text{cutoff}}^{\text{LR}}$ and the red dashed circle $k_{\text{cutoff}}^{\text{HR}}$. (c) 1D profile along $\phi = 30°$ in (b). (d) a measurement of the two incident beams in the back focal plane (BFP) of the objective. (e) Sweep of 1D profiles along $\phi = 30°$ for a varying in-plane wave vector $k_{||}$ (y-axis). (f) 1D profile along $\phi = 30°$ a Fourier transformed DM-LPSIM measurement featuring p-polarization. Note, panels (b) and (e) are shown on a logarithmic color scale.

Using this BFP imaging technique, distances between the two circles on the SLM image were converted into appropriate in-plane wave vectors $k_{||}$. Based on this calibration we performed a sweep of $k_{||}$ while acquiring a series of measurements. Figure 2.6(e) shows the results of this polar angle sweep as a series of 1D profiles of $\tilde{M}_j^{\text{HR}}$ along $\phi = 30°$. The wave vector components of the standing light grating $2k_{||}$ can be directly identified as the diverging linear features, and occur at angles matching the angle calibration. The grating wave vectors appear as vertical lines since their values are independent of the incident wave vector. Finally, the mixing of grating and illumination wave vectors causes the reflected lines that converge to zero wave vector at increasing $k_{||}$. The overlaid dashed curves show the expected $\pm k_{||}$, $G_{-1,1} + k_{||}$ and $G_{1,-1} - k_{||}$ values. The excellent agreement between the measured $\tilde{M}_j^{\text{HR}}$ peaks and the expected wave vector curves, that were derived from independent measurements [31] and the array pitch $p = 286\,\text{nm}$ defined in lithography, further validates our wave vector assignment. The horizontal dashed line indicates the wave vector and angle ($\theta_{\text{glass}} = 15°$), at which the DM-LPSIM measurements are performed, given that the involved wave vectors are equidistant in k-space, and only $2k_{||}$ falls within the NA $= 0.55$ bandwidth.

While the measurement clearly confirms that the DM-LPSIM geometry indeed introduces the relevant wave vectors for SR, a successful SIM experiment would also demand significant amplitude in these wave vectors. An important parameter that influences the amplitude in the desired grating diffraction features is polarization. When comparing s-polarized and p-polarized incident pump polarization (Fig. 2.6(b) versus 2.6(d)), it is evident that only s-polarization yields substantial grating diffraction amplitude. In particular, the mixed terms $\mathbf{G} \pm 2 \cdot \mathbf{k}_{\parallel}$ seem to disappear completely from the fluorescence pattern for p-polarized pump light. This is attributed to the fact that in-plane electric field polarization best matches the particle polarizability tensor, and hence also shows the strongest grating diffraction.

2.3.4. Reconstructions using experiment data

On the basis of the presence of the relevant wave vectors in s-polarized illumination, we proceeded to collect measurement sets for DM-LPSIM image reconstruction. To this end, we generate the two-beam interference illumination by maintaining a fixed polar angle of the incident wave vectors, yet setting three azimuthal angles and nine phase shifts, resulting in $L = 27$ measurements. With the Siemens star as the object for reconstruction, data was collected using the high NA objective. Digitally low-passed data corresponding to an NA $=$ 0.55 is used for reconstruction, while the high-resolution data is used as a verification benchmark.

Since in the case of actual experiments the perfectly resolved illumination patterns $\{P_j\}$ are strictly not known, finding the most suitable blind reconstruction method becomes important. Table 2.1 summarizes different established reconstruction algorithms in SIM and distinguishes them in terms of pattern flexibility and the use of prior information. In the Wiener reconstruction method, which was the originally proposed SIM reconstruction method, the illumination is assumed to be perfectly sinusoidal and its wave vectors $\mathbf{k}_{\parallel,j}$ and phase shifts φ_j are assumed to be approximately known [1]. Since this is not the case in DM-LPSIM we examine in the following iterative methods,

Table 2.1: Studied reconstruction algorithms with their specific requirements.

Method name	Pattern flexibility	Blind	A priori assumptions
Wiener	no	no	$\{P_j\}$ is sinusoidal, $\mathbf{k}_{\parallel,j}$ and φ_j approx. known
piFP	yes	no	$\{P_j\}$ is known
jRL	yes	no	$\{P_j\}$ is known
b-SIM	yes	yes	$\{M_j\}$ and s are positive
fb-SIM	yes	yes	$\{M_j\}$ and s are positive, pitch p is approx. known

which are flexible in terms of their illumination patterns. Two such methods are the aforementioned piFP reconstruction and the joint Richardson-Lucy (jRL) deconvolution [21, 32]. However, they do assume known illumination patterns. This requirement is lifted in blind-SIM (b-SIM) and filtered blind-SIM (fb-SIM). Blind-SIM retrieves the illumination patterns during the iterative reconstruction using a minimization approach. It was initially proposed for unknown speckle illumination and later also applied to plasmonic illumination schemes [17, 33–35]. In the case of fb-SIM the minimization is aided by k-space filtering of its search space [36]. Further details on the implementation of these reconstruction methods are provided in Appendix 2.B.

Figure 2.7 shows example results of different reconstruction algorithms and their k-space content, as applied to the low-NA data set. For reference purposes the widefield image result is shown in Fig. 2.7(a1), which was generated by averaging over $\{M_j^{\mathrm{LR}}\}$. It displays the resolution that is possible if one simply performs widefield imaging at the relevant NA (NA $= 0.55$). As an indication of the HR specimen reconstruction that one hopes to retrieve, Fig. 2.7(a5) displays an image obtained by averaging over the high NA data $\{M_j^{\mathrm{HR}}\}$ and performing five iterations of the RL deconvolution. Since the M_j^{HR} data set contains plasmonic grating features, we have apodized the image in Fig. 2.7(a5) by a Fourier filter, which removes the plasmonic grating orders.

The remaining panels in Fig. 2.7 show results for five different reconstruction approaches. The insets show cross-cuts along the blue dashed circles and were used to determine the MTF values given on the bottom right corner of each image. These MTF values were obtained by fitting a sine to the cross-cuts after removing any linear and quadratic trends from the data. For Figures 2.7(a2) and 2.7(a3) 600 iterations of the b-SIM algorithm were performed on a data set without a plasmon grating (labelled 'regular SIM') and the DM-LPSIM data set respectively. In Figure 2.7(a4), we performed 600 iterations of the fb-SIM algorithm on the same DM-LPSIM data set, while using the Fourier filter shown in Fig. 2.8(d). It is evident that all these three approaches improve resolution compared to the low-NA widefield imaging. At the same time, it is also evident that the improvement due to the plasmonic structuring is small, as a similar resolution is obtained when processing the regular SIM data set (i.e., the same 27 illuminations, but no plasmon grating). Fourier analysis of the illuminations reconstructed by b-SIM and fb-SIM in Fig. 2.8(b1) and 2.8(b2) do show that the reconstructed illumination patterns contain the plasmon grating and moiré wave vectors. However, differences of the b-SIM and fb-SIM reconstructions are minor and only visible upon closer inspection of the Fourier transformed illumination patterns.

Finally, the SR image reconstruction was attempted using algorithms that require illuminations to be specified as input. Not having access to the actual illumination patterns in the experiment, we used the illuminations that the b-SIM algorithm returned as inputs for piFP and jRL. The reconstruction, shown

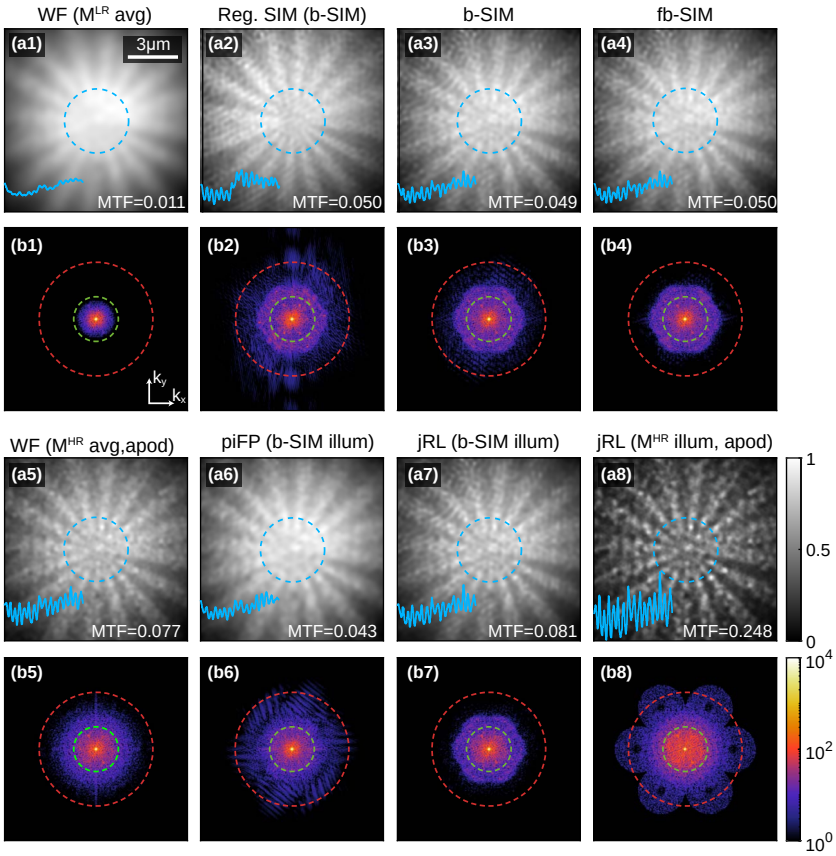

Figure 2.7: Experimental DM-LPSIM results. (a1) WF image calculated by averaging over the LR DM-LPSIM data set. (a2) b-SIM reconstruction using regular SIM illumination. (a3,a4) b-SIM and fb-SIM DM-LPSIM reconstructions. (a5) High-resolution WF image calculated by averaging over the HR DM-LPSIM data set. (a6,a7) piFP and jRL DM-LPSIM reconstructions using illuminations reconstructed with b-SIM. (a8) jRL reconstruction, which used the HR DM-LPSIM data set as illumination and was apodized with the Fourier filter shown in Fig. 2.8(c). Each of the insets in panels (a1)-(a8) shows a cross-cut along the blue dashed circle. The accompanying MTF values were obtained through a sine fit to these cross-cuts. (b1-b8) 2D Fourier transforms of (a1-a8). The green dashed circles indicate $k_{\text{cutoff}}^{\text{LR}}$ and the red dashed circles $k_{\text{cutoff}}^{\text{HR}}$. (a2) uses a regular SIM data set, while all the other panels use the same DM-LPSIM data set. Both data sets were recorded with 300 ms exposure time.

in Fig. 2.7(a6), used 200 iterations of the piFP algorithm using the b-SIM illumination reconstruction as input. The result looks similar to the b-SIM reconstructions alone. Figure 2.7(a7) displays the result of 14 iterations of the jRL algorithm using the b-SIM illumination reconstruction as input. Here, it is evident that the combined jRL and b-SIM approach achieves a resolution

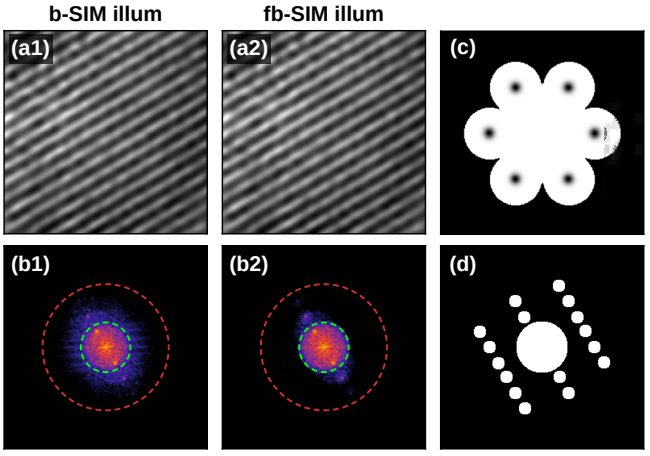

Figure 2.8: (a1,a2) The illumination patterns reconstructed using b-SIM and fb-SIM. (b1,b2) The Fourier transforms of (a1,a2). (c) The Fourier filter used to apodize the jRL reconstruction result in Fig. 2.7(a8). (d) The Fourier filter used during fb-SIM reconstruction.

comparable to that in the averaged HR reference images in Fig. 2.7(a5) while exceeding the result of the b-SIM reconstruction alone. As an alternative, approach to obtaining high-resolution illumination patterns, in Fig. 2.7(a8), we have also considered running the jRL algorithm taking the high-resolution DM-LPSIM measurements M_j^{HR} themselves as the illumination inputs. This has the disadvantage that the Siemens star itself, i.e., the object that one attempts to retrieve, is then also attributed in part to the illumination. Figure 2.7(a8) shows the reconstructed results after 6 iterations of the jRL algorithm. The reconstructed image was apodized using the Fourier filter, shown in Fig. 2.8(c), to remove the plasmonic grating features in the image. As can be seen from the high contrast of the cross-cut and the relatively large MTF value in the inset, jRL shows promising potential as a reconstruction algorithm for experimental DM-LPSIM data. At the same time, the fact that the assumed input illuminations contain the contrast variations of the object itself means that the contrast in such a reconstruction approach may not faithfully represent that in the actual object. These findings highlight that the main limitation in plasmonic-SIM scenarios not only comes from the need to realize sufficient energy density in the evanescent Fourier components but also from the need to have a precise estimate of the illuminating energy distribution in the unit cell. This estimate is not trivially available in real experiments. Importantly, one can not characterize the illuminations separately on a nominally identical plasmonic reference structure first, for later use in actual imaging, since the near-field in actual plasmonic gratings may strongly vary from realization to realization due to nanofabrication disorder.

2.4. Conclusion and discussion

In this chapter, we examined the potential of enhancing structured illumination microscopy resolution by combining the idea of using a nano-patterned grating to generate high spatial frequency illumination [15–17] with the concept of double moiré SIM [12] to cover a large area in Fourier space without blank patches. Using full-wave simulations it was shown that DM-LPSIM can indeed significantly extend the resolution enhancement possible by regular SIM, particularly for specimens sufficiently close to the grating to benefit from a strong field strength of the evanescent grating orders. The optical experiments indicate that in real samples the relevant spatial frequencies expected in DM-LPSIM indeed appear in the illumination. While the specimen reconstructions point at the possibility of resolution enhancements on par with, or in excess of, those that can be achieved with just SIM, the experiments also points out a suite of obstacles that would need to be overcome for artifact-free SR imaging.

A fundamental property of enhancing SIM by tapping into evanescent grating orders is that the strength of the evanescent orders rapidly vanishes with height above the grating. In this demonstration, we found a relatively low amplitude ratio of the high order frequency components to the zero-order component. At the same time, it is beneficial for SIM that all illuminations together homogeneously sample the unit cell. This requirement is hard to realize in plasmonic systems since hot spots tend to be fixed in space at the particle locations without significantly shifting their position in the unit cell when the incidence angle is changed. This causes algorithms to struggle to disentangle whether the plasmon grating is a feature of the specimen or the illumination, as is evident from the remaining structure in the simulation results. While it becomes easier to shift the location of hot spots in planes at larger heights above the particles, this comes at the expense of overall smaller amplitudes in the high-frequency components. Together these observations indicate important criteria for optimizing the grating structure. Overall, we are confident that there is significant room to optimize the strength of evanescent orders by, e.g., using a higher index medium between array and the image plane in combination with further array design optimizations. Nonetheless, the challenge is to *simultaneously* enhance the strength of the evanescent orders *and* gain control to manipulate their phase independently to shift hot spots through the unit cell. Previously proposed far-field mechanisms, that could enable control over near-field hot spots in a plasmonic grating, are based on time-reversal [37, 38], polarization multiplexing [39, 40] or spatial phase modulation [41, 42]. A further challenge as compared to creating multi-moiré patterns with just propagating waves is that evanescent waves inherently have a complicated polarization state, making high interference contrast harder [43].

Aside from the physical requirements on the illumination fields, the technique of DM-LPSIM would also benefit from algorithmic improvements. A

major challenge for any technique that uses structured illumination with near-field features is that it is practically impossible to have full knowledge of the applied near-field illumination. This implies that reconstruction algorithms are confined to be blind, i.e., to those that recognize the object at the same time as the illumination. A problem with blind-SIM reconstruction is that it can be shown that without any a priori assumptions about the experiment, blind-SIM can not recover illumination spatial frequencies higher than the frequency cutoff k_{cutoff} [44]. Therefore, to make full use of the plasmonic illumination for the resolution enhancement, additional a priori information such as sparsity or frequency content needs to be utilized during the reconstruction process. A further complication is that such benchmarking of illumination likely can not be done once and for all using calibration structures that are nominally identical to the transducer used in imaging, since fabrication disorder and small variations in illumination may significantly change the near-field. Thus, the technique might be most suited to applications in, e.g., liquid systems instead of using fixed specimens, as one can then envision first calibrating the transducer, and then using it to image, e.g., the evolution of the spatial organization of a specimen.

APPENDICES

2.A. Details of DM-LPSIM simulation

The FEM simulation of plasmonic nanodisk arrays were performed using the COMSOL Multiphysics software package version 5.2. The simulation uses Floquet periodic boundary conditions, with ports defined underneath and above the structure for the input and diffracted waves. The mesh employed to model the nanodisks in the configurations A_1 and A_2 are shown in Fig. 2.A.1(a,b). The Ag nanodisks have a height of 20 nm and a refractive index $n_{\mathrm{Ag}} = -13.62 - 0.41i$. The absorbance ($A$) spectra of arrays A_1 and A_2, shown in Fig. 2.2(c) and in Fig. 2.A.1(c), were calculated from the simulated reflectance (R) and transmittance (T) spectra as $A = 1 - R - T$. For these wavelength resolved calculations interpolated Ag refractive index data from Ref. 45 was used. The nanodisk diameter was selected to be $d = 99$ nm for A_1 and $d = 62$ nm for A_2. As depicted in Fig. 2.2(b), the sample consists of a glass substrate, Ag nanodisks embedded in sol-gel and a PMMA layer on top. The glass substrate has the refractive index $n_{\mathrm{glass}} = 1.46$ and is in contact with the bottom input port. The sol-gel layer is modelled as 30 nm thick layer with same index as the glass layer ($n_{\mathrm{sol-gel}} = 1.46$). On top of that, is the PMMA layer ($n_{\mathrm{PMMA}} = 1.6$), which is 50 nm thick for A_1 and 100 nm thick for A_2. The total height of the simulation domain in z direction is 1 µm.

The simulated complex x, y, z components of the electric field profiles were extracted in the x-y plane at different heights t above the nanodisk array and imported in a MATLAB script, which further processes the data. The resolution of the exported fields was 200×346, which resulted in an initial step size of around 0.58 nm for A_1 and 1.44 nm for A_2. A large illumination area is generated by copying the complex electric field in the simulated unit cell in x and y directions. For A_1 we combined 60×35 unit cells to create a field of view of around 7 µm and for A_2 57×33 unit cells for a field of view of around 16 µm. The phase profiles of the combined fields are corrected by multiplying neighboring unit cells with $\Delta\Phi_j = \exp\left(i\mathbf{k}_{\parallel,j} \cdot \mathbf{dr}_{l,m}\right)$, where $\mathbf{dr}_{(l,m)}$ is the distance vector of unit cell with index (l,m) from the origin. After that, the DM-LPSIM illumination patterns were constructed using Eq. 2.2 and down-scaled using bi-linear interpolation to 252×252 pixels. This resulted in an effective pixel size of 27.4 nm for A_1 and 64.0 nm for A_2.

Figure 2.A.1(d-l) corresponds to Fig. 2.2(d-l) but for the parameter configuration A_2 and at a distance $t = 80$ nm from the array. Figure 2.A.2 shows the piFP reconstruction results for DM-LPSIM configuration A_2 as compared to widefield imaging and regular SIM using the same NA $= 0.55$. The resolution enhancement ability of DM-LPSIM at the distances $t = [40, 60, 80, 100, 120]$ nm as compared to regular SIM can be more quantitatively assessed using the MTF plots in Fig. 2.4(b). The images in Fig. 2.A.2(a3,a4) have stronger artifacts resembling the plasmonic grating

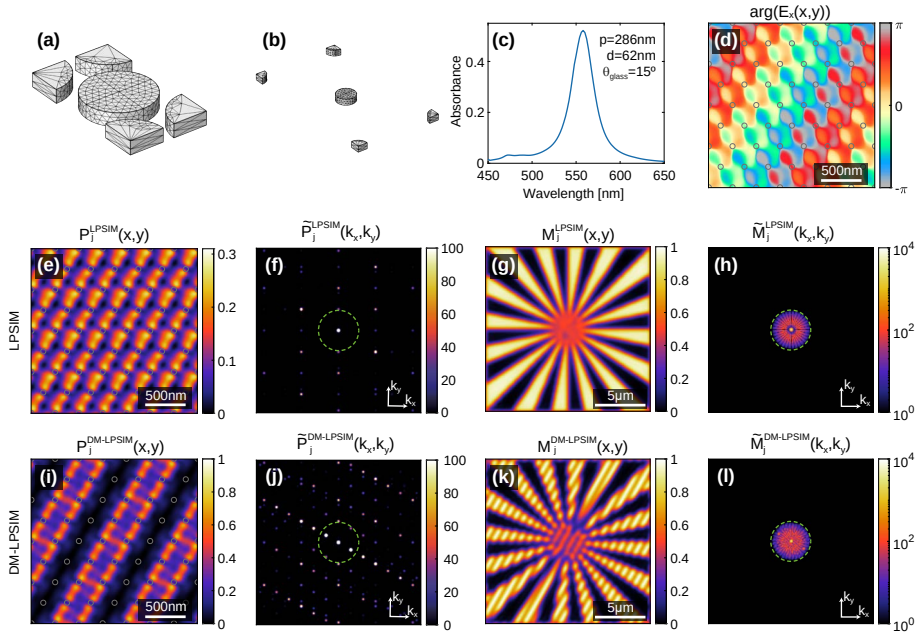

Figure 2.A.1: Simulation procedure for the A_2 array (a,b) The mesh of the nanodisk array A_1 and A_2, respectively. (c) The absorbance spectrum of the hexagonal Ag array A_2. (d) Phase profile $\arg(E_x(x,y))$ of 7×4 combined unit cells. (e,f) Example LPSIM illumination pattern and its Fourier transform. (g,h) A simulated LPSIM measurement and its Fourier transform. (i,j) Example DM-LPSIM illumination pattern and its Fourier transform. (k,l) A simulated DM-LPSIM measurement and its Fourier transform. The circles in the panels (d),(e), and (i) indicate the size and positions of the nanodisks. The green dashed circles in the Fourier plots indicate the cutoff frequency of WF imaging. Panels (d-l) show results at an extraction height $t = 80\,\text{nm}$ and an azimuthal angle $\phi = 150°$. The color scale in the panels (h) and (l) is logarithmic and otherwise linear.

itself compared to the results of configuration A_1. Such artifacts in plasmonic-SIM occur because the high wave-vector components of the structured illumination are largely concentrated in hot spots that reside at the plasmonic particles, and that can not be shifted through the unit cell by changing illumination conditions. It is hence a challenge to sample the entire unit cell for high-wave vector information. Additionally, note that since the pixel size of 64.0 nm[4] is much larger than some of the plasmonic near-field features, aliasing artifacts occur, which are visible at higher k values in the Fourier plots in Fig. 2.A.2(b3,b4).

[4]This pixel size is equal to the specimen pixel size expected in the experiment, where a camera with a pixel size of 6.45 μm and an optical system with 100× magnification are used.

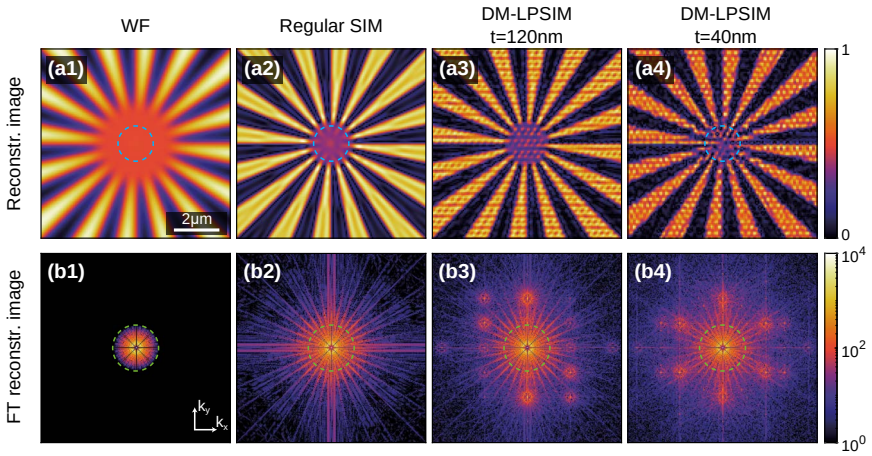

Figure 2.A.2: Reconstruction results for simulation configuration A_2. (a1) WF microscopy image for NA $= 0.55$. (a2-a4) Reconstructed images using regular SIM and DM-LPSIM illuminations at $t = 120$ nm and $t = 40$ nm respectively. (b1-b4) Fourier transforms of (a1-a4). The blue dashed circles in panels (a1), (a2) and (a4) indicate the radius of the cross-cuts shown in Fig. 2.4(d). The green dashed circles in panels (b1-b4) indicate the cutoff frequency of WF imaging.

2.B. Reconstruction algorithms

This section summarizes the various reconstruction algorithms tested to extract high-resolution specimen images from synthetic and experimental SIM data. At the beginning of each reconstruction method an initial guess of the specimen is created as an averaged sum of the raw measurements

$$s_0^{\text{est}}(x,y) = \frac{1}{L}\sum_{j=1}^{L} M_j(x,y). \tag{2.B.1}$$

and by performing five iterations of the Richardson-Lucy (RL) deconvolution [32]. Hereafter, different iterative reconstruction algorithms are used to further improve the resolution of the specimen image guess s_n^{est}, where $n = 1,...,N$ is the iteration index.

2.B.1. Pattern-illuminated Fourier ptychography with multiple patterns

The pattern-illuminated Fourier ptychography (piFP) algorithm allows to reconstruct high-resolution specimen images from LR pattern-illuminated measurement data [21, 22]. The piFP reconstruction can be understood as a minimization of the squared difference between the acquired data set $\left\{M_j\right\}$ and an iteratively refined estimate of the data set $\left\{M_{j,n}^{\text{est}}\right\}$ based on the forward model

of the imaging process

$$M_{j,n}^{\text{est}} = \left| \mathcal{F}^{-1} \left[\mathcal{F} \left(s_n^{\text{est}} \cdot P_j \right) \cdot \text{OTF} \right] \right|, \tag{2.B.2}$$

where $j = 1,..L$ is the pattern index, s_n^{est} is the n^{th} estimate of the specimen image and P_j is the j^{th} illumination pattern. The high-resolution part of the measurement estimate in Eq. (2.B.2) is in the following referred to as $M_{j,n}^{\text{HR,est}} = s_n^{\text{est}} \cdot P_j$. In each piFP iteration step, $M_{j,n}^{\text{HR,est}}$ is updated by following the update rule

$$\tilde{M}_{j,n}^{\text{HR,est}} = \tilde{M}_{n-1,j}^{\text{HR,est}} + \text{OTF} \cdot \left[\tilde{M}_j - \text{OTF} \cdot \tilde{M}_{n-1,j}^{\text{HR,est}} \right]. \tag{2.B.3}$$

After transforming $M_{n,i}^{\text{HR,est}}$ back to the spatial domain, it is used to update the super-resolved sample estimate using the following update rule

$$s_n^{\text{est}} = s_{n-1}^{\text{est}} + \sum_{j=1}^{L} \frac{P_j}{\max\left(P_j\right)^2} \left(M_{j,n}^{\text{HR,est}} - s_{n-1}^{\text{est}} \cdot P_j \right) \tag{2.B.4}$$

Note, that the originally proposed piFP implementation in Ref. 21 assumes only one illumination pattern, which is translated or rotated to different known positions on the sample. In contrast to that, here a series of L different patterns, which do not have to be translations of each other, is considered. The above extension of piFP was found to work reliably in combination with the simulated DM-LPSIM and regular SIM illumination patterns. However, the proposed illumination pattern recovery in Ref. 21, did not work for the case of a series of illumination patterns, which is why piFP was only used in combination with known illumination patterns. The convergence during each reconstruction is studied using the mean-square-error (MSE) of the sequential s_n images. Each of the reconstructions is terminated after $N = 2000$ iterations, which serves as a regularization of the piFP algorithm.

2.B.2. Blind and filtered blind-SIM

Similarly to piFP, the blind-SIM reconstruction approach is based on a minimization of the squared difference between the acquired data set $\left\{M_j\right\}$ and an iteratively refined estimate of the data set

$$M_{j,n}^{\text{est}} = \left| \mathcal{F}^{-1} \left[\mathcal{F} \left\{ s_n^{\text{est}} \cdot P_{j,n}^{\text{est}} \right\} \cdot \text{OTF} \right] \right| \tag{2.B.5}$$

The difference is that in blind-SIM the illumination patterns $P_{j,n}^{\text{est}}$ are themselves part of the reconstruction and a gradient descent algorithm is used to minimize the cost function

$$F\left(s_n^{\text{est}}, \{P_{j,n}^{\text{est}}\}\right) = \sum_{j=1}^{L} \left\| M_j - M_{j,n}^{\text{est}} \right\|^2. \tag{2.B.6}$$

The inverse problem defined by this minimization is ill-posed and needs to be regularized, since it is largely under-determined. Thus, in order to achieve regularization the minimization is stopped after a fixed number of iterations. It is well known that additional constraints to this inverse problem can yield an improved resolution of the reconstruction results [27]. Here, the positivity constraint is applied, which makes use of the fact that the specimen image and the illumination patterns can not be negative. This is achieved by redefining s_n^{est} and $P_{j,n}^{\text{est}}$ in terms of the positive auxiliary functions $s_n^{\text{est}} = \xi_n^2$ and $P_{j,n}^{\text{est}} = \eta_{j,n}^2$ as proposed in Ref. 33. Furthermore, in contrast to the originally proposed blind-SIM the sum of the illumination patterns is not assumed to be uniform, as this condition is not generally true in DM-LPSIM. The blind-SIM algorithm was implemented in MATLAB makes and using the L-BFGS (limited memory Broyden–Fletcher–Goldfarb–Shanno) algorithm from the minFunc package by M. Schmidt, which is a quasi-Newton minimization technique [35, 46, 47]. Each blind-SIM iteration performs 3 damped L-BFGS updates on the specimen image and the illumination patterns simultaneously. For the line-search in the L-BFGS algorithm the Wolfe condition with quadratic interpolation was used. Moreover, the descent directions of the L-BFGS algorithm are calculated using the following gradients for ξ_n and $\eta_{j,n}$:

$$\begin{aligned}\frac{\partial F\left(\xi_n,\{\eta_{j,n}\}\right)}{\partial \xi_n} &= -4\xi_{n-1}\sum_{j=1}^{L}\eta_{j,n-1}^2\left(M_j - M_{j,n-1}^{\text{est}}\right)\otimes \text{PSF}\\ \frac{\partial F\left(\xi_n,\{\eta_{j,n}\}\right)}{\partial \eta_{j,n}} &= -4\xi_{n-1}^2\eta_{j,n-1}\left(M_j - M_{j,n-1}^{\text{est}}\right)\otimes \text{PSF},\end{aligned} \tag{2.B.7}$$

where $\otimes$ denotes a convolution operation.

The so-called filtered blind-SIM (fb-SIM) approach introduces an additional constraint to the blind-SIM reconstruction by making use of the approximate knowledge of the illumination wave vector components [36]. This is achieved by Fourier filtering the illumination pattern gradient with a binary mask consisting of a central circle with a radius of $k_{\text{cutoff}}^{\text{LR}}$ and circles with a radius of 8 pixels at the expected illumination wave vector positions in k-space. This effectively guides the illumination reconstruction towards the expected k-components and was shown to make the algorithm more robust against optical aberrations and illumination imperfections [36].

2.B.3. Joint Richardson-Lucy deconvolution (jRL)

The joint Richardson-Lucy deconvolution (jRL) reconstruction approach was proposed by Ingaramo et al. for image scanning microscopy and was further adapted to multifocal structured illumination microscopy data by Ströhl et al. [32, 48]. While jRL reconstruction does not reconstruct the illumination pattern, its main strength is the ability to handle images with a varying PSF

and SNR and merge them into a single SR image. As the other reconstruction techniques jRL is based on modeling the underlying forward imaging model to establish a measurement estimate

$$M_{j,n}^{\text{est}} = \left| \mathcal{F}^{-1} \left[\mathcal{F} \left\{ s_n^{\text{est}} \cdot P_j \right\} \cdot \text{OTF} \right] \right|. \tag{2.B.8}$$

After that, the ratio between the actual measurement M_j and the measurement estimate $M_{j,n}^{\text{est}}$ is used to iteratively update the specimen image

$$s_n = s_{n-1} \cdot \left[\sum_{j=1}^{L} \left| \mathcal{F}^{-1} \left[\mathcal{F} \left(\frac{M_j}{M_{j,n-1}^{\text{est}}} \right) \cdot \text{OTF} \right] \right| \cdot P_j \right]. \tag{2.B.9}$$

2.B.4. Resolution characterization

The modulation transfer function (MTF) is calculated by first transforming the Siemens star image from Cartesian x/y coordinates to cyllindrical ρ/ϕ coordinates. Then at every slice in ρ a sine function (with 3 variables for contrast, phase and y-offset) is fitted to the data using a nonlinear least-squares fit. The contrast of this sine fit yields the MTF:

$$\text{MTF} = \frac{I_{\max} - I_{\min}}{I_{\max} + I_{\min}}. \tag{2.B.10}$$

The normalized wave vector, which is used as the x-axis of the MTF plots, is calculated from the radius ρ using:

$$\frac{k}{k_0} = \frac{N_{\text{cycles}}}{\rho \cdot k_0}, \tag{2.B.11}$$

where $N_{\text{cycles}} = 16$ is the number of black/white cycles in the Siemens star.

2.C. Measurement and alignment procedure

During the DM-LPSIM measurements, a set of light gratings is sequentially projected on top of a plasmonic grating. This incident light grating together with light scattered off the plasmonic grating form the pump intensity patterns that are used to illuminate the specimen. Before the measurements, the structured illumination unit was precisely calibrated to the objective and plasmonic grating in use. In the first step, the SLM image was centered on the back focal plane (BFP) of the objective. As described in Sec. 2.3.3, to achieve this we first move to a reflective region on the sample, remove the long-pass filter and switch to BFP measurement mode by flipping out lens L_6 from the setup shown in Fig. 2.5(a). This makes it possible to capture the SLM defined beam in the BFP. The x and y offset of the SLM image are calibrated using an image of a ring (filled with blazed phase gratings) with a diameter equal to

the BFP diameter, to achieve an alignment precision of only a few SLM pixels. The blazed phase gratings have a pitch of 6 px and are oriented at 45°. The setup, shown in Fig. 2.5(a), was aligned to transmit the first grating order of this blazed grating through the iris and towards the BFP of the objective.

The SLM images, which were used for the DM-LPSIM illumination, feature two circular modes of blazed phase gratings having a radius of 6 px and a distance of 69 px. A circle with a radius of 6 px on the SLM corresponds to a polar angle spread of around 2.7° on the sample plane. The orientation of and distance between the two circular modes controls the azimuthal and polar angle of the two-beam illumination pattern on the sample plane. The correct azimuthal and polar angles of this two-beam illumination depend on the precise orientation and pitch of the hexagonal plasmonic arrays. In order to align the light grating with respect to the plasmonic grating, the 2D Fourier transformed fluorescent image illuminated by the DM-LPSIM pattern was utilized. For an optimal DM-LPSIM pattern, the peaks in the Fourier transform should be uniformly distributed as described in Sec. 2.2.1. The two crucial alignment parameters are azimuthal angle and the distance of the two circular modes in the SLM image. To make this process more user friendly we implemented a Python GUI using wxPython that can Fourier transform a part of your screen in real-time.

After the alignment the DM-LPSIM measurements were performed, in which the 27 SLM images are successively displayed. As mentioned earlier, these images have 3 different orientations, each featuring 9 phase shifts. These phase shifts were achieved by increasing the phase offset of one of the blazed grating modes. Using a custom .NET-based software the phase shifted SLM images were displayed, while simultaneously capturing CCD images. For each azimuthal angle a 10^{th} measurement is performed, in which a black image is displayed on the SLM, and used for background subtraction. Additionally, for each new azimuthal angle HWP_2 was rotated using a motorized rotation mount to ensure s-polarization.

References

1. M. G. L. Gustafsson, *Surpassing the lateral resolution limit by a factor of two using structured illumination microscopy*, J. Microsc. **198**, 82 (2000).
2. R. Heintzmann and M. G. Gustafsson, *Subdiffraction resolution in continuous samples*, Nat. Photonics **3**, 362 (2009).
3. M. J. Rust, M. Bates, and X. Zhuang, *Sub-diffraction-limit imaging by stochastic optical reconstruction microscopy (storm)*, Nat. Methods **3**, 793 (2006).
4. E. Betzig, G. H. Patterson, R. Sougrat, O. W. Lindwasser, S. Olenych, J. S. Bonifacino, M. W. Davidson, J. Lippincott-Schwartz, and H. F. Hess, *Imaging intracellular fluorescent proteins at nanometer resolution*, Science **313**, 1642 (2006).
5. S. W. Hell and J. Wichmann, *Breaking the diffraction resolution limit by stimulated emission: stimulated-emission-depletion fluorescence microscopy*, Opt. Lett. **19**, 780 (1994).
6. L. Schermelleh, R. Heintzmann, and H. Leonhardt, *A guide to super-resolution fluorescence microscopy*, J. Cell Biol. **190**, 165 (2010).
7. F. Ströhl and C. F. Kaminski, *Frontiers in structured illumination microscopy*, Optica **3**, 667 (2016).
8. R. Heintzmann and T. Huser, *Super-resolution structured illumination microscopy*, Chem. Rev. **117**, 13890 (2017).
9. R. Heintzmann, T. M. Jovin, and C. Cremer, *Saturated patterned excitation microscopy-a concept for optical resolution improvement*, J. Opt. Soc. Am. A **19**, 1599 (2002).
10. M. G. Gustafsson, *Nonlinear structured-illumination microscopy: wide-field fluorescence imaging with theoretically unlimited resolution*, Proc. Natl. Acad. Sci. U.S.A. **102**, 13081 (2005).
11. E. H. Rego, L. Shao, J. J. Macklin, L. Winoto, G. A. Johansson, N. Kamps-Hughes, M. W. Davidson, and M. G. Gustafsson, *Nonlinear structured-illumination microscopy with a photoswitchable protein reveals cellular structures at 50-nm resolution*, Proc. Natl. Acad. Sci. U.S.A. **109**, E135 (2012).
12. Y. Blau, D. Shterman, G. Bartal, and B. Gjonaj, *Double moiré structured illumination microscopy with high-index materials*, Opt. Lett. **41**, 3455 (2016).
13. D. Shterman, B. Gjonaj, and G. Bartal, *Experimental demonstration of multi moiré structured illumination microscopy*, ACS Photonics **5**, 1898 (2018).
14. Z. Liu, S. Durant, H. Lee, Y. Pikus, N. Fang, Y. Xiong, C. Sun, and X. Zhang, *Far-field optical superlens*, Nano Lett. **7**, 403 (2007).
15. A. Sentenac, K. Belkebir, H. Giovannini, and P. C. Chaumet, *Subdiffraction resolution in total internal reflection fluorescence microscopy with a grating substrate*, Opt. Lett. **33**, 255 (2008).
16. J. L. Ponsetto, F. Wei, and Z. Liu, *Localized plasmon assisted structured illumination microscopy for wide-field high-speed dispersion-independent super resolution imaging*, Nanoscale **6**, 5807 (2014).
17. J. L. Ponsetto, A. Bezryadina, F. Wei, K. Onishi, H. Shen, E. Huang, L. Ferrari, Q. Ma, Y. Zou, and Z. Liu, *Experimental demonstration of localized plasmonic structured illumination microscopy*, ACS nano **11**, 5344 (2017).
18. A. Bezryadina, J. Zhao, Y. Xia, Y. U. Lee, X. Zhang, and Z. Liu, *Localized plasmonic structured illumination microscopy with gaps in spatial frequencies*, Opt. Lett. **44**, 2915 (2019).

19. A. Sentenac, K. Belkebir, H. Giovannini, and P. C. Chaumet, *High-resolution total-internal-reflection fluorescence microscopy using periodically nanostructured glass slides*, J. Opt. Soc. Am. A **26**, 2550 (2009).
20. S. Liu, C.-J. Chuang, C. See, G. Zoriniants, W. Barnes, and M. Somekh, *Double-grating-structured light microscopy using plasmonic nanoparticle arrays*, Opt. Lett. **34**, 1255 (2009).
21. S. Dong, P. Nanda, R. Shiradkar, K. Guo, and G. Zheng, *High-resolution fluorescence imaging via pattern-illuminated Fourier ptychography*, Opt. Express **22**, 20856 (2014).
22. N. Chakrova, R. Heintzmann, B. Rieger, and S. Stallinga, *Studying different illumination patterns for resolution improvement in fluorescence microscopy*, Opt. Express **23**, 31367 (2015).
23. G. Zheng, R. Horstmeyer, and C. Yang, *Wide-field, high-resolution Fourier ptychographic microscopy*, Nature Photon. **7**, 739 (2013).
24. Y. Fang, Y. Chen, C. Kuang, P. Xiu, Q. Liu, B. Ge, and X. Liu, *Saturated pattern-illuminated Fourier ptychography microscopy*, J. Opt. **19**, 015602 (2016).
25. Q. Liu, Y. Chen, W. Liu, Y. Han, R. Cao, Z. Zhang, C. Kuang, and X. Liu, *Total internal reflection fluorescence pattern-illuminated Fourier ptychographic microscopy*, Opt. Lasers Eng. **123**, 45 (2019).
26. C. Loebich, D. Wueller, B. Klingen, and A. Jaeger, *Digital camera resolution measurements using sinusoidal Siemens stars*, in *Digital photography III*, Vol. 6502, edited by R. A. Martin, J. M. DiCarlo, and N. Sampat, International Society for Optics and Photonics (SPIE, 2007) pp. 214 – 224.
27. G. De Villiers and E. Pike, *The limits of resolution*, Optics and Optoelectronics (CRC Press, Taylor & Francis Group, CRC, Boca Raton, 2016).
28. J. A. Davis, D. M. Cottrell, J. Campos, M. J. Yzuel, and I. Moreno, *Encoding amplitude information onto phase-only filters*, Appl. Opt. **38**, 5004 (1999).
29. E. Otte, C. Schlickriede, C. Alpmann, and C. Denz, *Complex light fields enter a new dimension: holographic modulation of polarization in addition to amplitude and phase*, in *Complex light and optical forces IX*, Vol. 9379, International Society for Optics and Photonics (SPIE, 2015) p. 937908.
30. F. López Arbeloa, J. Banuelos, V. Martínez, T. Arbeloa, and I. López Arbeloa, *Structural, photophysical and lasing properties of pyrromethene dyes*, Int. Rev. Phys. Chem. **24**, 339 (2005).
31. L. Dai, I. Gregor, I. von der Hocht, T. Ruckstuhl, and J. Enderlein, *Measuring large numerical apertures by imaging the angular distribution of radiation of fluorescing molecules*, Opt. Express **13**, 9409 (2005).
32. F. Ströhl and C. F. Kaminski, *A joint Richardson-Lucy deconvolution algorithm for the reconstruction of multifocal structured illumination microscopy data*, Method. Appl. Fluoresc. **3**, 014002 (2015).
33. E. Mudry, K. Belkebir, J. Girard, J. Savatier, E. Le Moal, C. Nicoletti, M. Allain, and A. Sentenac, *Structured illumination microscopy using unknown speckle patterns*, Nat. Photonics **6**, 312 (2012).
34. F. Wei, D. Lu, H. Shen, W. Wan, J. L. Ponsetto, E. Huang, and Z. Liu, *Wide field super-resolution surface imaging through plasmonic structured illumination microscopy*, Nano Lett. **14**, 4634 (2014).
35. A. Jost, E. Tolstik, P. Feldmann, K. Wicker, A. Sentenac, and R. Heintzmann, *Optical sectioning and high resolution in single-slice structured illumination microscopy by thick slice blind-SIM reconstruction*, PloS One **10**, e0132174 (2015).

36. R. Ayuk, H. Giovannini, A. Jost, E. Mudry, J. Girard, T. Mangeat, N. Sandeau, R. Heintzmann, K. Wicker, K. Belkebir, *et al.*, *Structured illumination fluorescence microscopy with distorted excitations using a filtered blind-SIM algorithm*, Opt. Lett. **38**, 4723 (2013).
37. M. I. Stockman, S. V. Faleev, and D. J. Bergman, *Coherent control of femtosecond energy localization in nanosystems*, Phys. Rev. Lett. **88**, 067402 (2002).
38. M. Aeschlimann, M. Bauer, D. Bayer, T. Brixner, F. J. G. De Abajo, W. Pfeiffer, M. Rohmer, C. Spindler, and F. Steeb, *Adaptive subwavelength control of nano-optical fields*, Nature **446**, 301 (2007).
39. Q. Xu, X. Zhang, Q. Yang, C. Tian, Y. Xu, J. Zhang, H. Zhao, Y. Li, C. Ouyang, Z. Tian, J. Gu, X. Zhang, J. Han, and W. Zhang, *Polarization-controlled asymmetric excitation of surface plasmons*, Optica **4**, 1044 (2017).
40. L. Langguth, A. Szuba, S. A. Mann, E. C. Garnett, G. H. Koenderink, and A. F. Koenderink, *Nano-antenna enhanced two-focus fluorescence correlation spectroscopy*, Sci. Rep. **7**, 1 (2017).
41. G. Volpe, G. Molina-Terriza, and R. Quidant, *Deterministic subwavelength control of light confinement in nanostructures*, Phys. Rev. Lett. **105**, 216802 (2010).
42. T. S. Kao, S. D. Jenkins, J. Ruostekoski, and N. I. Zheludev, *Coherent control of nanoscale light localization in metamaterial: Creating and positioning isolated subwavelength energy hot spots*, Phys. Rev. Lett. **106**, 085501 (2011).
43. G. F. Walsh, C. Forestiere, and L. D. Negro, *Plasmon-enhanced depolarization of reflected light from arrays of nanoparticle dimers*, Opt. Express **19**, 21081 (2011).
44. J. Idier, S. Labouesse, M. Allain, P. Liu, S. Bourguignon, and A. Sentenac, *On the superresolution capacity of imagers using unknown speckle illuminations*, IEEE Trans. Comput. Imaging **4**, 87 (2017).
45. P. B. Johnson and R.-W. Christy, *Optical constants of the noble metals*, Phys. Rev. B **6**, 4370 (1972).
46. M. Schmidt, *minfunc: unconstrained differentiable multivariate optimization in Matlab*, (2005) [retrieved 23 May 2017], `http://www.cs.ubc.ca/~schmidtm/Software/minFunc.html`.
47. D. C. Liu and J. Nocedal, *On the limited memory BFGS method for large scale optimization*, Math. Program. **45**, 503 (1989).
48. M. Ingaramo, A. G. York, E. Hoogendoorn, M. Postma, H. Shroff, and G. H. Patterson, *Richardson-Lucy deconvolution as a general tool for combining images with complementary strengths*, ChemPhysChem **15**, 794 (2014).

3

Optimized 2D target design for diffraction-based overlay metrology

Scatterometry is an optical metrology technique, in which light scattered from a specifically designed grating stack (overlay target) is measured in the far-field. Using 1D periodic overlay target designs the technique has been shown to have nanometer-scale sensitivity to spatial misalignments of subsequent patterned layers, which are also known as overlay errors. However, while scatterometry is highly sensitive to overlay errors, multiple sources of systematic errors hinder its absolute accuracy. This chapter investigates how an extended version of scatterometry called Fourier scatterometry in combination with more complex overlay target designs can help to address those challenges. To this end, a statistical method has been developed, which can determine the influence of 2D overlay targets on the overlay measurement uncertainty. The study involves periodic and deterministic aperiodic designs as well as designs that emerged from simulated annealing optimizations. The results suggest that current overlay target designs could be augmented by more complex 2D designs to fulfill specific purposes, such as fabrication robustness and high sensitivity over a large overlay range.

3.1. Introduction

CURRENT semiconductor manufacturing relies on highly accurate, real-time process monitoring techniques to achieve a high yield in modern integrated circuit fabrication despite hundreds of necessary processing steps. One important type of metrology involves the measurement of spatial misalignments of subsequent patterned layers, which are also known as overlay (OV) errors. To ensure working devices, the OV error has to be smaller than a fraction of the minimum feature size. Continuously shrinking node sizes and increasing product stack complexity have reduced OV error tolerances down to only a few nanometers, which is why OV metrology could become a limiting factor for further progress of the industry [1, 2].

A widely used OV metrology technique is diffraction-based overlay scatterometry (DBO) [3–10], in which diffraction patterns back-scattered from two gratings, that are stacked on top of each other, are analyzed to infer the OV error. Typical DBO implementations make use of spectroscopic or ellipsometric diffraction signals. The idea is that for perfect alignment the OV target possesses a symmetric scattering signature, similar to a single grating. A spatial misalignment ($|OV| > 0$) results in an unbalanced Fourier-plane intensity distribution in direction of the misalignment, as indicated in Fig. 3.1(a). Indeed, interference of light back-scattered by the bottom and the top grating transduce the misalignment into an intensity difference between diffraction orders. For simple line gratings, for instance, the intensity in the 1st and -1st diffraction orders I_{+1} and I_{-1} can be used to construct the asymmetry signal $\Delta I = I_{+1} - I_{-1}$, which for OV values much smaller than the grating pitch p possesses a linear dependence on the OV error with a proportionality factor K, see Fig. 3.1(b). The exact value of K depends on the target structure and implementation of the type of scattering signature measurement and is in practice calibrated by measuring the asymmetry signal of two grating pairs with a programmed overlay offset [9].

The focus of this work is Fourier scatterometry [7, 11–14], in which a cone of light is scattered off a sample and collected by a microscope objective. Relaying the image of the objective back focal plane onto a 2D pixelated detector provides a direct mapping of scattering angles to image positions in a single shot measurement [15]. Notably, Fourier scatterometry is fast since no angle or frequency scanning is required, and can be further enhanced to include polarization and phase resolution [12–14].

Because the full angle-dependent diffraction pattern is collected, the limitation to only periodic OV target designs is lifted. This allows the characterization of more complex (non-periodic) 2D geometries. The purpose of this work is to explore whether 2D OV targets provide advantages for Fourier scatterometry in terms of OV accuracy, range of OV sensitivity, and robustness in the face of measurement and fabrication noise. Figure 3.1(c, e) resp. 3.1(d,f) illustrate the rationale for this switch, demonstrating the diffraction patterns of a

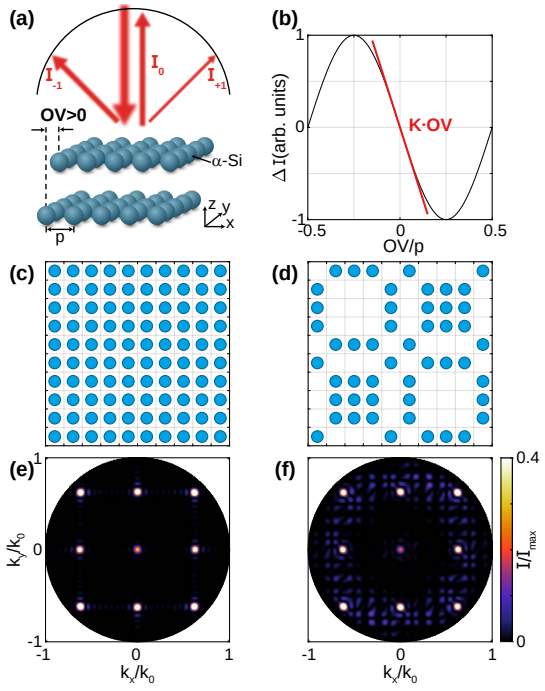

Figure 3.1: (a) Schematic of the measurement configuration in Fourier scatterometry, where scattered light is measured in the upper hemisphere above the sample. The spatial misalignment (OV error) between the top and bottom grating of the OV target causes an asymmetric back-scattering signal. (b) This asymmetry signal ΔI, which is comprised of the difference between the 1^{st} and -1^{st} diffraction orders, has a linear dependence (shown in red) on OV at small OV values. (c,d) Square and aperiodic (Rudin-Shapiro) lattice designs. (e,f) Diffraction patterns generated by grating stacks with designs from (c) and (d) at OV $= 0$.

2D periodic and a deterministic aperiodic OV target as calculated using a generalized Mie scattering modeling approach. Evidently, 2D arrays offer a larger design space as compared to line gratings. The fact that many diffraction features appear means that there may be richer information in them, as compared to the simple asymmetry signal ΔI arising from the first diffraction orders. The investigated 2D designs borrow ideas from the branches of nanophotonics for photovoltaics, metasurfaces and sensing [16–18] and in particular the study of deterministic aperiodic scattering structures [19–22]. In addition to periodic and deterministically aperiodic geometries, we investigate geometries that emerged from simulated annealing optimizations [23]. Further details on the implementation of the simulated annealing algorithm and the design search strategy are given in Ref. 24. In general, numerical optimization is a popular tool to improve device performance in a wide range of fields including mechanical design, nanophotonics, and optical metrology [25–28].

In this chapter, a library-based Monte-Carlo method is introduced, which aims to numerically characterize the performance of different OV target designs. To do this, initially data sets containing scattering patterns calculated for a range of OV values and different OV target designs were generated. The underlying simulation framework is generalized multiparticle Mie theory (GMMT), which is a method that can deal with finite clusters of scatterers at very low computation time, yet exact position accuracy[29, 30]. Next, a low dimensional feature extraction is performed on the data sets by means of singular value decomposition (SVD). This type of approach originated in the field of face recognition, where it is referred to as the 'eigenface' technique [31, 32]. The SVD results are used to construct libraries, which capture the effect of OV variation on the diffraction patterns of the different OV target types using only a few essential signatures. In subsequent Monte-Carlo simulations, these libraries are used to retrieve the OV values of new sampling data sets, which contain measurement or fabrication errors. Importantly, the prior knowledge that goes into building the library means that this OV retrieval is ultimately not limited by the optical resolution limit, but rather by the non-uniqueness of the inverse scattering problem or by unfitted fabrication and measurement fluctuations [2, 33]. The merit of this work thus includes both the analysis method and the provided comparison of OV target designs.

The chapter is structured as follows. In Section 3.2, the numerical framework is presented, which involves three main operations, namely, far-field scattering simulations, library creation, and Monte-Carlo analysis. Section 3.3 deals with the OV target optimization procedure and its outcome. After this, OV measurement uncertainty results in the presence of shot and fabrication noise are presented in Sec. 3.4. Finally, in Section 3.5, the effectiveness of the presented technique is summarized and an outlook on future prospects of this methodology is given.

3.2. Simulation and uncertainty estimation

3.2.1. Far-field scattering simulation

Fourier-plane distributions of light back-scattered from an OV target were simulated using the semi-analytic generalized multiparticle Mie theory. This method makes it possible to compute scattered far-fields of finite-sized grating stacks at a high speed, while taking multiple scattering interactions into account to all orders, and dealing with scatterer positions exactly, i.e., without any discretization step. Although the method has the disadvantage that only assemblies of spheroidal scatterers in homogeneous background media can be dealt with, it offers large advantages over other approaches. In particular, rigorous coupled wave analysis (RCWA), which relies on a Fourier expansion of the dielectric constant, is a commonly used simulation method in scatterometry [34, 35]. While it is known to be computationally efficient, it can not deal

with finite truncations of infinite lattices, or with aperiodic systems. Since in OV metrology one typically has targets of just 10 wavelengths across, the RCWA is of limited use unless one resorts to complex extensions to finite structures [36]. More computationally intensive mesh/grid discretization based techniques like the Finite Element Method (FEM) and Finite Difference Time Domain (FDTD) method have been used for detailed studies of the signal formation process in scatterometry, and have the advantage that more complex systems can be dealt with [25, 37, 38]. However, in this work it was found that discretization is inherently problematic for OV metrology simulations since the error in determining sub-nm OV from simulated data and libraries is limited by this discretization, and not by the OV target, fabrication noise, or measurement scenario that one wishes to explore. While GMMT has not been used in the context of OV metrology, it has the advantages of speed, accuracy, and requires no discretization of real space [39].

To further decrease computation time, we only include up to dipolar electric and magnetic interactions into the Mie scattering model, which means that the spherical Bessel functions of the first kind in the Mie scattering formalism are expanded up to order 1. This approximation is equivalent to evaluating a fully retarded electrodynamic multiple scattering model for the overlay targets that takes into account electric and magnetic dipole responses of each particle but that neglects multipole corrections. Such approximations are typically used for small particles. We verified that an increase of the expansion order did not cause noticeable changes to the far-field radiation patterns of the OV targets. The arrays are excited by normally incident monochrome excitation of wavelength $\lambda = 467.5\,\text{nm}$ and polarized in the y direction. Both of the arrays consist of spherical amorphous Silicon (α-Si) particles, which are modeled using dielectric data from Ref. 40, which leads to a refractive index of $n_{\alpha\text{-Si}} = 4.47 + i \cdot 1.37$ at $\lambda = 467.5\,\text{nm}$. The background medium is assumed to be glass-like with a uniform refractive index of $n_{\text{SiO}_2} = 1.5$. These parameters have by no means been chosen to, e.g., optimize the scattering cross section of the particles, with the rationale that OV metrology generally operates not with optimally chosen grating materials and dimensions, but within customer constraints. Since in modern technology nodes the available footprint for OV targets is limited [41], the selected array design takes up a total area of $(4.8 \times 4.8)\,\mu\text{m}^2$. This is done by limiting the design space to a 10×10 grid with a pitch $p = 500\,\text{nm}$, where every site can be filled or not filled by a nanoparticle with a radius $r = 150\,\text{nm}$. Figure 3.1(c,d) shows two possible particle arrangements following this design constraint. The complete OV target consists of two identical gratings in the bottom and top layer, which are $t = 400\,\text{nm}$ apart. Any value of OV is introduced by shifting the top grating in x-direction, as indicated in Fig. 3.1(a).

To mimick a practical optical set up scenario, a binary ring mask is applied to limit the scattering pattern to the angular range between $\text{NA} = 0.225$ and $\text{NA} = 1.42$, where $\text{NA} = n_{\text{SiO}_2} \sin(\theta)$ is the numerical aperture and θ the

polar angle. This is equivalent to using a high NA objective for capturing the first grating diffraction orders, with a beam block to remove directly reflected light, i.e., zero-order light. Figure 3.2(a) shows such a masked Fourier-plane image for an example design studied in this work, a so-called Rudin-Shapiro target. Note that the full design space will be discussed later, and this design is merely an example. To make the comparison of the different array designs independent of the number of scatterers, the far-field intensity $|E_{\mathrm{sim}}|^2$ is normalized to a constant photon count in the detected angular region. This normalization is computed as follows

$$I_{\mathrm{norm}}(\mathrm{OV}) = \frac{C_{\mathrm{tot}}\left|E_{\mathrm{sim}}(\mathrm{OV})\right|^2}{\sum_{k_x,k_y}\left|E_{\mathrm{sim}}(\mathrm{OV}_m)\right|^2}, \tag{3.1}$$

where C_{tot} is the total photon count in the masked region and OV_m is the OV value producing the largest integrated photon count. C_{tot} can be also expressed using the average photon count C_{avg} as $C_{\mathrm{tot}} = C_{\mathrm{avg}} N_{\mathrm{px}}$, where $N_{\mathrm{px}} = 27636$ is the number of pixels of the ring mask. It should be noted that the choice of any particular normalization will affect the outcome of studies related to measurement noise. The normalization with a constant integrated photon count roughly assumes that the detected signal will be limited by a total source photon budget used for the measurements, as opposed to, e.g., normalizing images to a maximum count rate, which would be applicable if measurements were limited by the dynamic range of a detector. Figure 3.2(a,b) shows examples of normalized Fourier images I_{norm} of the Rudin-Shapiro target design at OV shifts of 0 nm and 10 nm. In the OV = 10 nm case a slight asymmetry between the main grating orders on the left and right side arises due to the spatial misalignment of the two gratings. This asymmetry becomes more visible when plotting the difference between the two intensity patterns in Fig. 3.2(c). Further, Fig. 3.2(c) shows that also many other Fourier plane components of lesser amplitude, introduced by the a-periodic nature of the target, show asymmetries and hence carry information relevant for OV error determination.

3.2.2. Library generation using SVD

Given a complex Fourier-plane distribution that varies with OV, as in Fig. 3.2(c), it is not obvious how to quantify the performance of a target in terms of OV metrology. To accomplish this task, a library search approach in combination with feature extraction via singular value decomposition (SVD) is used. Library-based techniques are known to be robust solutions to the scatterometry inverse problem with an OV accuracy that only depends on the library step size [42]. Since the investigated approach relies on Fourier scatterometry, the library contains a series of Fourier images featuring the scattering of targets with a range of OV shifts, which are referred to as library

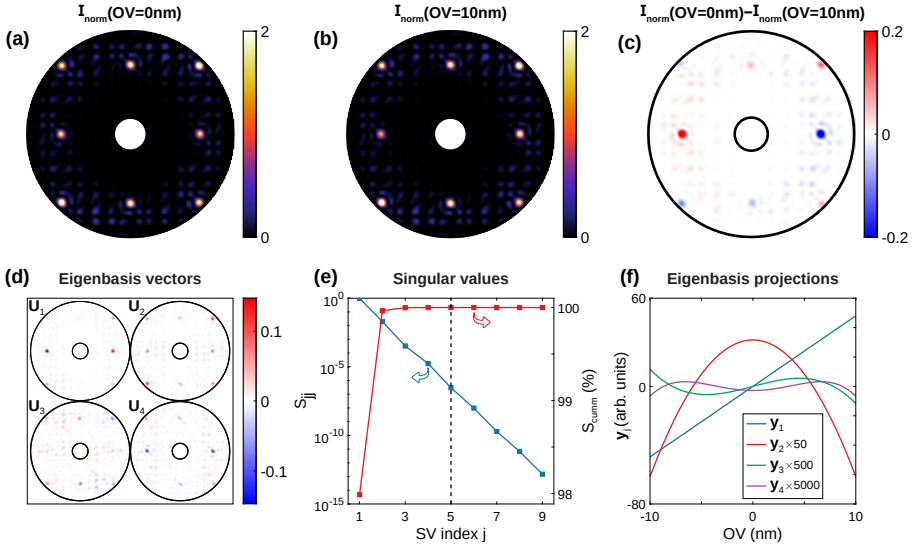

Figure 3.2: Library generation. (a,b) Normalized Fourier intensity maps for the Rudin-Shapiro OV target at an OV error of 0 nm and 10 nm. (c) Difference between (a) and (b). (d) Eigenbasis vectors and singular values obtained from the SVD of 101 far-field intensities with an OV value range of -10 nm to 10 nm. (e) The singular values S_{jj} are plotted in blue on a log-scale. The sum of the singular values is normalized to one. The red curve indicates the cumulative singular values S_{cum} in percent. (f) Projected coordinates of the library images in the SVD eigenspace as a function of OV. Note that the color scales in (a-c) are saturated at 80% of the maximum reflected intensity.

images. To make the library more efficient, an SVD-based feature extraction is performed, which is a technique well-known for its ability to greatly reduce the dimension of correlated data sets [31]. The SVD-based dimension reduction works by finding a new optimal orthonormal basis for the subspace containing all the library images of a particular OV target. Using this library eigenbasis, any new diffraction pattern of the OV target having an OV shift within the library range can be expressed by a linear combination without the loss of valuable information. This fact will subsequently allow the retrieval of OV values even if these values are not contained in the original data set.

In a first step, for each OV target a series of N_{sim} library images are calculated featuring linearly increasing OV values within two different OV ranges, namely, $[-10...10]$ nm and $[0...125]$ nm. The images have a width and height of $n = 201$ pixels, from which $N_{\text{px}} = 27636$ pixels are used after a binary masking step, as described in the previous section. For the purpose of SVD each of the N_{sim} library images is flattened to a column vector $\mathbf{f}_i$ and centered around their mean $\mathbf{f}_i^c = \mathbf{f}_i - \overline{\mathbf{f}}$, where $\overline{\mathbf{f}} = 1/N_{\text{sim}} \sum_i^{N_{\text{sim}}} \mathbf{f}_i$ is the average library image and $i = 1,...,N_{\text{sim}}$ is the library OV index. The centered vectors $\mathbf{f}_i^c$ form the columns of matrix $\mathbf{A} = [\mathbf{f}_1^c, \mathbf{f}_2^c, ..., \mathbf{f}_{N_{\text{sim}}}^c]$. The SVD technique performs a

factorization of matrix $\mathbf{A}$ ($n^2 \times N_{\text{sim}}$) of the form:

$$\mathbf{A} = \mathbf{U} \cdot \mathbf{S} \cdot \mathbf{V}^T, \tag{3.2}$$

where T denotes the transpose operation. The orthonormal matrices $\mathbf{U}$ ($n^2 \times n^2$) and $\mathbf{V}^T$ ($N_{\text{sim}} \times N_{\text{sim}}$) contain the left-hand and right-hand singular vectors, and $\mathbf{S}$ ($n^2 \times N_{\text{sim}}$) is a rectangular matrix consisting of the singular values arranged in decreasing order along its diagonal.

Figure 3.2(d,e) shows example SVD results for the Rudin-Shapiro target design in the OV range of $[-10...10]$ nm. The first four singular vectors are shown in Fig. 3.2(d). Figure 3.2(e) shows the first nine singular values on a logarithmic scale (in blue), where the sum of all N_{sim} singular values is normalized to unity. By calculating the cumulative normalized singular values S_{cum} (shown in red and on a linear scale in Fig. 3.2(e)), it can be determined how accurately the first few components represent the signal. In this case, with only the first five eigenbasis components, the representation error of the full library data set is on the order of 10^{-6} %. In other words, the main OV-dependent behavior of the far-field scattering signal is almost fully captured by a few singular vectors, which suggests a high degree of correlation in the library data. Thus, truncating the eigenbasis $\mathbf{U}$ does not lead to noticeable loss of valuable information, while greatly reducing computation load in subsequent analysis steps. The truncated eigenbasis $\tilde{\mathbf{U}}$ has a size of ($n^2 \times L$). The truncation indices L and the resulting errors (for the Rudin-Shapiro target) at both OV ranges are given in Table 3.1.

An important property of the SVD is that the column vectors constituting $\tilde{\mathbf{U}}$ form an orthonormal basis of the column space of matrix $\mathbf{A}$. This allows us to define a new coordinate space, wherein any diffraction pattern has as coordinate the linear expansion coefficients required to express $\mathbf{f}_i^c$ in $\tilde{\mathbf{U}}$. Thus, the eigenbasis coordinates of all the library images can be computed by projecting the centered images $\mathbf{f}_i^c$ onto library eigenspace for every library OV index $i = 1, ..., N_{\text{sim}}$ as

$$\mathbf{x}_i = \tilde{\mathbf{U}}^T \cdot \mathbf{f}_i^c. \tag{3.3}$$

The projected coordinates $\mathbf{x}_i$ form the columns of matrix $\mathbf{X}(N_{\text{sim}} \times L)$. The rows of matrix $\mathbf{X}$ will be referred to as $\mathbf{y}_j$. They reveal the OV-dependent behavior of the library images at the different eigenbasis indices $j = 1, ..., L$

Table 3.1: Library parameters. This table summarizes the number of interpolated and simulated OV shifts N_{interp} and N_{sim}, the simulated OV step size $\text{OV}_{\text{sim, step}}$, the singular value truncation index L and the remaining commutative error due to truncation $1 - S_{\text{cumm}}(L)$ for the two investigated OV ranges.

OV range	N_{interp}	N_{sim}	$\text{OV}_{\text{sim, step}}$	L	$1 - S_{\text{cumm}}(L)$
$[-10...10]$ nm	20001	101	0.2 nm	5	$9.9 \cdot 10^{-7}$ %
$[0...125]$ nm	125001	126	1 nm	10	$1.1 \cdot 10^{-6}$ %

and can be seen as an analogy to the asymmetry signal used in regular DBO. As an example, Fig. 3.2(f) shows the first four rows of $\mathbf{X}$ for the Rudin-Shapiro data set, where $\mathbf{y}_j$ with $j > 1$ were magnified for clarity. Interestingly, $\mathbf{y}_1$, which contains projections onto the first and most significant SV component, shows a linear behavior as a function of OV (shown in blue in Fig. 3.2(f)). This observation is in line with the simple analytic expectation for DBO based on the asymmetry of the main first diffraction orders [10]. It is evident that complex targets with more complex Fourier patterns carry more information if one considers that higher order eigenbasis coordinates show variations with overlay (see $\mathbf{y}_j$ with $j = 2, 3, 4$ in Fig. 3.2(f)). These non-linear contributions such as $\mathbf{y}_2$ aid OV sensitivity primarily at higher OV values, where their slope as a function of OV increases.

Finally, the continuous nature of $\mathbf{y}_j$ as a function of OV allows an interpolation to a much finer OV step size, which will greatly improve the accuracy of the library-based technique without the need of additional simulation runs. To this end, a cubic spline interpolation is performed in MATLAB with a step size of $\mathrm{OV}_{\mathrm{interp,\,step}} = 0.001\,\mathrm{nm}$ for the libraries of both OV ranges. For the resulting number of interpolated OV shifts N_{interp} see Table 3.1. A completed library for a particular OV target consists of the truncated eigenbasis $\tilde{\mathbf{U}}(n^2 \times L)$, the interpolated projected library coordinates $\mathbf{X}_{\mathrm{interp}}(N_{\mathrm{interp}} \times L)$ and the average library image $\bar{\mathbf{f}}$.

3.2.3. Uncertainty estimation using Monte-Carlo method

This section specifies how the SVD libraries, which contain characteristic features extracted from the scattering profiles of particular OV targets, are used to directly map new scattering profiles (sample images) to specific OV values, provided that these OV values are within the library OV range. Further, it is outlined how a Monte-Carlo analysis, which provides a numerical estimate of the OV retrieval uncertainty, can be set up. In the context of metrology, Monte-Carlo methods are often employed to determine measurement uncertainties [43, 44]. More specifically, this method is used to study the robustness of a particular OV target design to shot noise and process variations in simulated Fourier scatterometry measurements. For this purpose, first, N_{sample} Fourier images are simulated at randomly chosen sampling OV values. These images, which are assumed to have an unknown OV value, are in the following referred to as sampling images. Figure 3.3(a) shows three sampling images and the parameters used for their simulation. The sampling OV values were drawn randomly according to the Latin-Hypercube Sampling (LHS) method [45]. This sampling method was chosen because LHS has been previously shown to have a superior convergence speed compared to other sampling techniques and has been successfully applied in the field of scatterometry [46, 47]. An inset in Fig. 3.3(a) shows a histogram of the LHS distributed OV values that were used for the $[-10...10]$ nm OV range.

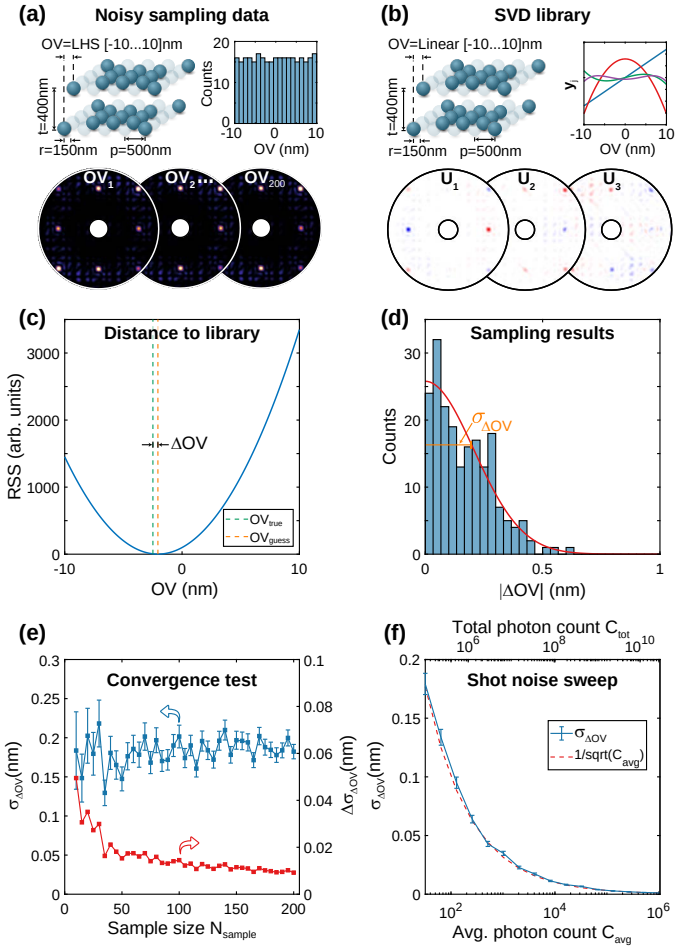

Figure 3.3: Monte-Carlo method. (a) A 3D sketch showing a part of the Rudin-Shapiro target design and the parameters used in the sampling simulations. The histogram shows the distribution of the OV values, which follow a Latin-hypercube sampling. Below, sample images at three different OV values are shown. (b) The SVD library consisting of the eigenbasis vectors **U** and the interpolated OV-dependant library image projections $\mathbf{y}_i$. The library is created using the same parameters as the sampling data but with a OV values varying linearly within the OV range of -10 nm to 10 nm. (c) Residual sum of squares (RSS) between projected sample image and the projected library images as a function of OV. (d) A histogram containing the |ΔOV| values of 200 sample images. Using a half-normal distribution fit (in red) a standard deviation of $\sigma_{\Delta OV} = 0.19 \pm 0.01$ nm was determined (in orange). (e) $\sigma_{\Delta OV}$ (in blue) and its error (in red) for a varying number of included sampling simulations. (f) $\sigma_{\Delta OV}$ as a function of the average photon count C_{avg} (bottom) and total photon count C_{tot} (top) in the sampling images. The red dashed line indicates the inverse square root of C_{avg}. The sample images used for (a) and (c-e) contain shot noise corresponding to $C_{avg} = 32$.

Once an SVD library is created, determining the OV value of a sampling image can be treated as a feature recognition task. Figure 3.3(b) depicts the main ingredients of such a library, which is simulated with identical parameters as the sampling images, but with equidistant OV values spanning in total the same range as the sampling image set. The OV value recognition works by projecting the sample image onto the library eigenspace and comparing this projection to each of the projections stored in the library. For this, the sample images are projected into the $\tilde{\mathbf{U}}$ subspace by calculating

$$\mathbf{x}_k = \tilde{\mathbf{U}}^T \cdot \mathbf{f}_k^c, \tag{3.4}$$

where $\mathbf{f}_k^c = \mathbf{f}_k - \bar{\mathbf{f}}$ are the flattened and centered sample images with $k = 1, ..., N_{\text{sample}}$. Then, the OV estimation is performed by calculating the residual sum of squares (RSS) between the sample coordinate vector $\mathbf{x}_k$ and the library coordinate vectors $\mathbf{x}_i$ with $i = 1, ..., N_{\text{interp}}$ as

$$\text{RSS}_{i,k} = \sum_{j=1}^{L} \left(x_{k,j} - x_{i,j} \right)^2. \tag{3.5}$$

The index i, which minimized Eq. (3.5) determines the OV estimate OV_{guess}. This approach corresponds to finding the library element with the minimal Euclidean distance to the sample image in the L-dimensional SVD coordinate space. An example RSS result as a function of OV is shown in Fig. 3.3(c). For this plot, a sampling image corrupted by shot noise corresponding to $C_{\text{avg}} = 32$ and with a 'true' OV value of $\text{OV}_{\text{true}} = -2.48\,\text{nm}$ was used, which resulted in an OV estimate of $\text{OV}_{\text{guess}} = -2.06\,\text{nm}$. Based on this estimate, the OV estimate error can be calculated as $\Delta\text{OV} = |\text{OV}_{\text{guess}} - \text{OV}_{\text{true}}|$, which in this example is 0.42 nm.

Repeating this OV estimation for each of the N_{sample} sampling images allows to construct a histogram of such OV estimate errors, as shown in Fig. 3.3(d). The variance $\sigma_{\Delta\text{OV}}$ of this histogram is indicated in Fig. 3.3(d). It characterizes the accuracy of the OV estimation and is obtained by fitting a half-Gaussian to the ΔOV data. The fit also returns a standard deviation of $\sigma_{\Delta\text{OV}}$, which is a measure for the quality of the fit and which is referred to as $\Delta\sigma_{\Delta\text{OV}}$. According to the central limit theorem $\Delta\sigma_{\Delta\text{OV}}$ should shrink with increasing sample size N_{sample}, and $\sigma_{\Delta\text{OV}}$ should converge for a large enough N_{sample}. To test this behavior and to determine an appropriate sample size, we performed convergence studies as suggested in Ref. 48. Figure 3.3(e) shows such a convergence test, where $\sigma_{\Delta\text{OV}}$ and its standard deviation is plotted in blue as a function of sample size in case of the Rudin-Shapiro target design and a photon budget set by $C_{\text{avg}} = 32$. In addition, Fig. 3.3(e) shows $\Delta\sigma_{\Delta\text{OV}}$ in red (right y-axis) to demonstrate how it decreases with an increasing sample size. For studies with a varying photon budget we found the results to converge sufficiently for a sample size of $N_{\text{sample}} = 200$ for the

$[-10...10]$ nm OV range and $N_{\text{sample}} = 300$ for the $[0...125]$ nm OV range. For the fabrication noise studies $N_{\text{sample}} = 300$ was used.

In Section 3.4, this Monte-Carlo technique will be used to quantify the accuracy of OV determination for different OV target designs in presence of noise in the sampling data, which will serve as a measure for noise robustness. For this sampling data sets containing a variety of measurement and fabrication errors are generated. As an example of such a study, Fig. 3.3(f) shows the dependence of $\sigma_{\Delta OV}$ on shot noise for the Rudin-Shapiro target. The shot noise is controlled by varying the photon budget of the sample images. An increasing photon budget leads to less shot noise and therefore decreased $\sigma_{\Delta OV}$. Additionally, it can be seen that $\sigma_{\Delta OV}$ scales similarly to the inverse square root of the average photon budget C_{avg} (red dashed line).

3.3. Overlay target optimizations

In this section, the simulated annealing approach is used to find target designs that allow for the greatest OV sensitivity. In simulated annealing one needs to minimize a chosen merit or cost function. Ideally, this function can be quickly evaluated to reduce total computation time. As the full SVD-based approach described in the last section requires significant computation time, we chose a cost function based on the correlation of the complex-valued far-fields at two different OV values. The cost function is calculated as follows

$$\Phi = \frac{2\langle E_{\text{OV}_1}, E_{\text{OV}_2}\rangle}{\langle E_{\text{OV}_1}, E_{\text{OV}_1}\rangle + \langle E_{\text{OV}_2}, E_{\text{OV}_2}\rangle} \tag{3.6}$$

in which

$$\langle E_{\text{OV}_1}, E_{\text{OV}_2}\rangle = \sum_{k_x,k_x} \left| E^*_{\text{OV}_1}(k_x,k_y) \cdot E_{\text{OV}_2}(k_x,k_y) \right|^2 \tag{3.7}$$

represents the cross-correlation of the far-field responses for two different OV values, namely $\text{OV}_1 = 0\,\text{nm}$ and $\text{OV}_2 = 5\,\text{nm}$ along the positive x direction. The idea behind this cost function is, that target designs minimizing Φ, will cause the most changes of the scattering signature as a function of OV and therefore enhance OV sensitivity. The spatial misalignment in the OV target generating E_{OV_2} causes a phase shift between the scattered waves originating from the bottom and top grating, which in turn alters their Fourier plane interference pattern. Since this spatial misalignment is only $5\,\text{nm}$ ($1/100$ of the pitch), the observable effect on the interference pattern is expected to be relatively small. Therefore, we expect that E_{OV_1} and E_{OV_2} are highly correlated, which is why even for the globally optimum scattering target the value of the cost function should be only slightly reduced from 1. We note that the performance of the Monte-Carlo technique for finding global minimums is in itself not dependent on the cost function contrast.

We constrain ourselves to identical particle arrangements in both particle planes, and start from a random distribution of particles given a particular

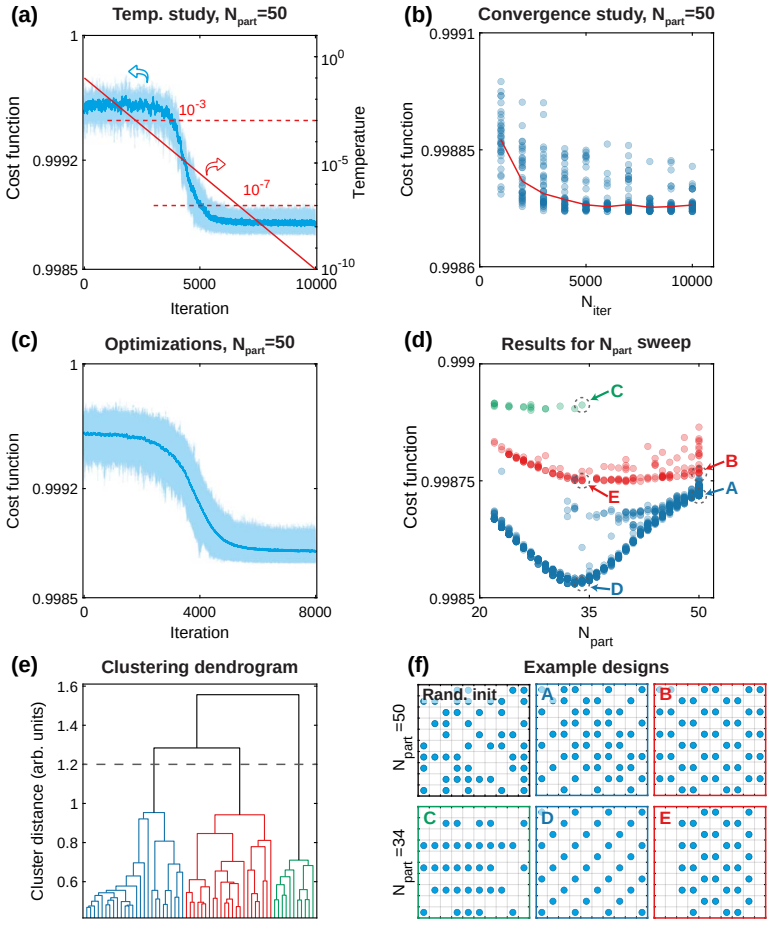

Figure 3.4: Overlay target optimizations. (a) Optimizations with temperatures varying between $T_{\max} = 10^{-1}$ and $T_{\min} = 10^{-10}$. The horizontal dashed lines indicate the temperature range we selected. The plot shows 12 optimizations in light blue and their average in dark blue. (b) Number of iterations N_{iter} study using the temperature extremes from panel (a). At each N_{iter} 36 optimizations are shown, while the red line represents the median values. (c) Cost function evolution using the optimized temperature extreme and N_{iter} settings. The light blue lines show 150 superimposed optimizations and the dark blue line shows their average. (d) Converged optimization results for a sweep of the number of particles per layer N_{part}. The circles are color-coded with respect to a 2D FFT-based hierarchical clustering, which identified different lattice families. Insets (A-E) indicate the cost functions of the target design realizations shown in panel (f). (e) A dendrogram of the clustering analysis. The subtree colors match the corresponding results in (d). The horizontal dashed line indicates the selected cutoff distance. (f) Examples of a randomly initiated geometry with $N_{\text{part}} = 50$ and optimized results for $N_{\text{part}} = 50$ and $N_{\text{part}} = 34$, respectively. Design C is referred to as rectangular array, A and D as diagonal arrays and B and E as alternating arrays.

lattice fill fraction. We generate new designs by randomly permuting filled and empty lattice sites. For each design, we compute the far-field response for the two OV values, and evaluate the cost function according to Eq. (3.6). The probability of accepting a new configuration depends on the change of the cost function $\Delta\Phi$ caused by the rearrangement of one particle. While in case of $\Delta\Phi \leq 0$ the new configuration is automatically accepted, for $\Delta\Phi > 0$ acceptance probability is calculated as follows

$$P(\Delta\Phi) = e^{-\frac{\Delta\Phi}{T}}, \tag{3.8}$$

where the control parameter T is referred to as the annealing temperature and is used to tune the acceptance probability of new candidate solutions with higher cost functions. We choose a fixed number of iterations N_{iter} over which we quench the temperature from T_{max} to T_{min}, so that at iteration step n the temperature reads

$$T(n) = T_{\text{max}} \left(\frac{T_{\text{min}}}{T_{\text{max}}} \right)^{n/N_{\text{iter}}}. \tag{3.9}$$

The search for optimal values of T_{max} and T_{min} relied on the same parameter-selection strategy as in Ref. 24. To this end, the temperature study shown in Fig. 3.4(a) was performed, where 12 optimizations (superimposed light blue lines) were performed using $N_{\text{part}} = 50$ particles per layer and $N_{\text{iter}} = 10^4$. The average cost function is shown in dark blue. The temperature is exponentially decaying in the range between $T_{\text{max}} = 10^{-1}$ and $T_{\text{min}} = 10^{-10}$. For large temperatures ($T > 10^{-3}$) any change in the OV target design is accepted, and the cost function fluctuates around the same higher values. For intermediate temperatures ($10^{-7} \leq T \leq 10^{-3}$) the cost function is effectively minimized, with a probability of converging to the global minimum. For temperatures $T < 10^{-7}$ the algorithm can only converge to local minima. After selecting the temperature extremes to be $T_{\text{max}} = 10^{-3}$ and $T_{\text{min}} = 10^{-7}$, the role of the cooling rate is investigated. This is done by varying the number of iterations N_{iter}, while keeping the temperature extremes T_{max} and T_{min} fixed. In Figure 3.4(b) the final cost function values of 36 optimization runs for each N_{iter} are shown, where the red line represents the median value. Following this, the cooling rate was set using the associated number of iterations $N_{\text{iter}} = 8000$, and 150 optimizations were performed using the chosen parameter settings, see Fig. 3.4(c) for a convergence history of all solutions. The results converge to two optimal particle distribution families, diagonal and alternating lattices, which account for about 85% and 15% of the results, respectively. Example realizations of these two solution families are shown in Fig. 3.4(f) (designs A and B).

Next, the dependence of the optimized solutions on the numbers of particles is investigated by performing optimizations with a particle number N_{part} varying from 22 to 49, while using the same optimization parameters as for the study in Fig. 3.4(c). At each N_{part}, 36 optimizations are completed. In

Figure 3.4(d) all final cost function values are shown as a function of N_{part}, including the 150 results obtained for $N_{\text{part}} = 50$. In order to group similar geometries of particle arrangements, a weighted-average distance hierarchical clustering is performed, which relies on the absolute value of the 2D FFT of the particles positions. This cluster analysis was able to identify three different design families remarkably well, despite the presence of a few misplaced particles. The three designs families were colored in blue, red, and green in Fig. 3.4(d). In the following, these solution families will be referred to as diagonal, alternating, and rectangular lattices, see Fig. 3.4(f) geometries D, B, and C, respectively. The dendrogram in Fig. 3.4(e) depicts the results of the cluster analysis[1]. The horizontal dashed line indicates the employed cutoff distance of 1.2. As can be seen in Fig. 3.4(d), the three solution families persist for a varying number of particles, whereby the rectangular design is only found up to a particle number of $N_{\text{part}} = 34$. When going from low to high particle numbers the grid is gradually filled. In case of the diagonal lattice for $N_{\text{part}} > 34$, the optimization introduces defects to the optimal solution, in order to accommodate more particles, see Fig. 3.4(f) geometry A. The alternating lattice design shows a similar behavior, where for $N_{\text{part}} = [30 - 50]$ sub-optimal solutions emerge, which are characterized by a higher cost function and a more irregular particle arrangement. The global optimum of the optimizations in Fig. 3.4(d), which corresponds to an OV target with minimal correlations between the far-fields at OV values $\text{OV}_1 = 0\,\text{nm}$ and $\text{OV}_2 = 5\,\text{nm}$, is a diagonal lattice with $N_{\text{part}} = 34$ particles.

3.4. Uncertainty analysis results

3.4.1. Designs overview

Figure 3.5 gives an overview over the OV target designs and their scattering patterns considered in this work. The designs are classified as being essentially 1D-like, 2D-periodic, and 2D-aperiodic. The class of 1D designs includes the 1D line grating, which was approximated using a very dense arrangement of Mie spheres with a distance of 150 nm in y direction and the same pitch $p = 500\,\text{nm}$ in x direction. Furthermore, the rectangular and diagonal designs that emerged from the optimizations in Sec. 3.3 were included in the following study. Compared to geometry C in Fig. 3.4(f), the rectangular lattice was completed to fill the whole grid. While the 1D line grating generates just two diffraction orders, all other designs in Fig. 3.5 result in more complex Fourier-plane light distributions, generally showing a multitude of (quasi)-diffraction orders. Qualitatively, the smallest and largest interparticle distances determine the largest and smallest diffraction angles respectively. This behavior can be easily observed in the case of the rectangular and diagonal target diffraction patterns.

[1] For clarity the number of shown leafs in the dendrogram was limited to 70.

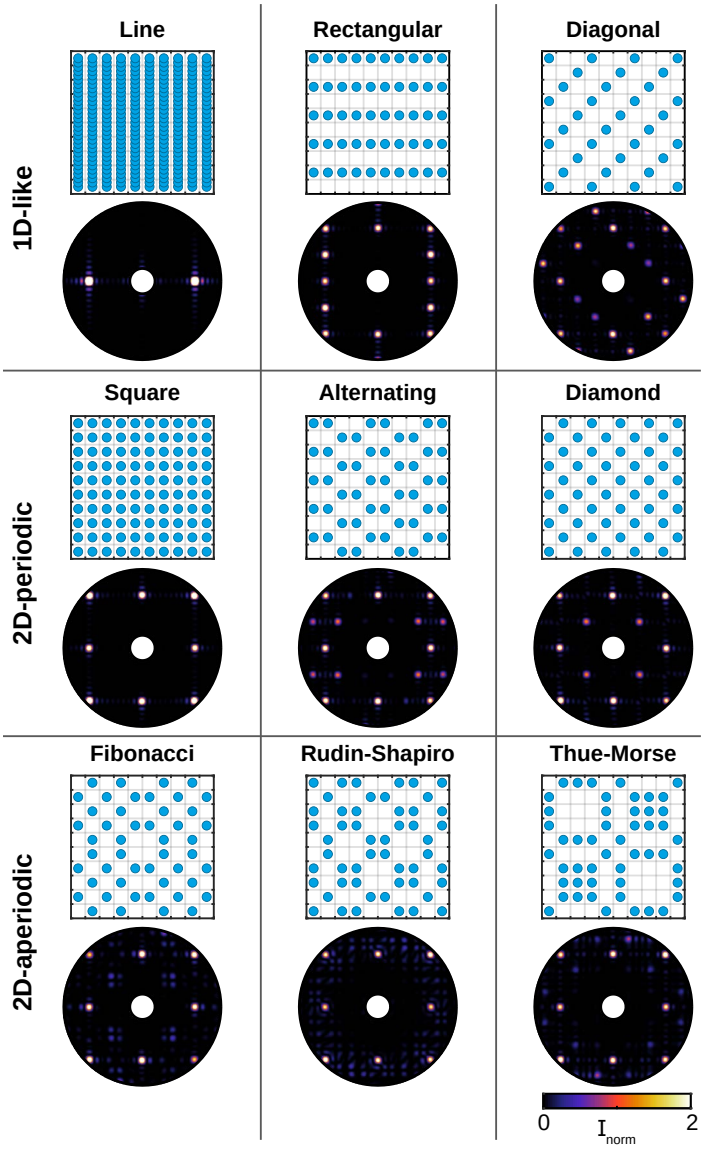

Figure 3.5: Designs overview. Overview of investigated OV target designs with the corresponding masked and normalized Fourier intensity profiles.

In addition to 2D-periodic designs, which include the square (all lattice sites occupied), the alternating (from optimization), and the diamond design, three 2D-aperiodic targets generated from deterministic design rules were considered. Deterministically aperiodic plasmonic and dielectric arrays have

been studied in the context of scattering, fluorescence control, and lasing [19–22]. On the basis of a square lattice, one can generate designs according to, e.g., the Fibonacci, Rudin–Shapiro, and Thue–Morse number sequences, as described in Ref. 19. The limitation to a finite size of only 10×10 scatterers prevents the full development of the Fourier patterns one would expect for their nearly infinitely-sized counterparts. Furthermore, the targets were required to maintain a 180° rotational symmetry, which is commonly utilized for calibration purposes. This calibration makes use of the fact that upon a 180° target rotation only the sign of the OV shift is flipped to remove any additional tool-induced errors, e.g., lens or illumination imperfections from the scattering signature [35]. In the case of the deterministically aperiodic designs, the 180° symmetry was achieved through a careful choice of the 10×10 truncation region from a larger aperiodic lattice. Surprisingly, the completed optimization designs already obey this rotational symmetry constraint, without the need of enforcing it during the optimization.

3.4.2. Shot noise robustness

In Figure 3.6(a), the effect of shot noise on the variance $\sigma_{\Delta OV}$ is examined in the selected OV range. The amount of shot noise is controlled by normalizing the sample images to a certain photon budget, which here is specified as the average count per pixel $C_{avg} = 2^l$ where $l = 5, 6, ..., 20$, and applying Poisson noise to the Fourier images. A lower photon count results in more shot noise, which leads to higher $\sigma_{\Delta OV}$ values. For large enough photon counts all lattice geometries converge towards an essentially zero $\sigma_{\Delta OV}$ (limited by the OV library step size of $OV_{interp,step} = 0.001\,nm$). The colored curves in Fig. 3.6(a) correspond to different target designs and are sorted according to their $\sigma_{\Delta OV}$ values at $C_{avg} = 128$. The idea behind this comparison is that a faster convergence speed implies better robustness to shot noise. The results in Fig. 3.6(c), which show the $\sigma_{\Delta OV}$ values at $C_{avg} = 128$, suggest that the line grating design has a vastly superior shot noise performance compared to the other designs. This outcome can be explained by the fact that the Fourier intensity signal of the line grating is concentrated on fewer pixels as compared to other target designs, which decreases the impact of shot noise. The three optimized designs (rectangular, diagonal, alternating) follow on positions 2 to 4 after the 1D line grating (which itself is not captured by the design space of the optimization). Figure 3.6(b) depicts a similar shot noise robustness study, but for a scenario where OV tolerances are much more relaxed and one aims to determine OV in a 125 nm range. These types of tolerances can occur during lithography steps of non-critical wafer layers. This time the results at $C_{avg} = 128$ in Fig. 3.6(d) feature overall larger and less distributed $\sigma_{\Delta OV}$ values. In addition, the line target does not show the best performance anymore. Instead, the diagonal target design is superior for large overlay ranges.

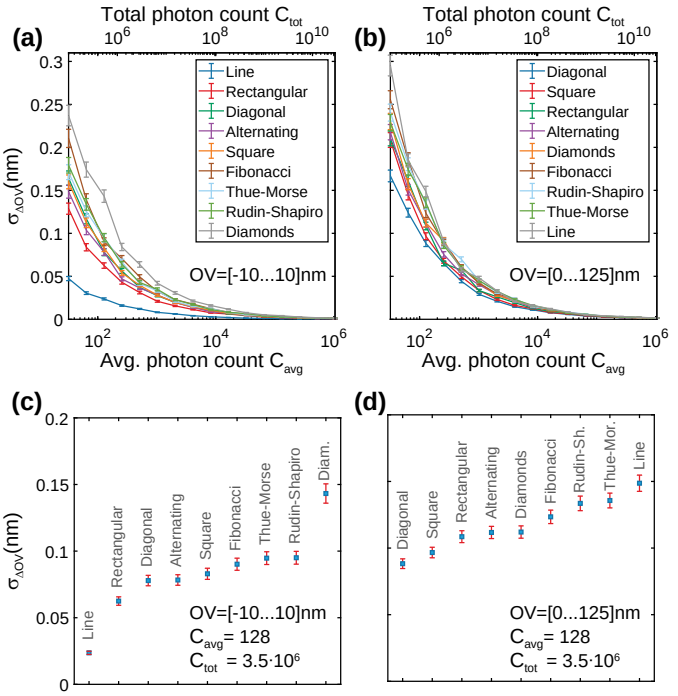

Figure 3.6: Shot noise robustness. (a,b) Photon count-dependent OV error variance ($\sigma_{\Delta OV}$) for the OV range of $[-10...10]$ nm and $[0...125]$ nm. The error bars denote the standard deviation of the variance ($\Delta\sigma_{\Delta OV}$) obtained from a half-Gaussian fit. (c,d) $\sigma_{\Delta OV}$ and $\Delta\sigma_{\Delta OV}$ values of the different OV targets at $C_{avg} = 128$ for the OV range of $[-10...10]$ nm and $[0...125]$ nm, respectively.

An additional factor causing the overall low $\sigma_{\Delta OV}$ values presented here is the noise reducing ability of the SVD algorithm; The noisy part of the data tends to be encoded in the higher eigenvectors, which were truncated during the library creation step. This property of the SVD is often employed for noise filtering in digital signal and image processing applications [49]. At the same time, as mentioned in the library generation section, the SVD based approach does allow to leverage information encoded in *multiple* basis functions, as opposed to only looking at the asymmetry between 1^{st} diffraction orders, which benefits the OV detection at larger OV values.

3.4.3. Fabrication noise robustness

The overall high OV detection accuracy (low $\sigma_{\Delta OV}$ values) in the shot noise study can be primarily attributed to the large amount of a-priori information on, e.g., array pitch, layer distance, radius, and refractive indices, that is assumed in the library generation. In an experimental setting, uncertainties

in these parameters, i.e. fabrication noise instead of detection shot noise, is often the dominating error source. In this section, the impact of three different sources of fabrication noise on the OV estimation accuracy is investigated. Process variability and imperfections of the product stack are reported to be the dominating source of error in scatterometry [1, 10]. Mitigating these systematic error sources is therefore of high interest for the semiconductor industry. To distinguish between the different detrimental effects, we performed separate studies for the three different fabrication noise sources and do not introduce additional shot noise. As in the shot noise study, the fabrication noise is introduced to the sampling data, while we use the same libraries with the OV range of $[-10...10]$ nm and OV as its only input parameter.

Figure 3.7(a) depicts OV uncertainty results in case the distance between the two lattices is fluctuating with a variance of $\sigma_t = 20\,\text{nm}$, which corresponds to 5% of the average layer distance $t = 400\,\text{nm}$. Next, Figure 3.7(b) shows OV uncertainty results with particle position variations $\sigma_{\Delta x} = 2.5\,\text{nm}$, which corresponds to 0.5% of the lattice pitch. The schematics in the inset of Fig. 3.7(b) show such position fluctuations, but exaggerated by a factor of 15 for visual clarity. Note, in case of the line grating, instead of fluctuating the position of every particle, we fluctuated the positions of the 10 complete lines. Lastly, Figure 3.7(c) shows OV uncertainty results in case of particle radius variations with $\sigma_{\Delta r} = 7.5\,\text{nm}$, which corresponds to 5% of the radius. The result of the radius variation study for the diamond design is $\sigma_{\Delta\text{OV}} = 2.4\pm0.1\,\text{nm}$, which is surprisingly high. It is omitted from the plot in Fig. 3.7(c), as it otherwise would skew the plot range for this data set. Figure 3.7(d-f) shows histograms of the 300 layer distance, position error, and particle radius values used for these fabrication robustness studies.

The results carry several messages. First, different fabrication error sources can be partially mitigated by using a particular target design, whereby the most suited design is different for each error type. Out of the three fabrication error sources investigated here, the 5% layer distance fluctuations have resulted in the most severe impact on OV determination. Therefore, the rectangular lattice might be the most suited target design for OV metrology applications, where other types of errors are negligible. A second message is that when one wants to be robust against multiple fabrication error sources at the same time, *combining* the scatterometry measurements with multiple target designs i.e., rectangular, square, and diagonal target designs could be advantageous. Furthermore, by expanding the library parameter space one could simultaneously determine overlay and dimensional variations (CD metrology, here radius variations are the 'critical dimension'). A third observation is that it is not obvious from the results by which mechanism a given target is more advantageous than another, and why optimality depends on the source of error considered. A third observation is that it is not obvious from the results by which mechanism a given target is more advantageous than another, and why optimality depends on the source of error considered.

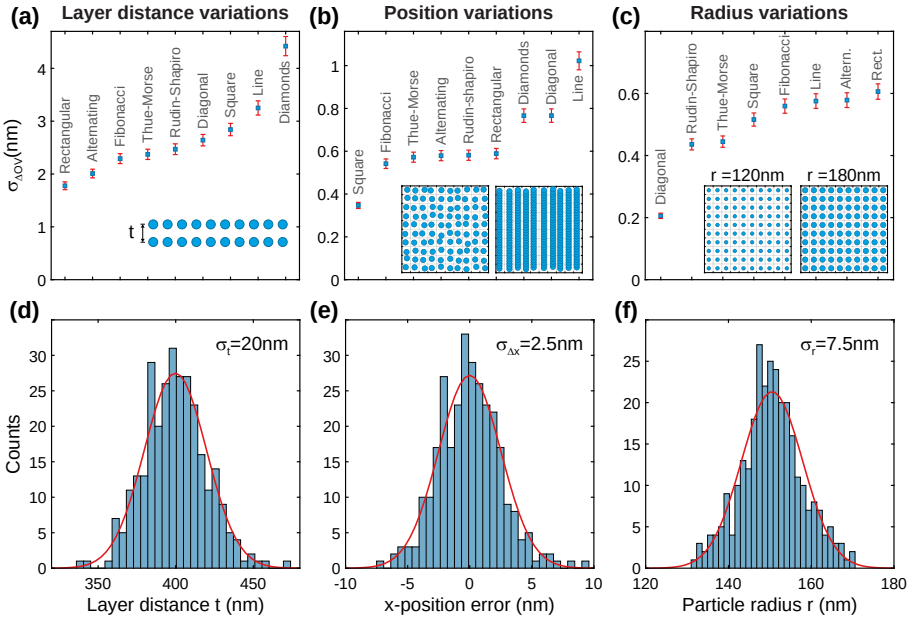

Figure 3.7: Fabrication noise robustness. (a-c) OV error variance results of different OV targets in case of layer distance fluctuations with a variance of $\sigma_t = 20\,\text{nm}$ (a), particle position fluctuations with a variance of $\sigma_{\Delta x} = 2.5\,\text{nm}$ (b) and radius fluctuations with a variance of $\sigma_r = 7.5\,\text{nm}$ (c). The insets in (a-c) depict the respective situations schematically. The position fluctuations in the inset of panel (b) were increased by a factor of 15 for visual clarity. (d-f) Histograms displaying the distribution of the fluctuations of layer distance (d) particle positions (e) and radius (f). The red line in the histograms is a Gaussian fit.

While it is not the ambition to explain in this chapter for each scattering structure the origin of its robustness to a given disorder, in the following we will provide a generic insight on how to leverage the SVD analysis approach for optimizing robustness/sensitivity. To exemplify this, we have performed simulation sweeps, where the layer thickness t is continuously varied in a range of 300 nm to 500 nm and OV in a range of −100 nm to 100 nm for the rectangular and square geometry, that are respectively optimal and quite poor in robustness. At first, using SVD the optimal eigenbasis for the $t = 400\,\text{nm}$ data set is determined, before projecting the complete data set into this eigenspace. As an example, the first two projected coordinates $\mathbf{y}_j$ for the rectangular and square lattice are shown in Fig. 3.8 as a function of OV and t. A large sensitivity to overlay comes with a large $|\partial \mathbf{y}_j / \partial \text{OV}|$, i.e., a large left-right gradient in the projected coordinate. At the same time, robustness against fabrication error requires a flat dependence on t, i.e., no derivative $|\partial \mathbf{y}_j / \partial t|$. Examining $\mathbf{y}_1$ in Fig. 3.8(a,b), it can be concluded that the higher robustness to t fluctuations of the rectangular lattice traces back to the the

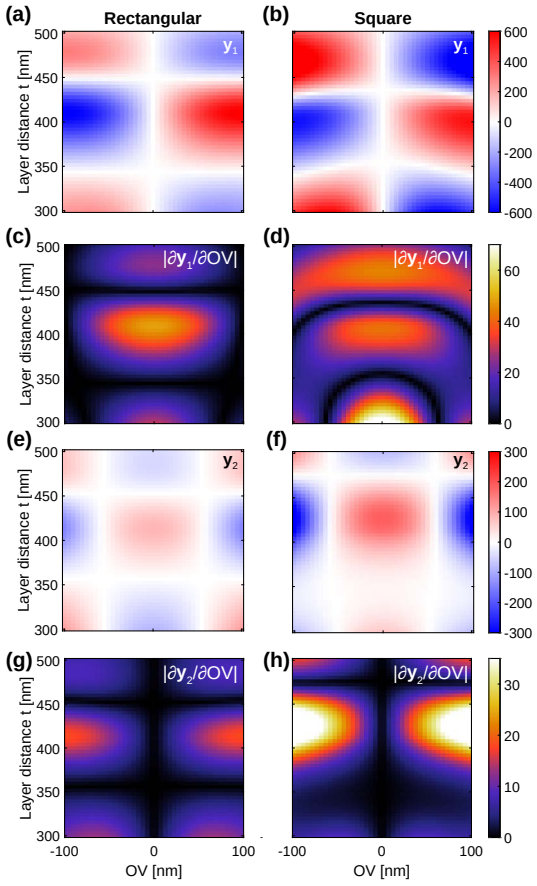

Figure 3.8: Parameter sweep. (a,b) Eigenbasis projection $\mathbf{y}_1$ as a function of layer distance t for the rectangular and square target respectively. (c,d) Absolute valued partial derivative of (a) and (b) with respect to OV. (e-h) Same as (a-d) but for the second eigenbasis projection $\mathbf{y}_2$.

more flat distribution of $\mathbf{y}_1$ as a function of t in the parameter region $t = [350-450]$ nm. Further, Figure 3.8(e,f) shows the same plots but for the second projected coordinate $\mathbf{y}_2$, which in the suggested OV determination method is expected to provide additional information on top of just the first coordinate. For both target designs at hand, $\mathbf{y}_1$ is most important for OV determination at small OV values ($|\mathrm{OV}| < 50$ nm), while $\mathbf{y}_2$ becomes more important at larger OV values. In general, the $|\partial \mathbf{y}_j / \partial \mathrm{OV}|$ plots show which parameter ranges have the highest OV sensitivity. In particular, one can identify parameter regions that have zero OV sensitivity ($|\partial \mathbf{y}_j / \partial \mathrm{OV}| = 0$) and should therefore be avoided, since there the solution of the inverse Fourier scatterometry problem is not unique.

Note that the results with a fixed choice of target and illumination parameters presented here by no means imply that any of the proposed structures are working at their optimum in parameter space. While outside of the scope of this work, such optimal parameters can be found by performing separate multi-parametric SVD analysis, as shown in Fig. 3.8 for each target design and each parameter combination. Thus, the presented results on performance variability between structures are to some degree incidental. However, the results highlight the importance of target design, which is often neglected in other OV metrology studies. In practice, there are several ways to decrease the impact of systematic errors, such as fabrication imperfections, to achieve lower $\sigma_{\Delta OV}$ numbers than the ones reported in Fig. 3.7. A common way to mitigate imperfections is to include them into the library as an input and therefore a fitting parameter for the sampling data. This would in turn increase the complexity of the library creation and library search process. Another approach to mitigate systematic OV errors is the fabrication and measurement of two neighboring OV targets with known programmed overlay [9]. Besides, one could improve upon the single-shot measurements presented here by combining several measurements with a varying angle of incidence, polarization, or wavelength. Such approaches can improve robustness to systematic errors caused by equipment or process fluctuations [50].

3.5. Conclusion and outlook

In summary, this chapter introduced a new Monte-Carlo-based method for characterizing the performance of non-periodic 2D Fourier scatterometry target designs. The workflow consists of rigorous electromagnetic simulations of 'reference' diffraction patterns featuring known overlay errors, SVD analysis in order to generate a library and an optimal basis onto which one should project sampling diffraction patterns at unknown OV values for the most efficient determination of OV.

We used this method to assess the overlay estimation uncertainty in face of measurement noise and nanofabrication disorder for nine different overlay target designs. Three of the investigated designs resulted from simulated annealing optimizations and another three were chosen as quasiperiodic motifs. The results suggest that 2D OV target designs might be a promising alternative to the well-established line grating design regarding some of the main challenges of diffraction-based OV metrology, such as systematic errors due to fabrication variations. One possible way to take advantage of the findings would be to perform OV measurements with multiple target designs, which have *complementary* fabrication noise robustness properties. Combinations would allow to simultaneously optimize robustness, sensitivity, range of OV detection, and multiplexing OV and CD detection.

In real-world conditions, the reported levels of uncertainty would likely be difficult to achieve, because of the large number of measurements required

to build up an accurate library and the precision with which the 'true' OV needs to be known. This underlines the importance of simulations for library construction and design exploration. In addition, this work demonstrates the strength of *semi-analytical* calculations for proof-of-principle metrology studies as compared to *discretization-based* full-wave solvers. For instance, initial tests with FDTD have shown that it tends to introduce meshing-based errors that far exceed the overlay values of interest. In this work, these issues were addressed using the GMMT approach, while limiting ourselves to spherical particles in free space. Other multipole multiple scattering methods for scatterers in stratified media [51], and the boundary element method in layered systems [52] can be employed in order to increase the realism of the simulations, yet avoiding the impractical gridding of FDTD and FEM.

As an outlook, the OV target design space used in this chapter could be further extended. For instance, the requirement of identical designs for the bottom and top gratings could be lifted. It could be advantageous to e.g. choose *different* tiles cut out from the *same* quasicrystal motifs as the lower and upper grating, since those tiles share similar diffraction patterns in terms of amplitude, but have differences in phase. Also, instead of using a fixed periodic lattice as the underlying template on which to place particles, one could consider continuous particle placements to optimize diffraction pattern correlations, in the vein of work on plasmonic Vogel spirals and hyperuniform designs [53–55]. Regarding numerical optimizations to generate designs, an outstanding challenge is to define the most effective cost function and optimization approaches, so as to optimize sensitivity, OV range, to multiplex OV and CD sensitivity, and to multiplex sensitivity to OV in both directions.

Finally, using the presented uncertainty estimation approach one could study more complex measurement schemes, that involve capturing signals at multiple wavelengths, multiple polarizations, or introducing phase sensitivity, which would increase the captured information content and allow more elaborate mitigation of systematic error sources. The following chapter presents such an extension of Fourier microscopy. Its performance is demonstrated by characterizing the phase and polarization profiles of several plasmonic nanoscatterers.

References

1. B. Bunday, E. Solecky, A. Vaid, A. Bello, and X. Dai, *Metrology capabilities and needs for 7nm and 5nm logic nodes*, Proc. SPIE **10145**, 102 (2017).
2. N. G. Orji, M. Badaroglu, B. M. Barnes, C. Beitia, B. D. Bunday, U. Celano, R. J. Kline, M. Neisser, Y. Obeng, and A. Vladar, *Metrology for the next generation of semiconductor devices*, Nat. Electron. **1**, 532 (2018).
3. K. P. Bishop, S. M. Gaspar, L.-M. Milner, S. S. H. Naqvi, and J. R. McNeil, *Grating line shape characterization using scatterometry*, Proc. SPIE **1545**, 64 (1991).
4. M. Lee, C. Galarza, W. Kong, W. Sun, and F. Terry Jr, *Analysis of reflectometry and ellipsometry data from patterned structures*, AIP Conf. Proc. **449**, 331 (1998).
5. X. Niu, N. Jakatdar, J. Bao, and C. J. Spanos, *Specular spectroscopic scatterometry*, IEEE Trans. Semicond. Manuf. **14**, 97 (2001).
6. W. Yang, R. Lowe-Webb, S. Rabello, J. Hu, J.-Y. Lin, J. D. Heaton, M. V. Dusa, A. J. den Boef, M. van der Schaar, and A. Hunter, *Novel diffraction-based spectroscopic method for overlay metrology*, Proc. SPIE **5038**, 200 (2003).
7. J. Petit, P. Boher, T. Leroux, P. Barritault, J. Hazart, and P. Chaton, *Improved CD and overlay metrology using an optical Fourier transform instrument*, Proc. SPIE **5752**, 420 (2005).
8. M. H. Madsen and P.-E. Hansen, *Scatterometry—fast and robust measurements of nano-textured surfaces*, Surf. Topogr. Metrol. Prop. **4**, 023003 (2016).
9. A. J. den Boef, *Optical wafer metrology sensors for process-robust CD and overlay control in semiconductor device manufacturing*, Surf. Topogr. Metrol. Prop. **4**, 023001 (2016).
10. K. Bhattacharyya, A. J. den Boef, G. Storms, J. van Heijst, M. Noot, K. An, N.-K. Park, S.-R. Jeon, N.-L. Oh, E. McNamara, *et al.*, *A study of swing-curve physics in diffraction-based overlay*, Proc. SPIE **9778**, 502 (2016).
11. H. J. Patrick, R. Attota, B. M. Barnes, T. A. Germer, R. G. Dixson, M. D. Stocker, R. M. Silver, and M. R. Bishop, *Optical critical dimension measurement of silicon grating targets using back focal plane scatterfield microscopy*, J. Micro/Nanolithogr. MEMS MOEMS **7**, 1 (2008).
12. C. Fallet, T. Novikova, M. Foldyna, S. Manhas, B. H. Ibrahim, A. De Martino, C. Vannuffel, and C. Constancias, *Overlay measurements by Mueller polarimetry in back focal plane*, J. Micro/Nanolithogr. MEMS MOEMS **10**, 1 (2011).
13. V. F. Paz, S. Peterhänsel, K. Frenner, and W. Osten, *Solving the inverse grating problem by white light interference Fourier scatterometry*, Light Sci. Appl. **1**, e36 (2012).
14. M. H. Madsen, P. Boher, P.-E. Hansen, and J. F. Jørgensen, *Alignment-free characterization of 2D gratings*, Appl. Opt. **55**, 317 (2016).
15. R. Röhrich, C. Hoekmeijer, C. I. Osorio, and A. F. Koenderink, *Quantifying single plasmonic nanostructure far-fields with interferometric and polarimetric k-space microscopy*, Light Sci. Appl. **7**, 65 (2018).
16. A. Polman and H. A. Atwater, *Photonic design principles for ultrahigh-efficiency photovoltaics*, Nat. Mater. **11**, 174 (2012).
17. A. Arbabi, Y. Horie, M. Bagheri, and A. Faraon, *Dielectric metasurfaces for complete control of phase and polarization with subwavelength spatial resolution and high transmission*, Nat. Nanotechnol. **10**, 937 (2015).
18. A. F. Koenderink, A. Alù, and A. Polman, *Nanophotonics: Shrinking light-based technology*, Science **348**, 516 (2015).
19. L. Dal Negro, N.-N. Feng, and A. Gopinath, *Electromagnetic coupling and plasmon*

localization in deterministic aperiodic arrays, J. Opt. A: Pure Appl. Opt. **10**, 064013 (2008).
20. L. Dal Negro and S. V. Boriskina, *Deterministic aperiodic nanostructures for photonics and plasmonics applications*, Laser Photonics Rev. **6**, 178 (2012).
21. D. S. Wiersma, *Disordered photonics*, Nat. Photonics **7**, 188 (2013).
22. A. H. Schokker and A. F. Koenderink, *Lasing in quasi-periodic and aperiodic plasmon lattices*, Optica **3**, 686 (2016).
23. S. Kirkpatrick, C. D. Gelatt, and M. P. Vecchi, *Optimization by simulated annealing*, Science **220**, 671 (1983).
24. G. Oliveri and J. T. Overvelde, *Inverse design of mechanical metamaterials that undergo buckling*, Adv. Funct. Mater. , 1909033 (2020).
25. H. Gross, R. Model, M. Bär, M. Wurm, B. Bodermann, and A. Rathsfeld, *Mathematical modelling of indirect measurements in scatterometry*, Measurement **39**, 782 (2006).
26. O. Sigmund and K. Maute, *Topology optimization approaches*, Struct. Multidiscip. Optim. **48**, 1031 (2013).
27. S. Molesky, Z. Lin, A. Y. Piggott, W. Jin, J. Vucković, and A. W. Rodriguez, *Inverse design in nanophotonics*, Nat. Photonics **12**, 659 (2018).
28. P.-I. Schneider, X. Garcia Santiago, V. Soltwisch, M. Hammerschmidt, S. Burger, and C. Rockstuhl, *Benchmarking five global optimization approaches for nano-optical shape optimization and parameter reconstruction*, ACS Photonics **6**, 2726 (2019).
29. D. W. Mackowski and M. I. Mishchenko, *Calculation of the T matrix and the scattering matrix for ensembles of spheres*, J. Opt. Soc. Am. A **13**, 2266 (1996).
30. B. Stout, J.-C. Auger, and J. Lafait, *A transfer matrix approach to local field calculations in multiple-scattering problems*, J. Mod. Opt. **49**, 2129 (2002).
31. L. Sirovich and M. Kirby, *Low-dimensional procedure for the characterization of human faces*, J. Opt. Soc. Am. A **4**, 519 (1987).
32. M. Turk and A. Pentland, *Eigenfaces for recognition*, J. Cognit. Neurosci. **3**, 71 (1991).
33. G. T. di Francia, *Resolving power and information*, J. Opt. Soc. Am. **45**, 497 (1955).
34. M. G. Moharam and T. K. Gaylord, *Rigorous coupled-wave analysis of planar-grating diffraction*, J. Opt. Soc. Am. **71**, 811 (1981).
35. X. Chen and S. Liu, *Optical scatterometry for nanostructure metrology*, in *Metrology*, edited by W. Gao (Springer Singapore, Singapore, 2019) pp. 1–37.
36. M. Pisarenco, J. Maubach, I. Setija, and R. Mattheij, *Aperiodic Fourier modal method in contrast-field formulation for simulation of scattering from finite structures*, J. Opt. Soc. Am. A **27**, 2423 (2010).
37. R. M. Silver, R. Attota, and E. Marx, *Model-based analysis of the limits of optical metrology with experimental comparisons*, Proc. SPIE **6617**, 266 (2007).
38. B. Xu, L. Ma, X. Zou, L. Dong, and Y. Wei, *A diffraction-based overlay model based on FDTD method*, Proc. SPIE **10959**, 632 (2019).
39. H. C. van der Hulst, *Light scattering by small particles*, Dover books on physics (Dover, New York, NY, 1981).
40. D. T. Pierce and W. E. Spicer, *Electronic structure of amorphous Si from photoemission and optical studies*, Phys. Rev. B **5**, 3017 (1972).
41. H.-J. H. Smilde, A. den Boef, M. Kubis, M. Jak, M. van Schijndel, A. Fuchs, M. van der Schaar, S. Meyer, S. Morgan, J. Wu, V. Tsai, C. Wang, K. Bhattacharyya, K.-H. Chen, G.-T. Huang, C.-M. Ke, and J. Huang, *Evaluation of a novel ultra small target technology supporting on-product overlay measurements*, Proc. SPIE **8324**, 83241A

(2012).
42. C. J. Raymond, M. E. Littau, A. Chuprin, and S. Ward, *Comparison of solutions to the scatterometry inverse problem*, Proc. SPIE **5375**, 564 (2004).
43. H. Schwenke, B. Siebert, F. Wäldele, and H. Kunzmann, *Assessment of uncertainties in dimensional metrology by Monte Carlo simulation: proposal of a modular and visual software*, CIRP Ann. **49**, 395 (2000).
44. M. Arnz, G. Klose, G. Troll, D. Beyer, and A. Mueller, *Monte-Carlo simulations of image analysis for flexible and high-resolution registration metrol*, Proc. SPIE **7470**, 1 (2009).
45. M. D. McKay, R. J. Beckman, and W. J. Conover, *Comparison of three methods for selecting values of input variables in the analysis of output from a computer code*, Technometrics **21**, 239 (1979).
46. J. C. Helton and F. J. Davis, *Latin hypercube sampling and the propagation of uncertainty in analyses of complex systems*, Reliab. Eng. Syst. Saf. **81**, 23 (2003).
47. S. Heidenreich, H. Gross, M. Bär, and L. Wright, *Uncertainty propagation in computationally expensive models: A survey of sampling methods and application to scatterometry*, Measurement **97**, 79 (2017).
48. J. Yang, *Convergence and uncertainty analyses in Monte-Carlo based sensitivity analysis*, Environ. Modell. Software **26**, 444 (2011).
49. K. Konstantinides, B. Natarajan, and G. S. Yovanof, *Noise estimation and filtering using block-based singular value decomposition*, IEEE Trans. Image Process. **6**, 479 (1997).
50. K. Bhattacharyya, M. Noot, H. Chang, S. Liao, K. Chang, B. Gosali, E. Su, C. Wang, A. den Boef, C. Fouquet, G.-T. Huang, K.-H. Chen, K. Cheng, and J. Lin, *Multi-wavelength approach towards on-product overlay accuracy and robustness*, Proc. SPIE **10585**, 326 (2018).
51. Y. T. Chen, Y. Zhang, and A. F. Koenderink, *General point dipole theory for periodic metasurfaces: magnetoelectric scattering lattices coupled to planar photonic structures*, Opt. Express **25**, 21358 (2017).
52. U. Hohenester and A. Trügler, *MNPBEM - A Matlab toolbox for the simulation of plasmonic nanoparticles*, Comput. Phys. Commun. **183**, 370 (2012).
53. J. Trevino, H. Cao, and L. Dal Negro, *Circularly symmetric light scattering from nanoplasmonic spirals*, Nano Lett. **11**, 2008 (2011).
54. K. Guo, M. Du, C. I. Osorio, and A. F. Koenderink, *Broadband light scattering and photoluminescence enhancement from plasmonic Vogel's golden spirals*, Laser Photon. Rev. **11**, 1600235 (2017).
55. M. Castro-Lopez, M. Gaio, S. Sellers, G. Gkantzounis, M. Florescu, and R. Sapienza, *Reciprocal space engineering with hyperuniform gold disordered surfaces*, APL Photonics **2**, 061302 (2017).

4

POLARIMETRIC AND INTERFEROMETRIC K-SPACE MICROSCOPY OF TWISTED LIGHT EMERGING FROM SINGLE NANOANTENNAS

Optically resonant nanoantennas are key building blocks for metasurfaces, nanosensors, and nanophotonic light sources due to their ability to control the amplitude, phase, directivity, and polarization of scattered light. This chapter introduces, an experimental technique for the full recovery of all degrees of freedom encoded in the far-field radiated by a single nanostructure using a high-NA Fourier microscope equipped with digital off-axis holography. This method enables the decomposition of antenna-physics in its multipole contributions and gives full access to the orbital and spin angular momentum properties of light scattered by a single nanostructure. These capabilities are demonstrated through a quantitative assessment of the purity of the 'selection rules' for orbital angular momentum transfer by plasmonic spiral nanostructures.

4.1. Introduction

A cornerstone of nanophotonics is to precisely control the resonances of individual metallic and dielectric scatterers that form elementary building blocks of nanophotonic devices such as metasurfaces and nanoantennas. The underlying physics is based on the fact that subwavelength geometric tailoring controls the near-field multipolar resonances of nanoscatterers, which in turn allows for a precise manipulation of the amplitude, phase, and polarization of light scattered into the far-field. For instance, the past decade has seen the realization of plasmonic nanoantennas [1–3] to tailor directivity [4–8] and polarization [9–12] of scattering and fluorescence, even down to the level of single-photon sources [13]. Additionally, metasurfaces based on metallic and dielectric nanoresonators provide near-arbitrary control over the phase, amplitude, spin, and orbital angular momentum content of transmitted wavefronts [14–17].

Even though a successful design requires a precise understanding of the type of multipolar resonances supported by a nanostructure, the complex superposition one can excite, and how these radiate into the far-field, such an understanding commonly relies largely on numerical results and is supported only indirectly by experimental evidence. In principle, a measurement of the *full* polarization, amplitude, and phase of light for each angle in the 4π far-field radiation pattern of a nanoantenna enables the full decomposition of the antenna's response in its locally induced multipoles (see Fig. 4.1). Thus, full field radiation pattern measurement at all angles can enable complete nanoantenna polarizability tomography. In this work, a phase- and polarization-resolved Fourier microscope is presented that meets this challenge over the NA spanned by a high-NA microscope objective. The potential of this method is demonstrated by phase resolving the radiation pattern of

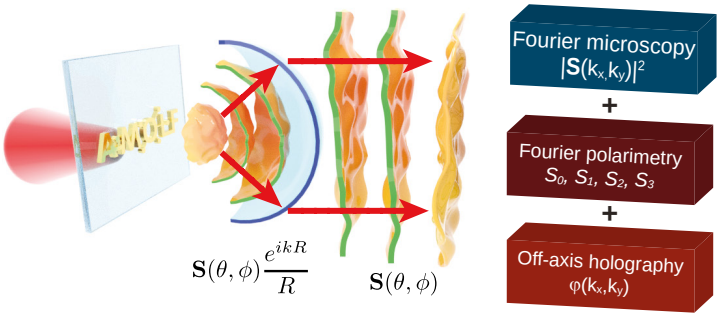

Figure 4.1: Conceptual sketch. A single nanoantenna radiating a spherical wave with a characteristic phase profile as well as amplitude and polarization. This spherical wave is transformed into a plane wave in the back focal plane of a microscope objective. Measuring the amplitude, polarization, and phase content of light over all angles enables a detailed reconstruction of the antenna physics.

single spiral-shaped nanoscatterers that generate orbital angular momentum (OAM) [18].

OAM beams have envisioned applications in optical communication technology [19, 20], quantum information processing [21] and optical manipulation [22]. Since these applications require precise knowledge of the OAM mode content, the detection and analysis of paraxial OAM beams have been a subject of great interest [23–26]. However, a quantitative assessment of the purity with which plasmonic nanostructures, such as spiral nanostructures, transfer OAM to scattered, spherical waves is still missing. The measurement results presented here do not only demonstrate this technique's capabilities but are also highly relevant in view of shrinking applications for OAM beams to length scales of, e.g., single-photon emitters. In addition to opening up new possibilities in the research of nanoantennas and metasurfaces, OAM decomposition in combination with nanoantennas could have a large impact on optical metrology applications [27].

4.2. Experimental setup

The proposed experimental technique for angle-resolved amplitude, polarization, and phase imaging of single nanostructures is based on a combination of Fourier microscopy, polarimetry, and digital holography. The setup is illustrated in Fig. 4.2(a). The light source is a frequency-stabilized HeNe laser λ =633 nm. The beam is expanded by a telescope ($f = -25$ mm and $f = 200$ mm) and transmitted through the first polarimeter consisting of a linear polarizer LP_1 (Thorlabs LPVIS100) and a quarter wave plate QWP_1 (Thorlabs AHWP10M-600), which are used to prepare the incoming polarization state. Just after LP_1 the beam is split in an object and reference beam by a 50/50 beamsplitter. The reference beam possesses a linear polarization and is transported in free-space parallel to the object beam. A $f = 125$ mm lens weakly focuses the object beam onto the glass substrate side of the sample, which features only the central aperture of the structures. Light scattered from the patterned gold side of the nanostructure is collected downstream by a high-NA microscope. This collection path is based on a 100× objective (Nikon LU Plan Apo, NA = 0.9), a 200 mm tube lens, and a CCD camera (Photometrics CoolSNAP EZ, pixel pitch 6.45 µm). In addition, the collection path encompasses a $4f$-telescope (two $f_T = 50$ mm lenses) with a circular pinhole (diameter of 400 µm) as a real space filter that selects only the light coming from the nanostructure.

A Fourier lens ($f_F = 200$ mm) is placed at a distance $4f_T + f_F$ from the objective back focal plane (BFP) so that it is focused on the BFP of the infinity-corrected objective. Thus, in the presence (absence) of the Fourier lens, a Fourier space (real space) image of the sample is projected onto the CCD camera. This projection maps the in-plane wave vectors $\mathbf{k}_{\|}$ of the scattered light with a high angular precision of approximately 0.5° over the full 70°

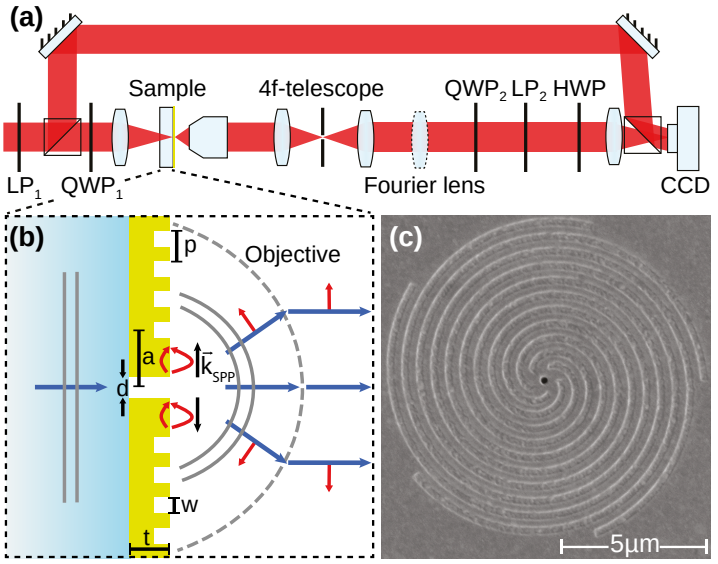

Figure 4.2: Schematic view of the setup and plasmonic spiral antenna. (a) Combined Fourier polarimetry and holography setup, consisting of a transmission microscope, two polarimeters, and a reference beam. The microscope contains a $4f$-telescope for spatial filtering of light from a single antenna. (b) Principle of plasmonic bullseye/spiral nanostructure. Light impinging from the glass substrate side excites the single aperture in a thick metal film. SPPs launched by the aperture at the air side scatter out at the spiral or concentric (bullseye) corrugation. The red arrows denote the directions of the SPPs and free-space electric fields. (c) SEM image of a $m = -5$ spiral antenna.

opening angle of the objective [28–30]. A second polarimeter consisting of a quarter wave plate QWP_2 and linear polarizer LP_2 projects the outgoing wave onto the desired polarization channel. Combined the two Stokes polarimeters enable one to control and measure the full polarization state of incoming and outgoing light for each wave vector [31]. To enable phase resolution using off-axis digital holography the two beams are recombined on the camera using a second 50/50 beamsplitter [32, 33]. A half waveplate HWP is used to rotate the linear polarization of the object beam back onto that of the reference beam, which improved the interference contrast.

To increase the dynamic range of the measurements beyond that of the CCD camera, the intensity and interference patterns were acquired at two different exposure times ($t_1 = 50\,\text{ms}$ and $t_2 = 2000\,\text{ms}$) and merged by using $I(t_1)$ in a circular region around the high-intensity part of the image and $I(t_2)$ for the remainder, while compensating for the ratio of integration times. The reference beam is attenuated by optical density filters to approximately half of the intensity maximum of the object wave in the co-polarized channel.

4.3. Spiral nanostructures

This work demonstrates the large potential of Fourier-space holography by applying it to single plasmonic bullseye and spiral nanostructures, which are expected to generate significant orbital angular momentum content and spin-orbit coupling signatures in their response [11, 31, 34, 35]. While a single subwavelength aperture is a non-directional scatterer, the addition of concentric or spiraling grooves causes directional outcoupling ('beaming') of surface plasmon polaritons (SPPs) that are launched when exciting the aperture, as indicated in Fig. 4.2(b) [4, 36]. According to earlier reports [34, 37], these structures should imprint OAM onto scattered light, governed by the propagation delay experienced by the SPPs en route from the aperture to the outcoupling grooves and through a phenomenon called spin-orbit coupling [38–40], which introduces changes between the incident and the outgoing spin angular momentum (SAM). For plane waves, SAM is associated with helicity so that $\sigma = +1$ and $\sigma = -1$ for right-hand circular (RHC) and left-hand circular (LHC) polarizations, respectively. Additionally, in this case, the term OAM does not refer to the common OAM studied for paraxial, cylindrical beams, but rather indicates that the scattered spherical wave $\mathbf{S}(\theta,\phi)\frac{e^{ikR}}{R}$ carries helical phase fronts of the form $\exp(il\phi)$ in its complex scattering amplitude function. Here, l is an integer and ϕ is the azimuthal angle, while θ denotes the angle relative to the optical axis through the gold film.

The nanostructures consist of $N = 10$ grooves milled approximately 80 nm deep into a 200 nm thick Au film using a focused ion beam (FEI Helios). The optically thick Au film is thermally evaporated on a 170 µm thick glass cover slide with a 5 nm thick chromium adhesion layer on top. Figure 4.2(b,c) shows a schematic and an SEM image of the sample. The central aperture with a diameter $d = 250$ nm is milled entirely through the gold and chromium. The distance between the first groove and the center is $a = 375$ nm. The pitch of grooves $p = 500$ nm and the width is $w = 250$ nm, which leads to a duty cycle of 50 %. These parameters were selected for operation near the wavelength of 633 nm by using the results of previous studies [31]. Throughout the text, the handedness of the spirals is defined when looking along the wave propagation direction. Using this convention, m denotes the number of spiral grooves with $m > 0$ for clockwise (CW), $m < 0$ for counterclockwise (CCW) spirals and $m = 0$ for bullseye structures. While for the bullseye structures, the grooves are concentric, for the m-armed spirals the radius r depends on the azimuthal angle ϕ according to:

$$r(\phi) = a + m \cdot p\frac{\phi}{2\pi}\,, \quad 0 \le \phi < 2\pi N. \tag{4.1}$$

In the case of $|m| > 1$, adjacent spiral arms are arranged using an angle offset of $\Delta\phi = 2\pi/|m|$. The minimal separation between neighboring spirals is 25 µm to prevent inter-structure coupling.

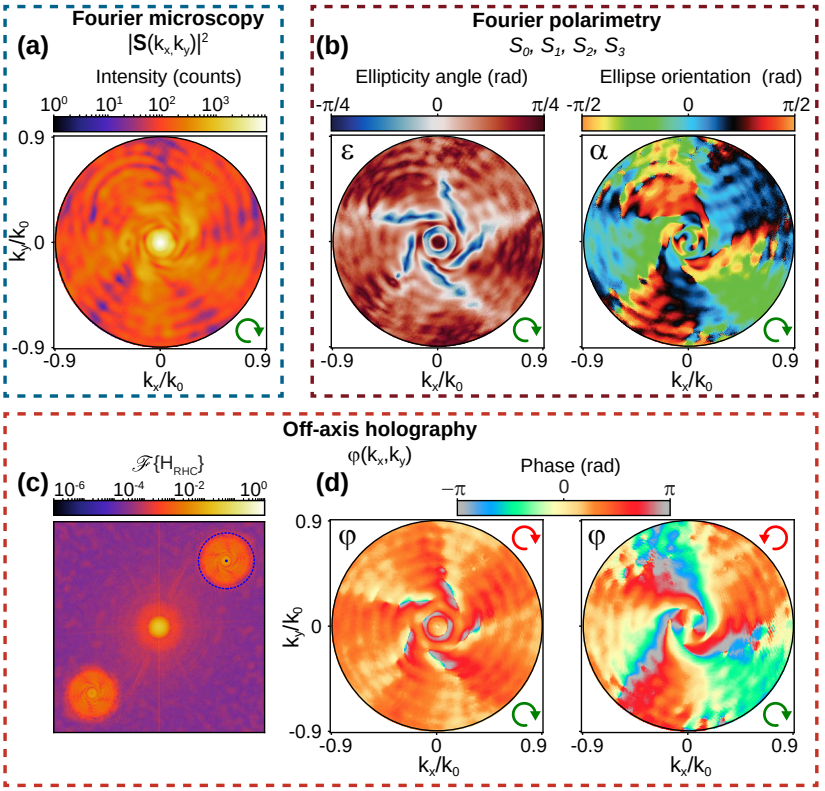

Figure 4.3: Demonstrations of Fourier microscopy, polarimetry and holography. (a) Fourier map of intensity, (b) polarization ellipse parameters ϵ and α, (c) Digital Fourier transform of an interferogram with RHC polarized detection, (d) reconstructed phase profiles for RHC and LHC polarized detection. In all sub-figures RHC polarized input and a $m = -5$ spiral nanostructure were used. The green and red arrows indicate the input and output polarizations, respectively.

4.4. Experimental workflow

Figure 4.3 highlights the main measurement modalities required to fully quantify an antenna radiation pattern, taking a $m = -5$ spiral nanostructure with RHC excitation (input polarization indicated as green arrows in all figures) as an example. First and foremost, the setup is a Fourier microscope, which enables one to record the intensity radiation pattern $|\mathbf{S}(\theta,\phi))|^2$ or more precisely $|\mathbf{S}(k_x,k_y)|^2 dk_x dk_y$ with $(k_x,k_y) = (\cos\phi\sin\theta, \sin\phi\sin\theta)$. The intensity distribution in Fig. 4.3(a) (logarithmic color scale) was measured by removing the polarization filters (QWP_2, LP_2 and HWP) in the collection path and blocking the reference beam in the setup shown in Fig. 4.2(a). It features a high intensity peak in its center, which signifies strong beaming into a narrow

cone of angles normal to the sample. As shown in previous studies, this is a consequence of diffractive outcoupling of surface plasmon polaritons by the grooves [4, 31, 36]. This beaming stands in sharp contrast to an isolated hole, which would produce an isotropic pattern [31]. The $|m|$ spiraling fringes and oscillations in the radial direction in the intensity map are caused by interference of the near-spherical wave scattered by the central aperture and the helical phase wave out-coupled by the spiral grooves [34].

The second capability of the setup, namely, polarization-resolved imaging, relies on measurements of intensity profiles in different output polarization bases (linear along $0°, 45°, 90°, 135°$ and circular left and right, red arrows indicate polarization in each panel) to determine the Stokes parameters. An example raw data set with the corresponding Stokes parameter results is reported in Appendix 4.A. The Stokes parameters S_i with $i = 0, 1, 2, 3$ fully characterize the polarization state of the wavefront for each collected wave vector in the radiation pattern [41] and can therefore be converted into a polarization ellipse for each detected wave vector in the radiation pattern (see Appendix 4.A). Figure 4.3(b) reports the polarization ellipse parameters, namely, the ellipticity angle ϵ ($\epsilon = 0$ for linear polarization, resp. $\pm\pi/4$ for RHC/LHC polarization) and the orientation α of the major axis of the ellipse relative to the k_x axis. In the particular case of RHC input polarization, $\epsilon = -\pi/4$ represents full helicity conversion, and $\epsilon = \pi/4$ represents the retained polarization. The wave vector-resolved ϵ map in Fig. 4.3(b) clearly shows complete helicity conversion ($\epsilon = -\pi/4$) in a doughnut-like shape with five spiraling arms around it. Regions close to these features are characterized by an equal distribution of LHC and RHC polarization ($\epsilon = 0$, linear polarization), with the remaining k-space containing an unchanged helicity $\epsilon = \pi/4$). This directly evidences helicity conversion at oblique scattering angles, i.e., spin-orbit coupling in scattering. The reader should note that since the nanostructure scatters the incident beam (cylindrical geometry) into a spherical wave, the polarization definition is not trivial. For instance, given that the input polarization RHC implies an input E-field vector along $(\hat{x} + i\hat{y})/\sqrt{2}$ (with z being the optical axis), the definition of the helicity conserving/reversing channel actually means projection of the full measured field $\mathbf{S}$ on $(\hat{\theta} \pm i\hat{\phi})/\sqrt{2}$.

Finally, while the Stokes parameter measurements allow for the retrieval of phase *differences* between two orthogonally polarized field components, adding digital holographic microscopy capabilities to the setup enables measurements of individual phase profiles of the respective polarization states. More specifically, digital off-axis holography is used for this task. Off-axis holography offers the advantage of operating in a single-shot manner by making use of single digitally Fourier-transformed camera images for phase resolution, as opposed to delay scanning. Although digital holographic microscopy was recently applied to nanophotonic structures [42–45], these studies were mostly aimed at real space, i.e., sample plane, imaging. However, real-space images of nanoantennas have the drawback of being restricted by

the diffraction limit and therefore, typically cover just a few camera pixels. In contrast, Fourier-space holography of single nanoantennas generates a signal over an entire CCD chip, providing far richer information. To this end, the reference beam E_R, polarized identical to the detection channel, is overlapped with the object wave $E_O = A_O \exp[-i\varphi]$, i.e., the Fourier-space image, on the CCD camera, which results in the hologram $H = |E_O + E_R|^2$. As discussed in Sec. 1.4.2, in the simplest case of the reference beam being a plane wave with $E_R = A_R \exp\left[i\vec{k}\cdot\vec{x}\sin\delta\right]$, where $\vec{k}$ is its wave vector and δ the angle between the object and reference beam, the hologram H can be mathematically expressed as

$$H = A_O^2 + A_R^2 + A_O \cdot A_R \exp\left[\pm i\left(\varphi + \vec{k}\cdot\vec{x}\sin\delta\right)\right]. \tag{4.2}$$

From this equation, it becomes apparent that only the cross-terms contain φ, which is the object wave phase information. The additional phase term $\vec{k}\cdot\vec{x}\sin\delta$ arises from the deliberately introduced tilt δ, which serves to separate the cross and direct terms upon digital Fourier transformation. Figure 4.3(c) shows such a digital Fourier transform of the hologram corresponding to a $m = -5$ spiral in circular co-polarization. This inclination angle δ is chosen to be sufficiently large such that upon Fourier transformation, the cross, and direct terms are well separated yet sufficiently small that the hologram fringes are well sampled by the pixelated detector. The remaining digital reconstruction process consists of selecting (i.e., binary masking), shifting, back-Fourier transforming one of the cross-terms, and a digital correction for residual parabolic phase aberrations in the imaging optics (see Appendix 4.B). Figure 4.3(d) shows two measured phase maps for the co- and cross-polarized channel. They reveal a helical evolution of the phase around the optical axis, which is especially evident for the cross-polarized channel. The phase profile in the co-polarized channel contains five spiraling arms, with an overall phase increment of $5 \cdot 2\pi$ when going full circle around the origin. The phase profile in the cross-polarized channel contains 2 fewer arms and an additional feature around its center. The origin of these effects will be further discussed in the next section.

4.5. Analysis of spiral radiation patterns

Having introduced the experimental workflow for full quantification of the amplitude, polarization, and phase information in the radiation of a nanostructure, this section presents an example of the type of rich insight one can gain. For this, an in-depth quantification of the OAM-conversion efficiency plasmonic spiral antennas depending on their geometry, i.e., the number and orientation of the spiral arms, was performed. Figure 4.4(a,c) demonstrates a subset of the measured full electric fields radiated into the polarization-

helicity-conserving and helicity-changing channel using RHC input polarization.

To support the measured results, the simulated field profiles of the corresponding spiral/ bullseye structures are shown in Fig. 4.4(b,d), which demonstrate a good qualitative agreement. These plots show simultaneously the field phase (from hologram) as hue and the field amplitude ($|\mathbf{S}(\theta,\phi)|$) as brightness (logarithmic scale). Figure 4.4 highlights results for CCW spirals with up to 9 arms ($m = -9$), starting from the case of a bullseye ($m = 0$). It is evident that the number of spiral grooves $|m|$ has a big impact on both the amplitude and phase in both co- and cross-polarized measurements. As in Figure 4.3(d), the number of spiraling arms in the Fourier maps coincides with the number of arms of the spirals in co-polarization, while in cross-polarization, the field profiles show 2 fewer arms. These arms are visible both in the amplitude and phase because they bring a phase increment of 2π per arm when traversing a circle at constant θ through the radiation pattern. These observations highlight that OAM conversion is controlled by a combination of propagation phase (number of arms) and SAM conversion (± 2 for helicity-reversing scattering). Figure 4.C.1 in the Appendix shows further examples with the same input/output polarization settings but with a reversed spiral orientation ($m > 0$). In this case, not only does the orientation of the field profiles flip but also the observed number of arms in cross-polarization is increased, instead of diminished, by an offset of 2 compared to the number of physical grooves. In all datasets, the overall pattern is quite different near the center of the images, i.e., for radiation angles near-normal to the gold film. All co-polarized radiation patterns show a bright feature exactly at $k_{\parallel} = 0$ with a flat phase, while the cross-polarized measurements reveal a donut-shaped feature with a phase advance of $2 \cdot 2\pi$ when traversing a circle around the optical axis. The OAM transfer corresponding to this donut-shaped feature is equal to the change in the SAM ($\Delta\sigma = \pm 2$), independent of the geometry or handedness of the grooves. Since this feature persists in the case of a bullseye geometry, it can be concluded that it arises from light that has undergone spin-to-orbital-angular-momentum conversion caused by the subwavelength aperture and scattered in the normal direction ($k_{\parallel} = 0$) into the far-field irrespective of the grooves [39]. This is confirmed at the end of this section by OAM decomposition of the measured fields. In any case, the above observations indicate that the radiation patterns do not map directly onto pure OAM-carrying Laguerre-Gauss beams. Instead, the spiral structures scatter into a variety of OAM contributions, the superposition of which is observed as a radiation pattern.

The observations indicate that the conversion of input plane waves into output OAM-carrying spherical waves leads to an OAM-mixture, in contrast to the 'binary' selection rules reported in Ref. 34. The expected selection rules originate from a simple picture, taking the central aperture as a point launching SPPs that then accumulate propagation delay due to the twist of the spiral

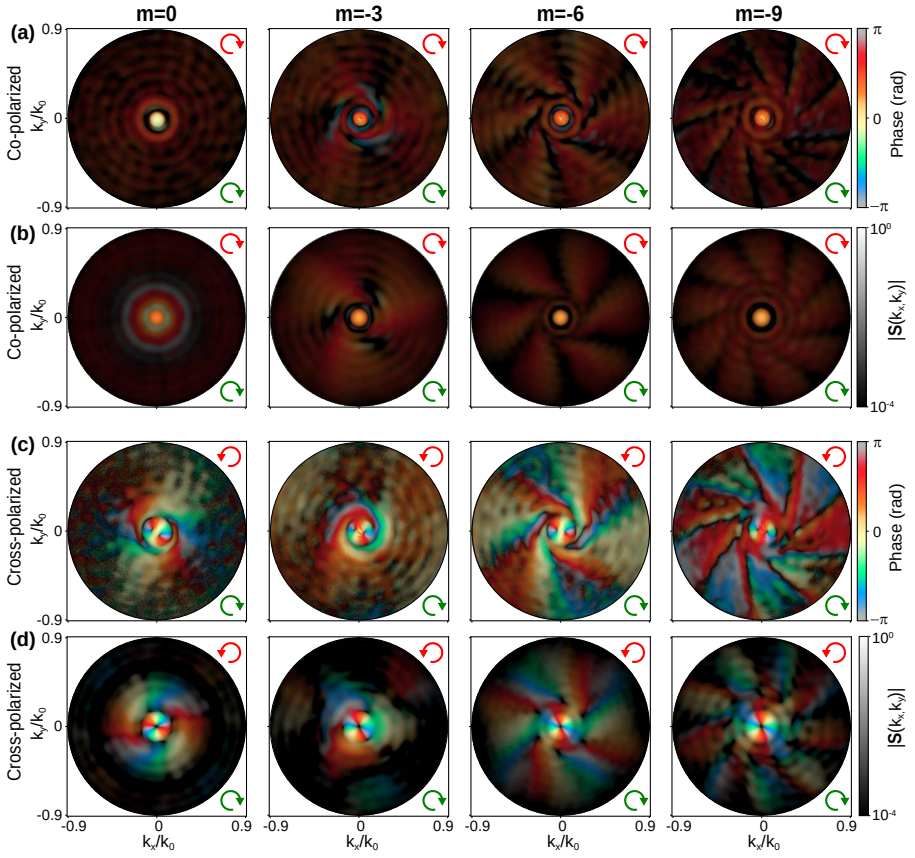

Figure 4.4: Example set of interferometric and polarimetric k-space microscopy measurement and simulation results. Measured ((a) and (c)) and simulated ((b) and (d)) Fourier plane field profiles of a bullseye ($m = 0$) and spirals with $m = -3, -6, -9$. The transmitted polarization channels are co-polarized (a,b) and cross-polarized (c,d) with RHC-polarized input. The green and red arrows indicate the input and output polarizations, respectively. The plots show a combined representation for the phase as hue and field amplitude as brightness (logarithmic scale). A circular representation of the color map is shown in Fig. 4.A.3(a). Each amplitude profile is normalized by its maximum.

grooves, where light is coupled into free space. The resulting superposition of wavefronts at an m-armed spiral results in an offset of m in the OAM index. Spin-to-orbital angular momentum conversion causes an additional offset of ± 2 in the generated OAM mode for helicity-non-conserving detection [38–40]. This leads to the selection rule proposed by Y. Gorodetski *et al.* [34]:

$$\Delta l = m + \Delta\sigma, \tag{4.3}$$

which states that the amount of generated OAM mode difference Δl compared

to the input wave (OAM = 0 in this work) should be equal to the number of spiral arms m plus the helicity change $\Delta\sigma = 0, \pm 2$ (conserving, resp. conversion from RHC to LHC or vice versa) [34].

A main strength of the proposed measurement scheme is that the purity of the selection rule can be quantitatively analyzed by computationally decomposing the complex field into the desired basis. This is done by representing the complex electric field $E(\theta, \phi)$ as a linear combination of OAM states:

$$E(\theta, \phi) = \sum_{l=-\infty}^{\infty} C_l(\theta) \exp(il\phi), \tag{4.4}$$

where, to consider the spherical nature of the scattered wave, spherical coordinates are used, with coefficients $C_l(\theta)$ defined as

$$C_l(\theta) = \frac{1}{2\pi} \int_0^{2\pi} E(\theta, \phi) \cdot \exp(-il\phi)\, \mathrm{d}\phi. \tag{4.5}$$

The complex-valued, azimuthal overlap integral results $C_l(\theta)$ can be used to calculate the polar angle resolved OAM mode density (see Fig. 4.E.1(a,b)). From this, the purity or power of an OAM mode l is derived as

$$p_l = \int_0^{\arcsin(\mathrm{NA})} \left| C_l(\theta) \right|^2 \cdot \sin(\theta)\, \mathrm{d}\theta. \tag{4.6}$$

Normalizing p_l by the sum of its values results in the modal power spectrum $P_l = p_l / \sum_{l=-\infty}^{\infty} p_l$. For further implementation details see Appendix 4.D.

As an example, Figure 4.5(a) reports the OAM power spectrum for a $m = -5$ spiral in the helicity-non-conserving channel with RHC input, showing dominant contributions at $\Delta l = +2$, $\Delta l = 0$ and $\Delta l = -3$. The corresponding OAM power spectrum in the helicity-conserving channel is shown in the Appendix in Fig. 4.E.1(a). In this case the main contributions are at $\Delta l = m = 0$ and $\Delta l = m = -5$. Figure 4.5(b-d) combines the OAM mode decomposition results for $m = -9$ to $m = 9$ spirals (each OAM power spectrum is normalized to unit integrated content) for three different input-output polarization combinations. Throughout, there are dominant features at the selection rule, i.e., at the diagonal $l = m$ in the helicity-conserving channels [Figs. 4.5(b) and 4.E.1(b)], $l = m \mp 2$ respectively for conversion from LHC to RHC [Fig. 4.5(c)] and vice versa [Fig. 4.5(d)]. In addition, a strong leakage into the $l = 0$ mode can be observed in case of the polarization-conserving measurement, resp. $l = \pm 2$ for the polarization non-conserving data. On average, the purities of the OAM modes following the selection rule are $(13 \pm 4)\%$ for co-polarization and $(38 \pm 3)\%$ for cross-polarization.

In general, the dominant OAM contributions fit the interpretation that only a fraction of the light interacted with the spiral grooves, while the remainder essentially gained no OAM upon direct transmission or gained only OAM

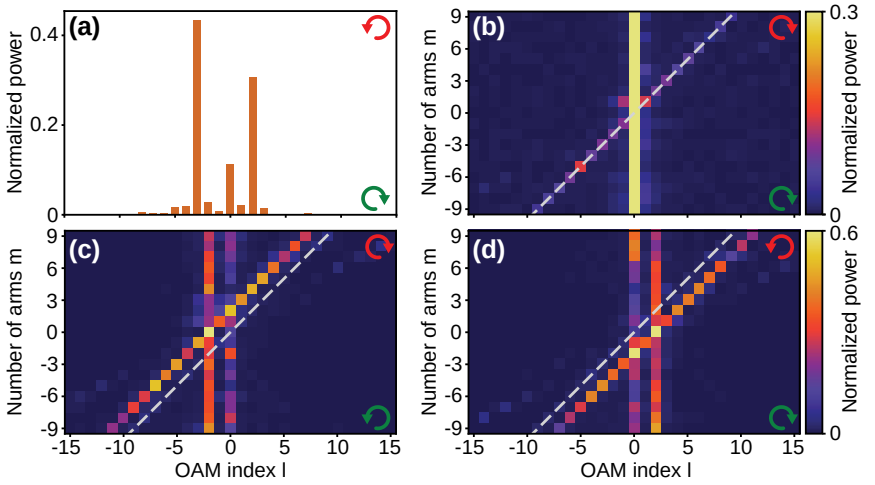

Figure 4.5: OAM decomposition results. (a) Individual OAM power spectrum for a $m = -5$ spiral with RHC input and LHC output. (b-d) OAM power spectra as a function of m in co- (b) an cross-polarization (c and d) with RHC (b and d) and LHC (c) polarized input. The dashed lines in (b-d) indicate $l = m$. Panels (c) and (d) possess the same color scale.

corresponding to a change of the SAM, i.e., spin-orbit coupling at the aperture. Additionally, the presence of the OAM mode $l = 0$ in cross-polarization is likely due to the non-perfect extinction ratio of the polarizers employed.

While from the perspective of functional nanostructures for generating OAM, it is evident that performance is imperfect, these measurements highlight that the proposed measurement method allows for an unprecedented quantification. The performance of the nanostructures in terms of OAM mode purity can be further improved by optimizing the geometrical parameters of the spiral such as the aperture radius or by using metal-insulator-metal arrangements as proposed in Refs. 46 and 47. The observations suggest a trade-off between overall transmission efficiency (requires a large central aperture) and leakage into OAM $= 0, \pm 2$ (requires low direct transmission). A more precise analysis of the full radiated field at hand allows us to gain additional insights into the underlying physics. For instance, one can precisely determine the OAM mode density within any given band of angles $\theta, \theta + \Delta\theta$, enabling one to determine the polar angles into which particular OAM content is scattered (see Fig. 4.E.1(c,d)).

4.6. Method validation and minimum redundancy

Returning to the proposed measurement scheme, note that polarimetry plus interferometry provides not only abundant but also redundant information

on the wavefront. The reason for this lies in the fact that polarimetry already determines the phase difference between orthogonally polarized field components, which should be strictly identical to the difference in phase profiles measured with holography in the same two crossed polarizations. For instance, the following simple combinations of Stokes parameters represent phase difference profiles

$$\arg(S_2 + iS_3) = \varphi_V - \varphi_H \tag{4.7a}$$
$$\arg(S_1 - iS_3) = \varphi_A - \varphi_D \tag{4.7b}$$
$$\arg(S_1 + iS_2) = \varphi_{LHC} - \varphi_{RHC}, \tag{4.7c}$$

where φ is the phase profile corresponding to the polarization state labeled in the subscript (V=vertical, H=horizontal, A=anti-diagonal, D=diagonal, taken to refer to the camera plane). On one hand, this redundancy can be used to check the consistency of the method by comparing maps of phase differences determined with polarimetry and holography. On the other hand, one can use the redundancy to reduce the total number of measurements required to fully determine $\mathbf{S}(\theta, \phi)$ (up to an arbitrary phase offset).

Figure 4.6(a) shows an example consistency check through a direct comparison of $\varphi_V - \varphi_H$ and $\arg(S_2 + iS_3)$ again for the case of a $m = -5$ spiral (the remaining two phase difference comparisons listed in Eqs. (4.7b)-(4.7c) are shown in the Appendix in Fig. 4.F.1). Evidently, these measurements confirm the consistency between phase difference maps obtained using holography and polarimetry, with the only notable distinction lying in the noise characteristics. Stokes polarimetry relies on pixel-by-pixel image subtraction, leading to uncorrelated shot-noise propagating into the phase map. Instead, the holography images are effectively low-pass filtered by the reconstruction procedure (Fourier transform & masking of interferogram). Figure 4.6(b) provides an example of how the Stokes parameters in combination with a single holography measurement (in this case φ_V) can be used to reconstruct the phase profile in any arbitrary polarization channel. Here, Figure 4.6(b) shows the reconstructed phase profile for a $m = -5$ spiral for RHC polarized detection, alongside a direct holographic determination of the phase for comparison. This illustrates how the number of measurements needed to fully quantify a radiation pattern can be reduced. Instead of independent polarimetry and holography measurements for each polarization, it is enough to perform a single holographic measurement plus the four measurements required to retrieve the Stokes parameters (required calculus is described in Appendix 4.F). In addition, the phase profile reconstructions for four additional polarization channels (vertical, diagonal, anti-diagonal, LHC) are shown in Fig. 4.F.1. These comparisons show excellent agreement.

The minimally redundant measurements could be advantageous both from the viewpoint of efficiency as well as reduced requirements on camera dynamic range in polarimetry compared to holographic measurements.

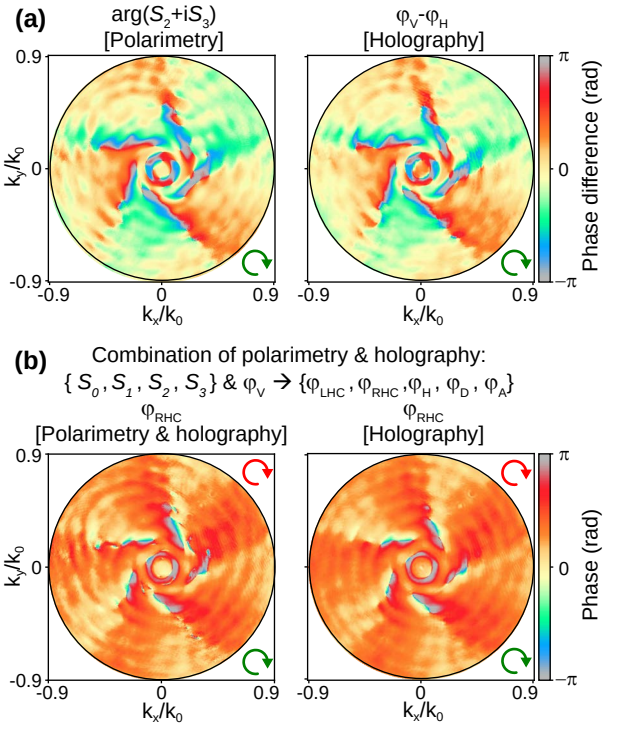

Figure 4.6: Validation and redundancy removal in combined holographic and polarimetric measurements. (a) Difference between phase profiles with vertical and horizontal output polarizations retrieved using polarimetry and holography. (b) Example of a phase profile with RHC polarized output, which was retrieved using a combination of polarimetry and holography with correspondent purely holographic profile for comparison. In both cases, a RHC polarized input and a $m = -5$ spiral were used. The green and red arrows indicate the input and output polarizations, respectively.

Holography works best with a large fringe contrast throughout the recorded interferogram, with fringe intensities spanning the camera dynamic range. This fringe contrast (visibility) increases as the intensity ratio of the two interfering waves (object and reference wave) gets closer to one [32]. For strongly focused radiation patterns, this requirement is difficult to fulfill. The data redundancy enables one to perform the holography in just a single polarization channel that has the most suited intensity distribution, i.e., polarization channels where directly transmitted light is (partially) blocked. On top of that, this approach allows for improvements in measurement speed, since the minimum number of required images can be reduced to only four: a single hologram to determine amplitude and phase in one polarization channel, and intensity measurements through three complementary polarizer settings.

4.7. Conclusion and discussion

In this chapter, we studied a measurement technique for the characterization of scattered radiation patterns from individual nanoscatters in terms of amplitude, vector, and phase. To demonstrate the remarkable insight that this technique can offer for studies of optical antennas, the OAM content of light scattered by a family of plasmonic spirals was analyzed. The quantitative analysis of the wavefronts scattered by spiral antennas revealed that the interaction process produces a more complex OAM state mixture than a binary mode distribution indicated by reported OAM selection rules [34]. Conversely, this shows that using our measurement technique the OAM mode purity of spiral antennas can be further increased through optimization of the nanoantenna design.

Contrary to other OAM measurement techniques, the proposed method does not require the use of spiral phase plates or holograms [23, 24]. In principle, the technique could be performed even with a single camera shot, given that off-axis holography requires just a single image and that polarization can be multiplexed [48]. The current limit to the technique presented here is the NA of the employed optical system. Extending the method to a 4π microscopy arrangement could fulfill the quest for full quantification of the multipole content of any scattering geometry using its far-field.

As such, we expect our work to directly apply to several important problems in nanophotonics, such as the use of plasmonic antennas for enhanced sensing and emission, metasurfaces for controlling transmitted and reflected wavefronts, and nonlinear metasurfaces, in which phase gradients imprinted in the metasurface geometry determine the efficiency and angular distribution of, e.g., frequency conversion. In all these cases, access to angle-resolved amplitude, polarization, and phase properties of the far-field is of paramount importance.

Finally, we are confident that the described approach will find applications in the field of optical nanometrology, where diffraction-based experiments are used to solve an inverse problem as described in Chapter 3. For instance, polarimetry using a differential Mueller matrix formalism [49, 50] as well as holography using a dark-field holographic microscopy approach [51, 52] were recently reported to offer benefits for overlay metrology.

APPENDICES

4.A. Details on Stokes polarimetry

Stokes polarimetry is a technique that can be used to completely characterize the polarization state of light, which includes partially polarized light, by using four measurable quantities called Stokes parameters (S-parameters) [41]. Experimentally these S-parameters S_i, where $i = 0,1,2,3$, were retrieved through six intensity measurements $I(\beta,\gamma)$, i.e., $I_H, I_V, I_D, I_A, I_{RCP}, I_{LCP}$ with the required angles β and γ of QWP_2 and LP_2

$$\begin{pmatrix} S_0 \\ S_1 \\ S_2 \\ S_3 \end{pmatrix} = \begin{pmatrix} \langle|E_x|^2\rangle + \langle|E_y|^2\rangle \\ \langle|E_x|^2\rangle - \langle|E_y|^2\rangle \\ \langle E_x E_y^*\rangle + \langle E_y E_x^*\rangle \\ i\left(\langle E_x E_y^*\rangle + \langle E_y E_x^*\rangle\right) \end{pmatrix} = \begin{pmatrix} I(0°,0°) + I(90°,90°) \\ I(0°,0°) - I(90°,90°) \\ I(45°,45°) - I(135°,135°) \\ I(0°,45°) - I(0°,135°) \end{pmatrix}, \tag{4.A.1}$$

where E_x and E_y are the orthogonal electric field components and x and y refer to camera coordinates. It should be noted that this set of 6 intensity measurement is redundant, as in principle four measurements suffice (e.g., I_H, I_V, I_D, I_{RCP}). An example set of such intensity measurements with six different outgoing beam polarizations (horizontal, vertical, diagonal, antidiagonal, LHC and RHC) for the $m = -5$ spiral and RHC polarized input is shown in Fig. 4.A.1(a). Simulation results for corresponding intensity profiles are shown Fig. 4.A.1(b). In addition to intensities, phase profiles in each of the six different polarization channels were measured using off-axis holography as shown Fig. 4.A.1(c). For comparison, simulated phase profiles in corresponding polarization channels are shown in Fig. 4.A.1(d).

Using the set of intensity measurements shown in Fig. 4.A.1(a) the S-parameters, shown in Fig. 4.A.2, were calculated. Each S-parameter S_i, $i = 1,2,3$ is normalized by S_0 and therefore ranges from -1 to $+1$. The physical connotation of the S-parameters can be described as follows:

- S_0 is equivalent to the total field intensity.
- S_1/S_0 quantifies whether the light is preferentially linearly polarized in the horizontal/vertical basis (positive, resp. negative values).
- S_2/S_0 quantifies whether the light is preferentially linearly polarized in the diagonal/antidiagonal basis (positive, resp. negative values).
- S_3/S_0 describes the degree of circular polarization (sign encoding for helicity).
- Additionally, $\sqrt{S_1^2 + S_2^2 + S_3^2}/S_0$ describes the degree of polarization.

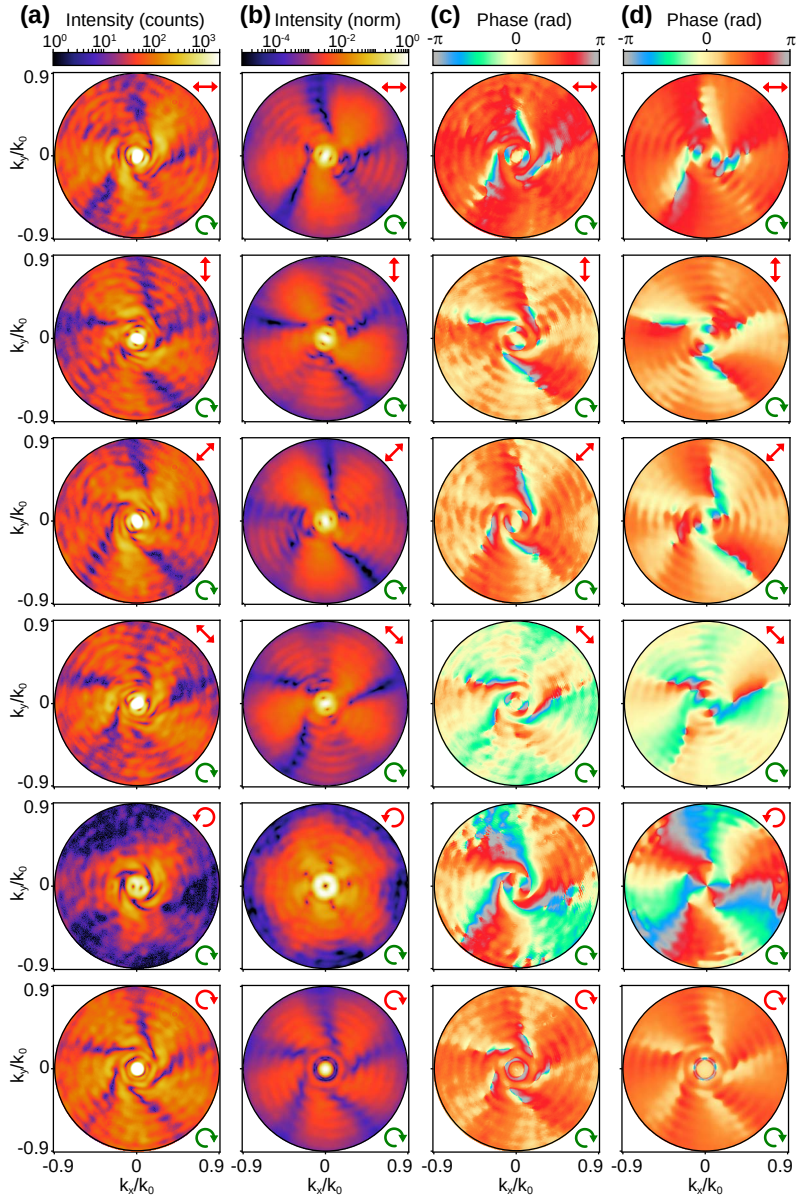

Figure 4.A.1: An example set for intensity and phase profiles. (a,b) Measured and simulated intensity profiles in units of CCD counts and normalized units, respectively. (c,d) Measured and simulated phase profiles. All panels use the same $m = -5$ spiral, 6 different outgoing polarizations, and RHC polarized input. The green and red arrows indicate the input and output polarizations, respectively.

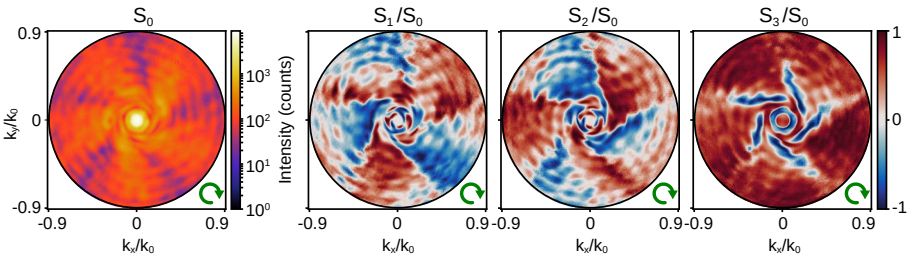

Figure 4.A.2: An example set of measured Stokes parameters for a $m = -5$ spiral with RHC polarized input.

Note, that while the field intensity $|S(k_x, k_y)|^2$, shown in Fig. 4.3(a), is the same physical quantity as the S-parameter S_0, shown in Fig. 4.A.2, operationally S_0 was determined by summing all 6 polarization channels, averaging over three measurement basis choices, i.e. $S_0 = (I_H + I_V + I_D + I_A + I_{RHC} + I_{LHC})/3$. The minor differences between the two plots are explained by a higher signal-to-noise ratio of the latter approach.

Further, the S-parameters can be converted into the so-called polarization ellipse parameters using

$$\epsilon = \frac{1}{2} \cdot \arg\left(\sqrt{S_1^2 + S_2^2} + iS_3\right) \tag{4.A.2a}$$

$$\alpha = \frac{1}{2} \cdot \arg(S_1 + iS_2), \tag{4.A.2b}$$

where ϵ denotes the ellipticity angle and α the elipse orientation. Example ϵ and α plots derived from the S-parameters from Fig. 4.A.2 are shown in Fig. 4.3(b). A geometric representation of ϵ and α is shown Fig. 4.A.3(a) by plotting the values that $\vec{E}_{\parallel}(t)$ can take at a fixed position z as a function of time t. From this sketch it becomes clear that $\epsilon = \pm\pi/4$ means complete circular polarization and $\epsilon = 0$ complete linear polarization.

4.B. Phase correction in off-axis holography

In digital holographic microscopy phase aberrations can occur due to the high NA microscope objective and a non-flat phase front for the reference beam [33, 53]. The aberration consists of an overall parabolic phase profile that is present already when imaging a single subwavelength aperture. We perform a numerical correction using the complex conjugate of the spherical phase term that results in the flattest residual when multiplied with the phase measured for a single aperture [33]. This phase correction calibration step needs to be repeated each time the sample position, objective focus, or reference beam tilt angle change. To ease this process we implemented a Python GUI using

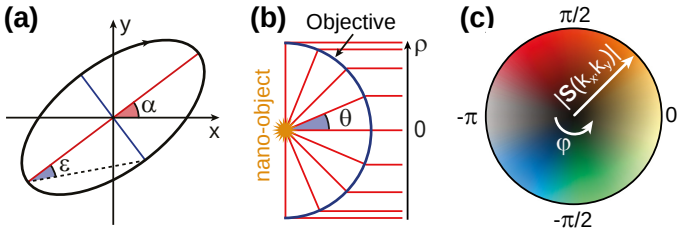

Figure 4.A.3: (a) Polarization ellipse representation of an elliptically polarized electric field $\vec{E}_{\parallel}(t)$ showing the parameters α and ϵ. (b) Illustration of the apodization effect occurring in high NA objectives. A point source radiates an isotropic, spheric wave, which turns into a collimated beam with a non-uniform intensity distribution in the back focal plane of the objective. The increased ray density at higher ρ indicates the higher intensities. (c) A circular representation of the color map used to jointly represent the amplitude and phase of the measured wavefronts.

wxPython. Note, that although the curvature of the parabolic phase correction value does not influence the retrieved OAM power spectrum, lateral misalignments of the phase correction with respect to the propagation axes can cause a minor mode crosstalk.

4.C. FDTD simulation procedure

Far-field profile simulations are performed using 3D finite-difference time-domain software (Lumerical FDTD). The bullseye/ spiral structures are modeled using the same parameters as the fabricated structures and are excited using two normally incident plane waves, which are shifted 90° in phase and rotated 90° in polarization (RHC polarized input) and have a wavelength of $\lambda = 633\,\mathrm{nm}$. The total simulation region has dimensions $(17 \times 17 \times 0.8)\,\mu\mathrm{m}^3$ and is enclosed by perfectly matched layers (PMLs). A mesh grid size of 12 nm is used to model the spiral grooves. The gold film permittivity was modeled using a Drude model fit to values reported in Ref. 54:

$$\epsilon_r = \epsilon_\infty - \frac{\omega_p^2}{\omega(\omega + i\gamma)}, \tag{4.C.1}$$

where $\epsilon_\infty = 9.54$, $\omega_p = 1.35 \cdot 10^{16}\,\mathrm{rad/s}$ and $\gamma = 1.25 \times 10^{14}\,\mathrm{rad/s}$. The electromagnetic field is recorded using a monitor on a plane located 10 nm above the nanoscatterer; the standard Lumerical Stratton-Chu near to the far-field projection technique is applied to calculate the field 1 m away from the structure. It should be noted that this technique is not rigorous for systems with interfaces.

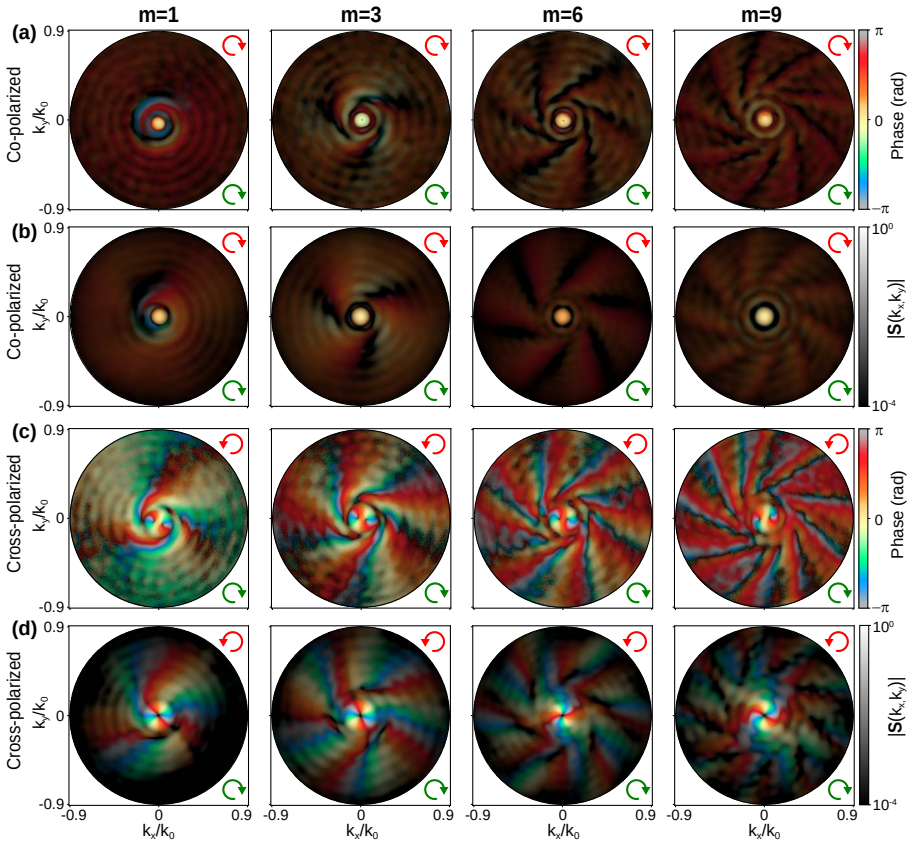

Figure 4.C.1: Additional set of interferometric and polarimetric k-space microscopy measurement and simulation results for spirals with positive m. Measured ((a) and (c)) and simulated ((b) and (d)) Fourier plane field profiles of spirals with $m = 1, 3, 6, 9$. The transmitted polarization channels are co- (a,b) and cross-polarized (c,d), with RHC-polarized input. The green and red arrows indicate the input and output polarizations, respectively. The plots show a combined representation for the phase as hue and field amplitude as brightness (logarithmic scale). A circular representation of the color map is shown in Fig. 4.A.3(a). Each amplitude profile is normalized by its maximum.

Table 4.D.1: Jacobian determinants for cylindrical to spherical and Cartesian to cylindrical transformations.

Cylindrical to spherical	Cartesian to cylindrical
$\det\left\{\frac{\partial(\rho,\phi)}{\partial(\theta,\phi)}\right\} = f\cos(\theta)$	$\det\left\{\frac{\partial(x,y)}{\partial(\rho,\phi)}\right\} = \rho$

4.D. Details on OAM decomposition procedure

In the following, we describe the implementation of the OAM decomposition method. As mentioned in the main text, the measured complex wave field forms the basis of this analysis. By computationally expanding the field as a series of the fundamental helical modes $\exp(il\phi)$, the underlying OAM mode powers can be identified. Since a regular CCD camera is used for image acquisition, the measured field $E_{\text{obs}}(x,y)$ is sampled on a Cartesian grid. To take this into account, Eqs. (4.5) and (4.6) were transformed into Cartesian coordinates. This can be achieved by substituting the coordinates and including the appropriate Jacobian. The Jacobian for the spherical to Cartesian coordinates transformation consists of the inverse of the two Jacobian determinants, that are shown in Tab. 4.D.1, and is given by:

$$J = \frac{1}{f\cos\theta}\cdot\frac{1}{\rho}, \tag{4.D.1}$$

where f is the objective focal length, $\cos(\theta) = \sqrt{1-\rho^2/f^2}$ and $\rho = \sqrt{x^2+y^2}$. By using this Jacobi determinant, substituting spherical coordinates and restricting the integration region to $\rho = f\sin(\theta)$, the integral in Eq. (4.5) can be rewritten as:

$$C_l(\theta) = \frac{1}{2\pi}\iint_{\rho=f\sin(\theta)} E(x,y)\cdot\exp(-il\phi)\cdot\frac{1}{f\cos(\theta)\rho}\,\mathrm{d}x\,\mathrm{d}y, \tag{4.D.2}$$

where $\phi = \arctan(y/x)$. In practice the integral in Eq. (4.D.2) is replaced by a discretized sum over x and y coordinates, while a ring-shaped, binary mask

$$R_\theta(x,y) = \begin{cases} 1 & \text{for } \theta - \Delta\theta/2 < \arcsin\left(\frac{\sqrt{x^2+y^2}}{f}\right) < \theta + \Delta\theta/2 \\ 0 & \text{else.} \end{cases} \tag{4.D.3}$$

is introduced as a factor in the integrand to confine the integral to a narrow, annular region, whereby the angle θ is varying in a range of $\theta = 0$ and $\theta = \arcsin(\mathrm{NA})$. For infinitesimally small $\Delta\theta$ this procedure becomes equivalent to the integration over ϕ described in Eq. (4.5). The angle θ was sampled in 100 steps to get accurately resolved $C_l(\theta)$ overlap integrals.

Furthermore, when using the Fourier imaging technique for quantitative purposes, a general property of high NA objectives called apodization needs to be considered. This purely geometric effect causes isotropic spherical waves to be transformed into collimated beams with non-uniform intensity profiles since the objective lens transformation causes increasing ray densities at increasing polar angles θ, as illustrated in Fig. 4.A.3(b) [28, 55]. Given that the employed objective satisfies Abbe's sine condition, this effect leads to the following relation between the electric field E and the observed electric

field E_{obs}: $E = E_{\text{obs}} \cdot \sqrt{\cos(\theta)}$. This results in the following modification of Eq. (4.D.2):

$$C_l(\theta) = \frac{1}{2\pi} \iint_{\rho = f\sin(\theta)} \underbrace{\frac{E(x,y)}{\sqrt{\cos(\theta)}}}_{E_{\text{obs}}} \cdot \exp\left(-il\phi\right) \cdot \frac{1}{f\sqrt{\cos(\theta)}\rho} \, \mathrm{d}x \, \mathrm{d}y. \qquad (4.D.4)$$

The OAM mode decomposition is performed for a finite range of OAM indices $l = -20...20$, whereby in the OAM power spectrum plots the index range was reduced to $l = -15,...,15$, where most of the signal is situated. Note that the apodization factor is included in all OAM power spectra, while in the presented amplitude and intensity plots the actually measured amplitude E_{obs} is shown, without the apodization factor.

4.E. Additional OAM decomposition results

With the full k-resolved field at hand, one can computationally determine the θ-resolved OAM density or in fact project the field on any desired basis function set. This is a large advantage over other reported measurement schemes to determine OAM in paraxial beams, which rely on sequential measurements of integrated transmission through a combined set of spatial filters (to select θ) and (digital) holograms (to select a target $e^{il\varphi}$) [24, 56]. Such results are reported as polar-angle-resolved plots of the integrand of Eq. (4.6), namely $\left(C_l(\theta)\right)^2 \cdot \sin(\theta)$ normalized by $\sum_{l=-\infty}^{\infty} p_l$ in Fig. 4.E.1(a,b) for co- and cross-polarization, respectively. One can see that the main contribution to the OAM density at around $\theta = 0°$ is the OAM mode $l = 0$, which is partially suppressed in cross-polarization in favor of $l = +2$. The high directionality of these two OAM modes can be explained by transmission of the weakly focused excitation light through the gold film. The presence of the OAM mode $l = 0$ in cross-polarization is likely due to the non-perfect extinction ratio of the polarizers. As the aperture itself is sub-wavelength it does radiate at off-center angles giving rise to contributions at $l = 0$ in the co-polarized and $l = +2$ in the cross-polarized channel. For co-polarized scattering, shown in Fig. 4.E.1(a), the maximal OAM density at $l = -5$ is at around $\theta = 18.9°$. For the cross-polarized case shown in Fig. 4.E.1(b) the maximal OAM density $l = -3$ is scattered at an angle $\theta = 16.4°$ and the maximal OAM density value of the parasitic OAM mode $l = 2$ at $\theta = 4.8°$. In general, for the spiral nanostructures studied here, the leakage channels with $l = 0$ and $l = \pm 2$ appear at lower angles than the desired, groove-number (m) dependent OAM modes.

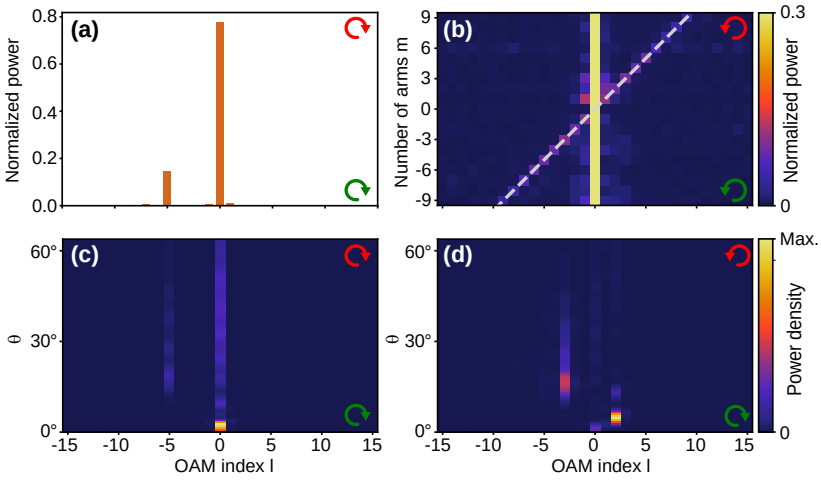

Figure 4.E.1: (a) Individual OAM power spectrum with RHC input and RHC output. (b) OAM power spectra as a function of m in co-polarization with LHC polarized input. The dashed line indicates $l = m$. (c,d) θ-resolved OAM density spectra in co- (c) and cross-polarization (d) with RHC input. The green and red arrows indicate the input and output polarizations, respectively. Panels (a), (c) and (d) feature a $m = -5$ spiral.

4.F. Details on validation and redundancy removal

The Fourier polarimetry technique provides access to wave vector-resolved phase differences between orthogonally polarized fields, as described in the main text. In Equation (4.7) three different combinations of S_1, S_2 and S_3 are shown and expressed in terms of phase differences between vertical and horizontal, anti-diagonal and diagonal and LHC and RHC polarizations. As an example, Figure 4.6(a) examines Eq. (4.7a) using polarimetrically and holographically determined phase differences between the vertical and horizontal polarizations for a $m = -5$ spiral. Here, the two remaining consistency checks are shown in Fig. 4.F.1 in accordance to the Eqs. (4.7b) and (4.7c), which again show a good visual match. As mentioned in the main text, off-axis holography contains an arbitrary phase offset. Here, the two phase offsets are equalized by minimizing the integrated difference between the phase difference profiles retrieved from holography and polarimetry, as suggested in Ref. 57.

Furthermore, the main text discusses the possibility of utilizing the information redundancy present in combined polarimetric and holographic approaches to reconstruct phase profiles in polarization channels, in which holographic measurements have not been performed. This becomes evident when taking a look at the electric field amplitudes in the horizontal and vertical

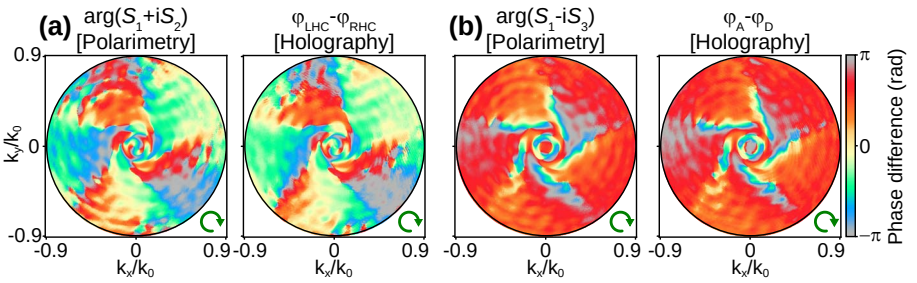

Figure 4.F.1: Validation of holography using polarimetric phase difference maps. (a,b) Difference phase maps with LHC and RHC (a) and anti-diagonal and diagonal (b) outgoing polarizations. Retrieved using polarimetry and holography for RHC polarized input light and a $m = -5$ spiral.

polarization basis:

$$E_H = E_x \exp(i\varphi_H), \tag{4.F.1a}$$
$$E_V = E_y \exp(i\varphi_V), \tag{4.F.1b}$$
$$E_D = \frac{1}{\sqrt{2}}\left[E_x \exp(i\varphi_H) + E_y \exp(i\varphi_V)\right], \tag{4.F.1c}$$
$$E_A = \frac{1}{\sqrt{2}}\left[E_x \exp(i\varphi_H) - E_y \exp(i\varphi_V)\right], \tag{4.F.1d}$$
$$E_{RHC} = \frac{1}{\sqrt{2}}\left[E_x \exp(i\varphi_H) - iE_y \exp(i\varphi_V)\right], \tag{4.F.1e}$$
$$E_{LHC} = \frac{1}{\sqrt{2}}\left[E_x \exp(i\varphi_H) + iE_y x \exp(i\varphi_V)\right], \tag{4.F.1f}$$

where φ_H and φ_V are the phase profiles in the x-direction and y-direction, respectively. Note, that since the integration time of the detector is much larger than the electric field oscillation time, the measured intensities are averaged, scalar quantities $I = \left\langle |\mathbf{E}|^2 \right\rangle$. As evident from Eqs. (4.F.1a)-(4.F.1f), only four quantities (E_x, E_y, φ_H and φ_V) need to be known to reconstruct all other polarization channels. This fact is utilized in the reconstruction procedure described below.

First, $\arg(S_2 + iS_3)$ in combination with the holographically determined phase profile φ_V are used to reconstruct φ_H, as given in Eq. (4.7a). Then, using these two phase profiles and E_x and E_y, which are also known from polarimetry measurements ($\sqrt{I(0°, 0°)}$ and $\sqrt{I(90°, 90°)}$), the remaining complex electric fields E_H,E_D,E_A,E_{RHC} and E_{LHC} were determined as specified in Eqs. (4.F.1a)-(4.F.1f). The phase profiles of these reconstruction complex fields are shown in Figs. 4.6(b) and 4.F.2(a). For comparison, the respective purely holographic phase profiles are also shown in Figs. 4.6(b) and 4.F.2(b). The

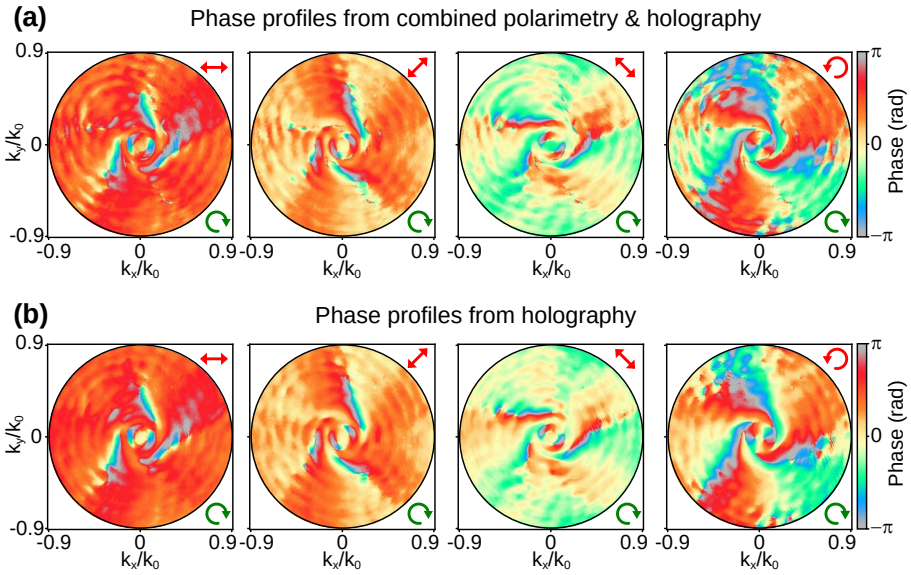

Figure 4.F.2: Phase profiles from the minimally redundant, combined holography and polarimetry approach. (a,b) Phase profiles in four polarization channels retrieved using a combination of polarimetry and holography (a) with correspondent purely holographic phase profiles for comparison (b). A $m = -5$ spiral and RHC input polarization are used. The green and red arrows indicate the input and output polarizations, respectively.

phase offsets for the combined phase reconstructions are adjusted such that the integrated phase differences between the phase profiles under comparison are minimized [57].

References

1. P. Mühlschlegel, H.-J. Eisler, O. J. F. Martin, B. Hecht, and D. W. Pohl, *Resonant optical antennas*, Science **308**, 1607 (2005).
2. P. Bharadwaj, B. Deutsch, and L. Novotny, *Optical antennas*, Adv. Opt. Photonics **1**, 438 (2009).
3. V. Giannini, A. I. Fernández-Domínguez, S. C. Heck, and S. A. Maier, *Plasmonic nanoantennas: fundamentals and their use in controlling the radiative properties of nanoemitters*, Chem. Rev. **111**, 3888 (2011).
4. H. J. Lezec, A. Degiron, E. Devaux, R. Linke, L. Martin-Moreno, F. Garcia-Vidal, and T. Ebbesen, *Beaming light from a subwavelength aperture*, Science **297**, 820 (2002).
5. A. G. Curto, G. Volpe, T. H. Taminiau, M. P. Kreuzer, R. Quidant, and N. F. van Hulst, *Unidirectional emission of a quantum dot coupled to a nanoantenna*, Science **329**, 930 (2010).
6. D. Dregely, R. Taubert, J. Dorfmüller, R. Vogelgesang, K. Kern, and H. Giessen, *3D optical Yagi-Uda nanoantenna array*, Nat. Commun. **2**, 267 (2011).
7. Y.-H. Chen, L. Huang, L. Gan, and Z.-Y. Li, *Wavefront shaping of infrared light through a subwavelength hole*, Light: Sci. Appl. **1**, e26 (2012).
8. T. Coenen, F. B. Arango, A. F. Koenderink, and A. Polman, *Directional emission from a single plasmonic scatterer*, Nat. Commun. **5**, 3250 (2014).
9. O. G. Rodríguez-Herrera, D. Lara, K. Y. Bliokh, E. A. Ostrovskaya, and C. Dainty, *Optical nanoprobing via spin-orbit interaction of light*, Phys. Rev. Lett. **104**, 253601 (2010).
10. S. S. Kruk, M. Decker, I. Staude, S. Schlecht, M. Greppmair, D. N. Neshev, and Y. S. Kivshar, *Spin-polarized photon emission by resonant multipolar nanoantennas*, ACS Photonics **1**, 1218 (2014).
11. C. I. Osorio, T. Coenen, B. J. M. Brenny, A. Polman, and A. F. Koenderink, *Angle-resolved cathodoluminescence imaging polarimetry*, ACS Photonics **3**, 147 (2016).
12. E. De Leo, A. Cocina, P. Tiwari, L. V. Poulikakos, P. Marqués-Gallego, B. le Feber, D. J. Norris, and F. Prins, *Polarization multiplexing of fluorescent emission using multiresonant plasmonic antennas*, ACS Nano **11**, 12167 (2017).
13. T. B. Hoang, G. M. Akselrod, and M. H. Mikkelsen, *Ultrafast room-temperature single photon emission from quantum dots coupled to plasmonic nanocavities*, Nano Lett. **16**, 270 (2015).
14. N. Yu, P. Genevet, M. A. Kats, F. Aieta, J.-P. Tetienne, F. Capasso, and Z. Gaburro, *Light propagation with phase discontinuities: generalized laws of reflection and refraction*, Science **334**, 333 (2011).
15. L. Huang, X. Chen, H. Mühlenbernd, H. Zhang, S. Chen, B. Bai, Q. Tan, G. Jin, K.-W. Cheah, C.-W. Qiu, *et al.*, *Three-dimensional optical holography using a plasmonic metasurface*, Nat. Commun. **4**, 2808 (2013).
16. E. Karimi, S. A. Schulz, I. De Leon, H. Qassim, J. Upham, and R. W. Boyd, *Generating optical orbital angular momentum at visible wavelengths using a plasmonic metasurface*, Light: Sci. Appl. **3**, e167 (2014).
17. K. Huang, Z. Dong, S. Mei, L. Zhang, Y. Liu, H. Liu, H. Zhu, J. Teng, B. Luk'yanchuk, J. K. Yang, and C. Qiu, *Silicon multi-meta-holograms for the broadband visible light*, Laser Photonics Rev. **10**, 500 (2016).
18. L. Allen, M. W. Beijersbergen, R. J. C. Spreeuw, and J. P. Woerdman, *Orbital angular momentum of light and the transformation of Laguerre-Gaussian laser modes*, Phys. Rev.

A **45**, 8185 (1992).
19. J. Wang, J.-Y. Yang, I. M. Fazal, N. Ahmed, Y. Yan, H. Huang, Y. Ren, Y. Yue, S. Dolinar, M. Tur, *et al.*, *Terabit free-space data transmission employing orbital angular momentum multiplexing*, Nat. Photonics **6**, 488 (2012).
20. A. E. Willner, H. Huang, Y. Yan, Y. Ren, N. Ahmed, G. Xie, C. Bao, L. Li, Y. Cao, Z. Zhao, J. Wang, M. P. J. Lavery, M. Tur, S. Ramachandran, A. F. Molisch, N. Ashrafi, and S. Ashrafi, *Optical communications using orbital angular momentum beams*, Adv. Opt. Photon. **7**, 66 (2015).
21. M. Erhard, R. Fickler, M. Krenn, and A. Zeilinger, *Twisted photons: new quantum perspectives in high dimensions*, Light: Sci. Appl. **7**, 17146 (2018).
22. M. Padgett and R. Bowman, *Tweezers with a twist*, Nat. Photonics **5**, 343 (2011).
23. J. Leach, M. J. Padgett, S. M. Barnett, S. Franke-Arnold, and J. Courtial, *Measuring the orbital angular momentum of a single photon*, Phys. Rev. Lett. **88**, 257901 (2002).
24. I. A. Litvin, A. Dudley, F. S. Roux, and A. Forbes, *Azimuthal decomposition with digital holograms*, Opt. Express **20**, 10996 (2012).
25. A. D'Errico, R. D'Amelio, B. Piccirillo, F. Cardano, and L. Marrucci, *Measuring the complex orbital angular momentum spectrum and spatial mode decomposition of structured light beams*, Optica **4**, 1350 (2017).
26. G. Kulkarni, R. Sahu, O. S. Magaña-Loaiza, R. W. Boyd, and A. K. Jha, *Single-shot measurement of the orbital-angular-momentum spectrum of light*, Nat. Commun. **8**, 1054 (2017).
27. D. J. Whitehouse, *Handbook of surface and nanometrology* (CRC press, 2010).
28. M. A. Lieb, J. M. Zavislan, and L. Novotny, *Single-molecule orientations determined by direct emission pattern imaging*, J. Opt. Soc. Am. B **21**, 1210 (2004).
29. I. Sersic, C. Tuambilangana, and A. F. Koenderink, *Fourier microscopy of single plasmonic scatterers*, New J. Phys. **13**, 083019 (2011).
30. M. Neugebauer, P. Woźniak, A. Bag, G. Leuchs, and P. Banzer, *Polarization-controlled directional scattering for nanoscopic position sensing*, Nat. Commun. **7**, 1 (2016).
31. C. I. Osorio, A. Mohtashami, and A. F. Koenderink, *K-space polarimetry of bullseye plasmon antennas*, Sci. Rep. **5**, 9966 (2015).
32. P. Hariharan, *Optical holography: Principles, techniques and applications* (Cambridge University Press, 1996).
33. E. Cuche, P. Marquet, and C. Depeursinge, *Simultaneous amplitude-contrast and quantitative phase-contrast microscopy by numerical reconstruction of Fresnel off-axis holograms*, Appl. Opt. **38**, 6994 (1999).
34. Y. Gorodetski, A. Drezet, C. Genet, and T. W. Ebbesen, *Generating far-field orbital angular momenta from near-field optical chirality*, Phys. Rev. Lett. **110**, 203906 (2013).
35. A. Mohtashami, C. I. Osorio, and A. F. Koenderink, *Angle-resolved polarimetry of antenna-mediated fluorescence*, Phys. Rev. Appl. **4**, 054014 (2015).
36. F. J. Garcia-Vidal, L. Martin-Moreno, T. W. Ebbesen, and L. Kuipers, *Light passing through subwavelength apertures*, Rev. Mod. Phys. **82**, 729 (2010).
37. H. Kim, J. Park, S.-W. Cho, S.-Y. Lee, M. Kang, and B. Lee, *Synthesis and dynamic switching of surface plasmon vortices with plasmonic vortex lens*, Nano Lett. **10**, 529 (2010).
38. L. Marrucci, C. Manzo, and D. Paparo, *Optical spin-to-orbital angular momentum conversion in inhomogeneous anisotropic media*, Phys. Rev. Lett. **96**, 163905 (2006).
39. L. T. Vuong, A. J. L. Adam, J. M. Brok, P. C. M. Planken, and H. P. Urbach,

Electromagnetic spin-orbit interactions via scattering of subwavelength apertures, Phys. Rev. Lett. **104**, 083903 (2010).
40. K. Y. Bliokh, F. Rodríguez-Fortuño, F. Nori, and A. V. Zayats, *Spin-orbit interactions of light*, Nat. Photonics **9**, 796 (2015).
41. D. Goldstein, *Polarized light*, 3rd ed. (CRC Press, Boca Raton, 2011).
42. S. Y. Suck, S. Collin, N. Bardou, Y. D. Wilde, and G. Tessier, *Imaging the three-dimensional scattering pattern of plasmonic nanodisk chains by digital heterodyne holography*, Opt. Lett. **36**, 849 (2011).
43. S. S. Kruk, Z. J. Wong, E. Pshenay-Severin, K. O'Brien, D. N. Neshev, Y. S. Kivshar, and X. Zhang, *Magnetic hyperbolic optical metamaterials*, Nat. Commun. **7**, 11329 (2016).
44. A. Martinez-Marrades, L. Greusard, Y. De Wilde, N. Bardou, S. Collin, M. Guillon, and G. Tessier, *Characterization of plasmonic nanoantennas by holographic microscopy and scanning near-field microscopy*, Opt. Commun. **359**, 455 (2016).
45. J. Babocky, A. Krizova, L. Strbkova, L. Kejik, F. Ligmajer, M. Hrton, P. Dvorak, M. Tyc, J. Collakova, V. Krapek, R. Kalousek, R. Chmelik, and T. Sikola, *Quantitative 3D phase imaging of plasmonic metasurfaces*, ACS Photonics **4**, 1389 (2017).
46. P. Zilio, G. Parisi, D. Garoli, M. Carli, and F. Romanato, *Bilayer holey plasmonic vortex lenses for the far field transmission of pure orbital angular momentum light states*, Opt. Lett. **39**, 4899 (2014).
47. D. Garoli, P. Zilio, Y. Gorodetski, F. Tantussi, and F. De Angelis, *Optical vortex beam generator at nanoscale level*, Sci. Rep. **6**, 29547 (2016).
48. T. Colomb, P. Dahlgren, D. Beghuin, E. Cuche, P. Marquet, and C. Depeursinge, *Polarization imaging by use of digital holography*, Appl. Opt. **41**, 27 (2002).
49. R. Ossikovski, *Differential matrix formalism for depolarizing anisotropic media*, Opt. Lett. **36**, 2330 (2011).
50. X. Chen, H. Gu, H. Jiang, C. Zhang, and S. Liu, *Robust overlay metrology with differential mueller matrix calculus*, Opt. Express **25**, 8491 (2017).
51. F. Dubois and P. Grosfils, *Dark-field digital holographic microscopy to investigate objects that are nanosized or smaller than the optical resolution*, Opt. Lett. **33**, 2605 (2008).
52. C. Messinis, V. T. Tenner, J. F. De Boer, S. Witte, and A. Den Boef, *Impact of coherence length on the field of view in dark-field holographic microscopy for semiconductor metrology: theoretical and experimental comparisons*, Appl. Opt. **59**, 3498 (2020).
53. P. Ferraro, S. D. Nicola, A. Finizio, G. Coppola, S. Grilli, C. Magro, and G. Pierattini, *Compensation of the inherent wave front curvature in digital holographic coherent microscopy for quantitative phase-contrast imaging*, Appl. Opt. **42**, 1938 (2003).
54. P. B. Johnson and R. W. Christy, *Optical constants of the noble metals*, Phys. Rev. B **6**, 4370 (1972).
55. J. A. Kurvits, M. Jiang, and R. Zia, *Comparative analysis of imaging configurations and objectives for Fourier microscopy*, J. Opt. Soc. Am. A **32**, 2082 (2015).
56. C. Schulze, A. Dudley, D. Flamm, M. Duparre, and A. Forbes, *Measurement of the orbital angular momentum density of light by modal decomposition*, New J. Phys. **15**, 073025 (2013).
57. J. A. Nelder and R. Mead, *A simplex method for function minimization*, Comput. J. **7**, 308 (1965).

5

SPATIAL COHERENCE MODULATION WITH MICROMIRRORS AND SURFACE WAVES ANALYZED VIA MIXED-STATE PTYCHOGRAPHY

Flexible and fast control of the phase and amplitude of coherent light, enabled by digital micromirror devices (DMDs) and spatial light modulators (SLMs), has been a driving force for recent advances in optical tweezers, nonlinear microscopy, and wavefront shaping. In contrast, engineering spatially partially coherent light remains challenging due to the lack of tools enabling a joint analysis and control sequence. In this Chapter, we first present a technique for spatial coherence measurement based on a ptychographic scanning microscope. We apply this method to two different spatial coherence engineering techniques. The first is based on a DMD to control the size of an LED source, while the second technique explores surface plasmon polariton (SPP) excitations in plasmonic nanostructures. The reported methods open up new routes to low-cost coherence control, with applications in micromanipulation, nanophotonics, and quantitative phase contrast imaging.

5.1. Introduction

OPTICAL coherence measures the degree of correlation that electromagnetic radiation exhibits in space and time [1]. Theoretical progress combined with experimental control of partially coherent light continues to advance modern technology [2]. For instance, temporally partially coherent light is leveraged for depth-gating and three-dimensional imaging in optical coherence tomography, a major scientific and technological breakthrough of the last decades [3]. An example of the utility of partial spatial coherence is very long-baseline interferometry (VLBI), where measuring spatial correlations enables imaging far distance incoherent sources using the van Cittert-Zernike theorem [4]. This has recently produced the first image of a black hole at radio frequencies [5]. These examples illustrate the importance of experimental access to both temporal and spatial coherence properties of electromagnetic radiation. However, for visible light the state of the art of coherence manipulation is arguably unbalanced. Measurement and control of temporally partially coherent light are possible thanks to the availability of high-resolution spectroscopy, supercontinuum light sources, pulse shaping devices, and a plethora of nonlinear optical phenomena allowing for frequency conversion and broadening [6]. The manipulation of spatially partially coherent light remains at a less advanced stage. While beam and coherence manipulating devices such as DMDs and SLMs are readily available, there are two primary factors that prevented efficient control of spatially partially coherent light. First, in contrast to VLBI, operating at radio frequencies and allowing to directly record phase, visible light coherence measurements require additional interferometric devices, which poses challenges in terms of stability. Second, a practical difficulty is the computational complexity of spatially partially coherent light, as it requires the specification of all two-point correlations within a beam cross-section, scaling with the fourth power of the number of samples per dimension upon discretization. This poses challenges both in terms of data acquisition and numerical processing.

Among the experimental techniques to quantify spatial coherence, Young's double slit is most prominent [7, 8]. Several techniques based on this concept have been brought forward such as redundant [9] and non-redundant aperture arrays [10] as well as non-parallel [11] and programmable slits [12, 13]. However, despite significant improvements in speed, these techniques are either limited in resolution by the spacing of the apertures or slow due to their sequential acquisition scheme. Other methods such as lateral-shearing Sagnac interferometry (LSSI) [14, 15] and phase-space tomography (PST) [16, 17] require sophisticated optical elements, potentially introducing aberrations in the coherence function to be measured. An additional complication in LSSI is the long measurement time [14]. PST is limited to paraxial optical fields and the experimental setup reported in [17] required three SLMs, driving up cost and calibration effort.

In this work, we use ptychography [18], a lensless imaging and wavefront sensing technique, for spatial coherence analysis. Ptychography has been demonstrated for label-free, quantitative phase imaging (QPI) [19, 20], and beam characterization [21–27], with added benefits through various self-calibration methods [21, 28–30]. An important extension is mixed-state ptychography, which uplifts the problem of fully coherent wavefront sensing to the computationally more complex problem of characterizing multiple incoherent contributions in a spatially partially coherent beam [31]. This technique can be used to retrieve orthogonal modes in the decomposition of the mutual intensity (MI) of a spatially partially coherent beam [32] and has become a standard tool in both x-ray and electron diffraction [33–35]. However, partial spatial coherence is considered a nuisance for high-resolution x-ray and electron diffraction imaging [33, 35–37], despite flux advantages as compared to fully coherent radiation [38]. In contrast, some visible light applications benefit from reduced spatial coherence. Examples include speckle noise reduction [39], enhanced optical sectioning [40], and partially coherent optical diffraction tomography [41]. A fast and low-cost experimental coherence control and analysis system could drive new insights in open research fields such as coherence transfer in nanophotonics [42–44] and optical tweezers with spatially partially coherent illumination [45, 46].

In Section 5.3, first a combined coherence analysis and control scheme is presented, which is based on a scanning microscope with a DMD-based programmable spatial filtering of an LED source. According to the van Cittert–Zernike theorem, which states that the intensity distribution of an incoherent source and its mutual intensity in its far-field are related through a Fourier transform, such an approach allows engineering a wide variety of spatial coherence responses by defining different source shapes and sizes. Also, a gap in the literature is the verification of the reconstruction accuracy of mixed-state ptychography for spatially partially coherent fields. We provide, to our knowledge, the first quantitative comparison of experimental mixed-state ptychography to theoretical predictions. Finally, in Section 5.4, we apply mixed-state ptychography to a novel topic in nanophotonics, which studies the influence of surface plasmon waves on statistical properties of light. To achieve this, we combine the ptychography setup with a high-NA transmission microscope. The presented initial measurement results highlight how mixed-state ptychography can benefit research on spatial coherence transfer in nanostructures.

5.2. Methods

5.2.1. Spatial coherence theory

Throughout this chapter, we restrict the discussion to quasi-monochromatic light, which allows us to omit the frequency dependence of all fields involved.

Under this assumption, spatial coherence is quantified using the mutual intensity $J(\mathbf{r}_1,\mathbf{r}_2)$, which captures correlations between pairs of points in two independent spatial variables $\mathbf{r}_1$ and $\mathbf{r}_2$. These spatial correlations can be decomposed into an orthonormal basis $\{\phi_m\}$ with $m = 1,...,M$,

$$J(\mathbf{r}_1,\mathbf{r}_2) = \sum_m \lambda_m \phi_m^*(\mathbf{r}_1)\phi_m(\mathbf{r}_2), \tag{5.1}$$

where the 'modes' ϕ_m are eigenfunctions with eigenvalues λ_m that fulfill the Fredholm integral equation as reviewed in Sec. 1.5.2 and in Refs. 32, 47. The normalized MI

$$\gamma(\mathbf{r}_1,\mathbf{r}_2) = \frac{J(\mathbf{r}_1,\mathbf{r}_2)}{\sqrt{I(\mathbf{r}_1)I(\mathbf{r}_2)}} \tag{5.2}$$

is bounded in magnitude by 0 and 1 and will be used in the following as a measure for spatial coherence. The distribution of the eigenvalues λ_m, which expresses the occupancy of the different modes, can be used to calculate an alternative coherence metric given by

$$\bar{\mu}^2 = \frac{\sum_m \lambda_m^2}{\left(\sum_m \lambda_m\right)^2}. \tag{5.3}$$

This quantity $\bar{\mu} \in [0,1]$ is referred to as the overall coherence. The inverse square of $\bar{\mu}$ provides an upper bound for the number of coherent modes required for an accurate mode representation in Eq. (5.1) [48]. In the following, we refer to this quantity as the effective number of modes $M_{\text{eff}} = 1/\bar{\mu}^2$.

5.2.2. Mixed-state ptychography

Ptychography is based on measurements of diffraction patterns generated by the interaction of a spatially bounded probe beam $P(\boldsymbol{r})$ and a scattering object $O(\boldsymbol{r})$, which is laterally scanned while a series of diffraction patterns is recorded [18]. The scan step is chosen small enough to guarantee adjacent diffraction signatures are correlated. High overlap promotes overdetermination in the inverse problem underlying ptychography, allowing to solve the inverse scattering problem by iteratively recovering the complex probe and object transmission functions [22, 23]. The mixed-state formulation of ptychography expands on this concept by recovering the orthogonal modes $P_m(\boldsymbol{r}) = \sqrt{\lambda_m}\phi_m(\boldsymbol{r})$ in the expansion of the MI of a spatially partially coherent illumination [31]. Partial spatial coherence manifests itself as reduced visibility in the diffraction intensities observed in ptychography. However, the loss of contrast in diffraction patterns is not exclusively caused by spatial decoherence but may for instance be caused by object vibrations or temporal incoherence [33, 49]. Therefore, in order to single out spatial incoherence one has to take some precautions by e.g., ensuring object stability and by spectrally filtering the light source. The forward model of ptychography assumes the

exit wave downstream of the specimen ($\boldsymbol{r}$) as product of the estimated probe and the object functions

$$\psi^n_{m,j}(\mathbf{r}) = P^n_m(\mathbf{r}) O^n(\mathbf{r} - \mathbf{t_j}), \tag{5.4}$$

where n is the iteration index and $\boldsymbol{t}_j$ is a translation vector. The exit waves for each illumination mode are propagated into the detector plane ($\boldsymbol{q}$) and incoherently added

$$I(\boldsymbol{q}) = \sum_m \left|\tilde{\psi}_m(\boldsymbol{q})\right|^2, \tag{5.5}$$

where $\psi_m(\boldsymbol{r})$ and $\tilde{\psi}_m(\boldsymbol{q})$ are related through free-space propagation. The forward model is inverted by iteratively applying gradient steps in the detector and object planes [23, 31], to wit

$$\tilde{\psi}^{n+1}_{m,j} = \frac{\sqrt{I_j}}{\sqrt{\sum_{m'} \left|\tilde{\psi}^n_{m',j}\right|^2}} \tilde{\psi}^n_{m,j}, \tag{5.6}$$

$$P^{n+1}_m = P^n_m + \frac{\beta}{\max |O^n|^2} O^{n*} \left(\psi^{n+1}_{m,j} - P^n_m O^n\right), \tag{5.7}$$

$$O^{n+1} = O^n + \frac{\beta}{\max \sum_{m'} \left|P^n_{m'}\right|^2} \sum_m P^{n*}_m \left(\psi^{n+1}_{m,j} - P^n_m O^n\right), \tag{5.8}$$

where β is a parameter that controls the step size of the probe and object updates. We omitted the functional dependencies for notational simplicity. The reconstructed probe state mixtures are iteratively orthogonalized, for instance using the Gram-Schmidt procedure or singular value decomposition. Further algorithmic details are provided in Refs. 31 and 50.

5.3. DMD-assisted coherence modulation

5.3.1. Experimental setup

The setup used for joint spatial coherence control and analysis is depicted in Fig. 5.1(a). A light control module (Texas Instruments DLP3010EVM-LC) combining an RGB LED source and a DMD is used to generate a beam with static, binary amplitude pattern encoded into it. The DMD consists of an array of 1280×720 micromirrors with a pitch of $5.4\,\mu$m. The micromirror pixels of the DMD are in the following denoted as dpx. We switch on only the red LED and further spectrally filter the light using a bandpass (BP) filter centered at $\lambda = 632.8\,$nm (FWHM of $1\,$nm) further downstream. An iris is used to limit the beam size to approximately half the angular range of the detector. After this a lens ($100\,$mm focal length) is focusing the probe beam, forming an image of the DMD $6.2\,$mm upstream of the object plane. This image is

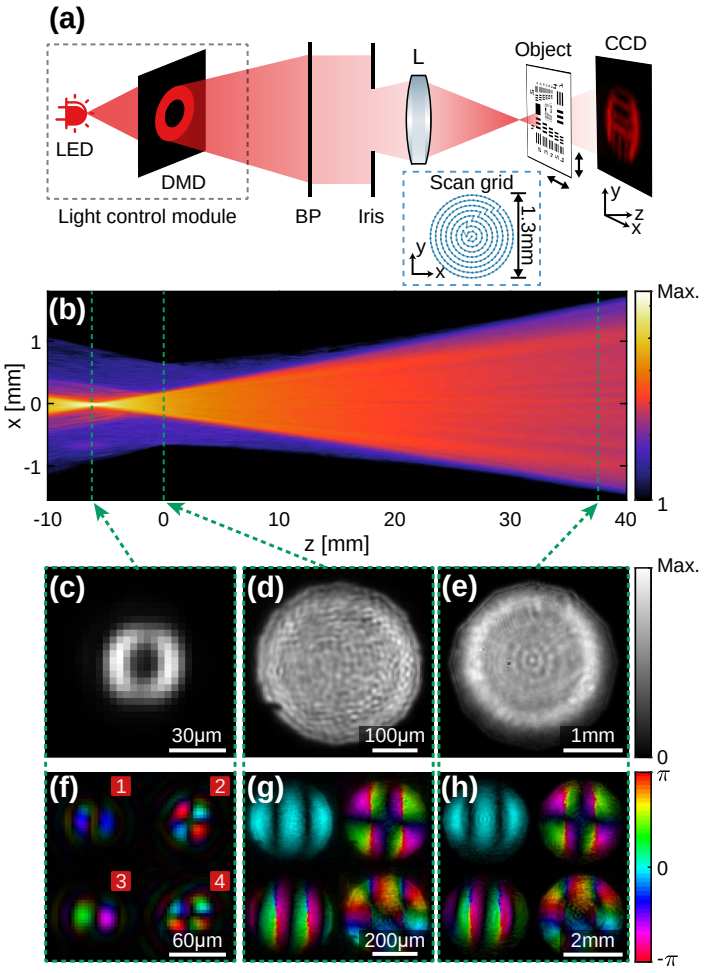

Figure 5.1: (a) Sketch of the micromirror-based mixed-state ptychography setup. The light control module consisting of an LED source and a DMD generates a beam with a binary amplitude pattern. This beam is spectrally filtered using a bandpass (BP) centered at $\lambda = 632.8\,\text{nm}$ (1 nm FWHM) and defined by an iris. A lens (L) images the DMD upstream of an object, which is mounted on a translation stage. The inset indicates the concentric object scan trajectory. A sequence of diffraction intensities is recorded on a CCD. (b) The reconstructed probe intensity in the xz plane. The planes of the DMD image, object, and CCD are indicated as dashed lines. The intensity is shown on a logarithmic color scale. (c-e) The probe intensities in the xy planes of the DMD, object, and CCD respectively. (f-h) The first four out of a total of 36 reconstructed coherent modes in the planes of (c-e). The amplitude is encoded as brightness and phase as hue. The phase curvature of the probe modes in panels (g) and (h) was removed. In panel (a) for simplicity, the reflective DMD is shown operating in transmission.

demagnified by approximately a factor 2 as compared to the original pattern displayed on the DMD. The object, a USAF resolution test target (Thorlabs R3L1S4P), is mounted on a xy-translation stage (Smaract SLC-1770-D-S, 70 nm repeatability). Finally, the scattered signals at each scan position are recorded by a CCD camera (AVT prosilica GX1920, 14 bit, 4.54 µm pixel size). The ptychography scans were performed on a concentric grid (shown as an inset in Fig. 5.1(a)). The scan grid consists of 260 steps with a step size of 70 µm and a FOV of $1.3\times1.3\,\mathrm{mm}^2$. Since in all our measurements the minimally observed beam size in the object plane had an FWHM of 262 µm, this resulted in a linear probe overlap of at least 73 %. Further setup implementation details are given in Appendix 5.A.

5.3.2. Setup characterization

The coherent mode representation offers flexibility in the characterization of partially coherent optical systems, as it allows to numerically propagate the beam to any desired propagation distance once a ptychography reconstruction has been completed. For propagation, we use the band-limited angular spectrum method described in Ref. 51. The observable intensity at a particular plane is calculated by individually propagating the coherent modes before summing them incoherently, as described by Eq. (5.5). In Figure 5.1(b), we show such a propagation result by plotting an xz-cross-section the intensity on a logarithmic scale. The plot displays a z range of $-10\,\mathrm{mm}$ to $40\,\mathrm{mm}$ with a step size of $0.1\,\mathrm{mm}$, whereby $z = 0$ is defined as the object plane. In this example, we use a ptychographic reconstruction of a measurement using a DMD image of a ring as its partially coherent source. The exact DMD image displayed a ring with an outer diameter of 15 dpx and width of 2 dpx. Figure 5.1(c-e) shows the reconstructed probe intensities at three z positions of particular interest. Fig. 5.1(c) displays the reconstructed intensity at $z = -6.2\,\mathrm{mm}$, which is an image plane of the DMD. The z position is indicated in Fig. 5.1(b) by a vertical dashed line. In addition to the mostly focused beam, the logarithmic color plot in Fig. 5.1(b) reveals the presence of background light, which is caused by the imperfect amplitude contrast of the DMD. This effect, which becomes more prominent when fewer DMD pixels are activated, did not hinder successful reconstructions since the background signal is usually captured by higher order coherent modes. The z coordinate of the DMD image plane was found manually by comparing the sharpness of the DMD pattern reconstruction in steps of $0.1\,\mathrm{mm}$. The demagnification factor of around 0.5 was obtained by comparing the size of the reconstructed DMD image to the size of the programmed DMD image (ring diameter multiplied by the DMD pixel size of 5.4 µm). Figure 5.1(d) shows the probe intensity at the object plane ($z = 0$), which for instance can be used to estimate the average probe overlap. The probe intensity in the CCD plane ($z = 37.6\,\mathrm{mm}$) is shown in Fig. 5.1(e). The probe was slightly cropped by an iris, which possesses an

image plane further downstream at around $z \approx 50\,\text{mm}$. The sample-detector distance was calibrated using the method described in Ref. 30.

The corresponding first four coherent modes are presented in Fig. 5.1(f-h). Figure 5.B.2 in the Appendix depicts all 36 reconstructed coherent modes of this example, where one can see that higher order modes contain the noisy part of the signal. Due to the focusing lens, the probe modes in the object and CCD plane have a quadratic phase curvature. To aid visual inspection, this phase curvature is compensated by multiplying with the conjugate phase of the respective primary coherent mode. This means that the phase of the coherent modes, shown in Fig. 5.1(g,h), is relative to the phase of the first coherent mode.

5.3.3. Quantitative coherence analysis

In this section, we first experimentally examine the coherence analysis capabilities of mixed-state ptychography by comparison to simulation results. Following this, we demonstrate how the two metrics described in Sec. 5.2.1, the MI $\gamma(\Delta y)$ and the overall coherence $\bar{\mu}$, can be controlled by variation of the source shape using the DMD.

In Figure 5.2, we compare experimentally obtained curves for $|\gamma(\Delta y)|$ (blue dots) to simulations (red line). The DMD images, used in these measurements are composed of a ring with a thickness of 2 dpx and the outer diameters $d = 15$ dpx and $d = 35$ dpx. We model these two extended sources as a collection of point sources, that emit mutually incoherent spherical waves from a ring-shaped area at $z = -6.2\,\text{mm}$ (conjugate plane of the DMD). To model the intensity distribution in this source area, we first generate a binary amplitude

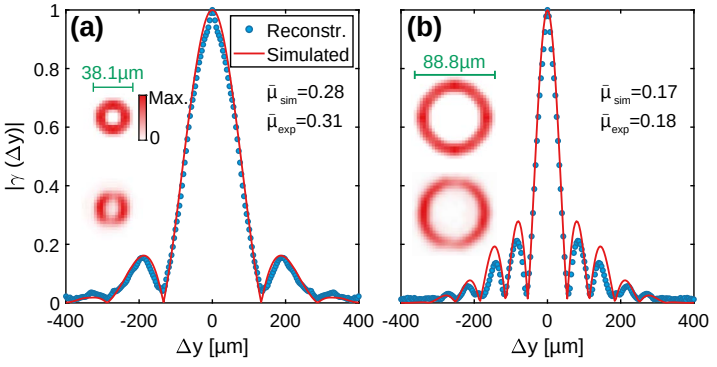

Figure 5.2: Measured and simulated magnitude of the normalized MI $|\gamma(\Delta y)|$ of two differently sized ring-shaped sources at $z = 10\,\text{mm}$. The ring diameters in the DMD images are 15 dpx (a) and 35 dpx (b). The insets show the simulated (top) and reconstructed (bottom) source intensity distributions together as well as their overall coherence $\bar{\mu}$.

mask and then blur its edges using a circular averaging filter with a radius of 2 px, approximating the low-pass filtering operation of the iris upstream of the lens in Fig. 5.1(a). The probe pixel size in both the simulated and reconstructed source images is 3.6 µm. The resulting simulated source intensities are shown in the insets of Fig. 5.2 above the corresponding experimentally reconstructed source intensities. All non-zero pixels of the simulated DMD plane act as mutually incoherent point sources. At the iris plane ($z = 50\,\mathrm{mm}$) a circular mask with a diameter of 3.6 mm is applied. Performing a singular value decomposition (SVD) on the set of spherical waves, an orthogonal mode representation of the spatially partially coherent beam is found. Finally, we propagate both the simulated and measured probe modes to $z = 10\,\mathrm{mm}$ and calculate the 2D normalized MI $\gamma(\mathbf{y}_1, \mathbf{y}_2)$ as given by Eq. (5.2) at $x = 0$. To reduce the influence of noise on the 1D cross-sections $\gamma(\Delta y)$, shown in Fig. 5.2, we average over the first 18 pixels above and below the main diagonal of the 2D mutual coherence. The simulated and measured magnitude of the normalized MI in Fig. 5.2 show an excellent agreement, quantitatively verifying the coherence measurement abilities of mixed-state ptychography.

We performed additional measurements to investigate the influence of the source shape on the MI and its associated coherence measures. In addition to the ring shape, we chose two source shapes to which we refer as Costas [52] and hexagonal arrays. Both the Costas and the hexagonal array consist of seven square elements but in different spatial arrangements. Costas arrays are latin squares in which every displacement vector is unique. Hexagonal arrays on the other hand consist of square elements arranged at the vertices and center of a regular hexagon. To give an overview over the investigated source shapes, six examples of reconstructed probe intensities in the DMD plane are shown in Figs. 5.3(a,b) and 5.4(a1-a4), where each source shape is present in two varying choices of size parameters (d, w, p). Note, that the successful reconstruction of the different source shapes through back-propagation of coherent modes further supports the validity of the presented results. The corresponding first nine coherent modes in the DMD plane are shown in Figs. 5.3(d,e) and 5.4(b1-b4). These modes can be used to gain insight into spatial correlations in the partially coherent source. Our data shows such insight beyond the fully expected localization of the reconstructed modes on the DMD mask, as an unexpected symmetry breaking, whereby the first modes preferentially show zero crossings in the horizontal direction. We attribute this to ensemble decoherence effects as a result of switching between on and off state of the micromirrors during the pattern streaming cycle, which appears even in static mode for the DMD control module deployed in our setup.

In Figure 5.3(c), we show reconstructed MI cross-sections for various sizes of the ring sources, evaluated at $z = 10\,\mathrm{mm}$. MI cross-sections results for the Costas and hexagonal array sources are shown in Fig. 5.5(a,b). Supporting details on DMD control are given in Appendix 5.A.2. The results in Figs. 5.3(c)

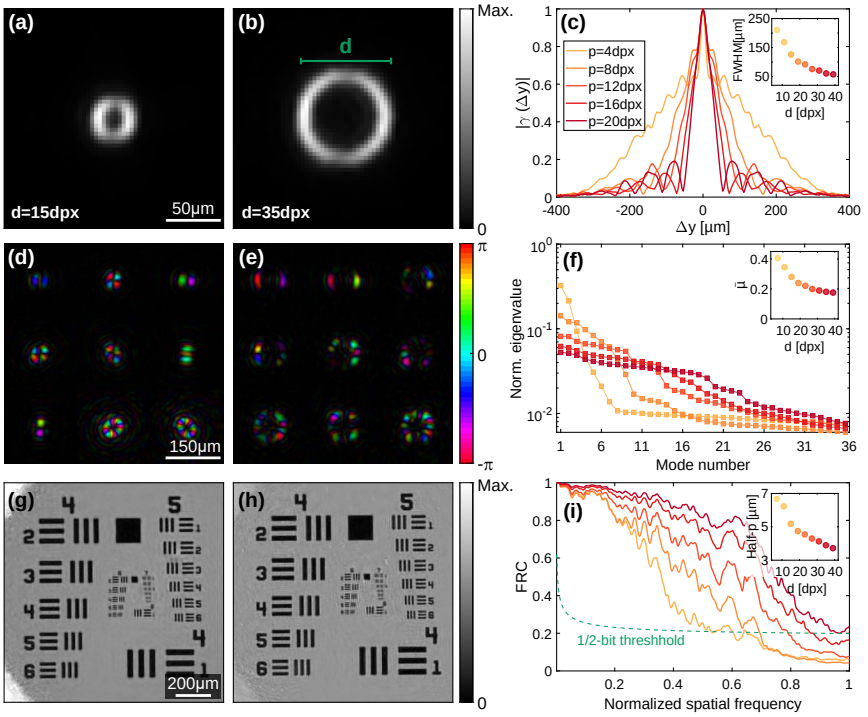

Figure 5.3: Reconstruction results for ring-shaped sources. Intensity distribution (a,b) and first nine coherent modes (d,e) of the probe at the DMD plane. (g,h) Reconstructed object intensity. (c) Magnitude of the normalized MI at $z = 10\,\text{mm}$. The inset shows the FWHM of $|\gamma(\Delta y)|$ as a function of the ring diameter d. (f) Normalized eigenvalue distribution plotted on a logarithmic scale. The inset shows the overall coherence $\bar{\mu}$. (i) Object Fourier ring correlation (FRC) as a function of normalized spatial frequency. The half-period resolution at the intersection of the FRC and the $1/2$-bit curves is shown as an inset.

and 5.5(a,b) demonstrate our ability to control and measure the MI $|\gamma(\Delta y)|$. From the insets in Figs. 5.3(c) and 5.5(a,b), we observe that an increasing source size leads to a decreasing FWHM of $|\gamma(\Delta y)|$ and therefore lower spatial coherence lengths. Since the sizes of the hexagonal arrays were chosen such that the largest separations approximately matched the ones in the Costas array, they possess FWHM values of a similar range. The 1D MI cross-section of the hexagonal array features side lobes, which are less pronounced in the other two source shapes. This can be understood as a consequence of the van-Cittert-Zernike theorem, which implies a Fourier-transform relationship between an incoherent source and its far-field mutual intensity [4]. Thus, periodic sources exhibit more pronounced correlation peaks than aperiodic sources, as seen here by comparing the MI of the hexagonal array with the MI of the Costas array.

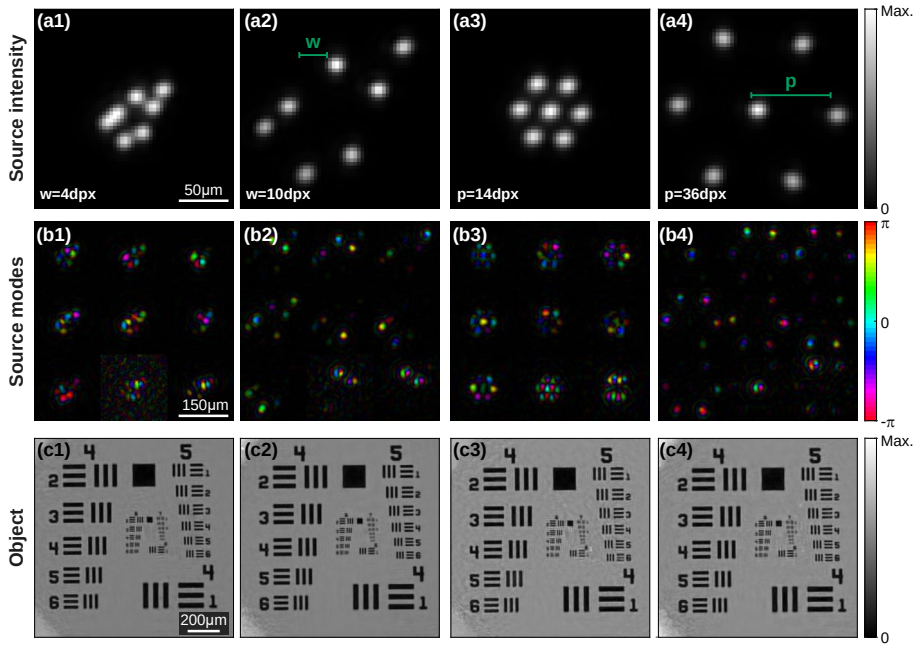

Figure 5.4: Reconstruction results for Costas and hexagonal array sources. The intensity distribution (a1-a4) and the first nine coherent modes (b1-b4) of the probe at the DMD plane. (c1-c4) The reconstructed object intensity.

The semi-logarithmic plots in Figs. 5.3(f) and 5.5(c,d) show the distribution of the eigenvalues λ_m over the first $m = 1,...,36$ modes for the three source shapes. The sum over the λ_m values was normalized to unity. For the ring-shaped source in Fig. 5.3(f), a higher diameter d continuously increases the number of occupied modes, due to the larger number of source points contained in the source. The overall coherence shown as an inset in Fig. 5.3(f) decreases from $\bar{\mu} = 0.41$ to $\bar{\mu} = 0.18$ as a function of d, which corresponds to an increase in effective modes from $M_{\text{eff}} = 6$ to $M_{\text{eff}} = 32$.

For the Costas and hexagon array sources in Fig. 5.5(c,d) the mode occupancy remains nearly unchanged during the size sweep, which is due to a fixed number of source points. Further, we observe that the eigenvalues of the Costas and hexagonal array undergo step-like changes between several plateaus of approximately constant values at integer-multiples of 7, indicating partial spatial coherence over each of the 7 active sub-areas displayed on the DMD. The insets in Fig. 5.5(c,d) show that the overall coherence for the Costas and hexagonal arrays are approximately equal. In case of the Costas array the overall coherence remains nearly constant and fluctuates around $\bar{\mu} = 0.24$, which corresponds to $M_{\text{eff}} = 17$. For the hexagonal array the overall coherence fluctuates around $\bar{\mu} = 0.22$, which corresponds to $M_{\text{eff}} = 20$.

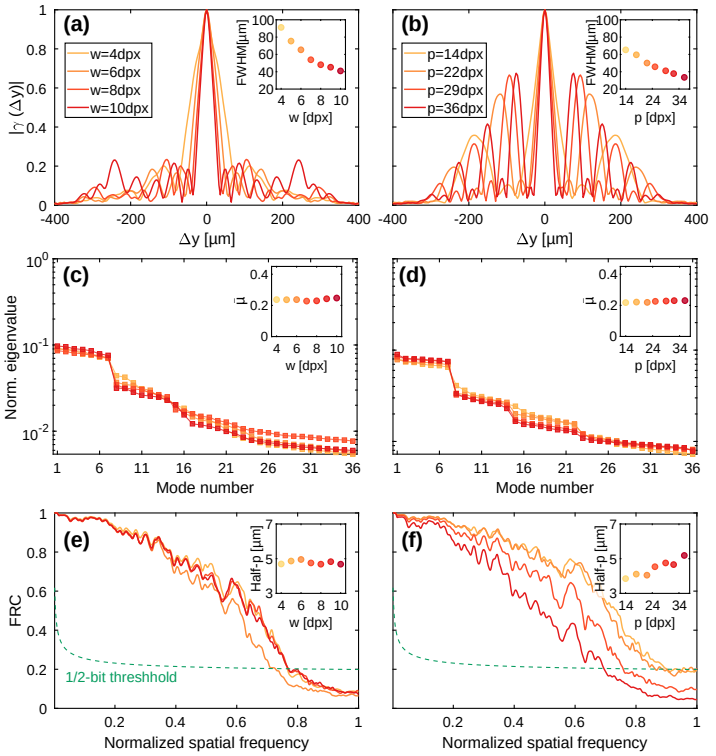

Figure 5.5: Quantitative characterization of the reconstruction results for Costas and hexagonal array sources. (a,b) Magnitude of the normalized MI at $z = 10\,\text{mm}$. The insets show the FWHM of $|\gamma(\Delta y)|$ as a function of w and p, respectively. (c,d) The normalized eigenvalue distribution plotted on a logarithmic scale. The inset panels show the overall coherence $\bar{\mu}$. (e,f) Object FRC as a function of normalized spatial frequency. The half-period resolution values are shown as insets.

5.3.4. Influence of illumination on object reconstruction

Above we have focused on the characterization of partially coherent illumination. In this section, we examine several aspects regarding the influence of partial spatial coherence on the object reconstruction quality. Structured illumination has previously been reported to offer advantages for fully coherent ptychography, due to relaxed detector dynamic range requirements [38, 53–56]. First, we investigate whether controlling the structure of partially coherent illumination affects the reconstruction quality. Second, by varying the source size we effectively alter degrees of coherence of the illumination. Previous studies have suggested that decreased spatial coherence generally leads to reduced reconstruction quality [36]. We test how the lateral spatial resolution depends on the illumination spatial coherence under variation of the source shape. Third, we compare the reproducibility of QPI via ptychogra-

phy, by comparing reconstruction obtained through fully coherent and mixed-state ptychography.

We use Fourier ring correlation (FRC) as a function of spatial frequency to quantify resolution [57]. In this method two object reconstructions, which are independently acquired under the same experimental conditions, are correlated on concentric rings in Fourier space. Here, we obtain these two independent object reconstructions by splitting the data into two half sets, each containing 130 diffraction patterns (see Appendix 5.B). Figures 5.3(i) and 5.5(e,f) summarize the FRC results for the same three source shapes as discussed in the last section with various sizes. The horizontal axis shows the spatial frequency as a fraction of the Nyquist limit. The spatial frequency at the intersection between the FRC and the 1/2-bit information threshold curve is converted into a half-period resolution value and used as a measure for spatial resolution [57]. The insets of Figs. 5.3(i) and 5.5(e,f) show all half-period results as a function of each respective scaling parameter. The results with a ring source in Fig. 5.3(i) show an improved FRC for increasing ring diameters d, with the corresponding half-period resolution shrinking from 6.7 µm to $d = 3.7$ µm. The reason for this behavior is the increased photon flux as a function of ring diameter, see Fig. 5.A.1(c) in the Appendix. Two examples of reconstructed objects with a small and large ring diameter are shown in Fig. 5.3(g) and 5.3(h), respectively. Next, in Figure 5.5(e,f), we show FRC results for the Costas and the hexagonal source arrays. Here, the source size variation changes the angles of illumination but keeps the total source area constant. The inset of Fig. 5.5(e) shows the half-period resolution extracted from the FRC results with Costas array illumination. The values do not show a clear trend but rather fluctuate around a resolution of 4.8 µm. For the hexagonal array the half-period resolution, shown in the inset of Fig. 5.5(f), seems to increase from 3.8 µm to 5.2 µm as a function of p. This is due to a decrease of incoming flux with larger p values, as shown in Fig. 5.A.1(i), caused by apodization of the source by the iris upstream of the lens in Fig. 5.1(a).

Next, we replaced the USAF target, which represents a binary amplitude object, with a biological sample containing a histological section of a human muscle. This sample features richer phase variations compared to the USAF target and is, therefore, better suited to demonstrate the QPI capabilities of mixed-state ptychography. In Figure 5.6, we compare the reconstructed object amplitude and phase under coherent and partially coherent illumination. The coherent source is a supercontinuum laser (NKT Photonics WhiteLase Micro), which was spectrally filtered to a wavelength of 708 nm (bandwidth 0.6nm) to achieve high temporal coherence and is expected to be fully spatially coherent. For the DMD-defined LED source, we used a Costas array with $w = 10$ dpx. The DMD reconstruction used 25 modes and the laser reconstruction a single mode. For further implementation details see Appendix 5.A.1. The reconstructed single mode object image was scaled to the same pixel size as the DMD reconstruction and a constant phase offset between the two images was

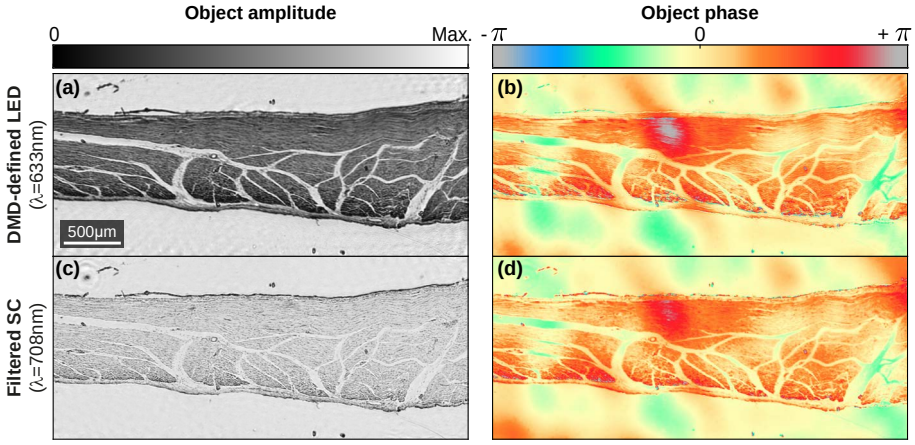

Figure 5.6: Amplitude and phase of a histological section of a human muscle imaged with mixed-state ptychography (a,b) and with fully coherent ptychography (c,d).

removed. As can be seen from Fig. 5.6(a,c), the two reconstructions show differences in the transmissivity of the object, which is caused by the stain (hematoxylin and eosin) of the sample. However, the quantitative phase profiles shown in Fig. 5.6(b,d) are in excellent agreement. This result affirms the reproducibility of mixed-state as compared to fully coherent ptychography.

5.4. Surface plasmon-assisted coherence modulation

In this section, we explore whether the above presented method can be used to study the coherence conversion induced by surface plasmon polariton (SPP) excitations in a plasmonic nanostructure. The ability of such electromagnetic surface waves to modulate the statistical properties of light has been the subject of increasing research interest [42–44, 58–62]. This effect was first observed in the well-known Young's double slit configuration [42–44]. Plasmonic waves, that are excited at either of the slits, propagate back and forth between slits before they are coupled out. The interference of the outcoupled waves with each other and the directly transmitted light causes a modulation of the spatial coherence properties of the output field. The increased or decreased correlation of waves emitted at the two slits is governed by the slit coupling efficiency and the slit separation. Other proposed surface plasmon-mediated coherence converting devices include the three-slit interferometer [58], subwavelength hole arrays [59] and metallic line gratings [62]. So far, most of the studies in this field focused on theoretical or numerical calculations [42, 43, 58–60, 62]. Experimental realizations as in Refs. 43 and 44 use the relatively simple far-field interference contrast method to experimentally characterize spatial coherence (as described in Sec. 1.5). In this work,

we leverage the reconstructed coherent modes to point out the insights the mixed-state ptychography technique can offer to this novel research field.

5.4.1. Sample fabrication

The nanostructure we study here is illustrated in the left inset of Fig. 5.7(a) and will be in the following referred to as triple bullseye (TBE) antenna. Similar designs have been used in Ref. 63 in the context of spectral imaging. The general idea behind this design is that the field scattered by this nanostructure consists not only of the directly transmitted fields from the three apertures but also of contributions mediated by SPP waves that traveled in-between the apertures and that are diffracted out by the apertures and grooves. Each bullseye antenna possesses a central aperture and three concentric grooves around it. The side-view sketch of a single bullseye antenna in Figure 5.7(b) points out the main design parameters. The sample is fabricated on a 170 µm thick glass cover slide, where a 5 nm thick Cr adhesion layer and a 250 nm thick layer of Au were deposited using electron beam physical vapor deposition (Polyteknik Flextura). The grooves were milled approximately 110 nm deep into the Au film using a focused ion beam (FEI Helios). The other parameters were chosen to be $d = 400\,\text{nm}$, $w = 220\,\text{nm}$, $p = 550\,\text{nm}$ and $a = 500\,\text{nm}$, which based on previous studies should achieve maximal transmission at around $\lambda = 640\,\text{nm}$. The distance L between the bullseyes is varied between 4.0 µm and 5.8 µm in steps of 0.2 µm. The minimal distance between different TBE structures is 40 µm. An SEM image of an example TBE structure with $L = 4.6\,\mu\text{m}$ is shown in Fig. 5.7(c).

5.4.2. Experimental setup

As shown in Fig. 5.7(a), the previous setup, shown in Fig. 5.1(a), was modified by essentially replacing the light control module with a high-NA transmission microscope. In addition, we switched the light source to a diode laser with a wavelength of 642 nm (Thorlabs LP642-SF20)[1]. This light source is assumed to be fully spatially and temporally coherent. As indicated in the left inset of Fig. 5.7(a), the linear polarization of the laser is oriented perpendicular to the connecting line of nanoapertures 1 and 3. After being coupled out of a single-mode fiber and collimated, the laser beam is focused onto the glass side of the nanoantenna sample by lens L_1, which has a focal length of 75 mm. On the other side of the sample a 100× objective (Nikon CFI L Plan EPI 100xCRA) with an NA of 0.85 is used to collect the scattered light. To image the sample plane, a mirror on a magnetic mount can redirect the beam through a tube lens L_2 with a focal length of 200 mm to CCD_1 (The

[1] This was done to achieve sufficient light transmission through the sample, to be able to perform ptychography measurements further downstream. In initial experiments, we found that the use of a focused high-powered LED source is also possible, which will be explored in follow-up work.

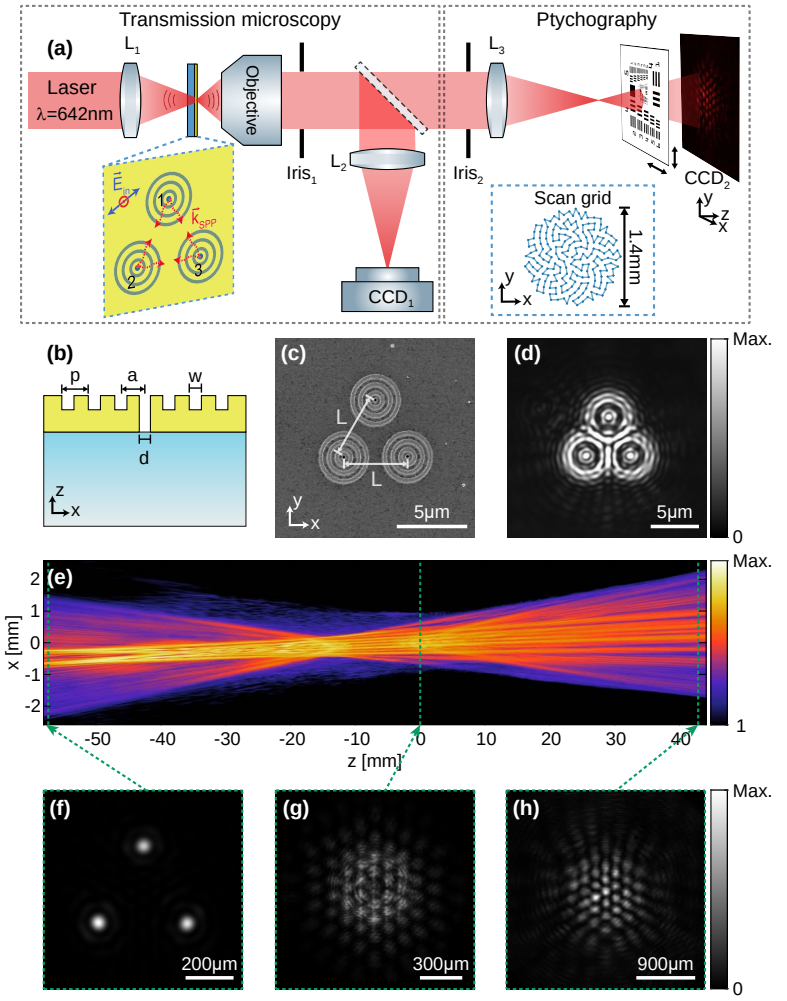

Figure 5.7: (a) Combined high-NA microscopy and ptychography setup. The left inset shows a sketch of the TBE antenna, where red arrows denote the in-plane SPP wave vectors and the blue arrow shows the incident polarization. The right inset shows the object scan trajectory. (b) Side-view sketch of a single bullseye antenna indicating the design parameters. (c) SEM image of a fabricated TBE antenna. (d) Defocused sample plane image captured by CCD_1. (e) Reconstructed probe intensity in the xz plane, showing the beam propagating from $z = -58\,\text{mm}$ to $z = 44\,\text{mm}$. The positions of the nanoantenna, object, and CCD planes are indicated as dashed lines. The intensity is shown on a logarithmic color scale. (f-h) Probe intensities in the xy planes of the nanoantenna, object, and CCD, respectively. Panels (c-h) feature a triple bullseye antenna with $L = 4.6\,\mu\text{m}$. Note, the difference in scale bars between panels (d) and (e-h) arises from the different focal distances of lenses L_2 and L_3 and the fact that the microscope image in panel (d) takes into account the 100× objective magnification.

Imaging Source DMK21AU04). This image is used to navigate and focus on the nanoantenna sample. An example image acquired with CCD_1 is shown in Fig. 5.7(d), displaying a slightly out of focus image of a TBE with $L = 4.6\,\mu m$. Such a defocus was also used during the ptychography measurements and allowed to use $Iris_1$ as a spatial filter to remove light of nearby scattering structures.

The ptychographic part of the setup is kept as described in Sec. 5.3.1. The lens L_3 (100 mm focal length) brings the probe beam in focus at around 13 mm in front of the scattering object (USAF target), which is mounted on a translation stage. The ptychographic scan grid uses now a Fermat spiral design, see inset in Fig. 5.7(a). It consists of 202 points with a step size of 90.2 µm and a FOV of $1.4 \times 1.4\,mm^2$. The probe beam size in the object plane has an FWHM of around 640 µm, which results in a linear probe overlap of around 86 %. In Figure 5.7(e), we show a propagated probe reconstruction by plotting an xz-cross-section the intensity on a logarithmic scale. The plot displays a z range of −58 mm to 44 mm with a step size of 0.2 mm. The z positions of the nanoantenna, object, and CCD planes are indicated as dashed lines. Due to the defocus of the objective, the image plane of the TBE antennas was found at around $z = -57\,mm$, see Fig. 5.7(f). Figure 5.7(g,h) shows the probe intensity further downstream in the object ($z = 0$) and CCD ($z = 42.9\,mm$) plane, respectively. As expected for three-beam interference, a hexagonal pattern emerges. This result shows that it is in principle procedurally and in terms of signal strength possible to perform ptychograpy in order to characterize the scattering properties of plasmonic nano-antennas. Due to the high degree of coherence, we used only a total of 9 modes and 500 iterations for the following reconstructions.

5.4.3. Coherence modulation results

We can now use the flexibility of the coherent mode representation to numerically propagate the beam to any desired position downstream of the sample. Propagating the beam to the TBE antenna plane enables us to evaluate the two-point correlation at the locations of the individual nanoapertures. Figure 5.8(a1-a4) shows four example probe intensity reconstructions in the plane of the TBE antennas for four aperture spacings L in the interval $L = [5 - 5.6]\,\mu m$. Some of the apertures appear darker, which is likely due to fabrication defects. The probe and the coherent modes were rotated counterclockwise by 27.5° to align the two apertures (indicated by the green and cyan dashed circles) along the y-axis. The x and y positions of nanoapertures 1 and 2, see Fig. 5.8(a1), were manually calibrated for each probe reconstruction. The position of aperture 1 was set to be in the center of the image ($x = y = 0$) by adjusting the image margins. The pixel size of the reconstructed probes was recalibrated by matching the reconstructed and expected aperture distance L, which is known from the nanofabrication design.

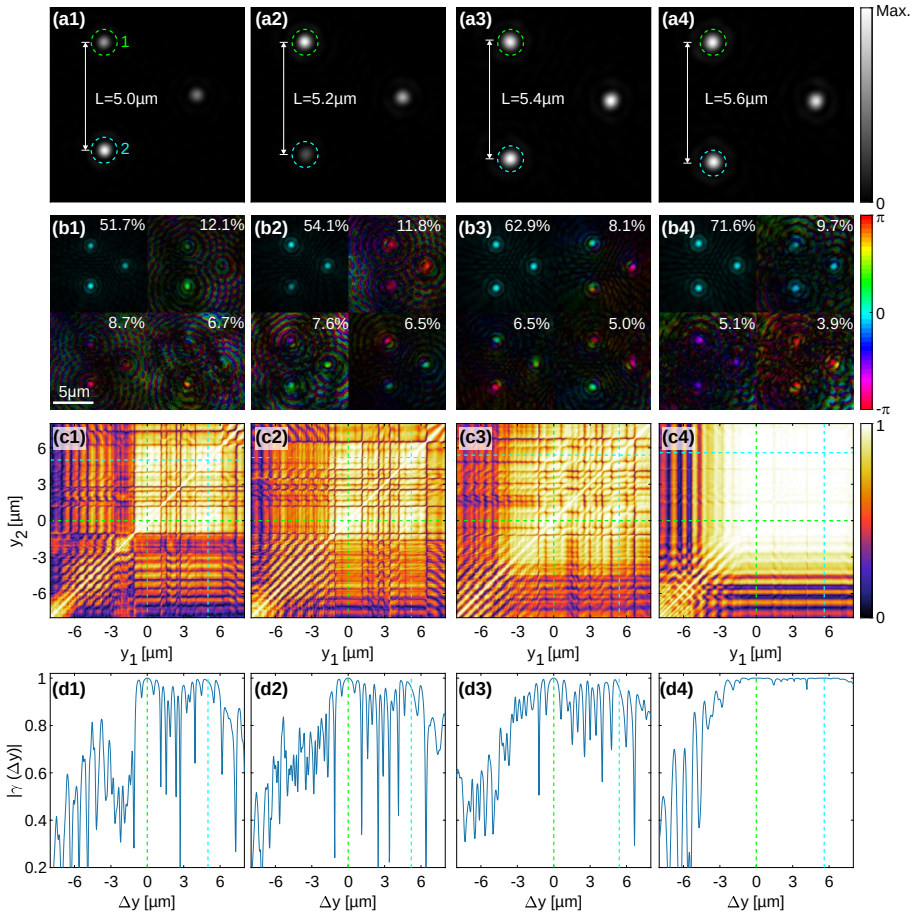

Figure 5.8: Probe reconstruction and spatial coherence analysis results for TBE antennas with $L = [5 - 5.6]\,\mu m$. Reconstructed probe intensities (a1-a4) and first four coherent modes (b1-b4) in the TBE antenna plane. The dashed circles in panels (a1-a4) indicate the manually determined positions of the two apertures. The percentages in panels (b1-b4) show the relative energies in each mode. The phase curvature of the modes in (b1-b4) was removed through multiplication with the conjugate phase of the first coherent mode. (c1-c4) Magnitude of the 2D normalized mutual intensity $|\gamma(y_1, y_2)|$ at $x = 0$ in the TBE antenna plane. (d1-d4) 1D cross-cuts of (c1-c4) along $y_2 = 0$. The green and cyan dashed lines indicate the positions of apertures one and two, respectively. The length scales were calibrated using the aperture distance L known from the fabricated design.

The corresponding first four coherent modes are shown in Fig. 5.8(b1-b4). The phase curvature contained in these modes, which is caused by the defocus of the objective, was removed by multiplying with the conjugate phase of the first coherent mode. These coherent modes allow further insight into the physics behind SPP-assisted coherence conversion effects. For instance, the

fact that all three apertures are visible in each of the first four modes indicates that waves emerging from these three apertures are highly correlated. In contrast to that, in initial measurements with a tightly focused LED beam each of the nanoapertures appeared in a separate probe mode. The fact that probe modes 2 to 4 contain considerable relative energies indicated the presence of decoherence effects, which we expect to be generated by surface plasmon propagation, i.e., the effects of cross-talk between apertures discussed by Gan *et. al.*, that can both raise and lower the partial coherence of radiated light relative to the illumination [42].

In follow up work, it would be highly interesting to investigate in detail how the coherent modes are affected by varying the spatial degree of coherence of the input light, for instance, comparing LED and laser illumination, and shaping the input light in phase and intensity. A crucial role is played according to theory by the properties of the guided modes that mediate the interaction between the apertures. By varying the wavelength, film thickness, and geometry (e.g., MIM plasmonic systems) one could hope to independently vary the SPP mode index, loss tangent, and the mixing ratio between direct and SPP-mediated transmission. The concentric features around each aperture have a periodicity that roughly corresponds to the laser wavelength. It is tempting to assign these features to a guided mode (SPPs, quasi-cylindrical waves) feature, out-coupled by surface roughness. However, we note that such an assignment is hampered by the fact that the periodicity of the fringes in the data cannot be determined within a very high accuracy from the few fringes at hand, meaning that the extracted periodicity cannot be uniquely matched to either SPPs, quasi-cylindrical waves, or the free-space wavelength.

Evaluating two point correlations allows to single out the contributions of the two apertures on the overall spatial coherence conversion. This ability to disentangle nanoaperture contributions represents a clear advantage of our technique compared to techniques that evaluate spatial coherence based on far-field interference contrast. Figure 5.8(c1-c4) shows 2D normalized MI $|\gamma(y_1, y_2)|$ plots at $x = 0$, calculated using Eq. (5.2) and the assumed nanoaperture positions indicated in Fig. 5.8(a1-a4). In these 2D color plots, values at $y_1 = y_2 = 0$ indicate the spatial correlation of the aperture 1 with itself and the values around $y_1 = y_2 = L$ show the correlation of the aperture 2 with itself. The respective L values are indicated in Fig. 5.8(a1-a4). The cross-correlation between the two apertures can be found at $y_1 = 0$ and $y_2 = L$ or $y_1 = L$ and $y_2 = 0$. Figure 5.8(d1-d4) shows 1D cross-sections $|\gamma(\Delta y)|$ extracted from the 2D normalized MI plots along $y_2 = 0$. These 1D cross-sections were averaged over the first 14 pixels above and below $y_2 = 0$ to reduce noise. Each of the 1D cross-sections features a maximum at $\Delta y = L$, indicating a high degree of spatial correlation between the two nanoapertures. In between the two apertures the $|\gamma(\Delta y)|$ curves show an oscillatory behavior, expect for the case of $L = 5.6\,\mu m$, where $|\gamma(\Delta y)|$ stays remarkably high.

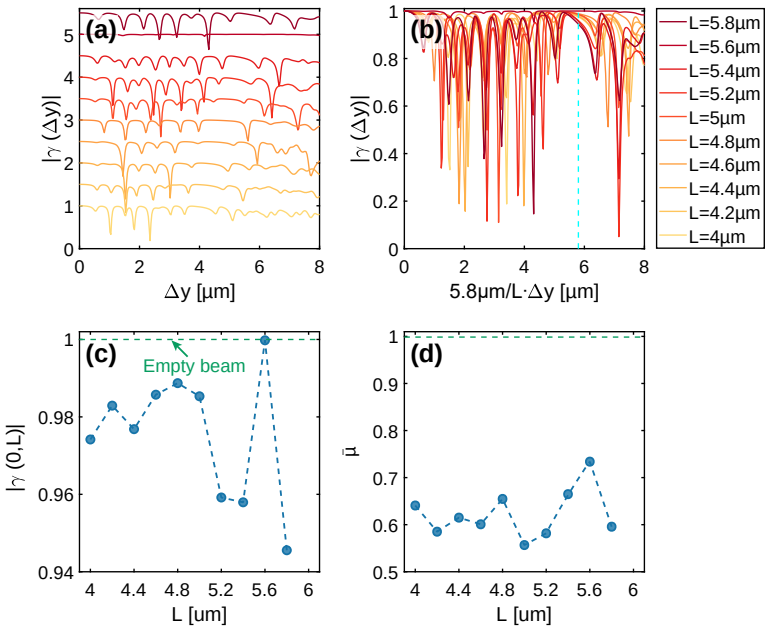

Figure 5.9: (a,b) 1D cross-cuts of the normalized MI for different aperture distances L shown as a function of Δy with an y-offset of 0.5 (a) and as a function of $5.8\,\mu m/L \cdot \Delta y$ without y-offset (b). The scaled x-axis in panel (b) causes the positions of the second aperture to coincide (indicated by vertical dashed line). (c) Correlation between the two points $(x_1 = 0, y_1 = 0)$ and $(y_2 = 0, y_2 = L)$ as a function of L. (d) Overall coherence $\bar{\mu}$ as a function of L. The green dashed line in (c,d) shows the $\gamma(\Delta y)$ and $\bar{\mu}$ results of the reference measurement from Fig. 5.C.1.

Figure 5.9(a,b) plots the retrieved $|\gamma(\Delta y)|$ results in two different manners. In Figure 5.9(a), the different $|\gamma(\Delta y)|$ curves are offset in y, which can help to identify eventual common peaks. In Figure 5.9(b), the x-axis was scaled by a factor of $5.8\,\mu m/L$. This re-scaling causes the positions of the second aperture to coincide and makes the fluctuations of $|\gamma(0,L)|$ more easily visible. In Figure 5.9(c), we show the values of $|\gamma(y_1, y_2)|$ for $y_1 = 0$ and $y_2 = L$ as a function of L. As reported in the literature for the double slit configurations in combination with thermal light sources, the mutual intensity is fluctuating as a function of the aperture separation [42–44]. The maximal value of $|\gamma(0,L)|$ is 0.9998 for $L = 5.6\,\mu m$ and the minimal value is 0.9456 for $L = 5.8\,\mu m$. Even though the observed coherence fluctuations are minor in the magnitude, our results suggest that mixed-state ptychography can successfully provide access to the physics of coherence manipulation by nanophotonic structures. In follow-up work, we intend to further optimize the fabrication process and nanostructure design, as well as use a less coherent source to systematically study the coherence converting effect. Another limitation of these initial re-

sults could be resolved by fabricating and measuring more TBE structures with a finer step size in L. This would provide a more precise sampling of the expected coherence fluctuations.

To assure ourselves that the spatial coherence modulation is not simply due to the illuminating probe beam itself, or at the experiment noise floor, we evaluated the spatial coherence of the probe beam by following the same procedure as described above but passing the beam through a large equilateral triangle with a side length of 5.8 µm that was milled into the gold film on the same sample. The results are shown in Fig. 5.C.1 in Appendix 5.C. Figure 5.9(c) shows the normalized MI $|\gamma(\Delta y)|$ result of this measurement as a dashed green line. This reference measurement resulted in a spatial coherence very close to unity over the evaluated distance of 5.8 µm. Therefore, any deviations from $|\gamma(0, L)| = 1$ in Fig. 5.9(c) indicate a modulation of the spatial coherence due to the TBE structure.

In Figure 5.9(d), an overview of the retrieved overall coherence as a function of the nanoaperture distance L is shown. The fluctuations reach a maximal value of $\bar{\mu} = 73.4\,\%$ for $L = 5.6\,\mu$m and a minimal value of $\bar{\mu} = 55.7\,\%$ for $L = 5.0\,\mu$m. The reason for the imperfect correlation between $|\gamma(0, L)|$ and $\bar{\mu}$ might be that $\bar{\mu}$ is influenced more strongly by parasitic scattering of nearby fabrication defects and surface roughness since it is a global coherence metric. In contrast, $|\gamma(0, L)|$ describes the correlation between two points and is therefore less influenced by such error sources. For comparison the horizontal dashed line shows the overall coherence ($\bar{\mu} = 99.9\,\%$) retrieved in the reference measurement from Fig. 5.C.1. The large difference in overall coherence between reference measurement and the TBE antennas can be explained by the fact that in the reference measurement most of the laser light is directly transmitted instead of being coupled into and out of SPP modes.

5.5. Conclusion and discussion

In this chapter, we presented a technique for a joint modulation and analysis of spatially partially coherent beams, relying on mixed-state ptychography. The coherence modulation was enabled by a DMD to achieve a programmable source shape and SPPs that propagate along a metal-dielectric interface. The suitability of this measurement method for quantitative retrieval of the MI was confirmed by comparing experimental and simulation results. Using three different types of DMD-defined source shapes in a variety of sizes, an extensive coherence study was performed by means of the MI and its associated spatial coherence length, as well as the distribution of mixed-state eigenvalues and the resulting overall coherence. Through back-propagation to the source plane, the different source shapes could be recovered successfully, offering an additional consistency check of the method. Furthermore, we systematically studied the relationship between the source size and the recovered object spatial resolution. The results suggest that for small illumination angles the

retrieved object resolution is mainly influenced by the light flux and not by the degree of coherence. However, despite requiring a longer reconstruction time, lower coherence was found not to be detrimental for spatial resolution, as suggested elsewhere [36]. For imaging applications, this means that in cases where the flux and coherence quantities are linked, one has the choice between reconstruction speed (low flux, high coherence) and high spatial resolution (high flux, low coherence). A measurement of a biological specimen confirmed the quantitative phase imaging abilities of mixed-state ptychography under partially coherent illumination, showing an excellent agreement with a laser-based, single-mode reconstruction. Finally, the technique was applied to study spatial coherence modulations caused by surface plasmon modes in a TBE geometry containing three nanoapertures, which were illuminated with coherent light. The initial results reveal intriguing new possibilities to characterize coherence conversion effects in nanophotonics.

Overall, mixed-state ptychography was found to be a robust and insightful measurement scheme, that allows the characterization of a broad class of spatially partially coherent beams with an arbitrary spatial structure. Commonly used spatial coherence analysis techniques that rely on interference contrast caused by, e.g. programmable apertures, rely on lengthy sequential acquisition schemes to sample the spatial coherence of the full beam. In contrast to that, the retrieved coherent-modes in mixed-state ptychography contain the full spatial coherence information of the beam, which allows one to a posteriori evaluate any desired two-point correlation in any propagation plane of the beam. We leverage this ability in Sec. 5.4 by propagating the partially coherent light back to the plane of the TBE nanostructure and analyzing the spatial correlations between the locations of the nanoapertures. This allows us to experimentally discern the source of coherence fluctuations.

Moreover, being a lensless technique, ptychography requires less sophisticated optical elements as compared to LSSI and PST and the operation wavelength is not limited to the visible range [15, 17]. A possible future improvement is a further increase in operation speed. This could be accomplished by incorporating a priori knowledge. As an example, Schell model sources can be represented as Toeplitz matrices, which could be used as a constraint during the reconstruction process [65]. In addition, when one is only interested in characterizing the probe, the object can be pre-characterized and provided as an initial guess, which significantly speeds up the convergence of the reconstruction. Together with further advancements in GPU hardware and software performance [66], we envision fast operation of the proposed technique, which would enable closed-loop coherence control. This would streamline the generation of engineered and optimized spatially partially coherent beams. On top of that, the presented method could yield a deeper understanding of the physics behind decoherence and coherence conversion in nanophotonics, paving the way for new types of flat metadevices that manipulate statistical properties of light.

APPENDICES

5.A. Setup details

5.A.1. Measurement procedure

In ptychography, a sample is laterally scanned through a stationary beam. The step size of the scan determines the overlap between successively illuminated areas on the sample and therefore the redundancy in the ptychographic data set. The linear probe overlap η is calculated using the FWHM of the probe σ_p and the scan step size s

$$\eta = \frac{\sigma_p - s}{\sigma_p}. \tag{5.A.1}$$

For the spatially partially coherent illumination condition studied here the overlap was approximately $\eta = 70\,\%$ [67, 68]. For the DMD-based illumination, shown in Fig. 5.1 of the main text, a concentric scan grid with 260 points and a step size of 70 µm was used. The size variation in the three investigated source geometries caused variable overlap in the object plane. Table 5.A.1 gives an overview over the encountered probe size and overlap values for the smallest and largest source size of each shape.

Figures 5.A.1(a,b), 5.A.1(d,e) and 5.A.1(g,h) show averages over the 260 recorded diffraction patterns, each for two sizes of the ring, Costas and hexagonal sources, respectively. The exposure time was 18 ms for the ring-shaped sources and to 19 ms for the Costas and hexagonal array sources. To estimate the available photon flux in the different data sets we plot the average integrated photon flux as a function of the three scaling parameters in Figs. 5.A.1(c), 5.A.1(f) and 5.A.1(i). These values were calculated by integrating over all pixels of each data set and dividing by the number of scan points.

For the measurements of the histological section of a human muscle, shown in Fig. 5.6, the scan grid was changed to encompass a larger field of view (FOV). Both the SC laser and the DMD measurement used a concentric grid with a FOV of $3.6 \times 1.5\,\mathrm{mm}^2$, 496 scan points and a step size of 95 µm, as shown in Fig. 5.A.1(l). For the DMD illumination, we used a Costas array source with $w = 10\,\mathrm{dpx}$. The probe had an FWHM of 440 µm in the object plane, which resulted in a beam overlap of 78 %. This higher probe

Table 5.A.1: The first and last probe size $\sigma_{x,y}$ and probe overlap η during the size sweep of the three different source shapes. $\sigma_{x,y}$ denotes the minimum of the FWHM in x and y direction. The first size indicates the smallest and last size the largest source size.

Source	$\sigma_{x,y}$ (first size)	$\sigma_{x,y}$ (last size)	η (first size)	η (last size)
Ring	421 µm	262 µm	83 %	73 %
Costas	394 µm	394 µm	82 %	82 %
Hexagonal	277 µm	270 µm	75 %	74 %

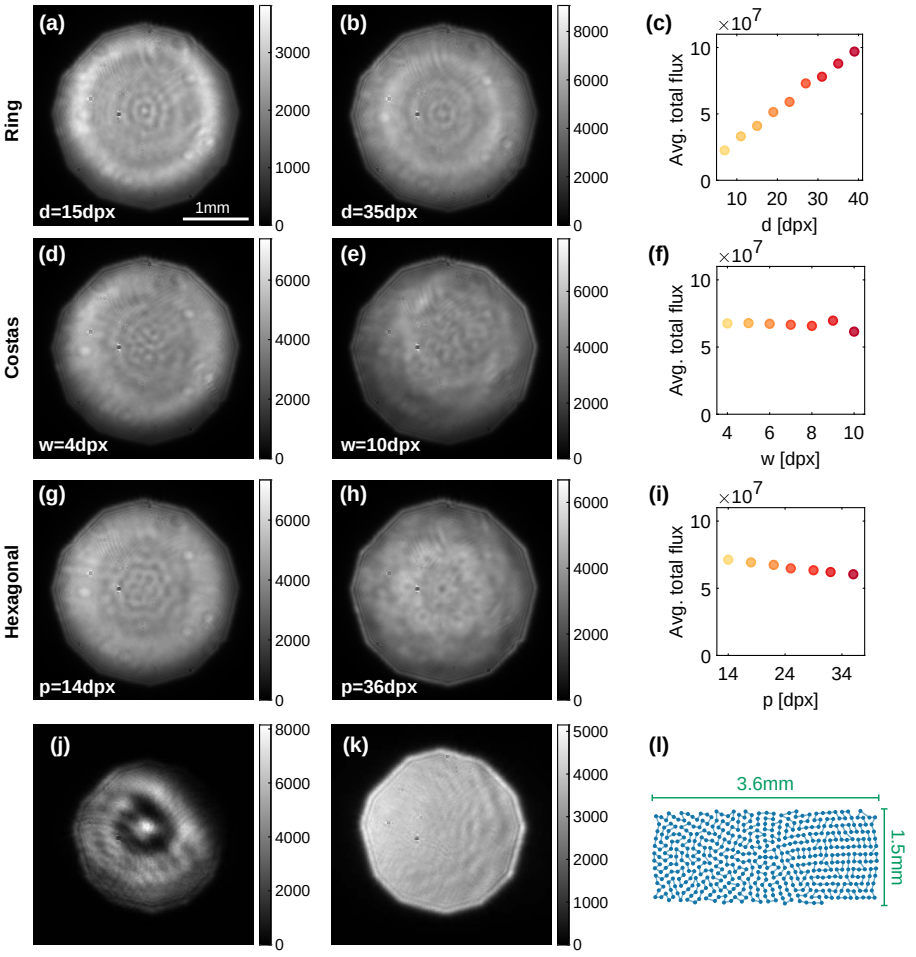

Figure 5.A.1: Average diffraction pattern for two differently sized ring (a,b), Costas (d,e), and hexagonal (g,h) array sources. (c),(f) and (i) Average integrated photon flux as a function of the three scaling parameters d,w and p. (j,k) Average diffraction pattern with the filtered supercontinuum laser (j) and DMD-defined LED (k) illumination that were used for the muscle section measurement. (l) Concentric scan grid with a rectangular FOV that was used for the muscle section measurement.

beam size was achieved by moving the focusing lens further away from the object. For the laser-based illumination, the probe had an FWHM of 160 µm, which resulted in a beam overlap of 41 %. In addition, for this measurement polarization filters were introduced before and after the object to rule out birefringence as a source for mixed states [69]. In previous measurements, this was not done since the object (USAF target) was assumed not to be birefrigent. The exposure time was set to 9 ms for the laser and 180 ms for

the DMD measurement, which resulted in average photoelectron counts of $3.5 \cdot 10^7$ for the laser and $5.6 \cdot 10^7$ for the DMD measurement. An average of the recorded 496 diffraction patterns for laser and DMD-based illumination are shown in Fig. 5.A.1(j,k).

The CCD image acquisition and stage scan procedure are automatically controlled by an in-house developed .NET software. Background signals were removed by subtracting a CCD image, which was acquired with a blocked DMD beam.

5.A.2. DMD control

The Digital Micromirror Device (DMD) consists of an array of almost a million micromirrors, which each can be set to an on or off state. The DMD is connected via HDMI to a computer as a second screen. The pattern is controlled using a Python GUI we implemented using wxPython and code from Ref. 70. To avoid pixel interpolation the Python script creates a window with the same resolution as the DMD (1280×720). Further DMD and LED settings were controlled with the DLP Display and Light Control EVM GUI tool by Texas Instruments. At low exposure times, flickering can occur due to a finite dark time of the DMD micromirrors, unless the DMD and CCD are synchronized. We attribute the ensemble coherence effects mentioned in the main text to be due to switching between the dark and bright states of the DMD.

Figure 5.A.2(a-c) shows cropped false-color versions of three different DMD images used to create the ring, Costas, and hexagonal array sources. The indicated parameters (d, w, p) were used to scale the three source shapes. The ring-shaped DMD images had a width, which remained 2 dpx and an outer diameter d, which was varied between 7 dpx and 39 dpx in steps of 4 dpx. For the Costas array, the source size was varied by increasing the distance w from 4 dpx to 10 dpx in steps of 1 dpx, while the edge length of each of the 7 square elements stayed 5 dpx. The size parameter p of the hexagonal array was chosen such that the largest distances in the Costas and hexagonal arrays approximately matched each other.

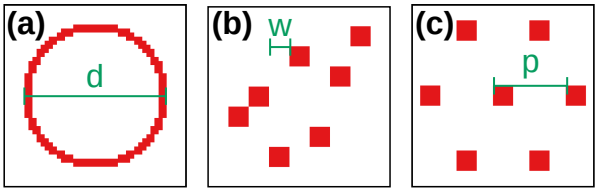

Figure 5.A.2: Examples of DMD images used to create the ring, Costas, and hexagonal array sources. Shown in false color. The indicated parameters (d, w, p) were used to scale the three source shapes.

5.B. Reconstruction details

The mixed-state ptychography algorithm was implemented in MATLAB. The feedback parameter β in Eqs. (5.7) and (5.8) in the main text is set to 0.25. As an initial guess of the probe reconstruction, a binary circle of 300 µm diameter is used.

Real-space sampling in the object plane is given by

$$\Delta r = \frac{\lambda z_o}{N \Delta q}, \tag{5.B.1}$$

where λ is the wavelength, z_o the object-detector distance, N the number of detector pixels, and Δq the detector pixel size. In addition to that, Δq also influences the probe field of view (pFOV), which is given by

$$\text{pFOV} = \frac{\lambda z_o}{\Delta q}. \tag{5.B.2}$$

We binned the detector images by a factor of 4, which leads to an effective detector pixel size of $\Delta q = 4.54\,\mu\text{m} \times 4 = 18.16\,\mu\text{m}$, while significantly reducing the reconstruction time. In the case of our DMD-based measurements, the binning resulted in an object plane sampling size of $\Delta r = 3.6\,\mu\text{m}$ and a probe FOV of $\text{pFOV} = 1.31\,\text{mm}$, which was still large enough to fully capture the probe beam in the object plane.

Each reconstruction for the DMD based source variations was run for 5000 iterations. In order to monitor the convergence during reconstruction, an error metric is calculated at every iteration as the difference between the measured and estimated diffraction patterns

$$\epsilon_n = \sum_j \left| I_{\text{meas},j}(\boldsymbol{q}) - \sum_m \left| \tilde{\psi}^n_{m,j}(\boldsymbol{q}) \right|^2 \right|. \tag{5.B.3}$$

Figure 5.B.1 shows the evolution of the error curves normalized to their maximum for the reconstructions of the three source shape size sweeps. One can see that for more incoherent cases the reconstructions tend to converge slower.

During the reconstruction in intervals of 10 iterations, the SVD-based orthogonalization of the probe is carried out [50]. The number of modes L was kept at 36 for most of the reconstructions. In Figure 5.B.2(a-c), we show all 36 reconstructed modes in the DMD, object and CCD plane, respectively for the data set with a ring-shaped source with $d = 15\,\text{dpx}$. The quadratic phase curvature of the modes, shown in Fig. 5.B.2(b,c), was removed through multiplication with the conjugate phase of the primary coherent mode. For the reconstructions with ring-shaped illumination with diameter $d = [27, 31, 35, 39]$ dpx the mode number was increased to 49 to take the lower overall coherence of those data sets into account. The MATLAB

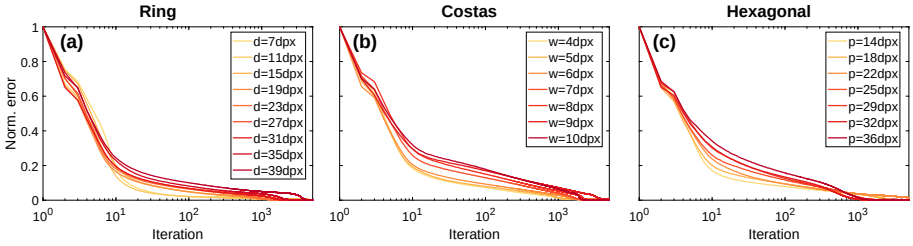

Figure 5.B.1: Convergence of the normalized error during the reconstruction of data sets using ring, Costas and hexagonal array sources of different sizes. The x-axis is shown on a logarithmic scale.

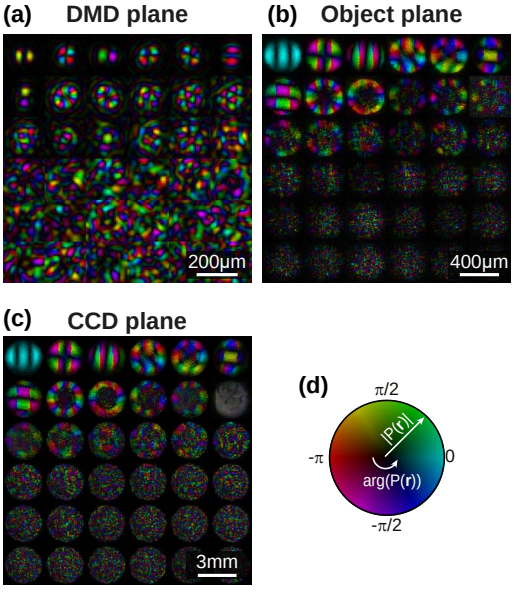

Figure 5.B.2: (a-c) Reconstructed 36 coherent modes for a ring-shaped source with $d = 15$ dpx in the DMD, object, and CCD plane, respectively. The phase curvature of the probe modes in panels (b) and (c) was removed. (d) A circular representation of the color map used to jointly represent the amplitude and phase of the mixed-modes.

reconstruction code was accelerated using NVIDIA CUDA. A reconstruction with 36 modes running for 5000 iterations took around 30 minutes on a workstation with an NVIDIA Geforce RTX 2080 Ti GPU.

For a quantitative resolution assessment of the reconstructed complex object function we use the Fourier ring correlation (FRC) approach. The FRC

results, shown in Figs. 5.3(i) and 5.5(e,f), were calculated using

$$\mathrm{FRC}(q) = \frac{\sum_{q' \in R_q} \tilde{O}_1^*(q') \cdot \tilde{O}_2(q')}{\sqrt{\sum_{q' \in R_q} \left|\tilde{O}_1(q')\right|^2 \cdot \sum_{q' \in R_q} \left|\tilde{O}_2(q')\right|^2}}, \tag{5.B.4}$$

where q denotes a spatial frequency magnitude, R_q defines a set of Fourier space pixels in a ring with radius q, $\tilde{O}_1$ and $\tilde{O}_1$ are the Fourier transformed object functions from two independent data sets. These two independent object reconstructions were obtained by performing 2000 mPIE iterations on two halves of each data set (130 images). Before the FRC is calculated the two images are spatially aligned using subpixel registration, the phase offsets are synchronized and a Hann window is applied, which removes reconstruction artifacts outside of the FOV.

5

5.C. Reference measurement for Section 5.4

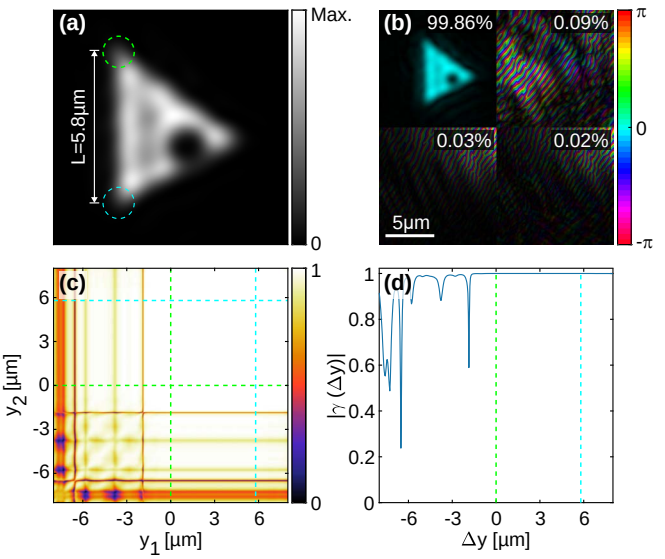

Figure 5.C.1: Reference measurement with a triangular aperture of side length 5.6 µm. Reconstructed probe intensity (a) and first four coherent modes (b) in the aperture plane. The percentages in panel (b) show the relative energies in each mode. (c) Magnitude of the 2D normalized MI $|\gamma(y_1, y_2)|$ at $x = 0$ in the aperture plane. (d) 1D cross-cuts of (c) along $y_2 = 0$. The green and cyan dashed lines indicate the positions of apertures one and two, respectively. The length scales were calibrated using the aperture size known from the fabrication design.

References

1. L. Mandel and E. Wolf, *Coherence properties of optical fields*, Rev. Mod. Phys. **37**, 231 (1965).
2. O. Korotkova and G. Gbur, *Chapter four - Applications of optical coherence theory*, in *Progress in optics*, Vol. 65, edited by T. D. Visser (Elsevier, 2020) pp. 43–104.
3. D. Huang, E. A. Swanson, C. P. Lin, J. S. Schuman, W. G. Stinson, W. Chang, M. R. Hee, T. Flotte, K. Gregory, C. A. Puliafito, and a. et, *Optical coherence tomography*, Science **254**, 1178 (1991).
4. E. Wolf, *Introduction to the theory of coherence and polarization of light* (Cambridge University Press, Cambridge, 2007).
5. K. Akiyama, A. Alberdi, W. Alef, K. Asada, R. Azulay, A.-K. Baczko, D. Ball, M. Baloković, J. Barrett, D. Bintley, and a. et, *First M87 event horizon telescope results. IV. Imaging the central supermassive black hole*, Astrophys. J. Lett. **875**, L4 (2019).
6. A. Weiner, *Ultrafast optics*, Wiley Series in Pure and Applied Optics (Wiley, 2011).
7. F. Zernike, *The concept of degree of coherence and its application to optical problems*, Physica **5**, 785 (1938).
8. B. J. Thompson and E. Wolf, *Two-beam interference with partially coherent light*, J. Opt. Soc. Am. **47**, 895 (1957).
9. J. J. A. Lin, D. Paterson, A. G. Peele, P. J. McMahon, C. T. Chantler, K. A. Nugent, B. Lai, N. Moldovan, Z. Cai, D. C. Mancini, and I. McNulty, *Measurement of the spatial coherence function of undulator radiation using a phase mask*, Phys. Rev. Lett. **90**, 074801 (2003).
10. Y. Mejía and A. I. González, *Measuring spatial coherence by using a mask with multiple apertures*, Opt. Commun. **273**, 428 (2007).
11. S. Divitt, Z. J. Lapin, and L. Novotny, *Measuring coherence functions using non-parallel double slits*, Opt. Express **22**, 8277 (2014).
12. H. Partanen, J. Turunen, and J. Tervo, *Coherence measurement with digital micromirror device*, Opt. Lett. **39**, 1034 (2014).
13. H. E. Kondakci, A. Beckus, A. E. Halawany, N. Mohammadian, G. K. Atia, and A. F. Abouraddy, *Coherence measurements of scattered incoherent light for lensless identification of an object's location and size*, Opt. Express **25**, 13087 (2017).
14. C. Iaconis and I. A. Walmsley, *Direct measurement of the two-point field correlation function*, Opt. Lett. **21**, 1783 (1996).
15. R. R. Naraghi, H. Gemar, M. Batarseh, A. Beckus, G. Atia, S. Sukhov, and A. Dogariu, *Wide-field interferometric measurement of a nonstationary complex coherence function*, Opt. Letters **42**, 4929 (2017).
16. M. G. Raymer, M. Beck, and D. McAlister, *Complex wave-field reconstruction using phase-space tomography*, Phys. Rev. Lett. **72**, 1137 (1994).
17. A. Cámara, J. A. Rodrigo, and T. Alieva, *Optical coherenscopy based on phase-space tomography*, Opt. Express **21**, 13169 (2013).
18. J. M. Rodenburg and H. M. L. Faulkner, *A phase retrieval algorithm for shifting illumination*, Appl. Phys. Lett. **85**, 4795 (2004).
19. K. Giewekemeyer, P. Thibault, S. Kalbfleisch, A. Beerlink, C. M. Kewish, M. Dierolf, F. Pfeiffer, and T. Salditt, *Quantitative biological imaging by ptychographic X-ray diffraction microscopy*, PNAS **107**, 529 (2010).
20. M. Rose, T. Senkbeil, A. R. von Gundlach, S. Stuhr, C. Rumancev, D. Dzhigaev, I. Besedin, P. Skopintsev, L. Loetgering, J. Viefhaus, *et al.*, *Quantitative ptychographic*

bio-imaging in the water window, Opt. Express **26**, 1237 (2018).
21. M. Guizar-Sicairos and J. R. Fienup, *Phase retrieval with transverse translation diversity: a nonlinear optimization approach*, Opt. Express **16**, 7264 (2008).
22. P. Thibault, M. Dierolf, A. Menzel, O. Bunk, C. David, and F. Pfeiffer, *High-resolution scanning X-ray diffraction microscopy*, Science **321**, 379 (2008).
23. A. M. Maiden and J. M. Rodenburg, *An improved ptychographical phase retrieval algorithm for diffractive imaging*, Ultramicroscopy **109**, 1256 (2009).
24. A. Schropp, P. Boye, J. M. Feldkamp, R. Hoppe, J. Patommel, D. Samberg, S. Stephan, K. Giewekemeyer, R. N. Wilke, T. Salditt, J. Gulden, A. P. Mancuso, I. A. Vartanyants, E. Weckert, S. Schöder, M. Burghammer, and C. G. Schroer, *Hard X-ray nanobeam characterization by coherent diffraction microscopy*, Appl. Phys. Lett. **96**, 091102 (2010).
25. J. Vila-Comamala, A. Sakdinawat, and M. Guizar-Sicairos, *Characterization of X-ray phase vortices by ptychographic coherent diffractive imaging*, Opt. Lett. **39**, 5281 (2014).
26. M. Du, L. Loetgering, K. S. Eikema, and S. Witte, *Measuring laser beam quality, wavefronts, and lens aberrations using ptychography*, Opt. Express **28**, 5022 (2020).
27. L. Loetgering, M. Baluktsian, K. Keskinbora, R. Horstmeyer, T. Wilhein, G. Schütz, K. S. Eikema, and S. Witte, *Generation and characterization of focused helical X-ray beams*, Sci. Adv. **6** (2020), 10.1126/sciadv.aax8836.
28. A. Maiden, M. Humphry, M. Sarahan, B. Kraus, and J. Rodenburg, *An annealing algorithm to correct positioning errors in ptychography*, Ultramicroscopy **120**, 64 (2012).
29. F. Zhang, I. Peterson, J. Vila-Comamala, A. Diaz, F. Berenguer, R. Bean, B. Chen, A. Menzel, I. K. Robinson, and J. M. Rodenburg, *Translation position determination in ptychographic coherent diffraction imaging*, Opt. Express **21**, 13592 (2013).
30. L. Loetgering, M. Du, K. S. Eikema, and S. Witte, *zPIE: an autofocusing algorithm for ptychography*, Opt. Lett. **45**, 2030 (2020).
31. P. Thibault and A. Menzel, *Reconstructing state mixtures from diffraction measurements*, Nature **494**, 68 (2013).
32. E. Wolf, *New spectral representation of random sources and of the partially coherent fields that they generate*, Opt. Commun. **38**, 3 (1981).
33. B. Enders, M. Dierolf, P. Cloetens, M. Stockmar, F. Pfeiffer, and P. Thibault, *Ptychography with broad-bandwidth radiation*, Appl. Phys. Lett. **104**, 171104 (2014).
34. S. Cao, P. Kok, P. Li, A. M. Maiden, and J. M. Rodenburg, *Modal decomposition of a propagating matter wave via electron ptychography*, Phys. Rev. A **94**, 063621 (2016).
35. Z. Chen, M. Odstrcil, Y. Jiang, Y. Han, M.-H. Chiu, L.-J. Li, and D. A. Muller, *Mixed-state electron ptychography enables sub-angstrom resolution imaging with picometer precision at low dose*, Nat. Commun. **11**, 1 (2020).
36. K. Stachnik, I. Mohacsi, I. Vartiainen, N. Stuebe, J. Meyer, M. Warmer, C. David, and A. Meents, *Influence of finite spatial coherence on ptychographic reconstruction*, Appl. Phys. Lett. **107**, 011105 (2015).
37. P. Li and A. Maiden, *Lensless LED matrix ptychographic microscope: problems and solutions*, Appl. Opt. **57**, 1800 (2018).
38. P. Li, D. J. Batey, T. B. Edo, A. D. Parsons, C. Rau, and J. M. Rodenburg, *Multiple mode X-ray ptychography using a lens and a fixed diffuser optic*, J. Opt. **18**, 054008 (2016).
39. B. Redding, M. A. Choma, and H. Cao, *Speckle-free laser imaging using random laser illumination*, Nat. Photonics **6**, 355 (2012).
40. L. Tian, J. Wang, and L. Waller, *3D differential phase-contrast microscopy with computational illumination using an LED array*, Opt. Lett. **39**, 1326 (2014).

41. J. M. Soto, J. A. Rodrigo, and T. Alieva, *Label-free quantitative 3d tomographic imaging for partially coherent light microscopy*, Opt. Express **25**, 15699 (2017).
42. C. H. Gan, G. Gbur, and T. D. Visser, *Surface plasmons modulate the spatial coherence of light in young's interference experiment*, Phys. Rev. Lett. **98**, 043908 (2007).
43. S. Divitt, M. Frimmer, T. D. Visser, and L. Novotny, *Modulation of optical spatial coherence by surface plasmon polaritons*, Opt. Lett. **41**, 3094 (2016).
44. D. Li and D. Pacifici, *Strong amplitude and phase modulation of optical spatial coherence with surface plasmon polaritons*, Sci. Adv. **3** (2017), 10.1126/sciadv.1700133.
45. L.-G. Wang, C.-L. Zhao, L.-Q. Wang, X.-H. Lu, and S.-Y. Zhu, *Effect of spatial coherence on radiation forces acting on a Rayleigh dielectric sphere*, Opt. Lett. **32**, 1393 (2007).
46. J. Auñón and M. Nieto-Vesperinas, *Partially coherent fluctuating sources that produce the same optical force as a laser beam*, Opt. Lett. **38**, 2869 (2013).
47. R. Martínez-Herrero, *Expansion of complex degree of coherence*, Il Nuovo Cimento B **54**, 205 (1979).
48. A. Starikov, *Effective number of degrees of freedom of partially coherent sources*, J. Opt. Soc. Am. **72**, 1538 (1982).
49. J. N. Clark, X. Huang, R. J. Harder, and I. K. Robinson, *Dynamic imaging using ptychography*, Phys. Rev. Lett. **112**, 113901 (2014).
50. L. Loetgering, M. Rose, D. Treffer, I. A. Vartanyants, A. Rosenhahn, and T. Wilhein, *Data compression strategies for ptychographic diffraction imaging*, Adv. Opt. Technol. **6**, 475 (2017).
51. K. Matsushima and T. Shimobaba, *Band-limited angular spectrum method for numerical simulation of free-space propagation in far and near fields*, Opt. Express **17**, 19662 (2009).
52. J. P. Costas, *A study of a class of detection waveforms having nearly ideal range-Doppler ambiguity properties*, Proc. IEEE **72**, 996 (1984).
53. A. M. Maiden, J. M. Rodenburg, and M. J. Humphry, *Optical ptychography: a practical implementation with useful resolution*, Opt. Lett. **35**, 2585 (2010).
54. A. M. Maiden, M. J. Humphry, F. Zhang, and J. M. Rodenburg, *Superresolution imaging via ptychography*, J. Opt. Soc. Am. A **28**, 604 (2011).
55. M. Guizar-Sicairos, M. Holler, A. Diaz, J. Vila-Comamala, O. Bunk, and A. Menzel, *Role of the illumination spatial-frequency spectrum for ptychography*, Phys. Rev. B **86**, 100103 (2012).
56. M. Odstrčil, M. Lebugle, M. Guizar-Sicairos, C. David, and M. Holler, *Towards optimized illumination for high-resolution ptychography*, Opt. Express **27**, 14981 (2019).
57. M. van Heel and M. Schatz, *Fourier shell correlation threshold criteria*, J. Struct. Biol. **151**, 250 (2005).
58. C. H. Gan and G. Gbur, *Spatial coherence conversion with surface plasmons using a three-slit interferometer*, Plasmonics **3**, 111 (2008).
59. C. H. Gan, Y. Gu, T. D. Visser, and G. Gbur, *Coherence converting plasmonic hole arrays*, Plasmonics **7**, 313 (2012).
60. Y. Chen, A. Norrman, S. A. Ponomarenko, and A. T. Friberg, *Coherence lattices in surface plasmon polariton fields*, Opt. Lett. **43**, 3429 (2018).
61. Y. Chen, A. Norrman, S. A. Ponomarenko, and A. T. Friberg, *Optical coherence and electromagnetic surface waves*, in *Progress in optics*, Progress in Optics, Vol. 65, edited by T. D. Visser (Elsevier, 2020) pp. 105 – 172.
62. T. Saastamoinen and H. Lajunen, *Increase of spatial coherence by subwavelength*

metallic gratings, Opt. Lett. **38**, 5000 (2013).
63. E. Laux, C. Genet, T. Skauli, and T. W. Ebbesen, *Plasmonic photon sorters for spectral and polarimetric imaging*, Nature Photonics **2**, 161 (2008).
64. P. B. Johnson and R. W. Christy, *Optical constants of the noble metals*, Phys. Rev. B **6**, 4370 (1972).
65. H. M. Ozaktas, S. Yüksel, and M. A. Kutay, *Linear algebraic theory of partial coherence: discrete fields and measures of partial coherence*, J. Opt. Soc. Am. A **19**, 1563 (2002).
66. K. Datta, A. Rittenbach, D.-I. Kang, J. P. Walters, S. P. Crago, and J. Damoulakis, *Computational requirements for real-time ptychographic image reconstruction*, Appl. Opt. **58**, B19 (2019).
67. O. Bunk, M. Dierolf, S. Kynde, I. Johnson, O. Marti, and F. Pfeiffer, *Influence of the overlap parameter on the convergence of the ptychographical iterative engine*, Ultramicroscopy **108**, 481 (2008).
68. N. Burdet, X. Shi, D. Parks, J. N. Clark, X. Huang, S. D. Kevan, and I. K. Robinson, *Evaluation of partial coherence correction in X-ray ptychography*, Opt. Express **23**, 5452 (2015).
69. P. Ferrand, A. Baroni, M. Allain, and V. Chamard, *Quantitative imaging of anisotropic material properties with vectorial ptychography*, Opt. Lett. **43**, 763 (2018).
70. S. M. Popoff, *slmPy*, Github (2017) [retrieved 30 October 2019], `https://github.com/wavefrontshaping/slmPy`.

SUMMARY

Unconventional metrology: Merging nanophotonics with computational imaging

The advent of nanofabrication enables the realization of ever smaller structures reaching down to scales below the wavelength of visible light. These opportunities ushered in a new era of nanosciences, which leverage extremely small structures to solve large problems. *Nanophotonics* is the part of nanoscience that aims to improve our understanding of the nature of light at very small length scales. On top of that, nanophotonic research has lead to the creation of novel ultra-compact devices that could help us to create a more sustainable future. Applications of nanophotonics include energy harvesting, single molecule sensing, super-resolution imaging, and computation at the speed of light. In this work, nanophotonic structures are explored to improve optical metrology and microscopy. Nanofabrication processes require extremely tight process control, and optical metrology and microscopy are measurement techniques that play an important part in benchmarking the required tolerances in position and dimensions of the fabricated nanostructures, both during and after the fabrication process.

Driven by significant advancements of computing speed and data processing algorithms, *computational imaging* has emerged as an intriguing new research area. For example, in recent years the field of smartphone photography has widely embraced computational imaging. By algorithmically fusing images, the dynamic range and sharpness of smartphone camera images have been drastically improved, which nowadays allows smartphone cameras to rival professional camera systems. Compared to traditional imaging, where images are formed directly on a detector, in computational imaging techniques images are formed indirectly after additional processing on a computer. The additional work that goes into this data processing is usually well worth it, since it enhances the measured data (e.g., super-resolution) or retrieves additional not directly detectable information (e.g., phase and coherence).

This thesis explores combinations of nanophotonic structures and computational approaches, intending to improve state-of-the-art optical microscopy and imaging. Nanophotonic structures are used in this thesis to generate extremely fine light gratings in Chapter 2 that in combination with an iterative image retrieval algorithm can improve the optical resolution in fluorescence microscopy. In Chapter 3, we propose structures to engineer far-field scattering patterns for sensitive detection of relative displacement (termed 'overlay',

in the wafer metrology community). Chapters 4 and 5 focus on the concepts of phase imaging and coherence, for which we leverage digital holography and ptychography. We show how quantitative phase imaging can give new insights into nanophotonic structures, such as nanophotonic antennas that create twisted light, while conversely investigating how nanophotonic structures can change the scattering profile and spatial coherence of light. The main conclusions of the studies in this work are summarized in the following.

In **Chapter 2**, we develop a new super-resolution fluorescence imaging technique, which we call double moiré localized plasmon SIM. It uses a combination of structured illumination and localized surface plasmons to improve the spatial resolution enhancement of SIM. In this technique, plasmonic arrays of hexagonal symmetry are illuminated with structured light. The resulting interference between the light grating and plasmonic grating creates a wide range of spatial frequencies above and below the cutoff of microscope passband. To investigate this technique we implement a rigorous simulation procedure, which simulates the near-field illumination of the plasmonic grating and uses it in a subsequent imaging forward problem. The inverse problem, of obtaining an SR image from multiple low-resolution images, is solved using different numerical reconstruction algorithms. The experimental realization proves the existence of the expected spatial frequencies and shows initial resolution improvement results.

Chapter 3 numerically investigates how more complex grating designs can offer benefits for overlay metrology. Overlay metrology characterizes spatial misalignments of subsequent patterned layers on a wafer. In Fourier scatterometry, overlay errors are determined by analyzing the light that was back-scattered by so-called overlay targets, which are grating stacks with approximately known size parameters. An outstanding challenge in Fourier scatterometry that limits the overall accuracy of the overlay determination is process variation. In this work, we study the influence of the overlay target design on its metrology performance. Specifically, we examine finite 2D arrays of scatterers as an alternative to the well-established 1D line gratings. The far-field scattering response of these arrays is simulated using generalized multi-particle Mie theory. Using an SVD-based feature extraction method a library of compressed scattering signatures is created, which allowed us to efficiently solve the inverse scattering problem of Fourier scatterometry. In subsequent Monte-Carlo simulations, periodic and deterministic aperiodic designs as well as designs that emerged from simulated annealing optimization are compared in terms of their accuracy in the presence of different noise sources. Our results reveal that, compared to the well-established line grating, the proposed 2D designs can maintain a superior overlay estimation accuracy in the presence of process variations.

Chapter 4 presents a measurement technique that combines digital off-axis holography, polarimetry, and Fourier-space microscopy to quantitatively measure amplitude, phase, directivity, and polarization of light scattered by

single nanostructures. Furthermore, we showcase how digital off-axis holography and polarimetry complement each other from the viewpoint of the practical implementation, such as measurement speed and dynamic range requirements, and can provide further insight into the underlying physics of the scattering objects. As a demonstration, we quantify the spin and orbital angular momentum imposed by plasmonic spiral nano-antennas. The results suggest that the interaction process of circularly polarized light with plasmonic spiral and bullseye antennas produces a more complex OAM state mixture than expected from theory. Therefore, the proposed method can be used to further optimize the OAM mode purity of such optical elements. From the viewpoint of scatterometry, we argue that phase and polarization contrast could give new degrees of freedom that may add sensitivity to optical metrology.

Chapter 5 studies the use of mixed-state ptychography for spatial coherence measurements of quasi-monochromatic wavefields. This lensless computational imaging technique is able to recover the coherent-mode representation of partially coherent beams, which is a computationally efficient way to fully represent spatially partially coherent light. To highlight the abilities of this method, we measure a broad class of spatially partially coherent beams, that were generated by spatially filtering an LED source using a DMD. The quantitative validity of the method is confirmed by comparing experimental and simulation results and by propagating back to the DMD plane. The retrieved spatial coherence results are further evaluated using three additional metrics, namely the spatial coherence length, the distribution of mixed-state eigenvalues, and the resulting overall coherence. After this, we assess the suitability of the presented method for studies of coherence transfer through nanophotonic structures. For this, we combine the ptychographic setup with a high-NA transmission microscope and fabricate plasmonic triple bullseye structures that exhibit SPP waves, traveling along the metal-dielectric interface. The coherent mode decomposition results hint at the emergence of decoherence effects due to the surface plasmons even for coherent illumination. Furthermore, we show our ability to a-posteriori correlate two points in the focus plane of a microscope objective, which could provide unique insights into the local influence that nanophotonic devices can exert on the statistical properties of optical beams.

SAMENVATTING

Onconventionele metrologie door nanofotonica en computationele beeldvorming te combineren

De ontwikkeling van nanofabricage technieken maakt het mogelijk om steeds kleinere structuren te realiseren, op lengteschalen veel kleiner dan bijvoorbeeld de golflengte van zichtbaar licht. Deze mogelijkheden luiden een nieuw tijdperk van nanowetenschap en nanotechnologie in, waarin extreem kleine structuren worden gebruikt om grote problemen op te lossen. *Nanofotonica* is die tak van de nanowetenschap die ons begrip van de natuurkunde en het gedrag van licht op zeer kleine lengteschalen wil verbeteren. Bovendien heeft nanofotonisch onderzoek geleid tot de ontwikkeling van nieuwe ultracompacte componenten die ons kunnen helpen een duurzamere toekomst te creëren. Toepassingen van nanofotonica zijn onder meer in het oogsten van energie uit bijvoorbeeld zonlicht, detectie van enkele moleculen, superresolutie beeldvorming en berekeningen met de snelheid van het licht. In dit werk worden nanofotonische structuren onderzocht met als doel de verbetering van optische metrologie en microscopietechnieken. Nanofabricageprocessen vereisen een extreem nauwe procescontrole en optische metrologie en microscopie zijn meettechnieken die in de halfgeleiderindustrie een belangrijke rol spelen bij het benchmarken van de vereiste toleranties in positie en afmetingen van de gefabriceerde nanostructuren, zowel tijdens als na het fabricageproces.

Gedreven door de aanzienlijke vooruitgang van rekensnelheid en algoritmen voor gegevensverwerking is *computationele beeldvorming* ontstaan als een intrigerend nieuw onderzoeksgebied. In de afgelopen jaren heeft bijvoorbeeld het gebied van de smartphonefotografie computationele beeldvorming breed omarmd. Door het algoritmisch samenvoegen van beelden zijn het dynamisch bereik en de scherpte van smartphone-camera's drastisch verbeterd, waardoor smartphone-camera's tegenwoordig kunnen wedijveren met professionele camerasystemen. In vergelijking met traditionele beeldvorming, waarbij beelden direct op een detector worden gevormd, worden bij computationele beeldvormingstechnieken de beelden indirect gevormd na extra verwerking op een computer. Het extra werk dat voor deze gegevensverwerking is vereist is meestal de moeite waard, omdat het de gemeten gegevens verbetert (bijvoorbeeld voor superresolutie) of extra niet direct detecteerbare informatie ophaalt (zoals fase en coherentie).

Dit proefschrift verkent combinaties van nanofotonische structuren en computationele benaderingen, met als doel het verbeteren van state-of-the-art optische microscopische beeldvorming en metrologie. Nanofotonische

structuren worden in dit proefschrift gebruikt om extreem fijne lichtroosters te genereren in Hoofdstuk 2 die in combinatie met een iteratief algoritme de optische resolutie in fluorescentiemicroscopie kunnen verbeteren. In Hoofdstuk 3 stellen we structuren voor om verre-veldverstrooiingspatronen te ontwikkelen voor gevoelige detectie van relatieve verplaatsing ('overlay' genoemd, in de wafermetrologiegemeenschap). Hoofdstukken 4 en 5 richten zich op de concepten van fasebeeldvorming en coherentie, waarvoor we gebruik maken van digitale holografie en ptychografie. We laten zien hoe kwantitatieve fasebeeldvorming nieuwe inzichten in nanofotonische structuren kan geven, zoals nanofotonische antennes die gedraaid licht creëren, en omgekeerd onderzoeken we hoe nanofotonische structuren het verstrooiingsprofiel en de ruimtelijke coherentie van licht kunnen veranderen. De belangrijkste conclusies van de studies in dit werk worden hieronder samengevat.

In **Hoofdstuk 2** ontwikkelen we een nieuwe superresolutietechniek voor fluorescentiebeeldvorming, die we double moiré localized plasmon SIM noemen. Het maakt gebruik van een combinatie van gestructureerde belichting en gelokaliseerde oppervlakteplasmonen om de ruimtelijke resolutie van SIM te verbeteren. In deze techniek worden plasmonische roosters met hexagonale symmetrie belicht met gestructureerd licht. De resulterende interferentie tussen het lichtrooster en plasmonisch rooster creëert een breed scala aan ruimtelijke frequenties boven en onder de cut-off van de doorlaatband van de microscoop. Om deze techniek te onderzoeken voeren we een volledige numerieke simulatie van het beoogde experiment uit, die de nabije-veldverlichting van het plasmonische rooster simuleert en daarna gebruikt in een voorwaarts beeldvormingsprobleem. Het omgekeerde probleem, het verkrijgen van een SR-beeld uit meerdere lage-resolutiebeelden, wordt opgelost met behulp van verschillende numerieke reconstructie-algoritmes. De experimentele realisatie bewijst het bestaan van de verwachte ruimtelijke frequenties en toont de eerste resultaten van de resolutieverbetering.

Hoofdstuk 3 onderzoekt numeriek hoe complexere roosterontwerpen voordelen kunnen bieden voor overlaymetrologie. Overlaymetrologie karakteriseert ruimtelijke uitlijnfouten van opeenvolgende lagen op een wafer. In Fourier-scatterometrie worden overlayfouten bepaald door het analyseren van licht dat terugverstrooid wordt door zogenaamde overlaytargets, wat gestapelde roosters zijn met ongeveer bekende afmetingen. Een open probleem in Fourier-scatterometrie die de totale nauwkeurigheid van de overlaybepaling beperkt zijn fabricagevariaties. In dit werk bestuderen we de invloed van het ontwerp van de overlaytargets op de metrologische prestaties. Specifiek onderzoeken we eindige 2D roosters van verstrooiers als een alternatief voor de huidige 1D lijnroosters. De verre-veldverstrooiingsrespons van deze roosters is gesimuleerd met behulp van gegeneraliseerde meer-deeltjes Mie-theorie. Met behulp van een op SVD gebaseerde methode om kenmerken te achterhalen wordt een bibliotheek

van gecomprimeerde verstrooiingssignaturen gecreëerd, die ons in staat stelt het inverse verstrooiingsprobleem van Fourier-scatterometrie efficiënt op te lossen. In daaropvolgende Monte-Carlo-simulaties worden periodieke en deterministische aperiodieke ontwerpen, alsook ontwerpen die voortkomen uit een simulated-annealing-optimalisatie, vergeleken in termen van hun nauwkeurigheid in aanwezigheid van verschillende ruisbronnen. Onze resultaten tonen aan dat, in vergelijking met het lijnrooster, de voorgestelde 2D-ontwerpen in staat zijn om een superieure nauwkeurigheid van de overlayschatting te behouden in aanwezigheid van fabricagevariaties.

Hoofdstuk 4 presenteert een meettechniek die digitale off-axis holografie, polarimetrie en Fourier-ruimte-microscopie combineert om kwantitatief de amplitude, fase, directiviteit en polarisatie te meten van licht dat verstrooid is door enkele nanostructuren. Verder laten we zien hoe digitale off-axis holografie en polarimetrie elkaar aanvullen vanuit het oogpunt van de praktische implentatie, zoals meetsnelheid en vereisten in dynamische bereik, en meer inzicht kunnen geven in de onderliggende fysica van de verstrooiende objecten. Als demonstratie kwantificeren we het spin- en baanimpulsmoment dat wordt opgewekt door plasmonische spiraalvormige nano-antennes. De resultaten suggereren dat het interactieproces van circulair gepolariseerd licht met plasmonische spiraal- en bullseye-antennes een complexer mengsel van OAM-toestandsen oplevert dan verwacht vanuit de theorie. Daarom kan de voorgestelde methode worden gebruikt om de zuiverheid van OAM-toestanden van dergelijke optische elementen verder te optimaliseren. We verwachten dat fase- en polarisatiemetingen in Fourier-ruimte microscopie ook voor optische metrologie belangrijke nieuwe vrijheidsgraden voor hogere gevoeligheid kunnen toevoegen.

Hoofdstuk 5 bestudeert het gebruik van mixed-state ptychografie voor metingen aan de ruimtelijke coherentie van quasi-monochromatische golfvelden. Deze lensloze computationele beeldvormingstechniek is in staat om de ontbinding in coherente toestanden van een gedeeltelijk coherente bundel te achterhalen, wat een computationeel efficiënte manier is om gedeeltelijk ruimtelijk coherent licht volledig te beschrijven. Om de mogelijkheden van deze methode te onderzoeken, meten we een brede klasse van gedeeltelijk ruimtelijk coherente lichtbundels die werden gegenereerd door het ruimtelijk filteren van een LED-bron met behulp van een "digital mirror device"(DMD). De kwantitatieve validiteit van de methode wordt bevestigd door de resultaten van experimenten en simulaties met elkaar te vergelijken en terug te propageren naar het DMD-vlak. De verkregen resultaten aan ruimtelijke coherentie worden verder geëvalueerd aan de hand van drie bijkomende metrieken, namelijk de ruimtelijke coherentielengte, de verdeling van de eigenwaarden van gemengde toestanden en de resulterende algemene coherentie. Daarna beoordelen we de geschiktheid van de gepresenteerde methode voor studies naar coherentieoverdracht in nanofotonische structuren. Hiervoor combineren we de ptychografie-opstelling met een hoog-NA transmissiemicroscoop en fabri-

ceren we plasmonische drievoudige bullseye-structuren die SPP-golven vertonen, reizend langs het metaal-diëlektricumoppervlak. De resultaten voor de ontbinding in coherente toestanden wijzen op het ontstaan van decoherentie-effecten als gevolg van oppervlakte plasmonen. Bovendien tonen we ons vermogen om a posteriori twee punten in het brandvlak van een microscoop-objectief te correleren, wat unieke inzichten zou kunnen opleveren in de lokale invloed die nanofotonische componenten kunnen uitoefenen op de statistische eigenschappen van optische bundels.

Acknowledgements

Like a mosaic, this thesis is pieced together from a collection of ups and downs, tedious endeavors, and perseverance. Looking back at the last four years, I see how this period boosted my personal development and made me a more confident person. All this would not have been possible without the amazing people I had the pleasure to meet along the way.

First of all, Femius, your guidance and support were invaluable to the completion of this work. The dedication and enthusiasm you have for science inspire your group members to achieve extraordinary things. Even though at the start of my PhD, I was not very familiar with all the topics I was getting myself into, you (and the other group members) seemed to be very optimistic about my eventual success. Your confidence in me and your open-mindedness allowed us to tackle optical metrology problems in unconventional ways and bit-by-bit lead to one successful project after the other. Even though it was stressful, your suggestions to pursue multiple projects simultaneously and to spend some *time* on *time planning* did ultimately pay off.

Being in a joint project between AMOLF and ARCNL, I had the opportunity to bring the two *physically* close institutes *thematically* a bit closer together. For enabling this opportunity and for his help with this manuscript, I would like to acknowledge my second promotor Stefan. Thank you also for welcoming me into your lab and for providing me with plenty of measurement time during these difficult times. Also, thank you to Huib and Joost for leading these two amazing research institutes.

I am also super thankful to the current and past members of the Resonant Nanophotonics group; Marko, Cocoa, Hugo, Kévin, Annemarie, Christiaan, Wouter, Isabelle, Sachin, Noor, Chris, Remi, Sylvianne, Ilse, Radoslaw, Beniamino, Tomas, Stefanos, Tom W., Ilan, and Debapriya. Thank you for your head-scratching scientific questions, for sometimes making me go for lunch or to the coffee break, and for all the great time we had together outside of AMOLF. Annemarie and Christiaan, thank you for being the best office mates I could have asked for. We should definitely go out for dinner soon. Annemarie, I really benefited from your super-duper cheerful mood and your great taste in plotting colors and food. Thank you also for the early morning breakfasts and runs (I didn't run at half my usual speed. It was more like three quarters the speed ;). Christiaan, thank you for all your support, for always providing me with the newest memes and political news, and the numerous uplifting postcards and stickers around the office. It was sad to see you leave. Even though you live in Utrecht, you managed to introduce

me to many entertaining, cultural after-work activities in Amsterdam and to arrange an apartment with housemates for me. I am very grateful for that! Isabelle, thank you for always having an open ear for me even if only to learn the latest gossip. Your ballroom dancing skills, fancy hats, and geeky jokes added an amazing flair to the group. Kévin, thank you for your politeness, spontaneousness, and for planting crazy science ideas in my head. I enjoyed playing poker and meeting strangers on Meetups with you. Hugo, thank you for your hip style, energetic dance moves, and your sharp scientific questions. Marko, thank you for teaching me the ins and outs of optical setups, showing me how to wear a beard, and being an endless source of answers to my lab-related questions. Chris and Stefanos, thank you for working with me on your MSc/BSc projects without being too intimidated by the large amounts of background literature I tend to send around. It was a pleasure to supervise both of you, and I am happy with how successful the projects turned out. Captain Tomas, thank you for the entertaining conversations at AMOLF and the great time on your sailboat. Radoslaw, thank you for all your scientific suggestions and for helping me with my COMSOL struggles. Tom W., thank you for broadcasting your calm attitude and friendliness to your surrounding, which helped me to handle the final PhD hassle. Ilan, thank you for our chats during coffee and your smooth nano-fabrication techniques. Deba, thank you for our talks on science, MATLAB, and socioeconomics. Don't forget to have fun and to avoid unnecessary meta-information.

As every former AMOLF PhD student would assure you, the institute possesses a unique, stimulating, and collaborative atmosphere. The diverse and relatively small groups at AMOLF participate in lively exchanges and collaborations to together achieve more than the sum of their parts. In particular, I want to thank the group leaders from the nanophotonics department; Albert, Femius, Ewold, Erik, Esther, Bruno, and Said for the organization of the nanocolloquia, poster sessions, and tutorials, which provide an excellent way to get an overview over all the different nanophotonics projects at AMOLF. On that note, I want to thank my collaborators from AMOLF and ARCNL. Nasim and Esther, thank you, I enjoyed working with you. The project helped me to deepen my knowledge of Fourier optics and demonstrated a nice use case of our structured illumination setup. Nick, Tom W., and Christiaan, thank you for the collaboration on the partially coherent propagation-based phase retrieval. I felt it was a really challenging but instructive undertaking. I am glad we could finish the project by pivoting to a more doable set of questions. Lukas and Wim, thank you for letting me help you measure directive emission from your beautiful self-assembled microhelices. Giorgio and Bas, thank you for your help with the optimization in the overlay sensor project. It was fantastic to see how your expertise in mechanical metamaterials can be applied to problems in nanophotonics. Lars, thank you for starting up the spatial coherence project and teaching me about ptychography. You are a true ptychography wizard! Arie and Vasco, thank you for our collaboration on the

overlay metrology project. I liked how your insights from the industry helped us to decide on which physical property to focus on.

One of the things that I appreciated hugely and what lured me to come to work at AMOLF was the broad range of experienced support personnel. I want to thank the excellent and super friendly people from all the support departments at AMOLF. I am especially grateful to the NanoLab team for their tremendous support with nano-fabrication in my PhD. Hans Z., Dimitry, Bob D., Andries, and Igor, thank you for providing me with training, always answering my many questions, and for keeping the NanoLab running (even when now and then all the equipment decides to fail at the same time). Sjoerd, Jorijn, and Marco K., thank you for writing great software for our setups and the quick bug fixes. Bob K. and Mels, thank you for supporting me when it came to electronics or LEDs. I am thankful to Carl, Wiebe, Rutger, and Richard for their skilled ICT support. I am grateful for the support from Jan v. d. L., Henk-Jan, Ricardo S., Ricardo E., Wessel, and Tom B. for creating setup parts and 3D renderings for me. Thank you for helping me with the laser cutter. I enjoyed laser-cutting crazy goggles for Open Day. And thank you to all AMOLF PV members, for organizing all the super fun borels and the best Christmas parties.

I am very grateful for the hospitality and friendliness that I experienced from all the people I got to know in Amsterdam. A big thank you to my amazing housemates. Remmert, thank you for all the late-night talks and your programming and life advices. Luuk, thank you for being the handyman of the house, the fun at Lowlands, and your super relaxed attitude. Matthias, welcome to the apartment! Thanks for being such a cool dude. I wish you a great PhD experience in Amsterdam. Thank you to my awesome colleagues from AMOLF and ARCNL; Alessandro, Lucie, Nasim, Mark A., Maisie, Jenny, Dario, Giovanni, Christian D., Benjamin D., Parisa, Tom V., Iaroslav, Ilya, Sophie, Magda, Jente, Jesse, Johneph, Marloes, Dolphine, Lorenzo, John, Giada, David, Andrea, Kevin L., Lucas P., Sander, Filipo, Hessel, Nikhil, Roberto, Alexander K., Ariane, Zhou, Sven, Carolyn, Nicola, Giulia, Federica, Sven, Susan, Yorick, Hinco, Olga, and Mareike. There are a couple of people that I would like to highlight here. Lukas, thank you for being a fantastic person and for organizing fantastic house parties and BBQs! I vividly remember the disco balls, laser lights, fog machines, aluminum foil, and lots of happy people. Giorgio, I very much enjoyed reading your well-structured MATLAB scripts, race biking, and talking about the stock market with you. Lars, I was amazed to see how passionate and talented you are when it comes to physics, beer brewing, and tiny house building. I am excited to hear about your future quests in life. Verena, thank you for teaching me how to use and clean the spin-coater and for being such a super friendly person. Hans H. and Arno, thank you for inviting me to many super fun activities (karaoke, poker, board games) and for being such amazing geeks. I even appreciated the backstabbing Among Us. Agustin, Dominique, Nick, Robin, Rene, and

Moritz, I found the extended coffee breaks with you highly *gezellig*. Teressa and Harshal, you really know how to get the crowd going on the dance floor. Mathijs, thank you for prepping me for the marathon. Anne, I really enjoyed our bike rides, bouldering at 1.5 m distance, and the nerd nites you organized.

I am most thankful for the support I received from my family and friends. Mama, Papa, and Valera, I feel very fortunate to have you, spasibo. Thank you to my friends from my hometown and from Aachen who managed to stay in touch with me, even though the distance between us has increased, and the rate of my replies to your texts has decreased. Finally, thank you, Inge, for all the encouragement and love!

About the author

Ruslan was born in Altajskoje, Russia, in 1990. At the age of ten, he moved to Germany and received his Abitur from Gymnasium Erwitte in 2010. After half a year of military service, he enrolled in a Bachelor of Science in Physics at the RWTH Aachen. During his Bachelor's, he took a part-time job as a research assistant at the Fraunhofer Institute for Production Technology IPT, where he worked on 3D laser writing of microstructures. For his Bachelor thesis, he used this technique to fabricate isotropic 3D metamaterials as part of a *collaboration* between the Infrared Nano Optics group of prof. dr. Thomas Taubner at the RWTH and the micro and nano metrology group of Dipl. Phys. Stephan Stürwald at the Fraunhofer IPT. For his Master's, Ruslan stayed at the RWTH and specialized in condensed matter physics and nano-optics. During the second Master semester, he traveled abroad to the TU Delft, where he discovered his passion for the Netherlands, nanotechnology applications, and the inner workings of start-ups. For his Master thesis at the RWTH, he chose again a collaborative project. The *collaboration* involved the Infrared Nano Optics group of prof. dr. Thomas Taubner and the Micro and Nano Structuring group of Dipl. Phys. Martin Reininghaus from the Fraunhofer ILT. After graduating, he left Aachen in 2016 for Amsterdam, where he started his PhD research in a *collaboration* between AMOLF and ARCNL under the supervision of prof. dr. A. Femius Koenderink and dr. Stefan M. Witte. In his free time, Ruslan enjoys doing sports (running, biking, snowboarding, and bouldering), tinkering with code, listening to audiobooks, watching movies, and playing board games with friends.

List of Publications

Related to this thesis

1. R. Röhrich, and A. F. Koenderink, *Double moiré localized plasmon structured illumination microscopy*, Nanophotonics, submitted (**Chapter 2**).

2. R. Röhrich, G. Oliveri, S. Kovaios, V. T. Tenner, A. J. den Boef, J. T. B. Overvelde and A. F. Koenderink, *Uncertainty estimation and design optimization of 2D diffraction-based overlay metrology targets*, ACS Photonics **7**, 10 (2020) (**Chapter 3**).

   All authors conceived the project idea. R.R and S.K. implemented the data analysis, G.O. implemented the optimizations, A.F.K. supervised the project. R.R. and A.F.K. wrote the manuscript, which was then revised by all authors.

3. R. Röhrich, C. Hoekmeijer, C. I. Osorio and A. F. Koenderink, *Quantifying single plasmonic nanostructure far-fields with interferometric and polarimetric k-space microscopy*, Light Sci. Appl. **7**, 65 (2018) (**Chapter 4)**.

   C.I.O. and A.F.K. conceived the project idea. C.H. and R.R. realized the set-up, fabricated and designed the samples and performed the measurements. All authors jointly conceived the data analysis method, which was implemented by R.R and C.H.; A.F.K. supervised the project. R.R. and A.F.K. wrote the manuscript, which was then revised by all authors.

4. R. Röhrich, A. F. Koenderink, S. Witte, and L. Loetgering *Spatial coherence control and analysis via micromirror-based mixed-state ptychography*, Optica, submitted (**Chapter 5**).

   L.L conceived the project idea. R.R. and L.L. realized the set-up and performed the measurements. L.L. implemented the reconstruction algorithm and R.R. and L.L implemented the data analysis. S.W and A.F.K. supervised the project. R.R. and L.L. wrote the manuscript, which was then revised by all authors.

5. R. Röhrich, A. F. Koenderink, S. Witte, and L. Loetgering *Experimental characterization of surface plasmon-assisted coherence modulation via mixed-state ptychography*, in preparation (**Chapter 5**).

   R.R, L.L and A.F.K. conceived the project idea. R.R. and L.L. realized the set-up and performed the measurements. L.L. implemented the reconstruction algorithm and R.R. and L.L implemented the data analysis. S.W and A.F.K. supervised the project.

Other

1. L. Helmbrecht, M. Tan, R. Röhrich, M. H. Bistervels, B. O. Kessels, A. F. Koenderink, B. Kahr, and W. L. Noorduin , *Directed Emission from Self-Assembled Microhelices*, Adv. Funct. Mater. **30**, 1908218 (2020).

2. N. Tavakoli, R. J. Spalding, P. Koppejan, G. Gkantzounis, C. Wan, R. Röhrich, E. Kontoleta, A. F. Koenderink, R. Sapienza, M. Florescu, and E. Alarcon-Llado, *Over 65 % sunlight absorption in a 1 μm Si slab with hyperuniform texture*, Nat. Commun., submitted.

3. N. J. Schilder, T A. W. Wolterink, C. Mennes, R. Röhrich, and A. F. Koenderink, *Phase-resolved Fourier microscopy on plasmonic bullseye antennas by defocused imaging using partially temporally incoherent light*, Opt. Express, submitted.